Peat's secret archive: Interpreting the geochemical and palaeodust record from Scottish peat as a potential index of North Atlantic storminess and Holocene climate change.

Helena K. Stewart

Submitted for the degree of Doctor of Philosophy

Biological and Environmental Sciences

Faculty of Natural Sciences

University of Stirling

2016

STATEMENT OF ORIGINALITY

I hereby confirm that the research contained in this thesis is original, has been completed by the author and all the work contained herein has not been submitted for any other degree.

All published material has been duly acknowledged and cited.

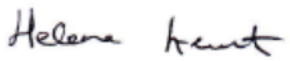

……..

Helena K. Stewart

Date: 19/01/2017

ABSTRACT

Four continuous high-resolution peat records for the Holocene have been reconstructed across a ~300km transect from Shebster in Caithness to Yell in the Shetland Isles. These records describe the nature and extent of North Atlantic climate changes inferred from indicators of storminess and minerogenic aeolian dust, and are supported by radiogenic isotope analysis, tephrochronology and radiocarbon dating. The environmental changes at all four sites displays a significant degree of synchrony in response to changes in the position of the polar front jet (PFJ) stream and the phase of the North Atlantic Oscillation (NAO). Bromine concentrations in the peat, derived from sea spray, are used to reconstruct storm frequency and storm intensity, and mire surface wetness is used as an indicator of longer-term climate shifts. The results suggest a strong link between positive phases of the NAO and storminess. Subtle differences between the bromine concentrations and the mire surface wetness suggest that high intensity but perhaps less frequent periods of storminess are not necessarily associated with a wetter climate. Atmospheric minerogenic dust concentrations are used to reconstruct large-scale climate changes across the wider North Atlantic region. The results suggest a sympathy between dust activity and periods of glacial advance and a negative index of the NAO. Radiogenic isotope analysis suggests that the smallest particles may originate from Iceland.

ABBREVIATIONS

AMO: Atlantic multidecadal oscillation

AMS: Accelerator Mass Spectrometry

AWB: Anticyclonic wave breaking

AO: Arctic Oscillation

Br: Bromine

Cal yr BP: Calibrated years before present (relative to AD 1950)

CWB: Cyclonic wave breaking

EA: Eastern Atlantic pattern

EMP: Electron Microprobe

ENSO: El Nino / Southern Oscillation

LIA: Little Ice Age

MSW: Mire surface wetness

MWP: Medieval Warm Period

NAO: North Atlantic Oscillation

PFJ: Polar front jet

SCA: Scandinavian pattern

SLP: Sea level pressure

SNAO: Summer North Atlantic Oscillation

SPV: Stratospheric polar vortex

SST: Sea surface temperature

STJ: Subtropical jet

VEI: Volcanic Explosivity Index

XRF: X-ray fluorescence

ACKNOWLEDGEMENTS

Firstly, I would like to express my thanks and gratitude to my principal supervisor Dr Robert McCulloch for all his support throughout this project and always being on hand when I needed help. I would especially like to thank him for his assistance during all fieldwork and teaching me the methods I used in the lab.

I would also like to thank my supervisors Dr Tom Bradwell and Professor Joanna Bullard for all their support and input throughout this project and their assistance during fieldwork in the Shetland Isles.

This thesis was funded through the Natural Environmental Research Council (NERC), British Geological Survey (BGS) and University of Stirling. I also received support from the Quaternary Research Association (QRA) for electron microprobe analysis and the Scottish Alliance for Geosciences, Environment and Society (SAGES) for attending conferences.

I am grateful to Mary McCulloch, James Blaikie and Melanie Kingsbury for their support in the field retrieving the cores from Shebster, Caithness and Heldale, Orkney. I would also like to thank Jane Bray and Sam Harris for their work on Loss on Ignition and Humification, and Jane especially for teaching me the acid digestion method.

I would like to thank the Natural Environmental Research Council Radiocarbon Laboratory in East Kilbride for radiocarbon support (Allocation: 1879.0415 and especially to Dr. Pauline Gulliver for assisting me with the radiocarbon dating process.

During the project, I worked in a number of specialist laboratory facilities: I would like to extend my gratitude to Dr Ian Millar for all his help and support of the radiogenic isotope analysis carried out at the British geological Survey (BGS) in Keyworth. I would also like to thank Dr Anthony Newton and Dr Chris Haywood for their assistance in preparing tephra samples and using the electron microprobe at Edinburgh University. Lastly, I would like to thank Dr Sarah Davies for all her help in operating the ITRAX™ micro-XRF Core Scanner at Aberystwyth University.

TABLE OF CONTENTS

LIST OF FIGURES

LIST OF TABLES

Chapter 1: Introduction

1.1: Scope of the Project

Northern Scotland is an ideal location for reconstructing the recent climate history of the North Atlantic (Figure 1.1). On a local scale, Scottish weather is regularly influenced by the position and movement of the jet stream and is frequently affected by high magnitude storms generated in the North Atlantic. These storms can be quite severe, sometimes causing damage to infrastructure, property and farmland through high winds and intense flooding (Kendon and McCarthy, 2015). On a wider scale, the frequency and intensity of these storms may be related to the phase of the North Atlantic Oscillation (NAO) (Clarke and Rendell, 2009). Positive phases correspond to wetter, stormier weather over the UK whereas negative phases are associated with drier and calmer weather (Burningham and French, 2013, Gómara *et al*., 2014). These large atmospheric circulation patterns may also influence the transport of minerogenic dust from far-travelled areas such as Iceland or the Sahara.

Where palaeo-records of storminess and climate have been studied before, they have typically been reconstructed using proxies such as tree rings (Grudd *et al*., 2000), pollen (Jong *et al*., 2006), Na^+ from the Greenland ice cores (Dawson *et al*., 2003), air temperature records (Dawson *et al*., 2004), sea surface temperatures (Hurrell, 1995) and wind speed (Clarke and Rendell, 2009). In Europe the deposition of coastal dunes has been used as a proxy for periods of increased wind strength (Clarke *et al*., 2002; Sommerville *et al*., 2003;

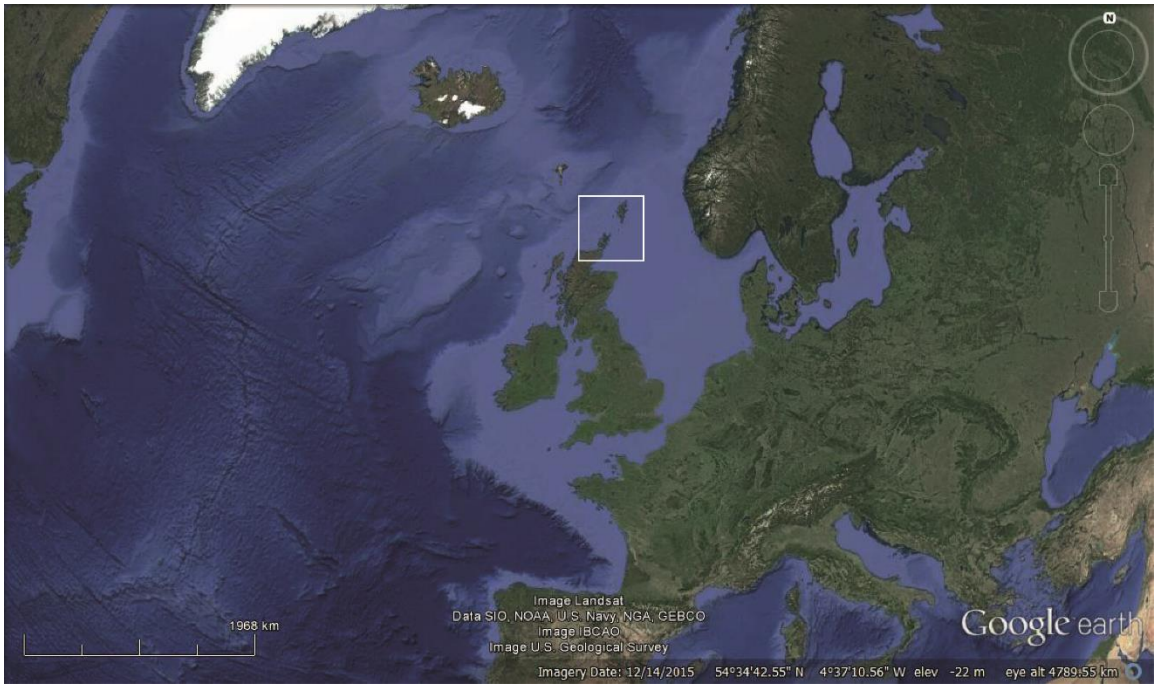

Figure 1.1 – The location of Northern Scotland in the North Atlantic region

Clarke and Rendell, 2006; Tisdall et al., 2013). Other geological / sedimentary evidence used includes over-wash deposits in coastal lagoons (Sabatier *et al*., 2012), cliff-top storm deposits left by extreme waves (Hansom and Hall, 2009), and marine records reflecting wind-blown current strength and storm deposits (Hass, 1996; Andresen *et al*., 2005). However, all of these methods have potential problems. As a biological indicator, tree rings may exhibit a non-linear response to climate changes (Briffa *et al*., 1996). Pollen records are measured at low resolution and there may be a time lag between species decline and another species becoming established (Cowie, 2013). Aeolian dunes are prone to re-working, which can bias the sedimentary record towards more recent events. Other palaeo-environmental records such as cliff-top storm deposits and sand layers within coastal lagoons show only the most extreme events, with erosion potentially also causing a bias towards more recent events (Haslett and Bryant, 2007). Proxies used to reconstruct the NAO have been identified in various settings and with varying success, these include: lake

sediment cores and deep water anoxia values (Olsen *et al*., 2012), speleothem records (Baker *et al*., 2015), sunspot activity (Solanki *et al*., 2004) and glacier fluctuations (Gudmundsson, 1997). However, the majority of these records only cover the last 1000-2000 years, and are not capable of identifying trends on a multi-centennial or millennial timescale. Therefore, a high-resolution empirical archive that can be used to reconstruct climate change over the whole Holocene is required.

1.2: Aims and Objectives

This aim of this project is to reconstruct a high-resolution record of North Atlantic storminess and climate change over the Holocene. The study is based on four peat cores taken along a ~300 km latitudinal transect in Northern Scotland, extending from Shebster in Caithness (N58°33'06.6", W003°42'39.0") to Kedills Mires on the island of Yell in the Shetland Isles (N60°41'12.8", W001°02'52.8") (Figure 1.2).

Figure 1.2 – Sampling site location map

Peat bogs are excellent archives of climate change as they are typically influenced solely by atmospheric inputs. Bromine is a common element in seawater and when found in peat is an indicator of sea spray and may, therefore, be an indicator of storm intensity. Elevated levels of bromine found in minerotrophic peats in Greenland have shown comparability to increased Na^+ ions in the Greenland GISP2 ice-core and has been linked to North Atlantic storminess (Turner *et al*., 2014). The degree of peat humification represents the balance between precipitation and evaporation and, therefore, gives a representation of mire surface wetness. This may indicate longer-term changes in precipitation with wetter conditions signalling an increased frequency of persistent moisture-bearing storms (Turner *et al*., 2014). Combining these two indicators of storminess from a number of sites along a latitudinal gradient could elucidate changes in the position of the polar jet stream. Microscopic peat-borne minerogenic sediment, herein referred to in this thesis as dust, may also be an indicator of large-scale atmospheric circulation patterns. These particles are less than 25 µm in size and show a high degree of roundness, which may indicate long-distance travel. The peat cores are supported with high-precision age depth models produced by tephrochronology and radiocarbon dating, enabling the reconstruction of a terrestrial North Atlantic climate record extending further back into the Holocene than previously established.

1.3: Outline of Thesis

This thesis is divided into six chapters. Chapter 1 presents the introduction to this project, outlines the rationale for understanding North Atlantic storminess, and presents the aims and objectives of this study.

Chapter 2 reviews the existing literature and the knowledge base that forms the background to this study. This leads to the framing of several research questions that define the aims and objectives of this thesis which are outlined in chapter 1.

Chapter 3 describes the various methods used in this study, including site selection and all laboratory techniques.

Chapter 4 presents the results of this study, and is divided into five sections: chronology; loss on ignition and mire surface wetness; X-ray fluorescence (ITRAX); dust; and radiogenic isotope data. Each section is further divided into sub-sections, one for each study site.

Chapter 5 discusses the results presented in chapter 4. This is divided further into three sections: indicators of storminess; indicators of dust; and radiogenic isotope analysis.

Chapter 6 presents the conclusion to this thesis and highlights the significant contribution of this study to the understanding of North Atlantic storminess over longer timescales, as well as outlining recommendations for future research.

Chapter 2: Literature Review

This chapter outlines the existing knowledge on North Atlantic storminess patterns and wind-blown dust movement during the Holocene. This chapter firstly explores the local effects of contemporary storminess in Scotland. Then it continues to the wider North Atlantic climate including the movements of the polar jet stream and the effects of the North Atlantic Oscillation and the existing proxies that have been used to reconstruct the longer-term changes in these systems. This then follows onto large-scale atmospheric circulation patterns and the origin and movement of dust and the current research available on this topic. Finally, the chapter ends by describing the background behind tephra and its uses as a geochronological tool.

2.1: North Atlantic Storminess

The location and intensity of mid-latitude storms are major influences on the climate of Europe (Hanna *et al*., 2008). These storms occur most frequently during winter, when the storm tracks are most intense, and extend in a north-westerly direction from the east coast of America, to Ireland, Great Britain and Norway (Cheng *et al*., 2011). The most intense and damaging storms affecting Europe originate in the Atlantic and may cause extensive flooding and damage to infrastructure (Kendon and McCarthy, 2015). For example, the storm of 31st January to 1st February 1953 is probably the most devastating to have affected Scotland over the last 500 years (Hickey, 2001). The storm was caused by a deep depression that crossed Scotland between the Orkney and Shetland Isles and led to coastal and inland flooding, destruction to coastal defences and extensive wind damage. On land, numerous injuries were reported as a result of flying debris and people being blown over and led to

nineteen fatalities (Hickey, 2001). Storm frequency is predicted to increase by the end of the current century due to anthropogenic climate change (Clarke and Rendell, 2009). Predictions suggest that over the next century storm tracks may shift northwards and storm frequency may increase in the British Isles due to an intensified jet stream (Pinto *et al*., 2009, Orme *et al*., 2015).

2.2: North Atlantic polar-front jet stream

Much of the Northern Hemisphere weather and climate is associated in some way with the mid-latitude upper-atmosphere westerly winds or jet streams. There are essentially two physical processes that give rise to the jet streams. The first is the westerly acceleration associated with poleward moving air in the upper branch of the tropical Hadley circulation. This results in a westerly air flow at upper levels at the poleward edge of the Hadley cell. The second is the momentum and heat-forcing arising from the effects of transient mid-latitude eddies. Because of these two mechanisms, it is common to refer to two different jet streams, named the subtropical jet (STJ) and polar front jet (PFJ) (Woollings *et al*., 2010). The PFJ stream variability is crucial for determining European and Northern Hemisphere weather patterns (Hall *et al*., 2015). Unlike the subtropical jet, which is relatively shallow and confined to the upper troposphere, at the level of the upper branch of the Hadley cell the PFJ extends through the depth of the troposphere and wind speeds increase with height (Woollings *et al*., 2010; Hall *et al*., 2015). The PFJ is also known as the eddy driven jet as it is driven by momentum and heat fluxes from cyclones in the mid-latitudes (Williams, 1979; Panetta and Held, 1988). The regions where these eddies occur are along the polar front, where a steep temperature gradient separates colder polar air from warmer tropical air. The PFJ is, therefore, intimately linked with storm tracks as storms are generated, steered

and reinforced by the flow of the jet stream (Hoskins *et al*., 1983; Hall *et al*., 2015) (Figure 2.1).

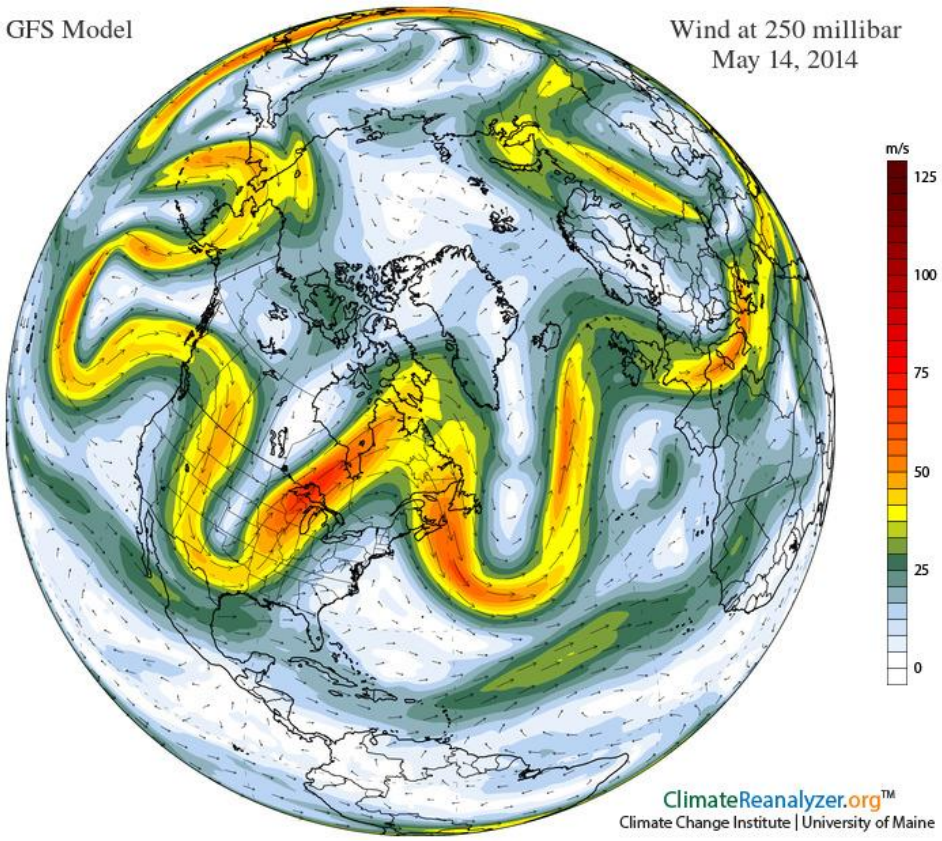

Figure 2.1 – The orientation of the PFJ stream (Climate Change Institute, University of Maine, 2016).

In the North Atlantic, a unique tripole latitudinal distribution of the jet stream is found which suggests three preferred location of the PFJ; a southern equatorward maximum, a northern poleward maximum and a central phase (Athanasiadis *et al*., 2010; Woollings *et al*., 2010, Woollings *et al*., 2014). In both the central and northern jet patterns, the PFJ is clearly separated from the subtropical jet. Only in the southerly position of the jet stream is there not a clear separation between the PFJ and the STJ. The central jet position can be

interpreted as the neutral state of the PFJ as it exhibits weaker tendencies and wind speeds than both the northern and southern jet positions (Woollings *et al*., 2010).

2.3 – North Atlantic Oscillation

Most extratropical atmospheric teleconnections are thought to be related to jet stream location and strength (Hall *et al*., 2015). The North Atlantic Oscillation (NAO) is the dominant pattern of atmospheric sea-level pressure (SLP) variability over the Atlantic Ocean, characterized by a meridional pressure dipole, with low pressure centred roughly over Iceland and high pressure over the Azores to the south (Hurrell, 1995; Thompson and Wallace, 2001; Dawson *et al*., 2002; Olsen *et al*., 2012; Feser *et al*., 2014). An increase in the pressure gradient between the Azores and Iceland results in a positive NAO index whereas a decrease results in a negative NAO (Hall *et al*., 2015). The phase of the NAO is influenced by the presence of North Atlantic storm tracks and the associated PFJ (Vallis and Gerber, 2008). Positive NAO phases are associated with a poleward shift in the PFJ and corresponds to wetter, stormier weather in northwest Europe, dominated by strong mid-latitude westerlies (Burningham and French, 2013, Gómara *et al*., 2014). Negative phases are associated with an equatorial shift in the PFJ and are associated with drier, calmer weather in northwest Europe and storms tracking into the Mediterranean (Burningham and French, 2013, Gómara *et al*., 2014). Cold events also occur more frequently in northern Europe under negative NAO conditions (Thompson and Wallace, 2001). The occurrence of extreme cyclones is enhanced during positive NAO phases while during negative NAO phases they are less frequent (Pinto *et al*., 2009, Gómara *et al*., 2014, Feser *et al*., 2014) (Figure 2.2).

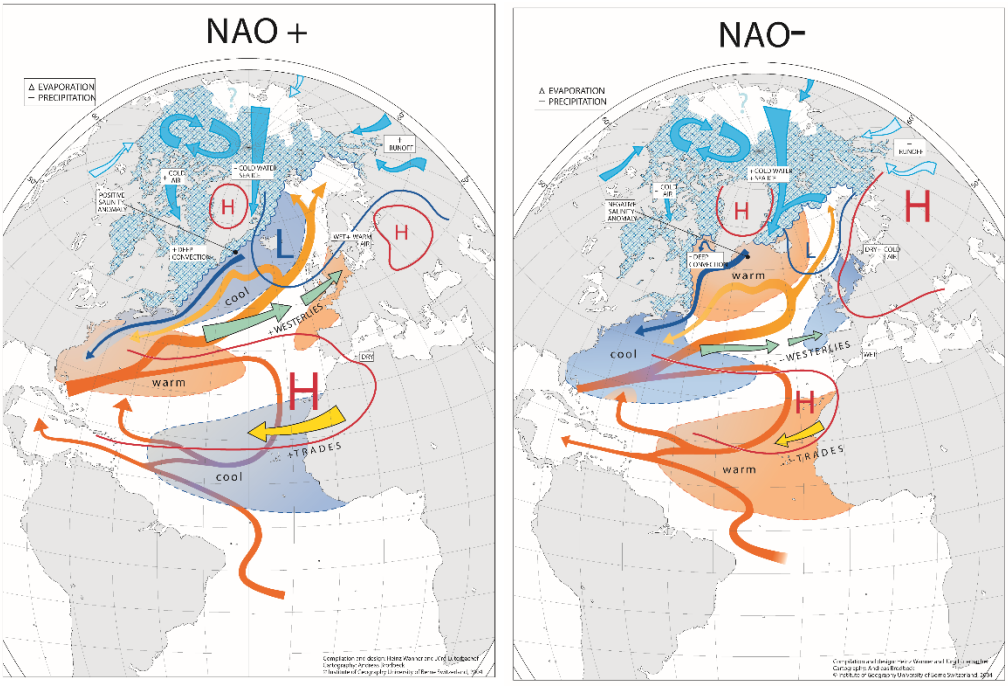

Figure 2.2 - Differences in North Atlantic climate between positive and negative NAO phases (Wanner *et al*., 2001)

The NAO alone does not describe all jet stream variability, being a simplified description of the North Atlantic dipole, with its centres of action remaining in the same place. In reality, shifts in location of the centres are observed because of the interaction of different modes of variability: the NAO, the Arctic Oscillation (AO) the Eastern Atlantic (EA) pattern and the Scandinavian (SCA) pattern (Athanasiadis *et al*., 2010; Moore *et al*., 2013; Woolings *et al*., 2014). The AO is the dominant mode of sea-level pressure variability extended over the Northern Hemisphere (Thompson and Wallace, 1998) and is closely linked to the NAO. The EA is the second mode of variability and consists of a monopole on the axis of the NAO west of Ireland, whereas the SCA centre is typically west of Bergen (Barnston and Livezey, 1987). The NAO is the dominant pattern of variability in describing latitude shifts, while changes in jet speed are explained equally by the EA and NAO (Woollings and Blackburn, 2012).

2.4 Rossby Waves and wave breaking

The movement of the jet stream is related to wave breaking in the flow orientation (Figure 2.3).

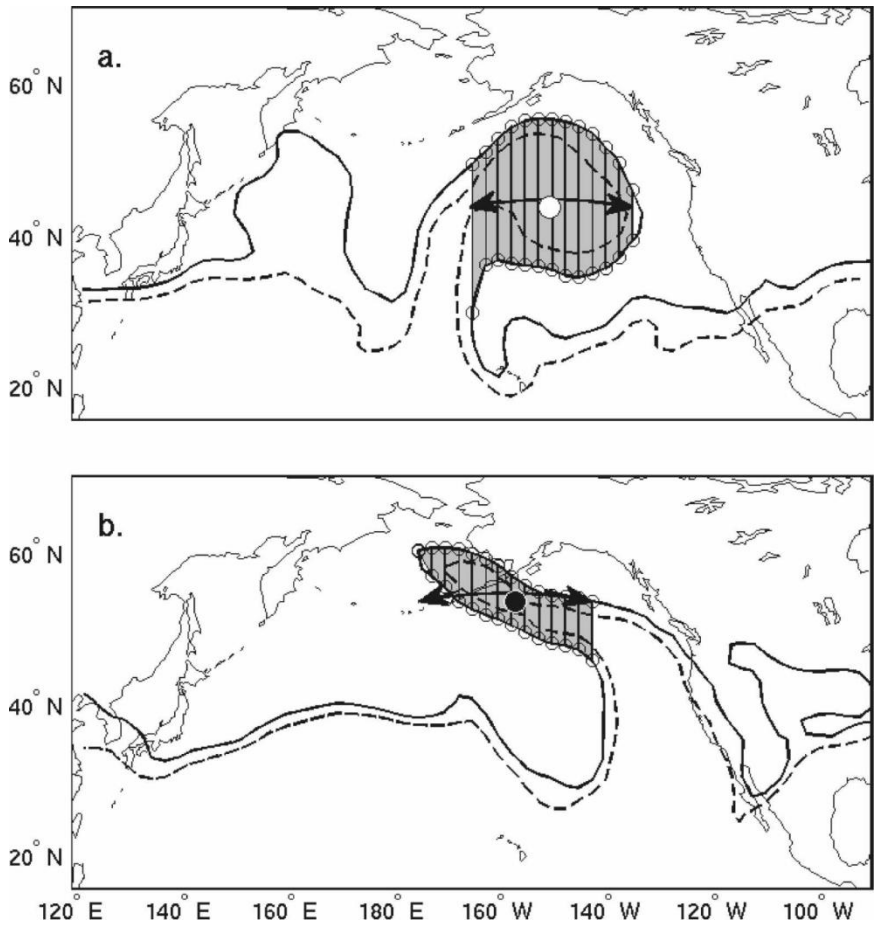

Figure 2.3 – a) anticyclonic wave breaking and b) cyclonic wave breaking orientations (Strong and Magnusdottir, 2008)

Anticyclonic wave breaking (AWB) occurs mainly equatorwards of the main jet, whereas cyclonic wave breaking (CWB) occurs mainly polewards of the main jet (Thorncroft *et al*., 1993). AWB occurs under strong zonal flow conditions and drives the PFJ northwards, leading to a positive NAO, whereas CWB occurs under weak zonal flow conditions and drives it to the south leading to a more negative NAO (Benedict *et al*., 2004; Franzke *et al*., 2004;

Strong and Magnusdottir, 2008; Woollings *et al*., 2008). AWB is more common and often precedes a shift in the NAO phase. Wave breaking and the NAO are also intimately connected to atmospheric blocking (Woollings *et al*., 2008; Hall *et al*., 2015). This occurs when a persistent stationary anticyclone develops in the mid-latitudes for several days or longer, blocking the westerly winds and weather systems (Rex, 1950; Woollings *et al*., 2008). When this blocking pattern occurs over Greenland it leads to more southward displaced PFJ and is associated with a negative NAO. When blocking occurs over southwest Europe it leads to a more northward displaced PFJ and is associated with a positive NAO (Woollings *et al*., 2010). In the North Atlantic, the normal pattern of cyclonic (anticyclonic) flow to the north (south) of the PFJ is often reversed (Woollings, 2011).

2.5: Seasonal jet stream and NAO changes

The NAO is the only teleconnection pattern consistently evident throughout the year in the Northern Hemisphere (Hurrell and Deser, 2009). It is well defined in all seasons (Hurrell and Deser, 2009) and is strongest during winter (Penland and Hartten, 2014) coinciding with the strongest phase of the jet stream (Woollings *et al*., 2014). In the spring and autumn, the NAO is highly variable, tending to change its phase from one month to another (Wang *et al*., 2011). Summer is a less dynamically active season (Msadek *et al*., 2011) as both the spatial extent and the amplitude of the NAO is smaller (Hurrell and Deser, 2009) because of a reduced, poleward-shifted temperature gradient (Hall *et al*., 2015). This distinct two-season winter/summer pattern in storminess is associated with the seasonal climatology of the jet stream and the mid-latitude westerlies (Lozano *et al*., 2004) as the jet stream rapidly weakens from its strongest in January to its weakest in May (Woollings *et al*., 2014). Summer jet streams are weaker than in winter and are displaced poleward, reaching its

maximum latitude in September (Woollings *et al*., 2014; Hall *et al*., 2015). However, jet streams can shift in latitude and exhibit changes in speed and position from year to year which has a profound effect on local climate variability (Hall *et al*., 2015). For example, the summers from 2007 to 2012 produced exceptionally wet conditions over the British Isles and northern Europe, whereas the Mediterranean regions were particularly warm and dry, and these are associated with a southward shift in the PFJ and a more negative summer NAO (Blackburn *et al*., 2008).

The summer North Atlantic Oscillation (sNAO) is smaller in extent, with a northward displacement of the centres of action, the southern node being centred over the northwest Europe instead of the Azores. The sNAO is able to explain the main variations of summer climate over Northern Europe, through changes in the Atlantic storm track and jet stream locations. The positive sNAO is associated with warm, dry and cloud-free conditions over northwest Europe with a poleward displacement of the jet stream, which are conditions found under a negative Atlantic multidecadal oscillation (AMO) regime, and vice versa (Hall *et al*., 2015)

2.6: Influences on the jet stream and NAO

The changing phases of the jet stream and NAO can be driven by a variety of factors including sea-ice reduction, snow cover, sea surface temperatures (SSTs), El Nino / Southern Oscillation (ENSO), solar variability, volcanic eruptions and the stratospheric polar vortex. Sea ice reduction may affect atmospheric circulation patterns through changes to heat fluxes from the ocean (Budikova, 2009). Sea ice also has a higher albedo than the sea surface and, therefore, reflects more of the incoming solar radiation. As sea ice decreases in

extent, more ocean is exposed, absorbing more incoming shortwave radiation (Francis and Vavrus, 2015; Hall *et al*., 2015). This additional energy raises water temperature in the summer, and reduced ice extent in autumn results in an increased heat loss to the atmosphere as warmer water from summer heating delays the onset of ice formation, which would otherwise insulate the atmosphere from the ocean (Screen and Simmonds, 2010; Stroeve *et al*., 2014). This leads to warming of the troposphere which has the effect of reducing the surface meridional temperature gradient, leading to a southward displacement of the jet stream and a negative NAO (Francis and Vavrus, 2015; Hall *et al*., 2015). In a similar way to changes in sea ice, a change in snow cover on the Northern Hemisphere land masses, particularly during spring snow melt or autumn snow fall, can impact on the temperatures of the lower layers of the atmosphere. Reduced snow cover presents a land surface with a decreased albedo, which will absorb more downward shortwave radiation, in turn emitting more longwave radiation to the atmosphere, with potential impacts on atmospheric circulation (Brown *et al*., 2010; Cohen *et al*., 2012). It is proposed that such heating leads to a weaker, strongly meandering jet stream and a negative NAO (Hall *et al*., 2015).

Atlantic sea-surface temperatures changes may also drive changes in the latitudinal position and intensity of the jet stream and the summer NAO (Smith *et al*., 2014) through the AMO. A positive (negative) AMO index, with higher (lower) SSTs is associated with lower (higher) mean SLP over the Atlantic and Europe, decreased (increased) precipitation over Southern Europe and the southern United States, and increased (decreased) precipitation over Northern Europe (Knight *et al*., 2006). The positive phase of the AMO correlates with the negative phase of the summer North Atlantic Oscillation (SNAO) whereas the negative

phase of the AMO correlates with a positive SNAO phase (Folland *et al*., 2009). Changes to other circulation drivers such as the El Nino / Southern Oscillation (ENSO) or Arctic oscillation (AO) can lead to changes in the NAO. Negative NAO conditions are often observed during El Niño in winter whereas positive NAO conditions may be seen during La Niña (Brönniman, 2007; Smith *et al*., 2014; Hall *et al*., 2015).

A slightly more controversial area is the role of solar variability in surface NAO variations. Cold northern European winters, and a negative NAO, may be linked to low solar activity and mild winters, and a positive NAO, to high solar activity (Smith *et al*., 2014). A further external influence on the NAO on seasonal to decadal time-scales may come from explosive volcanic eruptions. Eruptions can inject significant sulphate aerosols into the atmosphere, which reflect solar radiation, leading to a cooling of the Earth's surface while warming the equatorial lower stratosphere through absorption of terrestrial IR and near-IR solar radiation (Stenchikov *et al*., 2006). This may create a positive NAO in the winters, which follow with northward displacement of storm tracks and the polar jet stream (Robock and Mao, 1992; Stenchikov *et al*., 2006; Smith *et al*., 2014, Hall *et al*., 2015).

One of the main influences on jet stream movement is the stratospheric polar vortex. There are links between the stratosphere and troposphere that exert a downward influence and affect tropospheric weather. These links are strongest between November and January but can extend as late as April in the Northern Hemisphere (Kidston *et al*., 2015). In winter, the Northern Hemisphere stratospheric circulation is dominated by a polar vortex, characterized by strong westerly winds circulating around a deep cold polar cyclone. There is large variability in the strength of the vortex, represented by the Northern Annular Mode Index at

10 hPa. A positive index indicating a strong vortex and a negative index indicates a weak vortex (Baldwin and Dunkerton, 2001). Both weak and strong vortex anomalies often transfer to the troposphere, producing negative and positive NAO influences (Kodera *et al*., 1990). The tropospheric response to a weak stratospheric polar vortex (SPV) is a southward shift of the PFJ and a negative NAO whereas a strong SPV leads to a northwards shift of the PFJ and a positive NAO (Gerber and Polvani, 2009; Gerber *et al*., 2009; Kidston *et al*., 2015). Equatorial winds in the stratosphere alternate between easterlies and westerlies roughly every 28 months in what is known as the quasi-biennial oscillation (QBO) (Anstey and Shepard, 2014; Kidston *et al*., 2015). When the westerlies occur during winter the SPV is likely to be unusually strong which results in a more intense poleward-sifted jet stream, a more strongly positive NAO and more intensive storms. This can have a significant effect on climate for example the 2013/2014 winter was influenced by an intense PFJ and resulted in extreme rainfall, storm damage and flooding in the UK and Northern Europe (Kidston *et al*., 2015). A very weak SPV can have the opposite effect on climate and has been implicated in the extremely cold European winter on 1962/63 and in helping drive the winter NAO to its lowest value on record in 2009/10 (Fereday *et al*., 2012; Kidston *et al*.,2015).

2.7: Existing proxies for reconstructing jet stream patterns and the NAO

A variety of proxies have been used to reconstruct the NAO including tree rings (Cook *et al*., 1998; Grudd *et al*., 2000; Grudd *et al*., 2002), ice cores (Appenzeller *et al*., 1998; Meeker and Mayewski, 2002), sea surface temperatures (SST's) (Hurrell, 1995; Cullen *et al*., 2001), coastal dune deposition (Clarke *et al*., 2002; Clarke and Rendell, 2006), cliff top storm deposits (Hansom and Hall, 2009), deep water anoxia (Olsen *et al*., 2012), sunspot activity (Solanki *et al*., 2004; Smith *et al*., 2014) and speleothem data (McDermott *et al*., 2001; Baker

et al., 2015; Walczak *et al*., 2015) (Figure 2.4). Tree growth conditions can be analysed through the measurement of tree ring width. Stressful conditions unfavourable for tree growth, such as those experienced under negative NAO conditions, can therefore be identified by extremely narrow tree rings (Grudd *et al*., 2000). Ice cores have been analysed for sodium and chloride concentrations with higher levels suggesting increased wave action and storm activity and therefore a positive NAO phase (Meeker and Mayewski, 2002; McIlvenny *et al*., 2013). North Atlantic SST's have also been reconstructed from tree rings (D'Artigo and Cook, 1997; Cook *et al*., 1998) and ice cores (Appenzeller *et al*., 1998). Warmer SST's are associated with a positive NAO phase whereas colder SST's are associated with a negative NAO phase (Cullen *et al*., 2001). Increases in coastal dune deposition (Clarke *et al*., 2002; Clarke and Rendell, 2006) and cliff top storm deposits (Hansom and Hall, 2009) suggest an increase in stormier conditions and a positive NAO phase. The NAO index based on a south-west Greenland lake sediment core is reconstructed from deep water anoxia data.

A negative NAO is associated with above average temperatures and below average winter precipitation, leading to earlier ice melt and allows stronger vertical mixing of the water column. This weakens thermal stratification and hence increases oxygen transfer into the deep water zone, with associated implications for redox processes. A positive NAO, associated with colder conditions, leads to later ice melt which coincides with maximum solar radiation and results in limited water column mixing. This leads to the rapid onset of thermal stratification, and hence maintenance of hypoxic conditions. Deep water anoxia can alter cycling of redox-sensitive elements. The Mn/Fe ratio reflects the strength of seasonal thermal stratification and is therefore a proxy for dominant NAO circulation

patterns. A higher Mn/Fe ratio and carbonate concentration reflects predominantly weaker stratification and is associated with negative NAO conditions whereas a lower Mn/Fe ratio and carbonate concentration reflects stronger stratification and is associated with positive NAO conditions (Olsen *et al*., 2012). An increase in solar activity has been associated with a positive NAO period whereas reduced solar activity is more common during negative NAO periods (Smith *et al*., 2014). Variations in speleothem laminae thickness provide an annual growth-rate record that can be used as a proxy for past climate and environmental change. Growth rates are determined by changes in precipitation and low growth rates suggest a positive NAO period whereas high growth rates are associated with a negative NAO (McDermott *et al*., 2001; Baker *et al*., 2015). For records established in areas of the Mediterranean, the opposite trend is identified (Walczak *et al*., 2015). However, all these records have potential problems and the majority only extend to the past 1000-2000 years.

2.8: Interpreting existing proxy data

There is a high level of inconsistency between the existing proxy records used to reconstruct storminess and the NAO. Figure 2.3 shows that many records are incomplete and do not extend across the whole Holocene. For records that do extend over longer timescales such as the sunspot record (Solanki *et al*., 2004) and ice core record (NGRIP), the data is noisy and trends are difficult to identify. Table 1 displays four known periods of significant climate change across the late Holocene: the Little Ice Age, the Medieval Climate Anomaly, the Dark Ages Cold period and the Roman Warm period. Each proxy is presented individually with

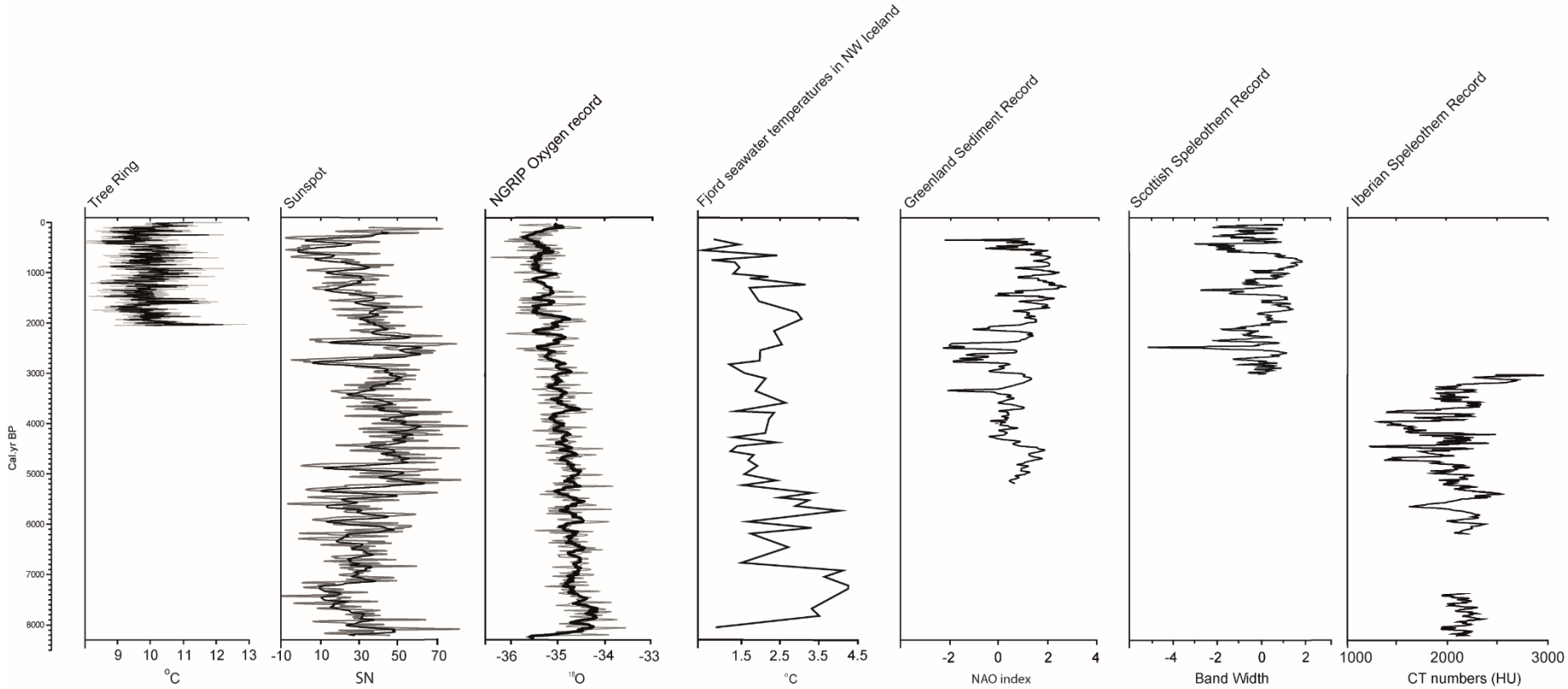

Figure 2.4: Proxy records of the NAO including: tree ring (Grudd *et al*., 2002), sunspot (Solanki *et al*., 2004), ice core (NGRIP), Icelandic fjord seawater temperature (Ólafsdóttir, 2010), Greenland sediment (Olsen *et al*., 2012), Scottish speleothem (Baker *et al*., 2015) and Iberian speleothem (Walczak *et al*., 2015)

the dates bracketing each climatic period. The dates are expressed in Cal. yr BP. The Iberian speleothem record is not included as the record does not begin until 3000 Cal. yr BP.

Table 1 – Periods of climate change in the late Holocene

Climate Period	Tree Ring	Sunspot	NGRIP Oxygen Record	Icelandic Fjord Temps	Greenland Sediment Record	Scottish Speleothem Record
Little Ice Age	450-250	800-300	550-100	600-300	550-300	600-250
Medieval Climate Anomaly	1100-900	1200-800	1100-900	1200-1000	1300-550	1300-700
Dark Ages Cold Period	1400-1100	1450-1200	1300-1100	1750-1200	1500-1300	1450-1300
Roman Warm Period	Not indicated	2300-1200	Not indicated	2500-1750	2050-1300	2050-1300

As indicated by Table 1 and Figure 2.4, each of the proxy records shows changes in relation to the periods of climatic change. However, the dates bracketing each event are significantly varied between each proxy and in the tree ring and ice core records, the Roman Warm period is not clearly indicated at all. This leads to much confusion and sheds doubt on the accuracy and reliability of these existing methods.

2.9: Dust as a palaeo-climate proxy

The position of the jet stream and corresponding phase of the NAO can also affect the production and transportation of minerogenic dust particles. The world's largest sources of dust are found in low-latitude arid regions and this is therefore where most aeolian research has been focused (Prospero *et al*., 2002). North Africa in particular serves as a huge reservoir of mineral dust. The dust sources located here are active all year, especially during the summer when they emit large plumes of dust across the Mediterranean to Europe

(Prospero, 1996). However the processes of dust production and dust emission in higher latitudes and colder climates have now become the focus of new research (Eden and Hammond, 2003; Hugenholtz and Wolfe, 2010; Bullard *et al*., 2016). Glaciers and small ice caps are sensitive indicators of climate change, however they are also important drivers of fine-grained (clay /silt-sized) sediment production (i.e. dust) in high latitude areas (Dyurgerov and Meier, 2005; Bradwell *et al*., 2006; Blascio *et al*., 2015).

2.9.1: Dust transport

The movement of dust depends on several factors including sediment type, soil moisture, vegetation cover and surface roughness (Gísladóttir, 2005, Jickells *et al*., 2005; Carslaw et al., 2010, Bullard et al., 2011, Schepanski et al., 2014). The dominant control on sediment concentrations is sediment availability (Bullard, 2012) and the supply of material that can be transported by wind (Jickells *et al*., 2005). Moisture is a common limiting factor for dust emissions because it increases particle cohesion (Neuman, 2003, Bullard, 2012). Moisture contents in the range of 4 to 6% have been suggested to limit dust transport. However where evaporation is high the effects can be short-lived (Bullard, 2012). Gradual heating of wet sediments in direct sunlight can lead to dust being mobile within 4 hours under low wind conditions, with this time envelope decreasing in windy conditions (Dagsson-Waldhauserova *et al*., 2014). A vegetated surface impedes dust movement as this stabilises sediments against wind erosion (Gísladóttir, 2005; McTainsh and Strong, 2007).

Fine sediment has three main modes of aeolian transportation. Saltation is the most efficient mode and involves a bouncing motion of the sediment grains. Soon after the grain is lifted into the air, ground forces are no longer applicable and the trajectory of the grain is

determined by gravity and wind. In most cases grains rise to a few centimetres height then descend and strike the ground where they bounce off again and may cause other grains to become airborne as well (Sigurjónsson *et al*., 1999). A small proportion of particles influenced by saltation are carried further up into the atmosphere for long-range transport (Jickells *et al*., 2005). The second transport mode is surface creep which involves the rolling of grains along the ground surface. This may be induced by surface topography or gravity, and grains that are moved by this process can be much larger than those moved in saltation. Lastly, particles can be transported by the method of aeolian suspension. This is the most important method for far-travelled dust particles reaching Scotland. Typically, only the smallest grains are involved in suspension (<50 μm) and they follow the turbulent motions of the air. Cohesive forces between small grains are strong which means that saltation bombardment is generally needed to break the inter-particle bonds and make grains enter suspension (Sigurjónsson *et al*., 1999).

Once a mineral particle is entrained in the atmosphere, it is transported away from the source area by advection and atmospheric circulation patterns. Aeolian dust transport systems are largely unconstrained (McTainsh and Strong, 2007) and dust transport paths can range in scale from local (over a few hundred metres) to global (over thousands of kilometres) (McTainsh and Strong, 2007, Goudie, 2009, Arnalds *et al*., 2013, Dagsson-Waldhauserova *et al*., 2014). The distance that dust is transported depends on wind energy, the removal of particles by gravitational settling and scavenging, and particle size (Lawrence and Neff, 2009). The size range of suspended particles is generally determined by wind velocity: as wind velocity increases, the size range of the suspended particles also increases (Durant *et al*., 2009). As wind is a particularly size-selective transport mechanism, large

particles have a tendency to be deposited closer to their source region as a result of their greater mass and settling velocities, while small particles can be transported much further, of the order of 100's to 1000's of kms (Lawrence and Neff, 2009, Stuut and Prins, 2014). This sorting process results in a gradual decrease in grain size with distance from the source (Durant *et al*., 2009). Generally most of the mineral dust particles that are suspended in air and collected further than 100 km away from their source are smaller than 20 µm (Stuut and Prins, 2014). During transportation, dust particles are continuously removed from the air column by processes of dry and/or wet deposition (Goudie, 2009, Lawrence and Neff, 2009). Dry deposition proceeds through gravitational settling of particles out of the atmosphere and is the dominant mechanism removing sand and large silt-sized particles (Tegen and Fung, 1994). In contrast, wet deposition results from the scavenging of particles by rain or snow (Lawrence and Neff, 2009). The deposition of silt-sized particles can occur through both processes (Kocak *et al*., 2005; Al-Momani *et al*., 2008). Rates of dust deposition depend on several factors including the concentration of dust in the atmosphere, the energy of the winds transporting the dust as well as the surface features of the depositional environment (Goossens, 2000). The influence of surface features varies in response to the vegetation, with some species being more effective at trapping atmospheric particles than others and affecting dust deposition rates (Tegen *et al*., 2002). The chemistry, mineralogy and size of dust particles can also be altered during emission, transport and deposition processes (Lawrence and Neff, 2009). The dust characteristics should be similar to the source sediment, however, the physical fractionation of sediment during dust emissions can lead to alterations. For example, wind erosion preferentially removes fine-textured organic soil particles therefore dust is often enriched in trace elements and metals (Li *et al*., 2008).

2.9.2: Effects of dust deposition

Mineral dust aerosols can affect several key parts of the Earth system, these include: the radiative budget, precipitation patterns, biological cycles, chemistry of the atmosphere and air pollution (Winckler and Mahowald, 2014). It may also affect soil development and vegetation as well as human health (Bullard *et al*., 2011, Thorsteinsson *et al*., 2011). Iron-rich dusts can significantly increase phytoplankton activity in the oceans (Goudie, 2009, Schroth *et al*., 2009, Carslaw *et al*., 2010, Bullard *et al*., 2011, Schepanski *et al*., 2014, Martinez-Garcia and Winckler, 2014). Iron is an essential nutrient for all organisms to carry out photosynthesis. However, despite being the fourth most abundant element in the Earth's crust, iron is in short supply in most near-surface remote oceanic waters especially in the so called high-nitrate low-chlorophyll oceanic regions (HNLC) (Johnson *et al*., 2011). Iron supply reaches the oceans mainly from rivers as suspended sediment in a vast global transport system. However, fluvial and glacial particulate iron is efficiently trapped in coastal sediment sinks (Jickells *et al*., 2005, Arnalds *et al*., 2014). Hence, the dominant external input of iron to the surface of the open ocean is aeolian dust transport (Jickells *et al*., 2005, McTainsh and Strong, 2007, Johnson *et al*., 2011, Arnalds *et al*., 2014).

2.9.3: Present dust research

Recent research into the movement of dust from high latitude and cold climate areas has been undertaken in both hemispheres, including sites in Alaska, Canada, Greenland, Antarctica, New Zealand and Patagonia. However, it is Iceland where the most research has been undertaken (Bullard *et al*., 2016) (Figure 2.5).

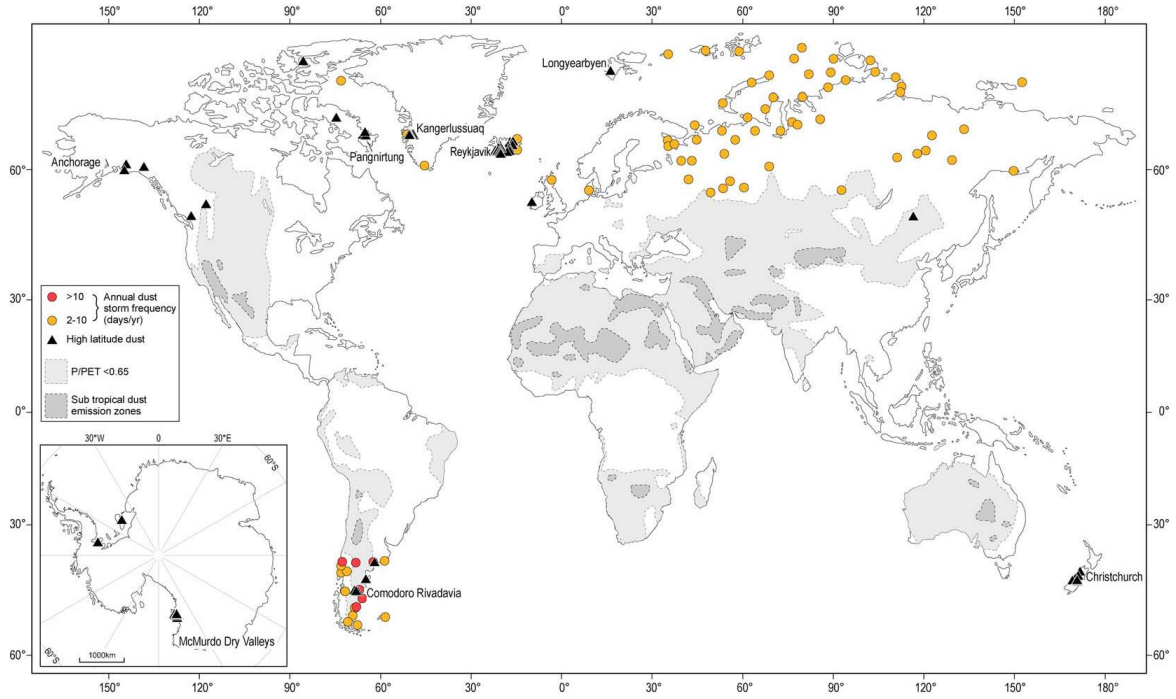

Figure 2.5 – The main sources of high latitude dust (Bullard *et al*., 2016)

Alaskan dust storms occur at many different locations along the Gulf of Alaska shoreline and are associated with seasonal changes in climate (Crusius *et al*., 2011). River discharge peaks during the summer months when glacier melt rates and runoff are at their maximum. This river discharge contains large quantities of fine glacial sediment, produced by glacial erosion of the underlying bedrock. In autumn, once the melt season has finished and discharge falls dramatically, but before snowfall begins, the expansive outwash plains covered in recently deposited glacial sediment are exposed. High-pressure systems over central Alaska, alongside autumn cooling, can drive strong northerly winds. This leads to resuspension of fine glacial sediment as dust which is then transported far over the ocean (Bullard *et al*., 2016). In Canada, dust emissions and transport are at their highest in autumn and early winter and are primarily associated with increases in wind speed. Relatively warm, dry föhn winds that descend from the Rocky Mountains in late winter and early spring are strongly

associated with dust emission from unprotected, tilled soils in western Canada. Cold, dense katabatic winds also play a role in reworking sediment in proglacial surfaces throughout northern Canada, particularly in the high and eastern Arctic. Topographic funnelling through deep glacial valleys leads to substantial acceleration of these winds which may exceed 100 km hr^{-1} in extreme situations (Bullard *et al*., 2016). In Greenland, dust sources are confined to the ice-free and vegetation-free glacial outwash plains. Warm-season meltwater floods deposit thick layers of fine sediment onto these outwash plains which leads to dust storms occurring most frequently in autumn (Bullard *et al*., 2016). Wind speed is also an important contributor to dust movement in Greenland and is often more important than meltwater in the transportation of sediment (Hobbs, 1931; Hobbs 1942).

In the southern hemisphere, the ice-free areas of Antarctica have recently been recognized as important local dust sources. Of these, the McMurdo Dry Valleys are the largest ice-free area (Doran *et al*., 2002) and the most notable dust sources originate from the dry river valleys and lake beds found here. Dust transport in these areas are dominated by strong katabatic and föhn winds (Bullard *et al*., 2016) and occur predominantly in winter (Ayling and McGowan, 2006). In New Zealand, the main sources of dust are the floodplains of extensive braided glacial river systems (McGowan, 1997; Eden and Hammond, 2003). Dust emissions are highest in spring and autumn and are influenced by strong westerly winds (McGowan *et al*., 1996). Patagonia in southern South America is the dominant source of dust in the Southern Hemisphere during glacial periods (Basile *et al*., 1997; Delmonte *et al*., 2008). The climate in this region is influenced by strong westerly winds and dust emissions are highest in spring and summer (Gaiero *et al*., 2003; Bullard *et al*., 2016). During Pleistocene and Holocene periods of glacier advance, extensive Patagonian ice sheets

provided a source of glacial sediment which is now largely contained within alluvial fans, braided rivers and glacial outwash plains (Bullard *et al*., 2016). However, during periods of glacial retreat, proglacial lakes formed which resulted in capture of the fine glacial sediment that had previously been deposited in the outwash plains. The rivers and outwash plains probably became deprived of fine sediment leading to a reduction in the dust flux (Ackert, 2009) (Figure 2.6)

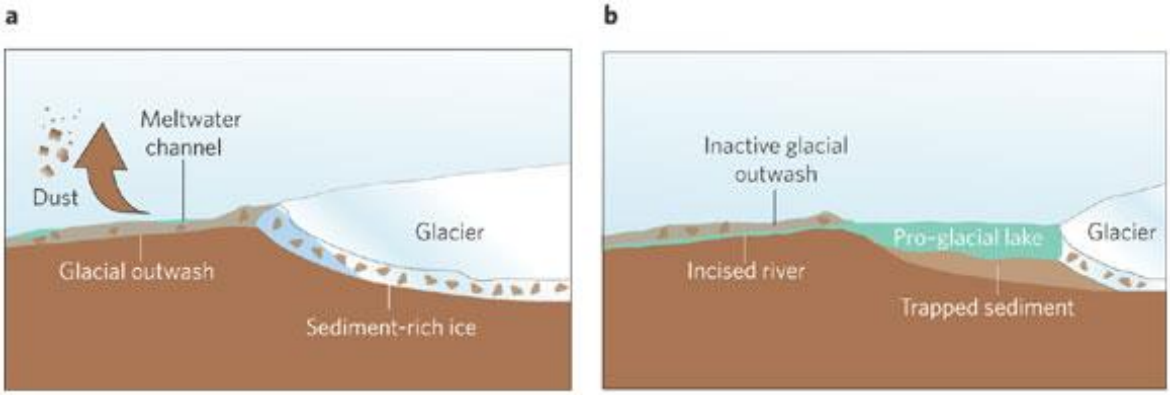

Figure 2.6 - Effects of a proglacial lake on dust production (Ackert, 2009)

2.9.4: Present dust research from Iceland

Iceland is an important location for the study of North Atlantic climate change owing its proximity to both atmospheric and oceanic polar front. Iceland lies in the centre of the North Atlantic Ocean in the path of storm tracks and south of the seasonal boundary between temperate and polar ocean waters (Cook *et al*., 1998; Mackintosh *et al*., 2002). During prolonged negative NAO phase, there is an excessive build-up of sea ice in the Iceland/Greenland Sea meaning that the climate of Iceland is cooler and drier (Bradwell et al., 2006). High pressure occurs over Iceland, storm tracks are deflected further south and Iceland is influenced by polar air. During prolonged positive phases, North Atlantic Drift waters originating at lower-latitudes dominate the ocean around Iceland making the climate milder and wetter. The Icelandic Low is quasi-stationary pressure system that drives stormy

temperate air masses cross Iceland (Mysak an Venegas, 1998; Mackintosh *et al*., 2002). Some studies have shown a link between glacier advance and a greater frequency negative NAO index years (Kirkbride, 2002; Bradwell *et al*., 2006; Kirkbride and Dugmore, 2008); whereas a positive NAO has been linked with periods of overall glacier retreat (Johannesson and Sigurðsson, 1998; Bradwell *et al*., 2006). Unlike Patagonia however, proglacial lakes do not form when glaciers retreat in Iceland.

Glaciers cover about 10% of Iceland generating unusually high levels of physical weathering which are accentuated by glacial and fluvial processes (Sigurjónsson *et al*., 1999, Arnalds *et al*., 2001, Gísladóttir, 2005). Glacial systems create large sources of windblown dust as the sediment-laden meltwater contains large amounts of dust-sized particles (Sugden *et al*., 2009). Iceland has 20,000 sq km (Sigurjónsson *et al*., 1999, Gísladóttir *et al*., 2005, Sugden *et al*., 2009, Arnalds, 2010, Thorsteinsson *et al*., 2011, Blechschmidt *et al*., 2012) of sandy deserts with active aeolian processes, which are a major source of atmospheric dust (Arnalds *et al*., 2001, Arnalds, 2010). The main source regions for dust storms are the outwash plains formed from the glacial meltwater, also known as the sandur plains, on the Southern coast of Iceland and regions close to the glaciers (Thorsteinsson *et al*., 2011). Due to its location inside the North Atlantic storm track, Iceland is frequently affected by synoptic scale cyclones. With wind speeds commonly exceeding 20 ms^{-1} during storm events (Gísladóttir, 2005) and with limited vegetation cover (Bullard and Austin, 2011), the exposed sandy areas are subjected to intense aeolian processes which can be seen in satellite imagery (e.g. NASA MODIS image, Figure 2.7) (Sigurjónsson *et al*., 1999, Dagsson-Waldhauserova *et al*., 2014).

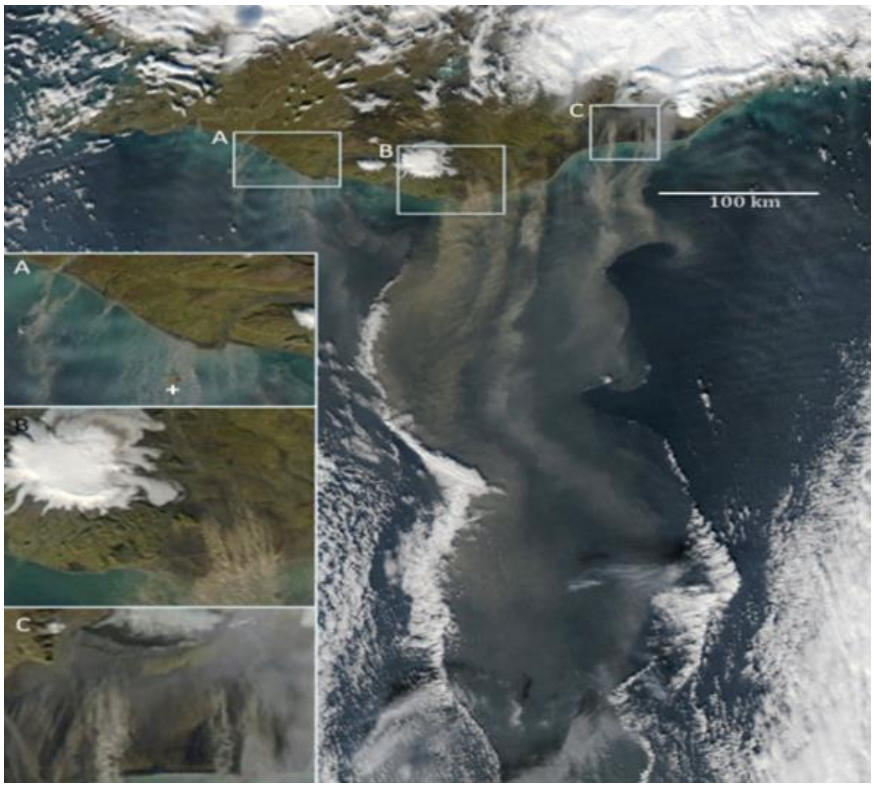

Figure 2.7 - NASA MODIS image of dust plumes emanating from outwash plains in southern Iceland. A, B, C: close-up of dust source areas adjacent to large, high turnover glaciers (Bullard, 2012).

Long-term observations of atmospheric dust show a high frequency of dust events in Iceland with around 135 dust days annually. Total emissions of dust from Icelandic sources are in the range of 30 to 40 million tonnes annually, with 5 to 14 million tonnes deposited annually over the Atlantic and Arctic oceans (Dagsson-Waldhauserova *et al*., 2014, Arnalds *et al*., 2014). The frequency of dust days measured ranks Iceland amongst the major dust emission areas of the world; with Icelandic dust storms measured as some of the most severe wind erosion events recorded on Earth (Dagsson-Waldhauserova *et al*., 2014).

Previous studies on dust movement in Iceland have been primarily focused on the dust source and the mechanics of dust production and transportation (Bullard *et al.*, 2016). Very few studies have been undertaken relating to the deposition areas, either contemporary or in a palaeo context, and none have reconstructed dust deposition around the North Atlantic over long timescales. Due to the relationship between the NAO, glacier advances and dust production, dust flux could be used as a novel proxy of climate change. In Iceland, records of glacial fluctuations have been documented and reliably reconstructed throughout the Holocene (Gudmundsson, 1997) (Figure 2.8) allowing comparisons between dust flux and glacier advance to be made.

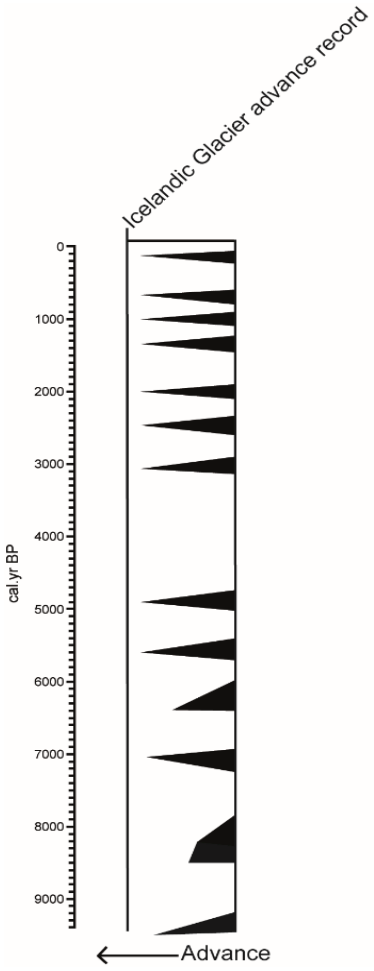

Figure 2.8 – Icelandic glacier advance record (Gundmundsson, 1997)

Previous studies have shown that dust sources have a specific radiogenic isotope signal. Therefore, far-travelled dust can be analysed and its origin identified (Figure 2.9).

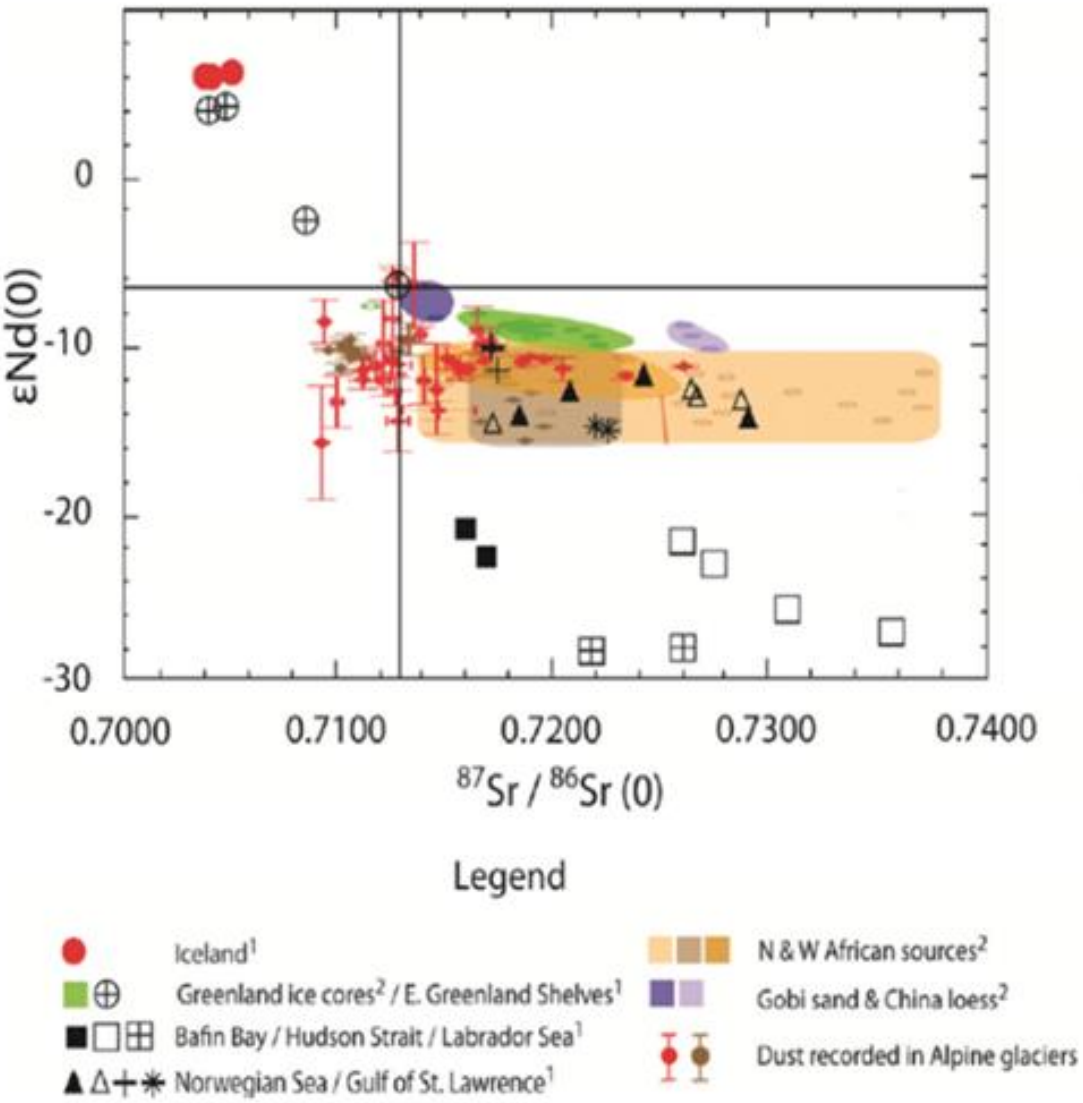

Figure 2.9 – The radiogenic isotope signal for common dust sources (Adapted from Farmer *et al*., 2003 and Thevenon *et al*., 2012)

Icelandic sources typically have $^{87}Sr/^{86}Sr$ ranges between 0.703253 and 0.703844 and a Epsilon Nd range around +6.0 (Farmer *et al*., 2003), which allows it to be differentiated from

other sources. By way of example, Saharan dust has much higher $^{87}Sr/^{86}Sr$ values between 0.714 and 0.738 and Epsilon Nd values between -10 and -16 (Thevenon *et al*., 2012).

2.10: Tephra

2.10.1: Tephra dispersal

Atmospheric circulation patterns primarily influence tephra dispersal. During a volcanic eruption in Iceland tephra is more likely to be transported towards mainland Europe when winds are from the west or NW, a situation most often associated with negative phases of the North Atlantic Oscillation (NAO) – as seen in Spring 2010 during the eruption of Eyjafjallajökull (Langmann *et al*., 2012) (Figure 2.10).

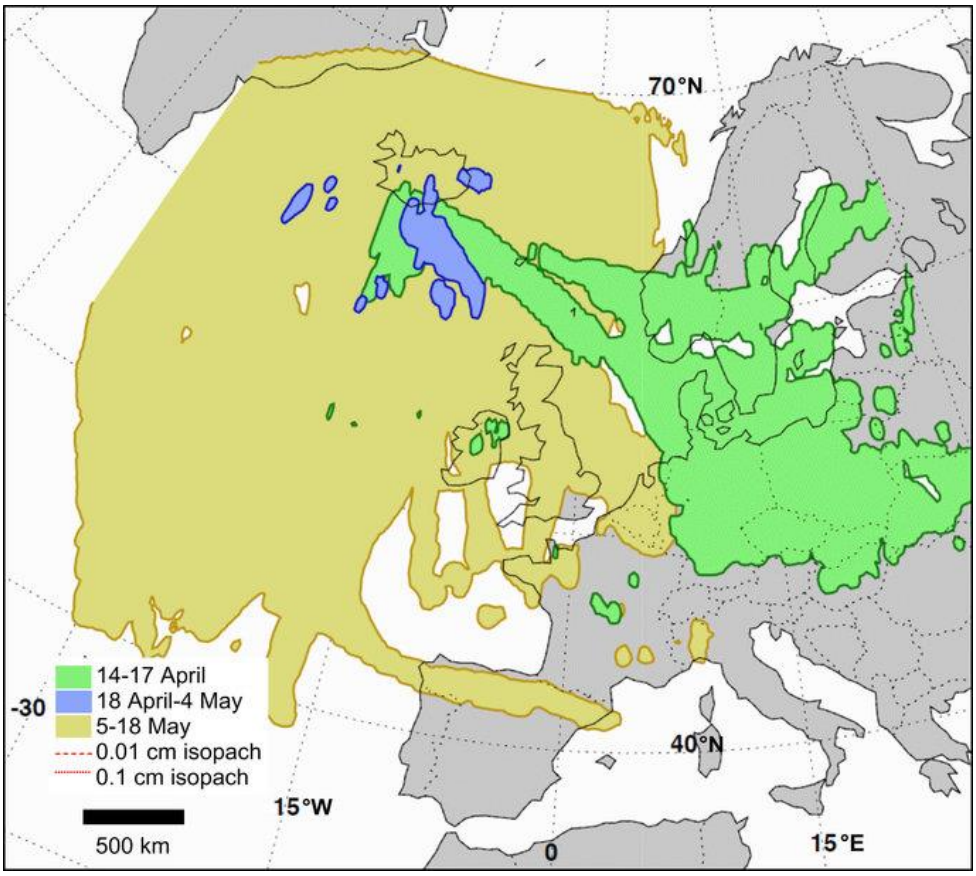

Figure 2.10 - Dispersal pattern of tephra from the 2010 eruption of Eyjafjallajökull (Gudmundsson *et al*., 2012)

Iceland is a highly volcanic country and eruptions are a frequent occurrence. Tephra is the collective term for all airborne volcanic material, including both air-fall and pyroclastic flow material (Haflidason *et al*., 2000). This incorporates a wide range of different sized fragments and only the smallest sized particles (<2.00 mm) are transported long distances away from the volcano (Haflidason *et al*., 2000). High-magnitude volcanic eruptions can eject a large amount of tephra into the atmosphere with eruptions having a Volcanic Explosivity Index (VEI) of 3 or more ejecting a substantial amount of material into the troposphere and eruptions with a VEI in excess of 5 additionally ejecting a significant amount of tephra higher into the stratosphere. The tephra component of these ejecta, particularly the glass shards, can be distributed over a wide geographical area and are often preserved in a range of glacial, terrestrial and marine deposits (Abbott and Davies, 2012).

The factors influencing tephra dispersal can broadly be divided into those governed by the type, intensity and magnitude of the eruption, including height of the eruption column and duration of the eruption, and those governed by external factors such as wind strength, wind direction and changes in wind direction during an eruption (Gudmundsson *et al*., 2008). Large particles (>256 mm) follow brief ballistic trajectories and reach the surface within a few kilometres of the volcano. Millimetre to centimetre sized particles (>16mm) settle from the column within a few minutes and usually land at a distance less than 15 km from the volcano. Smaller particles, with diameters ranging from 63 µm to 16mm, are transported to the column top and settle from the high-level spreading cloud within tens of minutes to an hour. The smallest particles, <63 µm in diameter, are transported in the

dispersing cloud and remain suspended in the atmosphere for hours to days, or longer and can therefore be transported much longer distances (Durant *et al*., 2010).

Two major features control the trajectories of tephra from Iceland; persistent westerly winds in the lower stratosphere between 9 and 15 km and a seasonal shift in wind direction above 15km that becomes more significant at higher elevations – with strong westerlies during the winter, and relatively weak easterlies during the spring and summer (Durant *et al*., 2010). A shift in wind direction occurs above 15.5 km during May and June. This shift becomes more significant with increasing elevation; with westerlies dominating from January to March, to dominant easterlies, from May to August. The transition occurs mainly in April, which is the period of highest variability. Between August and September an abrupt change occurs, leading to the return of dominant westerly winds from September to December. Surface winds do not exceed a mean velocity of 5 m/s throughout the year, however, they display high variability in speed and direction due to the influence of low-pressure systems. Wind velocities increase more rapidly with elevation during the winter and autumn when compared to summer (Lacasse, 2001). For example, westerlies blowing up to 40-45 m/s have been observed from October through January at about 48 km. However, at the same elevations, summer easterlies remain weak, from less than 5 to 10/12 m/s in April-May and August, whereas they increase up to 25 m/s in June and July (Lacasse, 2001). These broad-scale circulation patterns influence the dispersal of tephra away from Iceland and towards Europe (Langmann *et al*., 2012).

2.10.2: Tephra Morphology

Tephras range in composition and morphology: from colourless to coloured and vesicular to flaky (Hall *et al*., 1994). However, most have an angular and irregular shape (Durant *et al*., 2010) (Figure 2.11).

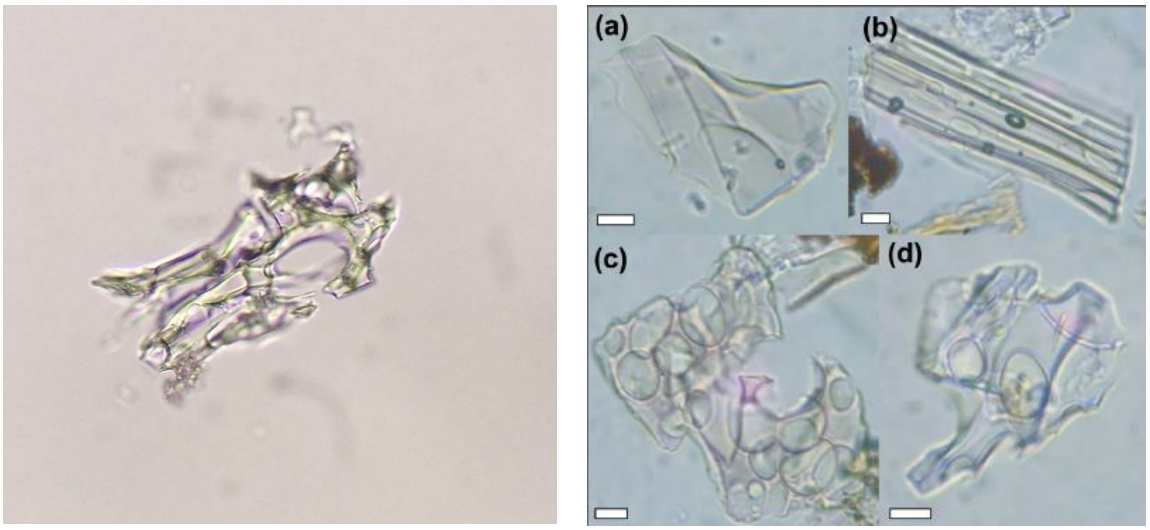

Figure 2.11: (left) a tephra particle from the Hekla 4 eruption identified by this study; (right) different tephra morphologies (Stevenson *et al*., 2013)

Tephra consists mainly of silicate glass and crystalline material reflecting the chemical composition of the magma from which it derives and that of the conduit rocks eroded during the eruption (Langmann *et al*., 2012). During some silicic Icelandic eruptions the silica content of the tephra frequently decreases over the time of the eruption. This is particularly evident in the case of the volcano Hekla. The silica content for the Hekla-4 eruption ranges between 74% and 57%, with the latter erupted towards the end of the eruption (Langdon and Barber, 2004). There are also differences between the silicic phreatoplinian eruptions and basaltic phreatomagmatic eruptions. The phreatoplinian eruptions are relatively short-lived, high-intensity events that inject large quantities of

tephra into the upper layers of the troposphere and lower layers of the stratosphere in a matter of hours. Most of the basaltic phreatomagmatic eruptions begin as subglacial events that become subaerial after 2-36 hours and although they may last for weeks and produce large volumes of tephra, their intensity is generally lower and the potential for long-distance transport is, therefore, smaller (Larsen and Eiríksson, 2008). Furthermore, basaltic tephra eruptions often produce denser, less vesicular tephra particles than acidic eruptions and these may be more likely to rain out from the atmosphere before reaching the continent.

2.10.3: Effects of tephra deposition

Tephra dispersal and deposition can have similar effects on the environment as dust. Tephra shards can lead to fertilisation of the oceans, and the release of SO_2 into the atmosphere can scatter solar radiation and lead to an increase in atmospheric albedo and tropospheric cooling (Bay *et al*., 2004, Kockum *et al*., 2006, Payne and Blackford, 2008, Durant *et al*., 2010, Payne *et al*., 2013). In recent times, the detrimental effects of tephra on aviation and air travel have been a major issue. Tephra particles are considered dangerous to aircraft engines because they commonly have a glassy groundmass that will change its material properties upon heating. This transition from solid to liquid-like behaviour will start far below the typical melting temperatures of crystals or rocks. Some constituents of tephra can become sufficiently liquid to cause damage on the thermal barrier coatings of turbine blades at temperatures which are generally exceeded in jet engine turbines. Aside from the adverse effects on turbine airfoils, other damage such as the erosion and blinding of windows or clogging of aeronautic sensors can occur (Weinzierl *et al*., 2012). The April 2010 eruption of Eyjafjallajökull was the most disruptive event in aviation history and caused widespread airport closures due to emissions dispersing through European airspace

(Durant *et al*., 2010). As this is one of the busiest air corridors in the world with, on average, 250 jet planes per day flying across the Icelandic Oceanic Control Area (IOCA) (Lacasse *et al*., 2004), the probabilities of major disruption are likely to increase even more in the future because of increased air traffic (Langmann *et al*., 2012). The eruption of Grímsvötn in 2004 also led to the closure of airspace in limited areas of Northern Europe, but the disruption was short-lived as the tephra was dispersed rapidly in a north-north-easterly direction (Davies *et al*., 2010).

2.10.4: Tephra as a chronological tool

When tephra layers are rapidly dispersed and widely deposited, they can form effective isochrones. The precision of these marker horizons can vary from hours to days and weeks, but in practical terms, they form unusually well-defined environmental marker horizons. A tephra layer is therefore useful for dating and correlation, both in relative and absolute terms (Óladóttir *et al*., 2012). The main assumptions behind tephrochronological dating of peat are: the tephra is deposited instantaneously (in geological terms), the tephra from each eruption possesses a unique geochemical signature and the shards are not mobile within the peat profile (Langdon and Barber, 2004). It is generally accepted that tephra layers are deposited instantaneously, although spatial variations in fallout can occur, and this often results in each tephra layer displaying a patchy spatial distribution (Langdon and Barber, 2004, Wastegård and Davies, 2009, Davies *et al*., 2010). The patchy airfall patterns of tephra in Scotland are probably due to the rainfall distribution at that time. In the pioneering days of tephrochronology, the principal method for tracing the origin of a tephra layer was by mapping its dispersal (Óladóttir *et al*., 2012). The emphasis was originally on silicic tephra layers that had distinct macroscopic characteristics such as colour. Mapping of

basaltic tephra layers was more difficult due to less distinct field characteristics and the presence of multiple layers with similar characteristics and this occasionally led to the incorrect identification of sources for basaltic layers (Óladóttir *et al*., 2012). Some recent tephra layers have been assigned calendar dates using documentary evidence, while others have been dated using high-precision wiggle-matching radiocarbon techniques (Swindles *et al*., 2011). Tephra layers can also be detected and identified by light microscopy (Pilcher *et al*., 1996). However, since many tephras are morphologically similar confirming the identity of microtephra is most accurate by geochemical fingerprinting of single shards through wavelength-dispersive electron microprobe analysis (Dugmore, 1989; Hunt and Hill, 1993, Hayward, 2012).

2.10.5: Tephra in the British Isles

Thin, fine-grained deposits of Icelandic tephra have fallen in the British Isles and North West Europe on over 20 occasions during the Holocene, with a wide geochemical

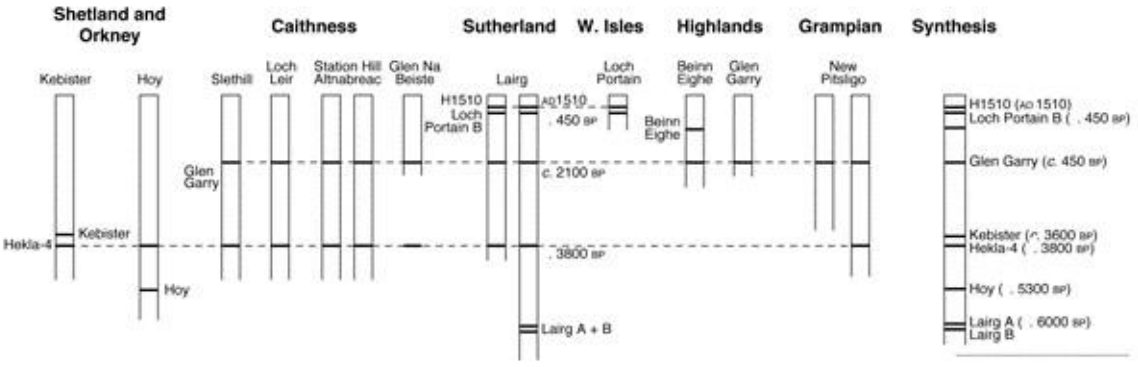

Figure 2.12 - An example of tephra layers found in Scotland and the differences in their distribution (Dugmore *et al*, 1995)

compositional range from basaltic to rhyolitic products (Dugmore and Newton, 1992; Dugmore *et al*., 1996; Davies *et al*., 2010, Boygle, 2004) (Figure 2.12).

The Holocene tephrochronology for the British Isles utilises layers that are generally submillimetre in thickness and rarely visible to the naked eye (Pilcher *et al*., 1996). In Iceland large numbers of tephra layers are readily visible in stratigraphic sections of soils and peats however in the British Isles, ~1000 km from Iceland, almost all of these layers are represented in peats and lake sediments at microscopic level only (Hall and Pilcher, 2002). The first finds of Icelandic tephra were in peats in Caithness in Northern Scotland (Dugmore, 1989) from an eruption of the Hekla volcano, identified as Hekla 4, which is one of the most geographically widespread tephra layers in Scottish and Irish deposits (Hall *et al*., 1994).

2.11; Summary and Project Aims

A review of the existing literature has highlighted the link between jet stream movement, storminess and the North Atlantic Oscillation. However, the proxy data that has been used to reconstruct these systems only currently exists for relatively short timescales (<2000 yr). A link between the NAO and glacier fluctuations has been established in Iceland and Norway, alongside an independent link between glacier activity and dust production in cold climate areas around the world. However, there is a lack of knowledge in the long range transport and deposition of dust from high-latitude glaciated areas and no data currently exists for reconstructing dust deposition patterns, climate change and glacier fluctuations over long timescales. As such, the following research aims for this project are proposed:

- to reconstruct a high-resolution record of North Atlantic storminess – to inform our knowledge of changes in the Jet stream and NAO over longer timescales than currently exist;
- to use tephrochronology and radiocarbon dating to construct robust age/depth models to constrain the records of storminess and dust.
- to reconstruct a high-resolution record of far-travelled minerogenic dust and compare it to changes in glacier activity over the Holocene;
- to use radiogenic isotope analysis to identify the probable source of the dust;

Chapter 3: Methodology

This chapter describes all the scientific procedures that were undertaken in this project. The chapter starts with descriptions of the field study sites and peat sampling methods. The study sites in this project were chosen as they are exposed to various atmospheric influences from around the North Atlantic; and lie along a longitudinal climate transect. A Russian corer was used to extract the peat cores to ensure a complete sediment sequence was recovered. This chapter then describes the techniques used to derive organic content, humification and ITRAX analysis of the peat. Measuring organic content ensured that the cores were composed solely of peat and were not influenced by any underlying sediment. Humification was used to analyse mire surface wetness which could then be used as a climate proxy. ITRAX analysis of the peat cores was originally used as an alternative method of identifying dust and tephra in the peat cores. Due to the microscopic nature of the particles though, and the beam only being able to analyse the peat surface, this was not achievable however the element analysis did provide a bromine curve that has been used as a successful climate proxy. This chapter is then followed by descriptions of the minerogenic separation technique by acid digestion, and dust and tephra analysis by microscopy and radiogenic isotope analysis. Acid digestion was the best method to separate dust and tephra from the peat. A combustion technique was considered however this would have altered the tephra composition. The mineral material was then analysed using light microscopy. Tephra shards were counted individually and viewed under polarised light and dust abundance was measured using a quantitative percentage-based score to determine the abundance of particles on the slide (Terry and Chilinger, 1995). As described above,

ITRAX was used as an alternative method to identify dust and tephra particles however this was unsuccessful. A weight based method was also tested however this could not determine the proportions of the larger, heavier particles and smaller, lighter particles and could not distinguish between the dust and tephra therefore was deemed unsuitable. Radiogenic isotope analysis was used to identify the source of the dust particles. Finally, this chapter ends describing the chronological methods used, namely tephrochronology and radiocarbon dating. These were used to construct high-precision age depth models.

3.1: Study sites

Analyses for this project are based on four peat cores that have been sampled along a ~300 km transect across Northern Scotland from Caithness to northern Shetland. Northern Scotland provides an excellent study site as the Scottish climate is regularly influenced by North Atlantic storms driven by the position of the polar front jet stream. The four study sites were chosen as they are exposed to various atmospheric influences from around the North Atlantic; and lie along a longitudinal climate transect. In addition, Icelandic tephras, important chronological marker horizons, have been previously identified in Caithness, Orkney and Shetland (Dugmore, 1989; Dugmore et al., 1995). To isolate the minerogenic aeolian dust record this study focused on mires where sediment accumulation solely comprised of organic matter and fluvial sediment inputs were topographically excluded. Therefore, any mineral content of the peat should be transported by aeolian processes.

3.1.1: Shebster

Shebster (N58°33’06.6”, W003°42’39.0”, altitude 82m, 4.8 km from coast) is located in Northern Caithness (Figure 3.1). Continuous high-resolution peat cores (to 6.08m depth)

were obtained from the central part of the Shebster mire. The mire surface slopes towards the Burn of Shebster that drains northwards around the mire (Figure 3.2). Bedrock underlying the site is Middle Devonian sandstone of the Bighouse Formation (Auton et al., 2005).

3.1.2: Heldale

Heldale is a blanket mire (Figure 3.3) on the island of Hoy, Orkney (N58°48'44.0", W003°15'52.3", altitude 73 m, 1.5 km from coast) (Figure 3.4). The underlying bedrock is Devonian Sandstone.

3.1.3: Pettawater

Pettawater (N60°18'58.1", W001°15'02.0", altitude 70m, 3.97 km from coast) is located on the Shetland mainland (Figure 3.5). The coring site is located on a raised bog 3-4 m above, but adjacent to, Pettawater loch and the bedrock is Dalradian (Figure 3.6).

3.1.4: Kedills Mires

Kedills Mires (N60°41'12.8", W001°02'52.8", altitude 67 m, 2.5 km from coast) is located on the island of Yell, Shetland Isles (Figure 3.7). The coring site is located on a blanket mire with close proximity to the coast (Figure 3.8) and the underlying bedrock is Moine psammite (metamorphosed sandstone and siltstone). The area is relatively flat and is not influenced by slope activity.

Figure 3.1 – Blanket mire at Shebster, Caithness

Figure 3.2 – The location of the Shebster core site

Figure 3.3 - Blanket mire at Heldale, Hoy, Orkney.

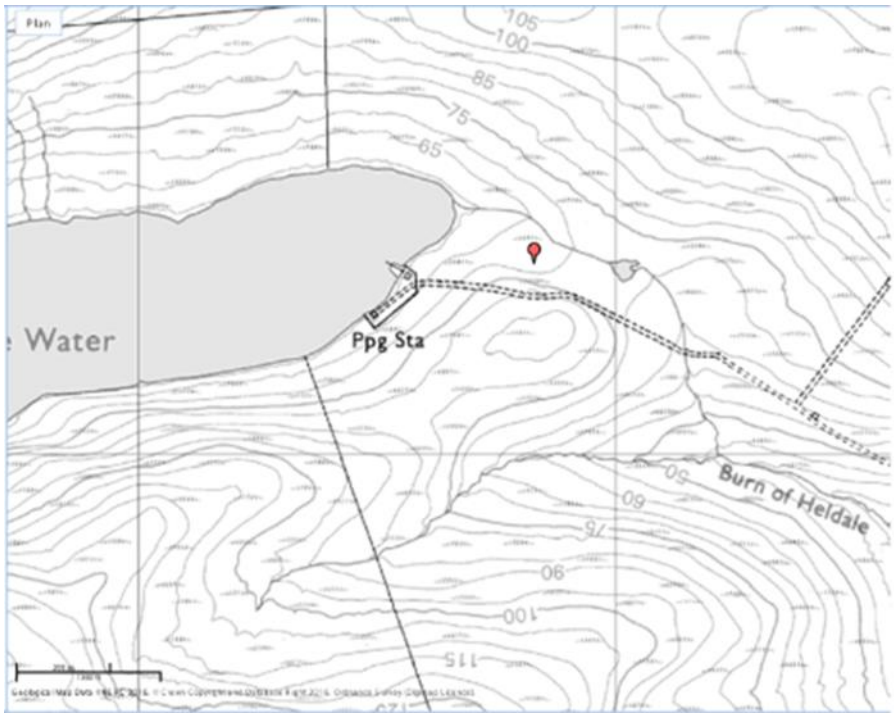

Figure 3.4 – The location of the Heldale core site

Figure 3.5 –Raised mire at Pettawater, Shetland Isles

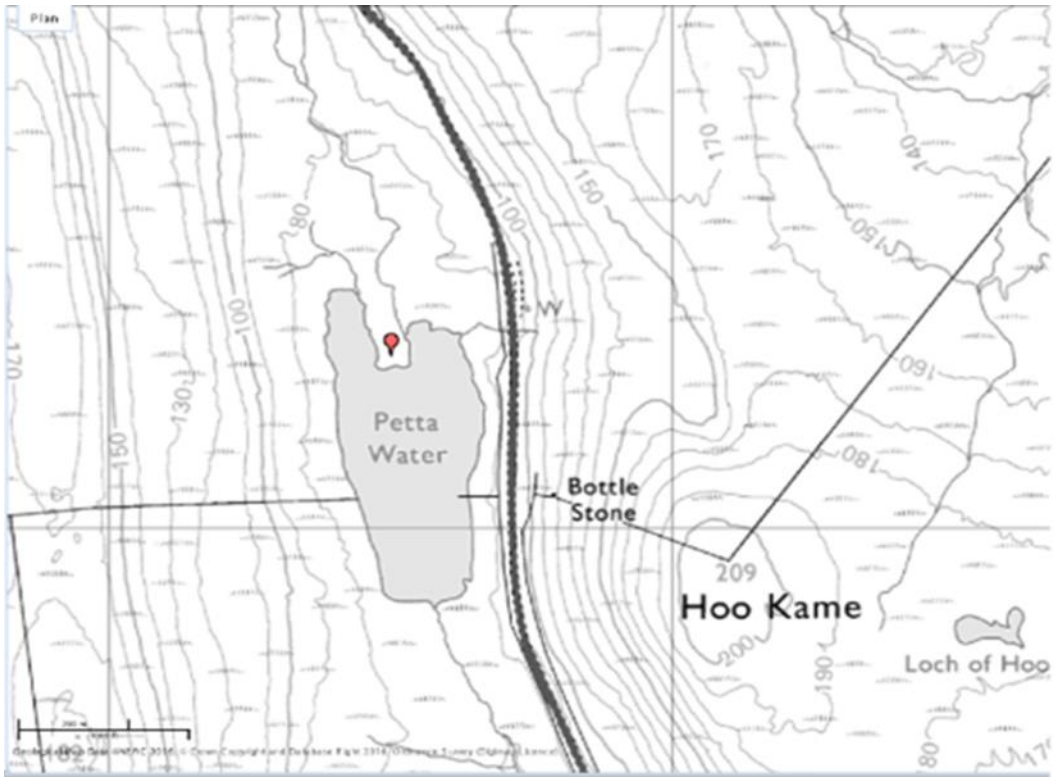

Figure 3.6 – The location of the Pettawater core site

Figure 3.7 – Blanket mire at Kedills Mires, Yell, Shetland Isles

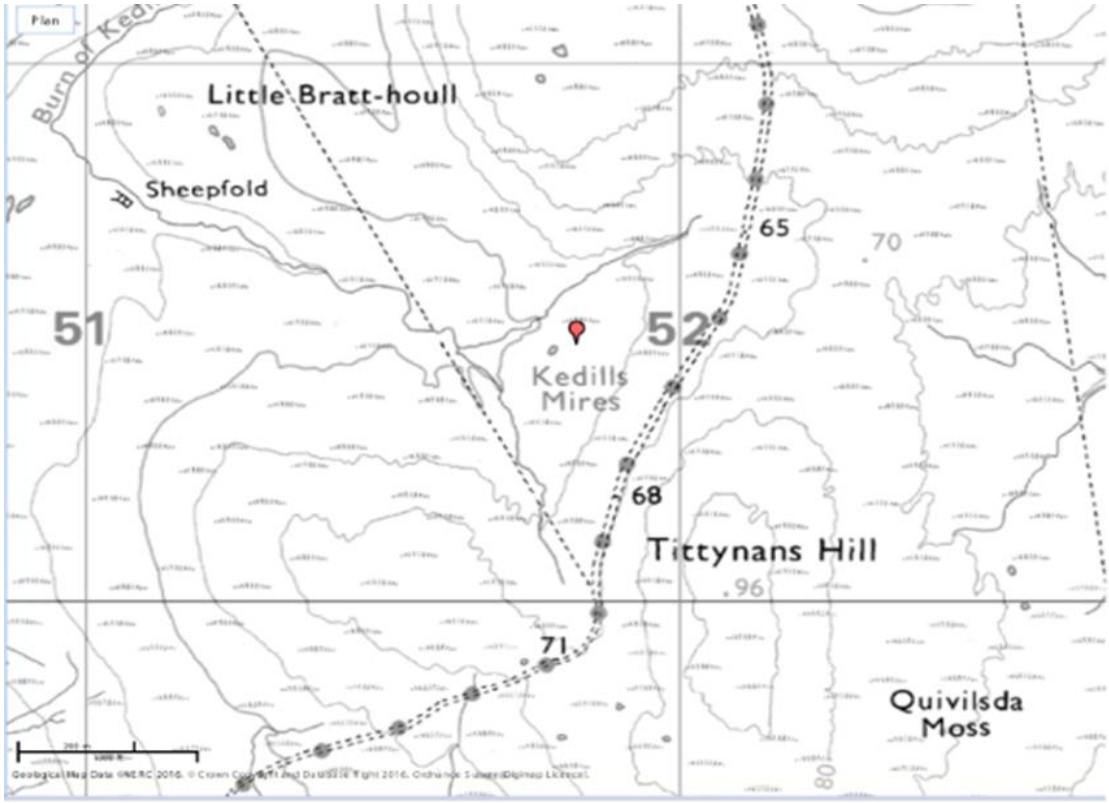

Figure 3.8 – The location of the Kedills Mires core site

3.2: Field Sampling

Cores were sampled using a 1 metre, 75 mm diameter, Russian D-section corer (Jowsey, 1966). Cores were sampled with 10 cm overlaps to ensure a complete sediment sequence was recovered. Recovered cores were transferred into plastic guttering and wrapped in lay-flat tubing. Core sections were transported horizontally to the University of Stirling and cold-stored at 4°C.

3.3: Organic content

To reconstruct changes in the bio-productivity through time, the percentage organic content of the core was measured. Bio-productivity is a function of the degree of plant growth, which in turn is related to the climate record, the degree of preservation of the plant material and sediment supply. This procedure was based on the method by Dean (1974). Contiguous samples of 2 cm depth were combusted in a muffle furnace at 550°C for 4 hours. The results are expressed as the percentage loss-on-ignition (LOI_{550}).

3.4: Peat humification

The degree of peat humification within the core can be taken as a proxy for mire surface wetness. Humification was measured using a modified alkali extract method (Blackford, 1993). At each sample interval, approximately 2 cm^3 of peat was dried at 80°C for at least 24 hours. To obtain relatively homogenous material the dry sample was ground using a small rotating blade grinder. 0.2g of the ground material was sub-sampled in 50 ml falcon centrifuge tubes. 50 ml of NaOH 8% w/v was added to each sample and the centrifuge tubes placed in a boiling water bath for 1 hour and intermittently stirred. The centrifuge tubes were subsequently removed from the boiling bath and centrifuged at 3000 rpm for 5

minutes. A 0.5 ml aliquot was pipetted into a 10 mm cuvette with 2.5 ml distilled water. The cuvette was analysed in a spectrophotometer and the % transmitted light measured at 540nm. Under drier conditions peat is more oxidised, the accumulation rate is slower and there is an increase in humic material. Under wetter conditions the rate of peat growth increases, the deposit is better preserved under anoxic conditions, and less humic material is produced. The greater the humic content the darker the extract solution and lower transmitted light values. Therefore, a low percentage transmission values indicates drier peat accumulation conditions whereas high transmission suggests wetter conditions.

3.5: Micro X-ray Fluorescence Geochemistry

Micro X-ray Fluorescence (μ-XRF) scanning was undertaken at the University of Aberystwyth using an ITRAX™ core scanner (Figure 3.9) to determine the proportions of chemical elements in the peat. It is important to note that the percentages are not equivalent to whole rock compositional data obtained by traditional XRF techniques.

The Shebster, Kedills Mires and Pettawater cores were analysed at 2000 μm intervals. The Heldale core was analysed at 500 μm intervals and Kedills Mires was re-analysed at 500 μm to assess if a more sensitive record could be obtained. Cores were analysed using a molybdenum (Mo) anode X-ray tube (settings: 30 kV, 50 mA, count time 10 seconds). Density and colour information was provided using X-radiography and digital RGB optical imagery. Scanning at a higher resolution did not make a difference to the accuracy of the data set. It is thought that the penetration and sensitivity of the micro-XRF was insufficient to detect microscopic dust and tephra layers. However due to the large volume of tephra associated with Hekla 4, this tephra layer was identified by μ-XRF analysis as a discrete titanium peak in the Shebster core. Micro-XRF is less accurate in peat due to its high

moisture and organic content (Jarvis et al., 2015). To counteract the uncertainty produced by the organic and water content of the peat, results are expressed as the ratio of the element/incoherent + coherent values (Davies et al., 2015). Magnetic susceptibility analysis was carried out on the Shebster core but was unable to detect the dust and tephra content. Due to a malfunction of the magnetic susceptibility equipment, this data only exists for the Shebster core.

Figure 3.9 – The ITRAX core scanner at the University of Aberystwyth

3.6: Acid Digestion of peat for separation of minerogenic content (i.e. dust and tephra)

Acid digestion was used to remove the peat organic matter and leave the minerogenic dust and tephra particles behind for analysis. This procedure was based on a method by Dugmore (1995). Minerogenic sediment (dust and tephra) were isolated from the peat by using the Sulphuric and Nitric acid digestion procedure developed by (Dugmore *et al.*,

1992). Contiguous peat samples of 1 cm or 2 cm depth, depending on the anticipated accumulation rate, were placed into 250 ml volumetric flasks. Between 75 and 100 ml of concentrated sulphuric acid were then added to each flask. The flasks were then heated on a hot plate for ~ 2 hours at 280 degrees. After the peat had dissolved into the sulphuric acid, nitric acid was added slowly in 1ml aliquots. This accelerates the digestion of the organic material and left a clear supernatant and mineral material. The samples were left to cool for approximately one hour and then ~200 ml of distilled water was very slowly added to dilute the sulphuric acid. The samples were left overnight to cool and to allow the mineral material settle.

The liquid contents of the flasks were drained with particular care not to disturb the sediment at the bottom of the flask. The mineral residue was then transferred to centrifuge tubes and 50 ml of distilled water added and then centrifuged at 2500 rpm for 5 minutes. To avoid losing sample material the supernatant was not poured out of the centrifuge tube but gently aspirated using a fine Pasteur pipette. A further 50 ml of distilled water was added to neutralise the samples, shaken and centrifuged at 2500 rpm for 5 minutes. This procedure was repeated until the acid content was neutralised and then after the final centrifuge, samples were transferred to 10 ml glass vials.

The mineral material was then analysed using light microscopy. An Olympus BX43 at x400 magnification was used to identify and quantify dust and tephra content. Tephra shards were counted individually and viewed under polarised light. Dust abundance was measured using a quantitative percentage-based score to determine the abundance of particles on the slide (Terry and Chilinger, 1995).

For the Kedills Mires and Heldale cores, the mineral residue was also weighed using a precision balance in an attempt to test the accuracy of the microscope estimation of abundance. Before digestion, the glass vials were weighed and the peat samples were dried for at least 48 hours and weighed in the 250ml conical flasks. After digestion and transfer to the glass vials, the samples were then dried in a heat block and the tephra and dust residue weighed. However, this method was not as accurate as expected. The five figure calibrated balance was unable to reliably measure the small sample weights. In addition, this method could not determine the proportions of the larger, heavier particles and smaller, lighter particles. Therefore, the weight data may have been influenced by local dust flux. Furthermore, this method also could not distinguish between the dust and tephra.

3.7: Radiogenic Isotope Analysis

Radiogenic isotope analysis was conducted at the National Isotope Geochemistry Laboratory (NIGL), British Geological Survey (BGS), Keyworth to potentially determine the source of the minerogenic dust. Selected samples from the Shebster, Kedills Mires and Heldale cores were dried and weighed before being spiked with 84Sr and 150Nd isotope tracers to allow calculation of Sr and Nd concentrations as well as isotope compositions. The volume of spike added was in relation to the weight of the sample. 1 ml of 16M HNO3 and 29M HF were then added and the samples were left on a hot plate overnight to dissolve.

1.5 ml of nitric acid was then added to ensure no fluoride was left over and dried on the hot plate. When dry, the beakers were filled with HCl and left to dry overnight.

Columns containing Eichrom AG50x8 cation exchange resin were prepared using 2.5M HCl. Once dry, 2 ml of 2.5M HCl was added to the samples and then centrifuged. They were then pipetted into columns, being careful to leave any residue behind in the centrifuge tube to avoid clogging up the columns. The columns are then rinsed with 1 ml of 2.5M HCl to wash the entire sample into the resin and then topped up with 46 ml of 2.5M HCl to wash off all major elements. 12 ml of 2.5M HCl were then added to catch the Strontium. Once collected the samples were left on a hotplate to dry overnight. Using a new beaker, 20 ml of 6M HCl was added to the columns to collect the rare earth elements. Once collected these were left to dry on a hot plate overnight.

New columns containing 2ml of Eichrom LN-SPEC resin were prepared by washing twice with 6M HCl and conditioning with one rinse of 0.2M HCl. 100µl of 0.2M HCl was added to each sample and left to dissolve. The rare-earth element concentrates from the first columns were then carefully pipetted onto the columns and rinsed with 4x1 ml of 0.2M HCl that were discarded. The samples were then rinsed with 10 ml of 0.2M HCl that washed off the La, Ce and Pr, and was discarded. 3 ml of 0.3M HCl was then run through the columns and collected in beakers to collect the Nd. This was left to dry overnight on the hotplate. 4mls of 0.6M HCl was then ran through the column and collected as this contained Sm. This was then left on the hot plate overnight to dry. This left two different elements separated for analysis on the mass spectrometer – strontium and neodymium.

Strontium was analysed on a Thermo Scientific Triton thermal ionisation mass spectrometer (Figure 3.10). Strontium was introduced into the ion source of the Tritonthermal ionization mass spectrometer as a solid salt on a rhenium filament and ionised by heating the filament.

Neodymium was analysed on a Thermo Scientific Neptune + plasma ionisation mass spectrometer, and was introduced into the mass spectrometer by aspiration in solution using an Aridus II desolvating nebuliser. In both cases, the resulting ions were then accelerated via high voltage through a magnetic field that deflects and separates ions of different mass (and the same charge) into a mass spectrum. Lighter mass isotopes are deflected more strongly than heavier isotopes. The relative amounts are of the different masses were measured by the current produced when they strike ion detectors positioned downstream from the magnetic field. Since different isotopes of an element are a measure of their relative isotopic abundances, measurement of isotope ratios by this method is much more accurate and precise than measurement of absolute isotope abundances. The Earth's crust and mantle have distinct ranges of isotopic ratios owing to their distinct mineral assemblages. As Iceland is highly volcanic and influenced by the upper mantle, $^{87}Sr/^{86}Sr$ ratios are relatively low whereas Scotland, which is based upon older crustal rocks, has much higher ratios (Banner, 2003). This provides the means to identify the source of the minerogenic dust layers found within the peat cores.

Strontium data was obtained for all cores. Neodymium data was obtained for Kedills Mires and Heldale sites. However, concentrations in the Shebster core were too low to be analysed.

Figure 3.10 – The Triton Mass Spectrometer

3.8: Electron Microprobe Analysis

Tephra layers were analysed by the SX100 Cameca electron microprobe at the University of Edinburgh (Figure 3.11) using methods established by Hunt and Hill (1993) and Hayward (2012). To prepare the samples, slides were frosted and grease was removed using soap. Slides were then titled to identify which samples they correspond to and sample boxes were carefully drawn on the slides in pencil and labelled. The slides were then placed on a hotplate at 80°C and the samples were carefully pipetted into labelled sections. When dry, a resin was made up and mixed with the samples on the slides. The slides were left to cure overnight.

Once dry, the sample/resin mixture was ground using a sequence of graded papers: 400, 800, 1200 then 2500 to expose the tephra shards on a flat surface prior to polishing. A micrometer was used to ensure a consistent sample thickness. Following grinding the slides were placed in a slide holder in a beaker of pet-ether and placed in an ultrasonic bath do 5-10 mins to remove grinding media and any loose but trapped sample cuttings.

Lastly, samples were polished using a 6 µm diamond polishing lap followed by a 1 µm polishing lap with a cleaning in pet ether in between. Once the samples were well polished they were carbon coated before electron microprobe analysis.

Figure 3.11 – The Cameca SX100 electron microprobe and author

Tephrabase (Newton, 1996) was referred to in this project to assist in the identification of tephra layers discovered in the cores. However, in the case of the Shebster core, only one layer had enough shards to be positively identified, and in the Kedills Mires core, two layers could not be identified from geochemical records held in Tephrabase. Therefore, radiocarbon dating on these cores was essential to construct accurate age/depth models.

3.9: Accelerator Mass Spectrometry Radiocarbon Dating

Shebster - Five samples were radiocarbon dated using Accelerated Mass Spectrometry (AMS) to enable the construction of a Bayesian age-depth model alongside the Hekla 4 tephra layer. All samples were wood material and were pre-treated with an acid/alkali/acid treatment sequence. Samples were analysed by AMS at Beta Radiocarbon laboratories in Miami, Florida. Dates were calibrated using BACON v2.2 (Blaauw and Christen) and Intcal13 (Reimer et al., 2013).

Kedills Mires - Seven samples were chosen for radiocarbon dating. All samples were bulk peat and were analysed at the NERC radiocarbon facility in East Kilbride (funded by NERC RCL steering committee). Samples were digested in 1M HCl (80°C, 8 hours), washed free from mineral acid with deionised water then digested in 0.5M KOH (80°C, 2 hours). The digestion was repeated using deionised water until no further humics were extracted. The residue was rinsed free of alkali, digested in 1M HCl (80°C, 2 hours) then rinsed free of acid, dried and homogenised. The total carbon in a known weight of the pre-treated sample was recovered as CO_2 by heating with CuO in a sealed quartz tube. The gas was converted to graphite by Fe/Zn reduction then analysed using the AMS. Dates were calibrated using BACON v2.2 (Blaauw and Christen) and Intcal13 (Reimer et al., 2013).

3.10: Summary

The methods described form a unique suite of analytical techniques which have been used together for the first time to reconstruct a record of North Atlantic storminess and climate change over the Holocene. The carefully chosen study sites are from 4 peat bogs across maritime Northern Scotland: Shebster in Caithness; Heldale on Orkney; and Kedills Mires and Pettawater, on Shetland. LOI, humification and ITRAX analysis have been used to estimate changes in storminess whereas acid digestion, microscopy and radiogenic isotope analysis have been used to estimate changes in dust. Tephrochronology and radiocarbon dating have been used to derive age models for each core.

Chapter 4:

Results

This chapter presents all the results obtained in this project. Firstly, the chronology is constructed using the available radiocarbon dates and tephrochronology data, then these age-depth models are used to constrain the palaeoenvironmental records from each site. This is followed by a description of the results of the LOI_{550}, humification and micro-XRF analyses as proxies for local storminess and climate. The dust index, an indicator of glacial activity and wider atmospheric circulation intensity, is then described; followed by the radiogenic isotopic data as an indicator of dust provenance and transport path.

4.1 – Chronology

4.1.1 – Shebster

Five organic samples at various depths were AMS dated to enable the construction of a Bayesian age-depth model supplemented by the age of the Hekla 4 tephra layer (Table 2).

Depth (cm)	^{14}C yr BP (1σ)	$\delta^{13}C_{VPDB}$‰	Cal. yr BP (2σ)	Weighted Mean Age (Cal. yr BP)	Lab. Code
150	1740 ± 40	-28.3	1621 - 1876	1737	Beta 251972
271	3010 ± 40	-28.0	3139 - 3407	3278	Beta 251973
346	3826 ± 12[1]	n/a	4207 - 4348	4257	n/a
405	4110 ± 40	-29.4	4786 - 5249	4899	Beta 251974
500	5730 ± 40	-25.6	6430 - 6695	6565	Beta 251975
612	7530 ± 50	-24.7	8123 - 8473	8344	Beta 251976

Table 2 - Shebster calibrated radiocarbon and tephra ages.

[1] Hekla 4 tephra layer (Dugmore et al., 1995a)

All samples were wood material and were pre-treated with an acid/alkali/acid treatment sequence. Samples were analysed by AMS at Beta Analytic Radiocarbon laboratories in Miami, Florida. Ages were calibrated using BACON v2.2 (Blaauw and Christen, 2011) and Intcal13 (Reimer et al., 2013) in 2 cm intervals with a mean accumulation rate of 13 yrs cm^{-1}. The BACON parameters were an accumulation shape of 1.5, and MEM strength of 4 and an MEM mean of 0.3 (Figure 4.1.1).

The tephra layer was analysed by the SX100 Cameca electron microprobe at the University of Edinburgh using methods established by Hunt and Hill (1993) and Hayward (2012) and identified using reference data provided in Tephrabase (Newton, 1996).

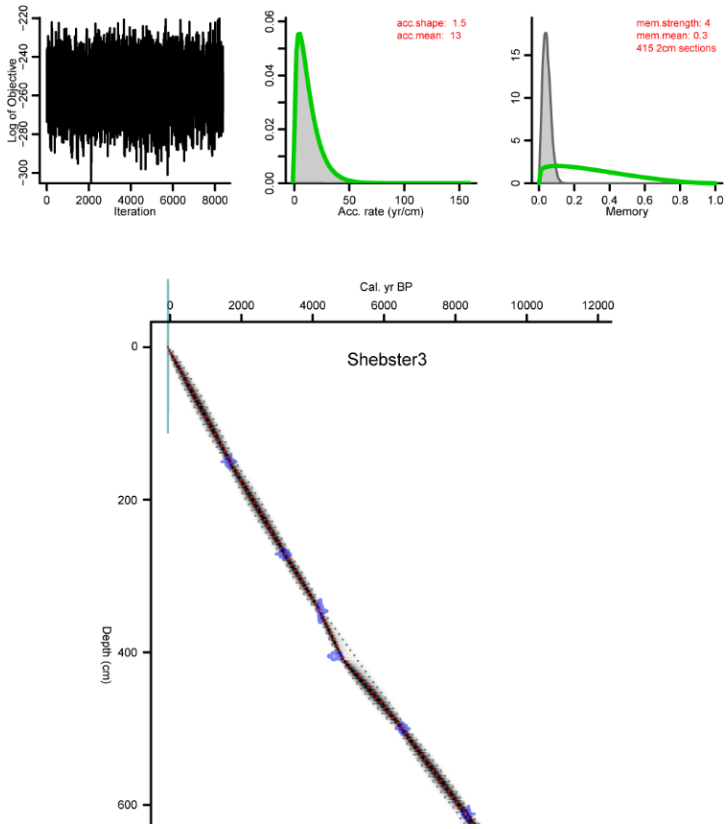

Figure 4.1.1 - Shebster BACON age-depth model

4.1.2 - Heldale

Tephrochronology was used to constrain the age of the Heldale core. Three tephra layers were analysed which include Lairg A, Hoy and Hekla 4 (Table 3).

Table 3: Heldale calibrated radiocarbon ages for the identified tephra layers.

Depth (cm)	^{14}C yr BP (1σ)	Cal. yr BP (2σ)	Weighted Mean Age (Cal. yr BP)
178[3]	3826 ± 12	4108 - 4410	4251
260[2]	5560 ± 90	6291 - 6694	6486
271[1]	6000 ± 50	6660 - 6984	6836

[1] Lairg A tephra layer (Dugmore et al., 1995b)
[2] Hoy tephra layer (Dugmore et al., 1995a)
[3] Hekla 4 tephra layer (Dugmore et al., 1995a)

The ages were calibrated using BACON v2.2 (Blaauw and Christen, 2011) and Intcal13 (Reimer et al., 2013) to construct the age/depth model. This was calibrated in 2cm intervals with an average accumulation rate of 22 yrs cm^{-1}. The BACON parameters were an accumulation shape of 1.5, and MEM strength of 4 and an MEM mean of 0.3. A basal date was not analysed and an estimated basal age was calculated from the average accumulation rate of 22 yrs cm^{-1} to 8294 Cal. yr BP (Figure 4.1.2).

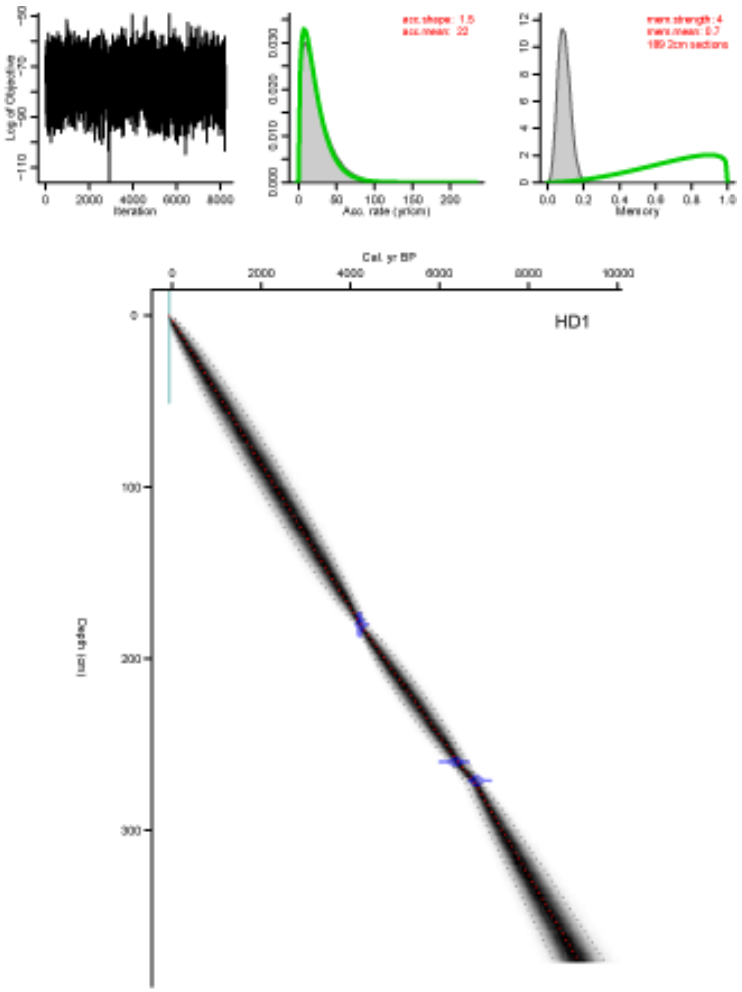

Figure 4.1.2: Heldale BACON age-depth model

4.1.3: Pettawater

Tephrochronology was used to age constrain the Pettawater core. Five tephra layers were analysed which include Hekla 4, Kebister, Hekla 3, Glen Garry and Oraefajokull 1362 (Table 4).

Table 4: Pettawater calibrated ages for the tephra layers.

Depth (cm)	^{14}C yr BP (1σ)	Cal. yr BP (2σ)	Weighted Mean Age (Cal. yr BP)
63[5]			651
225[4]	2120 ± 60	2242 - 2821	2645
294[3]	2879 ± 34	3270 - 3832	3665
306[2]	3695 ± 35	3574 - 4006	3899
334[1]	3825 ± 12	4087 - 4312	4258

[1] Hekla 4 tephra layer (Dugmore et al., 1995a)
[2] Kebister tephra layer (Owen and Lowe, 1999)
[3] Hekla 3 tephra layer (Dugmore et al., 1995a)
[4] Glen Garry (Dugmore et al., 1995a)
[5] Oraefajokull 1362

The tephra ages were calibrated using BACON v2.2 (Blaauw and Christen, 2011) and Intcal13 (Reimer et al., 2013) to establish the construction of an age-depth model. This was calibrated in 2 cm intervals with an average accumulation rate of 11 yrs cm^{-1}. The BACON parameters were an accumulation shape of 1.5, and MEM strength of 4 and an MEM mean of 0.7. A basal date was not analysed therefore an estimated date was calculated from the average accumulation rate of 11 yrs cm^{-1} to 4477 Cal. yr BP (Figure 4.1.3).

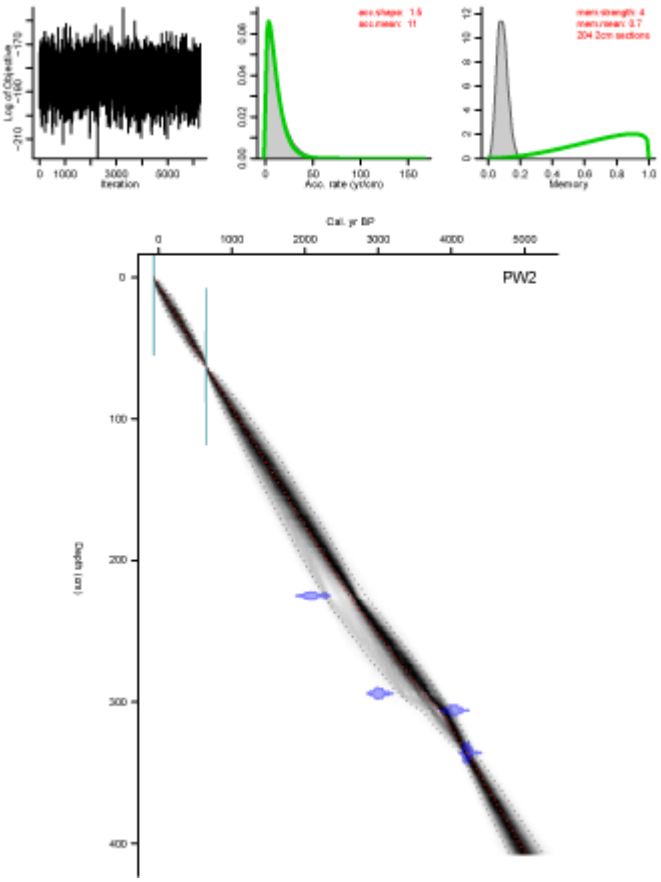

Figure 4.1.3: Pettawater BACON age-depth model.

4.1.4 – Kedills Mires

Seven organic samples were AMS dated, alongside the Hekla 4, Kebister, Glen Garry and Hekla 1158 tephra layers (Table 4), to enable the construction of a Bayesian age-depth model

Depth (cm)	^{14}C yr BP (1σ)	$\delta^{13}C_{VPDB}$‰	Cal. yr BP (2σ)	Weighted Mean Age (Cal. yr BP)	Lab. Code
40	649 ± 35	-28.1	613 - 761	693	SUERC-63942
63*	2205± 35	-28.3	n/a	n/a	SUERC-63941
63**	2295±37	-28.4	n/a	n/a	SUERC-66568
93*	2841± 37	-26.9	n/a	n/a	SUERC-63940
93**	2926±35	-28.4	n/a	n/a	SUERC-66567
120.5[4]	n/a	n/a	n/a	792	n/a
193	1172 ± 37	-27.7	1215 - 1645	1338	SUERC-63936
243	1821 ± 35	-29.1	1792 - 2352	1936	SUERC-63935
265[3]	2120 ± 60	n/a	2147 - 2733	2342	n/a
330.5[2]	3550 ± 50	n/a	3902 - 4143	4032	n/a
344.5[1]	3826 ± 12	n/a	4183 – 4365	4266	n/a
390	4352 ± 36	-28.0	4908 – 5214	5041	SUERC-63934
426	5027 ± 35	-28.7	5584 - 5901	5728	SUERC-63933

Table 5: Kedills Mires calibrated radiocarbon and tephra ages

*Reversed ages (excluded from BACON age-depth model)
** Repeat analysis dates (excluded from BACON age-depth model)
[1] Hekla 4 tephra layer (Dugmore et al., 1995a)
[2] Kebister tephra layer (Owen and Lowe, 1999)
[3] Glen Garry tephra layer (Dugmore et al., 1995a)
[4] Hekla 1158

All radiocarbon samples were bulk peat and were pre-treated with an acid/alkali/acid treatment sequence. Samples were analysed by AMS at the NERC radiocarbon facility in East Kilbride. Dates were calibrated using BACON v2.2 (Blaauw and Christen, 2011) and Intcal13 (Reimer et al., 2013). Unfortunately, a dating reversal was found in the samples at

63 cm and 93 cm, which may indicate peat cutting and older material being placed on top of newer material. The reversed samples were taken from the top meter core (0-100 cm) which also contains the radiocarbon date at 40 cm (~650 BP) consistent with its depth near the modern surface. Although peat cutting on Yell is very common the site was chosen because there was no evidence of peat cutting at the surface. It is also puzzling that the material has been placed on top of the younger material the right way up rather than upside down (which is more common during peat cutting practices) and without any further disturbance to the core stratigraphy. Note that duplicate samples at 63 cm and 93 cm depth were re-analysed on the AMS (free of charge at NRCL-East Kilbride) to check whether the reversal was due to a laboratory error or labelling mistake but the older/reversed ages were confirmed. As the younger age of AD 1158, provided by the Hekla tephra layer at 120 cm depth lies beneath the older radiocarbon ages of c. 2205 to 2296 ^{14}C yrs BP these two anomalous ages have been excluded from the age-depth model which leaves a hiatus between ~40 cm and 90 cm and led to construction of two separate age-depth models. The age-depth model from 0-40 cm was calibrated in 1 cm intervals with an accumulation rate of 20 yrs cm^{-1}. The age-depth from 120-426 cm was calibrated in 2 cm intervals with an accumulation rate of 14 yrs cm^{-1}. The BACON parameters were an accumulation shape of 1.5, and MEM strength of 4 and an MEM mean of 0.7. (Figure 4.1.4).

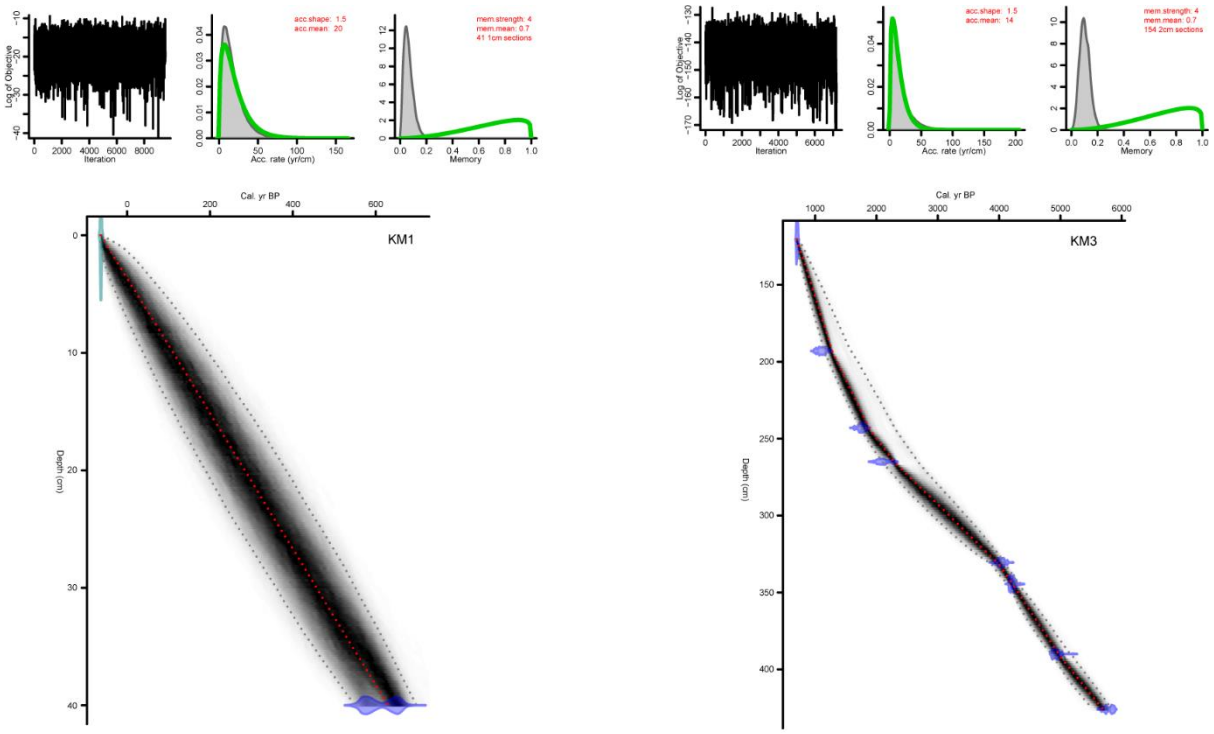

Figure 4.4: Kedills Mires BACON Age/Depth Models (right) 0-40 cm and (left) 120-426 cm

The age-depth models for Shebster, Heldale, Pettawater and Kedills Mires will now be applied to constrain the timing of the stratigraphical data presented from each site in sections 4.2, 4.3, 4.4 and 4.5 respectively.

4.2 – Loss on Ignition (LOI) and Humification

4.2.1 - Shebster

The percentage LOI_{550} and % transmission results, an indication of the degree of peat humification, for the Shebster core are shown in Figure 4.2.1. The surface peat lies within the acrotelm above the water table. This is subject to aerobic activity and therefore does not provide a mire surface wetness signal. The longer term MSW signal is only provided by the humified peat locked in the catotelm beneath the water table. Therefore, the humification record ends at 12 cm depth. The LOI_{550} is analysed to the base of the peat but to avoid any dilution effects from the underlying minerogenic lacustrine material (at a depth of 608 cm) the humification was only analysed to 590 cm depth. The results are divided into 8 zones based on marked changes in the Shebster humification record. The Hekla 4 tephra layer is indicated by a pale grey dashed line.

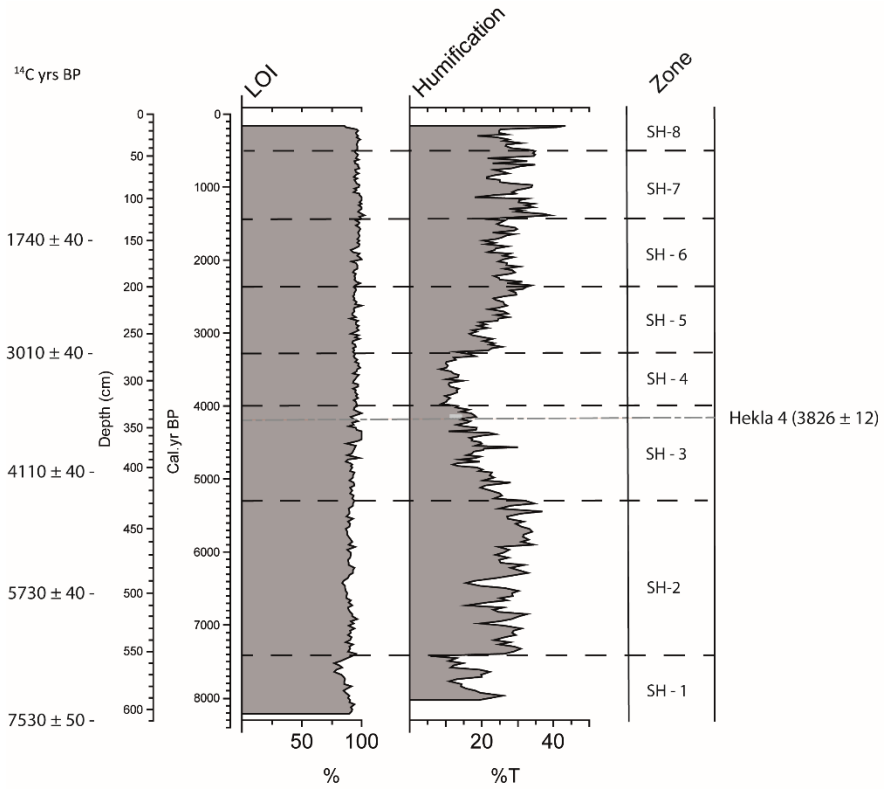

Figure 4.2.1 – Shebster LOI_{550} and peat Humification (% Transmission) profile.

SH-1 – 8207 – 7400 Cal. yr BP: LOI_{550} declines from 94 % at the base of the core to 77 % at 7490 Cal. yr BP. Humification was not measured to the base of the peat to avoid any potential influence from the underlying lake sediment and values commence at 590 cm depth. Humification values decrease from 22.7 %T at *c.* 7960 Cal. yr BP to 11 %T at *c.* 7740 Cal. yr BP before rising to a small peak of 22.2 %T at *c.* 7610 Cal. yr BP. Values then decline dramatically to ~13 % at *c.* 7420 Cal. yr BP.

SH-2 – 7400 - 5270 Cal. yr BP: LOI_{550} remains stable around 90 % with a small dip to 83 % at *c.* 6390 Cal. yr BP. Humification values fluctuate between 25 %T and 30 %T then decline to 24.9 %T at *c.* 6070 Cal. yr BP and remain stable before rising to 34.4 %T at *c.* 5860 Cal. yr BP. Values then decline briefly to 27 %T at *c.* 5470 Cal. yr BP before increasing to a peak of 36.8 %T at *c.* 5400 Cal. yr BP.

SH-3 – 5270-4000 Cal. yr BP: LOI values are on a gradually increasing trend. Humification values steadily decline to 13.4 %T at *c.* 4760 Cal. yr BP but increase to a small peak of 30.1 %T at *c.* 4540 Cal. yr BP.

SH-4 – 4000-3300 cal a BP: LOI values are on a gradually increasing trend. Humification values steadily decline to a value of 10.1 %T at *c.* 3390 Cal. yr BP.

SH-5 – 3300 – 2400 Cal. yr BP: LOI values are on a gradually increasing trend. Humification values rise to a peak of 25.6 %T at *c.* 3160 Cal. yr BP before declining to 17.5 %T at *c.* 3010 Cal. yr BP.

SH-6 – 2400-1400 Cal. yr BP: LOI values are on a gradually increasing trend. Humification values rise steadily to a peak of 33.9 %T at *c.* 2320 Cal. yr BP before declining to 20.4 %T at *c.* 1710 Cal. yr BP.

SH-7 – 1400 – 600 Cal. yr BP: LOI values are stable between 95 % and 100 %. Humification values increase to a peak of 39.1 %T at *c.* 1370 Cal. yr BP then decline to a lull of 18 %T at *c.* 1110 Cal. yr BP. Values then increase again to 34.1 %T at *c.* 950 Cal. yr BP before decreasing to 21.5 %T at *c.* 840 Cal. yr BP then rise again to 34.8 %T at *c.* 670 Cal. yr BP.

SH-8 – 600-0 Cal. yr BP: LOI remains stable between 95 % and 98 %. Humification values decline to 21.6 %T at *c.* 580 Cal. yr BP then rise to a peak of 34.8 %T at *c.* 490 Cal. yr BP. Values then decrease to 18.8 %T at *c.* 280 Cal. yr BP before rising to a peak of 43.3 %T at *c.* 140 Cal. yr BP.

4.2.2 – Heldale

The percentage LOI_{550} and % transmission results, an indication of the degree of peat humification for the Heldale core are shown in Figure 4.2.2. The surface peat lies within the acrotelm above the water table. This is subject to aerobic activity and therefore does not provide a mire surface wetness signal. The longer term MSW signal is only provided by the humified peat locked in the catotelm beneath the water table. Therefore, the humification

record ends at 20 cm depth. Both records are analysed to the base of the peat at 377 cm depth. The results are divided into 5 zones based on marked changes in the Heldale humification record. The Lairg A, Hoy and Hekla 4 tephra layers are indicated by pale grey dashed lines.

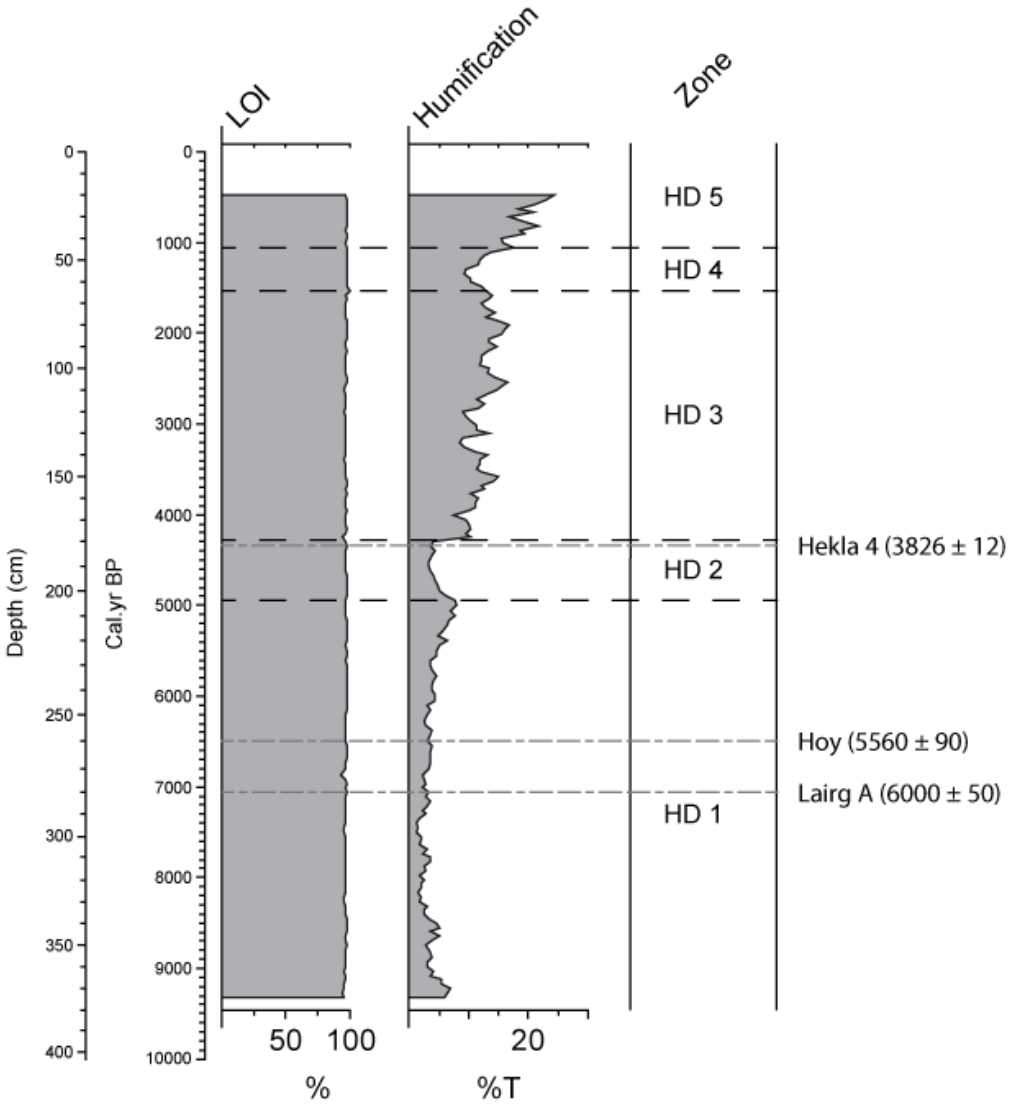

Figure 4.2.2 – Heldale LOI_{550} and peat Humification (% Transmission) profile

HD 1 – 9365 – 4950 Cal. yr BP: LOI is stable around 97 % with the exception of a small dip to 93 % at *c.* 6870 Cal. yr BP. Humification values increase to 7 %T at *c.* 9220 Cal. yr BP then

decline and are very low ranging between 1.3 and 4.5 %T. Values then follow a gradually increasing trend to 8 %T at *c.* 5000 Cal. yr BP.

HD 2 – 4950 – 4280 Cal. yr BP: LOI remains stable around 97 % with the exception of a slight decline to 94 % at *c.* 4250 Cal. yr BP. Humification values decline to 3.2 %T and remain low.

HD 3 – 4280 – 1540 Cal. yr BP: LOI remains stable around 97 %. Humification values increase sharply to 10.3 %T at *c.* 4250 Cal. yr BP then fluctuate between 16.5 %T and 8.5 %T.

HD 4 – 1540 – 1050 Cal. yr BP: LOI remains stable around 97 %. Humification values decline to 9.2 %T at *c.* 1340 Cal. yr BP.

HD 5 – 1050 – 0 Cal. yr BP: LOI remains stable around 97%. Humification values are on an increasing trend to 24.2 %T at *c.* 480 Cal. yr BP.

4.2.3 – Pettawater

The percentage LOI_{550} and % transmission results, an indication of the degree of peat humification for the Pettawater core are shown in Figure 4.2.3. The surface peat lies within the acrotelm above the water table. This is subject to aerobic activity and therefore does not provide a mire surface wetness signal. The longer term MSW signal is only provided by the humified peat locked in the catotelm beneath the water table. Therefore, the humification record ends at 8 cm depth. Both records are analysed to the base of the peat at 406 cm depth. The results are divided into 8 zones based on marked changes in the

Pettawater humification record. The Hekla 4, Kebister, Hekla 3, Glen Garry and Oraefajokull 1362 tephra layers are indicated by pale grey dashed lines.

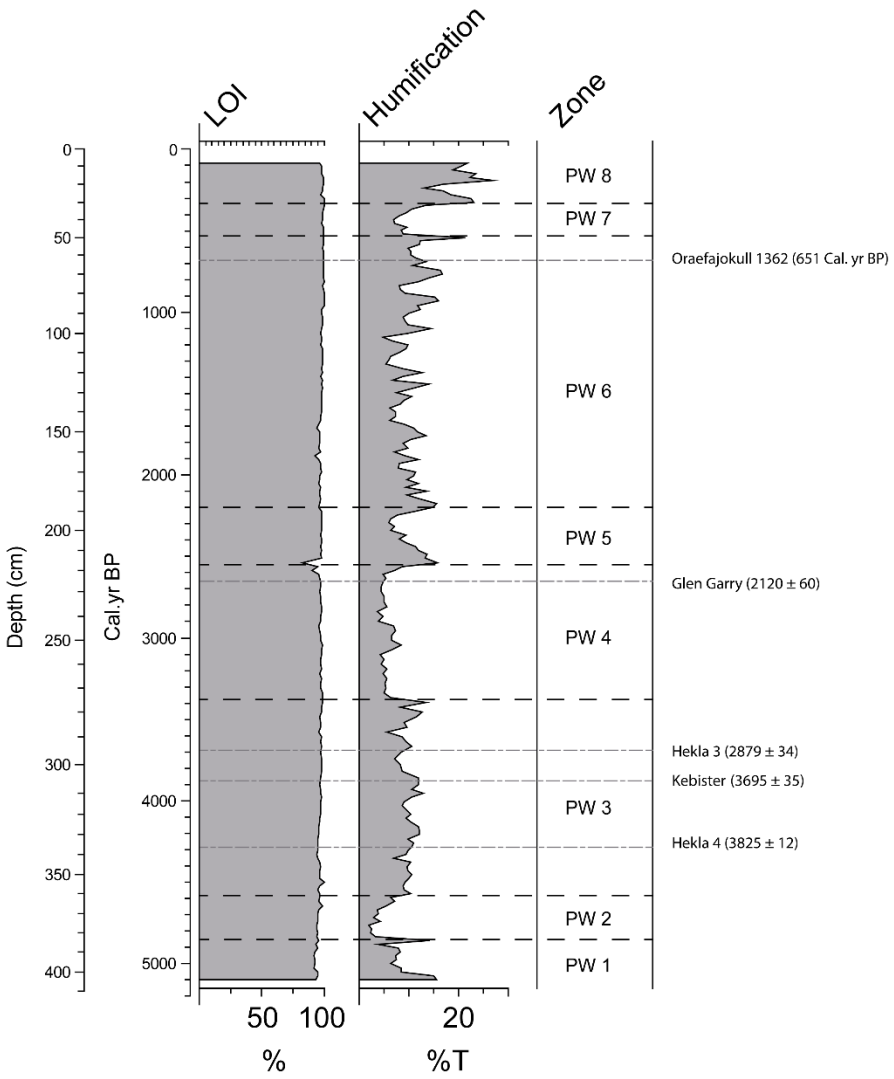

Figure 4.2.3 – Pettawater LOI_{550} and peat Humification (% Transmission) profile

PW1 – 5130 - 4850 Cal. yr BP: LOI values are measured at 93 % at the base of the core however they are following a gradually increasing trend. Humification values decline from 15.6 %T at *c.* 5100 Cal. yr BP to 6.5 %T at *c.* 5000 Cal. yr BP then rise sharply to a peak of 14.2 %T at *c.* 4860 Cal. yr BP.

PW 2 – 4850 – 4580 Cal. yr BP: LOI values are following a gradually increasing trend. Humification values decline dramatically to 2 %T at *c.* 4760 Cal. yr BP and remain low.

PW 3 – 4580 – 3380 Cal. yr BP: LOI values follow a gradually increasing trend then remain stable around 98 %. Humification values increase and fluctuate between 5.6 %T and 13.5 %T.

PW 4 – 3380 – 2550 Cal. yr BP: LOI values are stable around 98 %. Humification values decrease and remain steady around 5 %T with the exception of a small peak of 8.6 %T at *c.* 3040 Cal. yr BP.

PW 5 – 2550 – 2200 Cal. yr BP: LOI values are stable around 98 % with the exception of a sharp decline to 83 % at *c.* 2540 Cal. yr BP. Humification values increase rapidly to a peak of 15.8 %T at *c.* 2540 Cal. yr BP then decline to 6.1 %T at *c.* 2290 Cal. yr BP.

PW 6 – 2200 – 530 Cal. yr BP: LOI values are stable between 97 % and 99 %. Humification values rise to a peak of 15.6 %T at *c.* 2170 Cal. yr BP then are continually fluctuating between 5 %T and 17 %T before values increase rapidly to a peak of 21.4 %T at 540 Cal. yr BP.

PW 7 – 530 – 330 Cal. yr BP: LOI values are stable around 99 %. Humification values decline to 7 %T at *c.* 430 cm.

PW 8 – 330 – 0 Cal. yr BP: LOI values are stable around 97 %. Humification values rise quickly to 23.1 %T at *c.* 330 Cal. yr BP then decrease to 13.2 %T at *c.* 240 Cal. yr BP. Values then rise to 26.9 %T at *c.* 190 Cal. yr BP before declining to 21.7 %T at *c.* 80 Cal. yr BP.

4.2.4 – Kedills Mires

The percentage LOI_{550} and % transmission results, an indication of the degree of peat humification for the Kedills Mires core, are divided into 5 zones based on marked changes in the humification record (Figure 4.2.4). The surface peat lies within the acrotelm above the water table. This is subject to aerobic activity and therefore does not provide a mire surface wetness signal. The longer term MSW signal is only provided by the humified peat locked in the catotelm beneath the water table. Therefore, the humification record ends at 10 cm depth. Both records are analysed to the base of the peat at 426 cm depth. The Hekla 4, Kebister, Glen Garry and Hekla 1158 tephra layers are indicated by pale grey dashed lines.

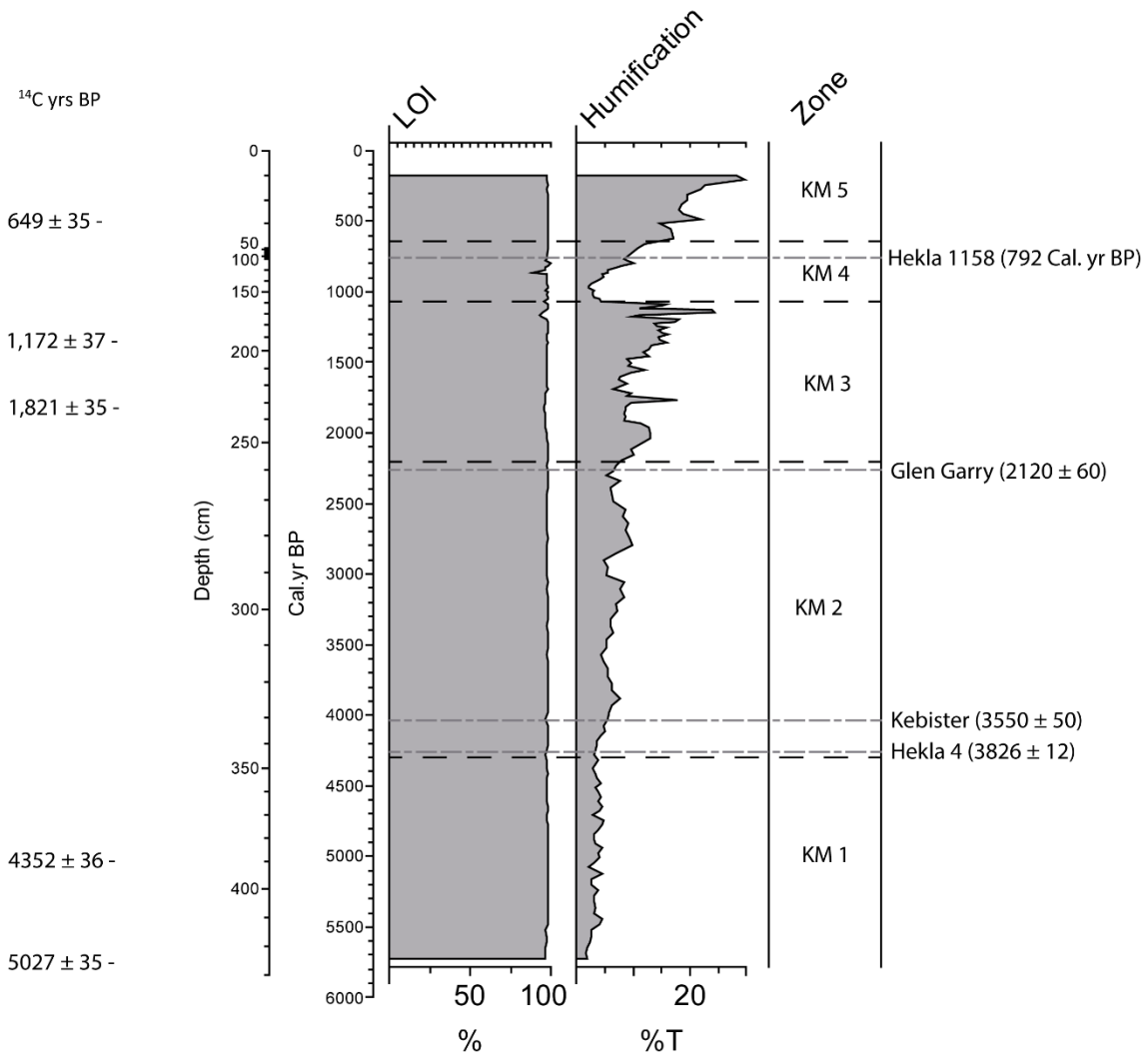

Figure 4.2.4 – Kedills Mires LOI_{550} and peat Humification (% Transmission) profile

KM 1 – 5730 - 4300 Cal. yr BP: LOI values are stable around 98 %. Humification values are low at the base of the core measuring below 5 %T.

KM 2 – 4300 - 2200 Cal. yr BP: LOI values are stable around 98 %. Humification values steadily increase to 7.6 %T at *c.* 3880 Cal. yr BP before following a declining trend to 4.2 %T at *c.* 3570 Cal. yr BP. Values then rise to around 8.5 %T at *c.* 3060 Cal. yr BP before declining

to around 5 %T at *c.* 3010 Cal. yr BP. Values then rise again to 9.9 %T at *c.* 2800 Cal. yr BP before declining to 5.3 %T at *c.* 2310 Cal. yr BP.

KM 3 – 2200-1090 Cal. yr BP: LOI values are stable around 98 % with the exception of a small decline to 95 % at *c.* 1840 Cal. yr BP and 93 % at *c.* 1160 Cal. yr BP. Humification values increase to 13 %T at *c.* 2040 Cal. yr BP before declining to around 8.5 %T then rising to a peak of 17.9 %T at *c.* 1770 Cal. yr BP. Values are then on a declining trend to 6.4 %T at *c.* 1700 Cal. yr BP before rapidly increasing to a peak of around 24 %T at *c.* 1150 Cal. yr BP.

KM 4 – 1090- 640 Cal. yr BP: LOI values remain around 98 % with the exception of declining to 89 % at *c.* 860 Cal. yr BP and increasing to 99.6 % at *c.* 800 Cal. yr BP. Humification values decline to a low of 2.1 %T at *c.* 970 Cal. yr BP.

KM 5 – 640-0 Cal. yr BP: LOI values are stable around 98 %. Humification values are on an increasing trend to 29.6 %T at *c.* 210 Cal. yr BP.

4.3: Micro X-Ray Fluorescence (Itrax) sediment geochemistry

The following sub-chapter presents the sediment chemistry analysed using micro X-ray fluorescence (μXRF) on the Itrax core scanner at Aberystwyth University. High-resolution XRF geochemical analysis of peat is a relatively new but valuable tool in palaeoenvironmental research. It has been previously used to deduce changing catchment dynamics such as glacier advance and retreat, variations in run-off and soil erosion, weathering rates and processes and grain-size fluctuations through the analysis of lacustrine sediments (Davies *et al*., 2015). The following results describe the downcore trends for bromine (Br), potassium (K), calcium (Ca), titanium (Ti), manganese (Mn), iron (Fe) and zirconium (Zr). Aluminium (Al), silica (Si), phosphorous (P), sulphur (S), chlorine (Cl), vanadium (V), chromium (Cr), nickel (Ni), copper (Cu), zinc (Zn), rubidium (Rb), yttrium (Y), barium (Ba), cerium (Ce), tungsten (W), argon (Ar), tatalum (Ta), strontium (Sr) and lead (Pb) were also analysed on the Itrax core scanner but these elements show no obvious environmental indicators and so are not used in this project. To counteract the uncertainty produced by the organic and water content of the peat, results are expressed as the ratio of the element/incoherent + coherent values (Davies et al., 2015).

4.3.1 – Shebster

The Shebster μXRF results are shown in Figure 4.3.1.

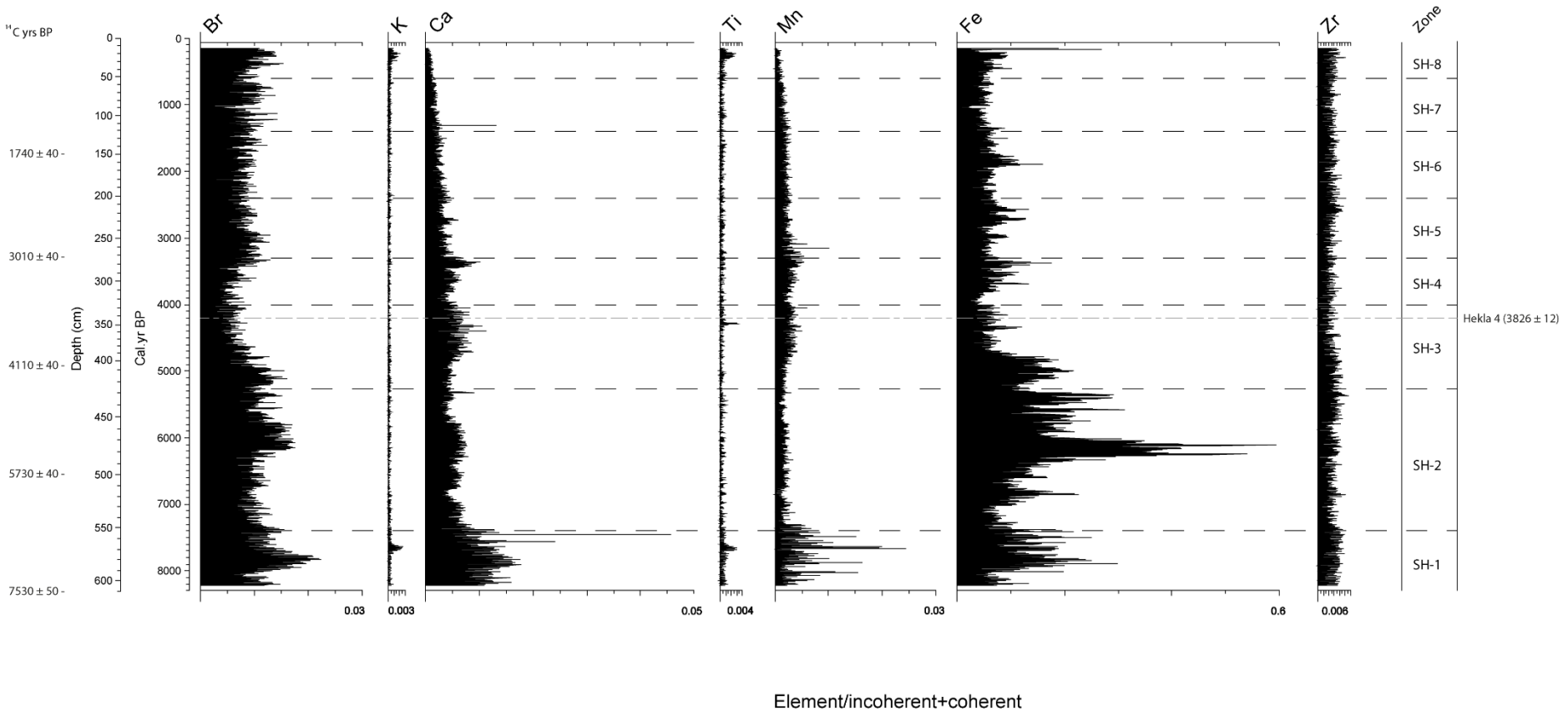

Figure 4.3.1 – The Shebster µXRF stratigraphies. The zones refer to those determined from the Humification values in the previous section.

Zirconium is not present in sufficient levels therefore will not be described in this section.

SH-1 – 8190 – 7400 Cal. yr BP: At the base of the core, the bromine record has a relatively high value of 0.0146. However, this value declines and is very low at *c.* 8090 Cal. yr BP, measuring 0.0105. Values then increase dramatically to a peak of 0.0225 at *c.* 7830 Cal. yr BP before decreasing to 0.0128 at *c.* 7600 Cal. yr BP. Potassium levels increase to a peak of 0.0026 at *c.* 7650 Cal. yr BP. Calcium levels increase steadily to 0.0178 at *c.* 7910 Cal. yr BP then decrease to 0.0131 at *c.* 7730 Cal. yr BP before rising to a small peak of 0.0241 at *c.* 7560 Cal. yr BP. Values then increase rapidly to a peak of around 0.0457 at *c.* 7450 Cal. yr BP. Titanium values increase to a peak of 0.0031 at 7650 Cal. yr BP. Manganese values are high and measure four peaks: of 0.0155 at *c.* 8020 Cal. yr BP, 0.0162 at *c.* 7870 Cal. yr BP, 0.0244 at *c.* 7660 Cal. yr BP and 0.0150 at *c.* 7480 Cal. yr BP. Iron values are high over this zone with peaks measuring 0.2981 at *c.* 7890 Cal. yr BP and 0.2504 at *c.* 7510 Cal. yr BP.

SH-2 – 7400 - 5270 Cal. yr BP: Bromine values rise to a peak of 0.0168 at *c.* 7400 Cal. yr BP before following a decreasing trend to 0.01 around *c.* 6760 Cal. yr BP. Values then remain relatively stable between 0.0118 and 0.0129 before increasing to around 0.0175 at *c.* 6150 Cal. yr BP and remain high. Bromine values then decline to a low point of 0.0107 at *c.* 5500 Cal. yr BP. Potassium, titanium and manganese values are low. Calcium levels decline to 0.0058 at *c.* 7140 Cal. yr BP then increase to 0.0074 at *c.* 7090 Cal. yr BP before declining to 0.0042 at *c.* 6790 Cal. yr BP. Values then remain steady between 0.0057 and 0.0074 before declining to 0.0037 at *c.* 5650 Cal. yr BP and remain low. Iron values decline to 0.0685 at *c.* 7140 Cal. yr BP before increasing to 0.2264 at *c.* 6850 Cal. yr BP. Values are then on a declining trend to 0.1077 at *c.* 6790 Cal. yr BP before rapidly increasing to a large double

peak of 0.5399 and 0.5954 at *c.* 6250 Cal. yr BP and *c.* 6110 Cal. yr BP. Iron values then decline and fluctuate between 0.1810 and 0.2459 before rising to a second double peak of 0.3115 and 0.2792 at *c.* 5580 Cal. yr BP and *c.* 5360 Cal. yr BP. Values then decline to 0.1484 at *c.* 5320 Cal. yr BP.

SH–3 – 5270 – 4000 Cal. yr BP: Bromine values increase to a peak of 0.0161 at *c.* 5110 Cal. yr BP then follow a declining trend to 0.0067 at *c.* 4460 Cal. yr BP. Potassium levels remain low. Calcium levels rise and fluctuate between 0.0067 and 0.0091 with a slight peak of 0.0112 at *c.* 4400 Cal. yr BP before declining and fluctuating between 0.0049 and 0.0067. Titanium values increase to a major peak of 0.0031 at *c.* 4280 Cal. yr BP. Manganese levels are on an increasing trend. Iron values increase to 0.2174 at *c.* 5000 Cal. yr BP then decline and fluctuate between 0.0591 and 0.0849 with the exception of a small peak of 0.1108 at *c.* 4360 Cal. yr BP.

SH-4 – 4000 – 3300 Cal. yr BP: Bromine values remain low and stable before increasing to 0.013 at *c.* 3330 Cal. yr BP then fluctuate between 0.0089 and 0.0123. Potassium, titanium and manganese levels remain low. Calcium levels are on an increasing trend. Iron values are on a declining trend to 0.0350 at *c.* 3970 Cal. yr BP before increasing to two small peaks of 0.1338 at *c.* 3690 Cal. yr BP and 0.1767 at *c.* 3380 Cal. yr BP.

SH-5 – 3300 - 2400 Cal. yr BP: Bromine values remain relatively stable throughout this period, with small fluctuations occurring between 0.0089 and 0.0123. Potassium and titanium values are low. Calcium values are following a declining trend. Manganese values rise to a peak of 0.01 then follow a declining trend. Iron values decline and remain around

0.0678 with the exception of a small peak of 0.0952 at *c.* 2990 Cal. yr BP and a double peak of 0.1282 and 0.1337 at *c.* 2700 Cal. yr BP and *c.* 2570 Cal. yr BP.

SH-6 – 2400 - 1400 Cal. yr BP: Bromine values remain relatively stable throughout this period, with small fluctuations occurring between 0.0089 and 0.0123. Calcium, potassium, titanium and manganese are low. Iron values increase to a small peak measuring 0.1600 at *c.* 1900 Cal. yr BP.

SH-7 – 1400 - 600 Cal. yr BP: Two small peaks in bromine activity are seen at *c.* 122 Cal. yr BP and *c.* 1130 Cal. yr BP measuring 0.0143. Values then decline dramatically to 0.0093 at *c.* 970 Cal. yr BP before rising to a double peak of 0.0138 at *c.* 860 Cal. yr BP and 0.0135 at *c.* 750 Cal. yr BP then declining to 0.0092 at *c.* 600 Cal. yr BP. Potassium, manganese and titanium remain low. Calcium levels remain low however a peak of 0.0132 is measured at *c.* 1300 Cal. yr BP. Iron values decline and fluctuate between 0.0473 and 0.0685.

SH-8 – 600 - 0 Cal. yr BP: Bromine values rise suddenly to a peak of 0.0155 at *c.* 380 Cal. yr BP then decline to 0.0126 at *c.* 329 Cal. yr BP. Values then increase to around 0.014 between *c.* 260 and 210 Cal. yr BP before decreasing to 0.0094 at *c.* 150 Cal. yr BP. Potassium values increase suddenly to a large peak of 0.0024 at *c.* 220 Cal. yr BP then decline to 0.0005 at *c.* 160 Cal. yr BP. Calcium levels are very low during this period and follow a decreasing trend to 0.0004 at *c.* 150 Cal. yr BP. Titanium levels decrease to 0.0006 at *c.* 440 Cal. yr BP before rising to a peak of 0.0029 at *c.* 230 Cal. yr BP. Manganese levels are very low and are on a decreasing trend to 0.0002 at *c.* 160 Cal. yr BP. Iron levels increase rapidly to a peak of around 0.2693 at *c.* 170 Cal. yr BP.

4.3.2 - Heldale

The Heldale µXRF results are shown in Figure 4.3.2.

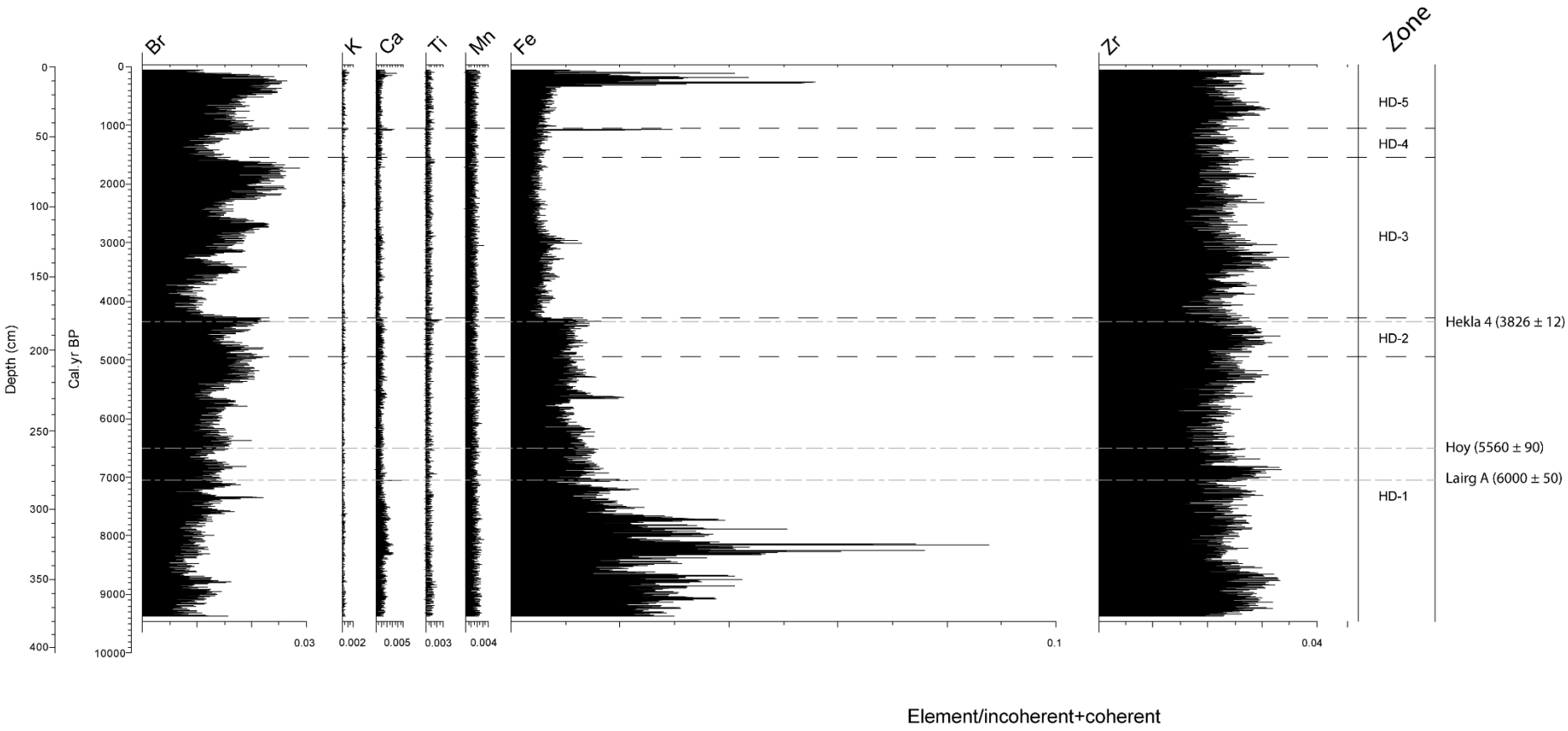

Figure 4.3.2 – The Heldale µXRF stratigraphies. The zones refer to those determined from the Humification values in the previous section.

Potassium, calcium, titanium and manganese are not present in sufficient levels therefore will not be described in this section.

HD 1 – 9365 – 4950 Cal. yr BP: Bromine values decline from 0.01600 at the base of the core to 0.00792 at *c.* 9250 Cal. yr BP. Values then increase to a double peak of 0.01448 at *c.* 8950 Cal. yr BP and 0.01619 at *c.* 8770 Cal. yr BP then decline to 0.00846 at *c.* 8680 Cal. yr BP. Values are then on an increasing trend to 0.02209 at *c.* 7340 Cal. yr BP then fluctuate between 0.01013 and 0.01995. Values then decline to 0.01445 at *c.* 5620 Cal. yr BP before increasing to 0.02059 at *c.* 5330 Cal. yr BP. Iron values fluctuate between 0.04248 and 0.02888 then decline to 0.01982 at *c.* 8620 Cal. yr BP before increasing rapidly to a double peak of 0.07585 at *c.* 8250 Cal. yr BP and 0.08782 at *c.* 8160 Cal. yr BP. Values then decline and fluctuate between 0.00831 and 0.01557 with the exception of peaks measuring 0.05063 at *c.* 7880 Cal. yr BP, 0.03924 at *c.* 7730 Cal. yr BP and 0.02072 at *c.* 5630 Cal. yr BP. Zirconium values are high at the bottom of the core and fluctuate between 0.02824 and 0.03329. Values then decline to 0.02223 at *c.* 8420 Cal. yr BP and remain fluctuating between 0.02189 and 0.02823 with the exception of 3 peaks measuring 0.03027 at *c.* 7320 Cal. yr BP, 0.03361 at *c.* 6880 Cal. yr BP, 0.03120 at *c.* 5260 Cal. yr BP.

HD 2 – 4950 – 4280 Cal. yr BP: Bromine values remain high then decline to 0.01472 at *c.* 4690 Cal. yr BP before increasing again to 0.02341 at *c.* 4350 Cal. yr BP. Iron values fluctuate between 0.01667 and 0.00938. Zirconium values remain fluctuating between 0.02189 and 0.02823 then increase to 0.03332 at *c.* 4600 Cal. yr BP.

HD 3 – 4280 – 1540 Cal. yr BP: Bromine levels decline and are low measuring between 0.00891 and 0.01180 before increasing to 0.01901 at *c.* 3410 Cal. yr BP then declining to 0.00932 at *c.* 3290 Cal. yr BP. Values then increase steadily to 0.02313 at *c.* 2740 Cal. yr BP before declining and are low ranging between 0.01443 and 0.01657. Values then increase to 0.02542 at *c.* 2190 Cal. yr BP and remain high before rising to a peak of 0.02891 at *c.* 1730 Cal. yr BP. Iron values decline and remain low with the exception of a small peak of 0.01305 at *c.* 3010 Cal. yr BP. Zirconium values decline and fluctuate between 0.02294 and 0.02717 with the exception of peaks measuring 0.03048 at *c.* 2310 Cal. yr BP, 0.02874 at *c.* 1830 Cal. yr BP and 0.02836 at *c.* 1590 Cal. yr BP.

HD 4 – 1540 – 1050 Cal. yr BP: Bromine values decline to 0.01129 at *c.* 1410 Cal. yr BP then increase to 0.02141 at *c.* 1070 Cal. yr BP. Iron values remain low with the exception of a peak measuring 0.02958 at *c.* 1080 Cal. yr BP. Zirconium values are fluctuating between 0.02572 and 0.02148.

HD 5 – 1050 – 0 Cal. yr BP: Bromine values fluctuate between 0.01679 and 0.02032 before rising to a peak of 0.02653 at *c.* 250 Cal. yr BP. Iron values remain low before increasing to a trio of peaks measuring 0.05581 at *c.* 270 Cal. yr BP, 0.04365 at *c.* 190 Cal. yr BP and 0.04108 at *c.* 120 Cal. yr BP. Zirconium values rise to 0.03134 at *c.* 720 Cal. yr BP then decline to 0.02290 at *c.* 520 Cal. yr BP and fluctuate before rising to a small peak of 0.03039 at *c.* 120 Cal. yr BP.

4.3.3 – Pettawater

The Pettawater µXRF results are shown in Figure 4.3.3.

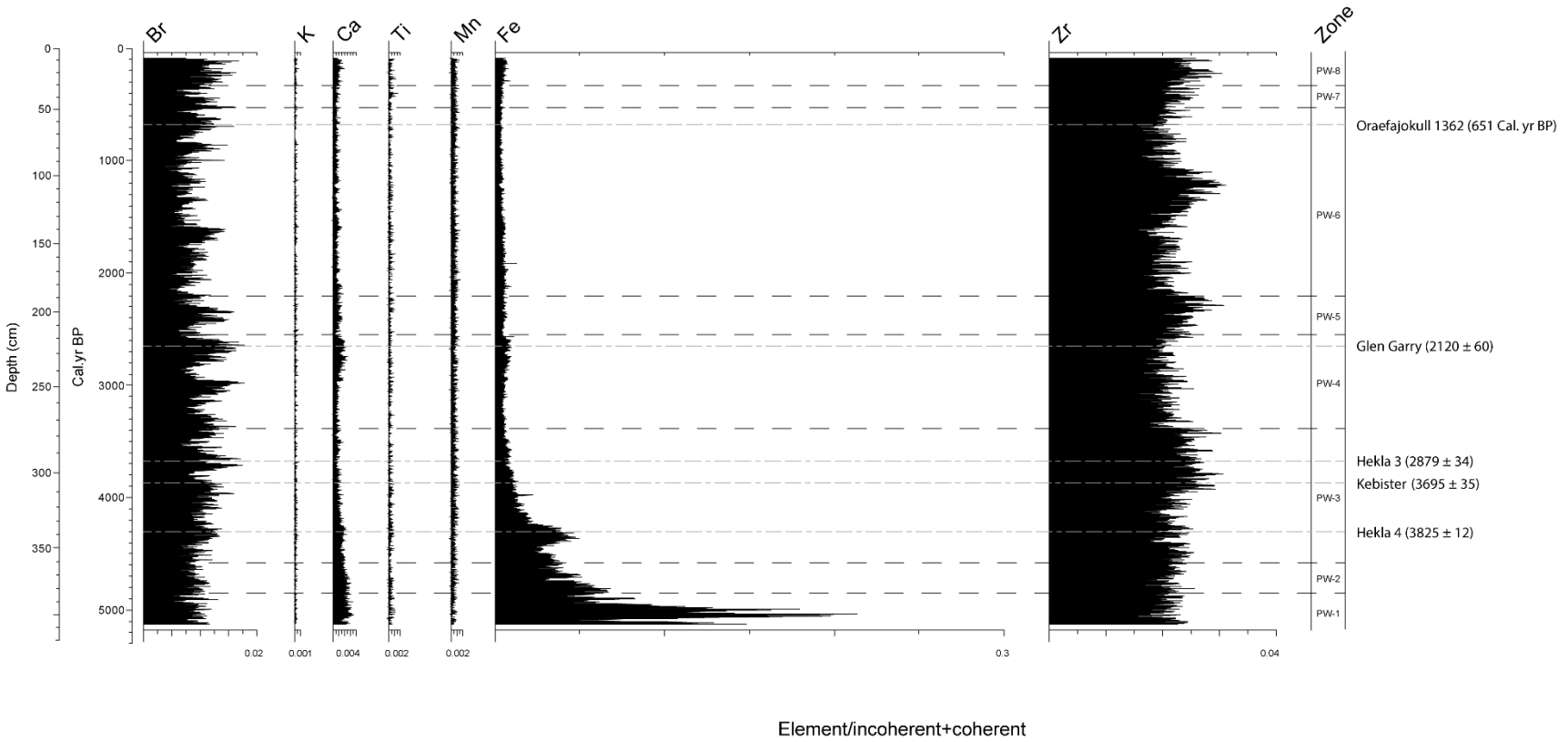

Figure 4.3.3 – The Pettawater µXRF stratigraphies. The zones refer to those determined from the Humification values in the previous section.

Potassium, calcium, titanium and manganese are not present in sufficient levels therefore will not be described in this section.

PW1 – 5134-4850 Cal. yr BP: Bromine values are relatively stable ranging between 0.00942 and 0.01314. Iron values decline from 0.14817 at *c.* 5130 Cal. yr BP to 0.06315 at *c.* 5080 Cal. yr BP then increase rapidly to a peak of 0.21385 at *c.* 5040 Cal. yr BP. Zirconium values fluctuate between 0.01958 and 0.02444.

PW 2 – 4850 – 4580 Cal. yr BP: Bromine values decline to 0.00892 at *c.* 4600 Cal. yr BP. Iron values are on a declining trend. Zirconium values fluctuate between 0.02045 and 0.02573.

PW 3 – 4580 – 3380 Cal. yr BP: Bromine values increase to a peak of 0.01600 at *c.* 3960 Cal. yr BP then decline to 0.01165 at *c.* 3800 Cal. yr BP before rising to a double peak measuring 0.01753 at *c.* 3720 Cal. yr BP and 0.01719 at *c.* 3650 Cal. yr BP. Values then decline to 0.00830 at *c.* 3580 Cal. yr BP. Iron values follow a decreasing trend with the exception of a small increase to 0.04997 at *c.* 4360 Cal. yr BP. Zirconium values fluctuate between 0.01842 and 0.02533 before rising to 0.02940 at *c.* 3920 Cal. yr BP and remain high fluctuating between 0.03063 and 0.02329.

PW 4 – 3380 – 2550 Cal. yr BP: Bromine values increase to 0.01627 at *c.* 3360 Cal. yr BP then decline to 0.00879 at *c.* 3250 Cal. yr BP before increasing to a peak of 0.01780 at *c.* 2980 Cal. yr BP. Values decline again to 0.00833 at *c.* 2910 Cal. yr BP before increasing to 0.01788 at *c.* 2640 Cal. yr BP. Iron values are very low for the rest of the core and will

therefore not be described any further. Zirconium values decrease and fluctuate between 0.01944 and 0.02560.

PW 5 – 2550 – 2200 Cal. yr BP: Bromine values decline to 0.00933 at *c.* 2530 Cal. yr BP before increasing to a double peak of 0.01478 at *c.* 2420 Cal. yr BP and 0.01596 at *c.* 2350 Cal. yr BP. Zirconium values rise to a peak of 0.03090 at *c.* 2290 Cal. yr BP.

PW 6 – 2200 – 530 Cal. yr BP: Bromine levels are on a steep decreasing trend to 0.00583 at *c.* 2160 Cal. yr BP then are on an increasing trend to 0.01437 at *c.* 1630 Cal. yr BP before declining and fluctuating between 0.00680 and 0.01132. Values then rise to two peaks measuring 0.01440 at *c.* 1000 Cal. yr BP and 0.01482 at *c.* 860 Cal. yr BP before following a sharp decreasing trend to a low of 0.00564 at *c.* 830 Cal. yr BP then increase to a peak of 0.01608 at *c.* 690 Cal. yr BP. Values then decline to 0.00825 at *c.* 570 Cal. yr BP. Zirconium values decline and fluctuate between 0.02202 and 0.02516 then decline further to 0.01871 at *c.* 620 Cal. yr BP before increasing to a peak of 0.03127 at *c.* 1220 Cal. yr BP. Values then decline to 0.02223 at *c.* 1040 Cal. yr BP and fluctuate between 0.02054 and 0.02517.

PW 7 – 530 – 330 Cal. yr BP: Bromine levels rise to a peak of 0.01637 at *c.* 520 Cal. yr BP before declining to a low of 0.00733 at *c.* 380 Cal. yr BP. Zirconium values are on an increasing trend.

PW 8 – 330 – 0 Cal. yr BP: Bromine values rise to 0.01624 at *c.* 220 Cal. yr BP before falling to 0.01158 at *c.* 180 Cal. yr BP then rise again to 0.01685 at *c.* 110 Cal. yr BP. Zirconium

values increase to 0.03051 at *c.* 230 Cal. yr BP, decline to 0.02310 at *c.* 170 Cal. yr BP then increase again to 0.02876 at *c.* 110 Cal. yr BP.

4.3.4 – Kedills Mires

The Kedills Mires µXRF results are shown in Figure 4.3.4.

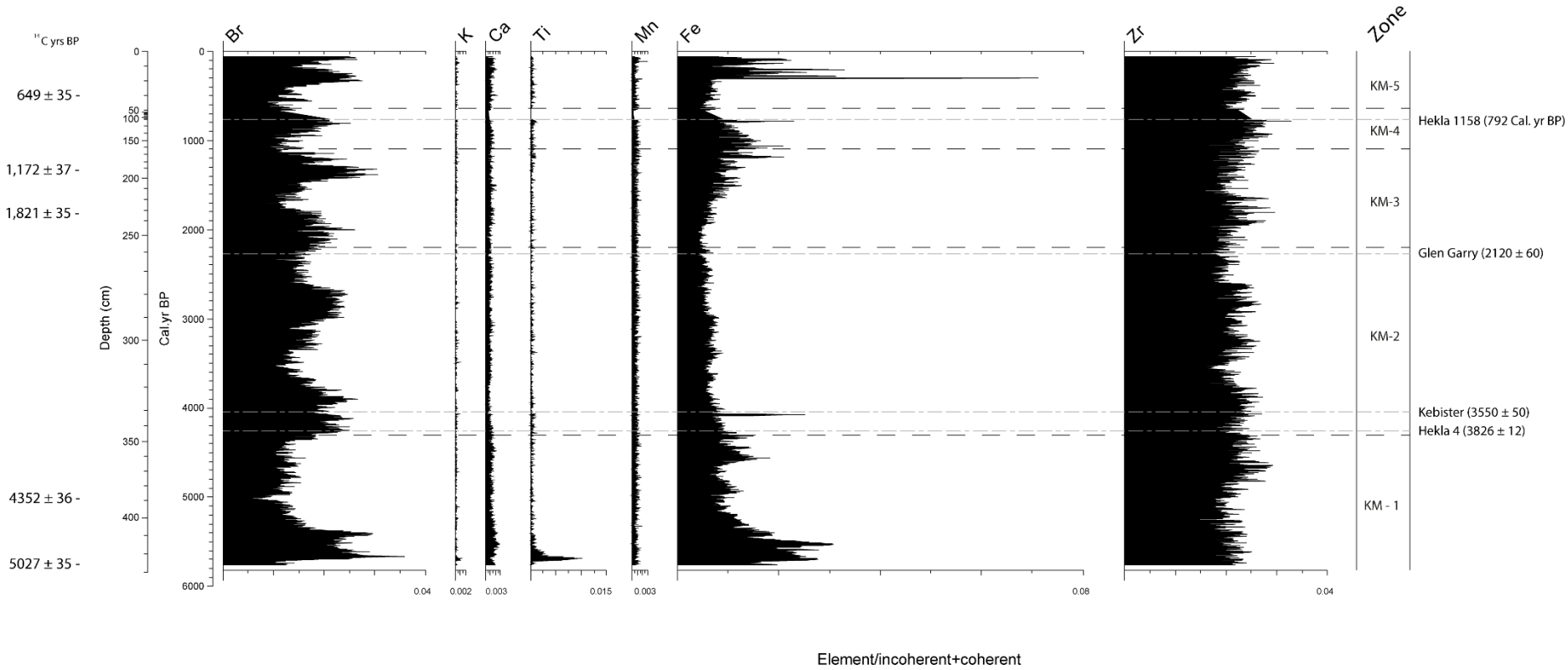

Figure 4.3.4 – The Kedills Mires µXRF profiles. The zones refer to those determined from the Humification values in the previous section.

Potassium, calcium and manganese are not present in sufficient levels therefore will not be described in this section.

KM 1 – 5760 - 4300 Cal. yr BP: Bromine values increase from 0.0145 at *c.* 5730 Cal. yr BP to a peak of 0.0360 at *c.* 5660 Cal. yr BP then decline to 0.0231 at *c.* 5540 Cal. yr BP cm before rising again to a peak of 0.0292 at *c.* 5400 Cal. yr BP. Values then decline rapidly and remain low ranging between 0.0122 and 0.0145 with the exception of a small peak of 0.0163 at *c.* 4560 Cal. yr BP. Titanium values rapidly increase to a large peak of 0.0100 at *c.* 5690 Cal. yr BP then remain very low and therefore will not be described in any more detail. Iron values increase steadily to a peak of 0.0306 at *c.* 5520 Cal. yr BP then follow a decreasing trend to 0.0079 at *c.* 4700 Cal. yr BP. Values then increase and fluctuate between 0.0100 and 0.0182. Zirconium values fluctuate between 0.0211 and 0.0251 before declining to 0.0190 at *c.* 5040 Cal. yr BP. Values then increase and fluctuate between 0.0233 and 0.0292.

KM 2 - 4300 - 2200 Cal. yr BP: Bromine values increase to 0.0250 at *c.* 4250 Cal. yr BP and fluctuate between around 0.0193 and 0.0267. Values then decline to 0.0141 at *c.* 3650 Cal. yr BP before increasing to around 0.0187 at *c.* 3340 Cal. yr BP and remain steady. Values then increase again to 0.0239 at *c.* 2980 Cal. yr BP where values remain between 0.0235 and 0.0246. Between *c.* 2610 Cal. yr BP and 2310 Cal. yr BP, values decline and remain low, measuring between 0.0161 and 0.0175. Iron values following a decreasing trend to 0.0047 at *c.* 2310 Cal. yr BP with the exception of a peak of 0.0251 at *c.* 4080 Cal. yr BP. Zirconium values fluctuate between 0.0233 and 0.0292 before declining to 0.0200 at *c.* 3570 Cal. yr BP. Values increase again and fluctuate between 0.0217 and 0.0268 then sharply decline to 0.0197 at *c.* 2560 Cal. yr BP and values remain low.

KM 3 – 2200 - 1090 Cal. yr BP: Bromine values are high between *c.* 2190 Cal. yr BP and *c.* 1810 Cal. yr BP measuring between around 0.0194 and 0.0226 with a small peak of 0.0262 at *c.* 2000 Cal. yr BP. Values then decline to 0.0110 at *c.* 1770 Cal. yr BP before following an increasing trend to a double peak of 0.0306 at *c.* 1390 Cal. yr BP and *c.* 1330 Cal. yr BP. Values then follow a declining trend to 0.0111 at *c.* 1160 Cal. yr BP. Iron values increase to 0.0211 at *c.* 1190 Cal. yr BP then decline to 0.00107 at *c.* 1140 Cal. yr BP. Zirconium values rise steadily to a peak of 0.0297 at *c.* 1810 Cal. yr BP before declining to 0.0196 at *c.* 1530 Cal. yr BP. Values are then on an increasing trend.

KM 4 – 1090- 640 Cal. yr BP: Bromine values follow a slowly increasing trend to 0.0252 at *c.* 810 Cal. yr BP then decline to 0.0144 at *c.* 660 Cal. yr. Iron values increase to 0.0208 at *c.* 1060 Cal. yr BP then follow a declining trend to 0.0059 at *c.* 670 Cal. yr BP with the exception of a peak measuring 0.0229 at *c.* 790 Cal. yr BP. Zirconium values are on an increasing trend to 0.0330 at *c.* 790 Cal. yr BP then decline to 0.0210 at *c.* 650 Cal. yr BP.

KM 5 – 640 - 0 Cal. yr BP: Bromine levels remain low with the exception of a peak measuring 0.0175 at *c.* 560 Cal. yr BP. Values then rise to 0.0272 at *c.* 330 Cal. yr BP before declining to 0.0159 at *c.* 190 Cal. yr BP then increasing to 0.0265 at *c.* 90 Cal. yr BP. Iron values increase rapidly to a peak of 0.0713 at *c.* 300 Cal. yr BP before declining to 0.0122 at *c.* 190 Cal. yr BP. Values then increase to 0.0225 at *c.* 100 Cal. yr BP. Zirconium values follow an increasing trend to 0.0295 at *c.* 140 Cal. yr BP.

4.4: Dust

This section of the results focuses on the small minerogenic non-volcanic particles, found within each of the four sampled peat cores. These particles measure < 25 µm in diameter and have a generally rounded shape, morphologically distinct from tephra shards, and are referred to as dust. These dust particles are thought to have been transported by aeolian processes (Figure 4.1).

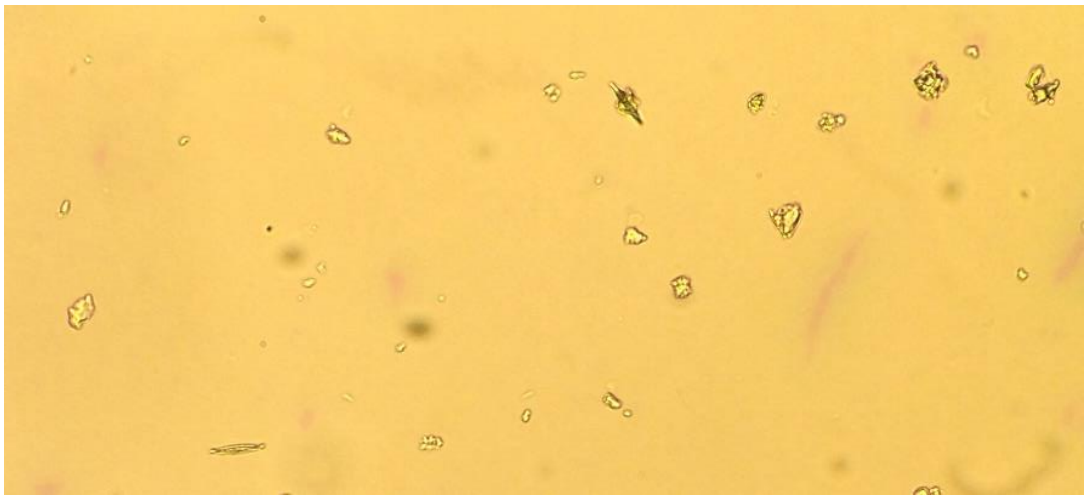

Figure 4.1 – Down-microscope photograph of typical minerogenic dust particles found within the peat cores

4.4.1 – Shebster

The downcore dust analyses for the Shebster core are shown in Figure 4.4.1 and are presented as percentage of abundance. To facilitate comparison with the other environmental proxies the dust profile is divided into 8 zones defined by the Shebster humification record (see Section 4.2.1). The Hekla 4 tephra layer is indicated by a pale grey dashed line.

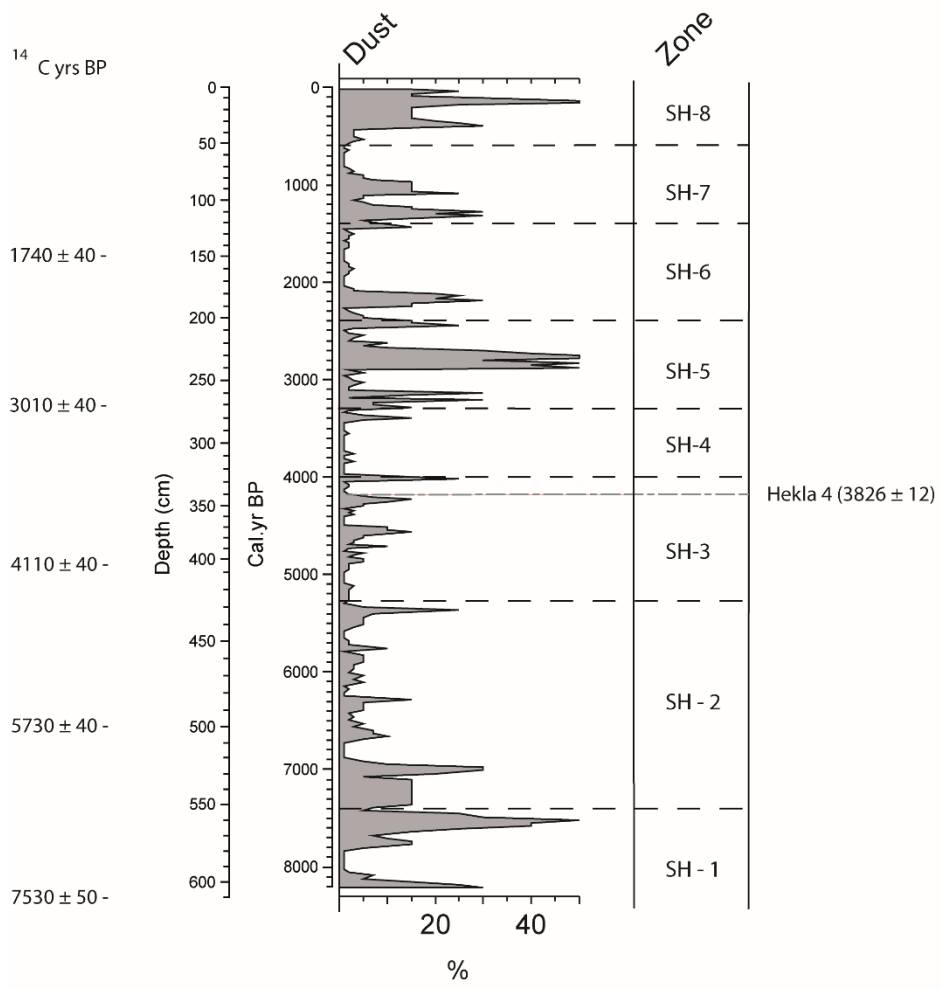

Figure 4.4.1 – Shebster dust profile

SH-1 – 8207 – 7400 Cal. yr BP: At the base of the core, Shebster dust levels have a relatively high value of 30%. This value declines and is very low at *c.* 8070 Cal. yr BP, measuring 1%, before increasing to 15% at *c.* 7830 Cal. yr BP. Values then suddenly increase to ~50% between *c.* 7680 and 7530 Cal. yr BP.

SH-2 - 7400-5270 Cal. yr BP: Dust values fall to 15% between *c.* 7360 and *c.* 7120 Cal. yr BP before rising to a peak of ~30% at *c.* 6990 Cal. yr BP. Values then decline rapidly at *c.* 6930 Cal. yr BP and remain very low for the remainder of this period with the exception of peaks

measuring 10% at *c.* 6680 Cal. yr BP, 15% at *c.* 6300 Cal. yr BP, 10% at *c.* 5770 Cal. yr BP and 25% at *c.* 5390 Cal. yr BP.

SH-3 – 5270-4000 Cal. yr BP: Dust values remain low with the exception of peaks measuring 15% at *c.* 4570 Cal. yr BP, 15% at *c.* 4240 Cal. yr BP and 25% at *c.* 4040 Cal. yr BP.

SH-4 – 4000-3300 Cal. yr BP: Shebster dust values are very low (<3%) throughout this period.

SH-5 – 3300 – 2400 Cal. yr BP: Dust levels begin to rise with two peaks of 30% at *c.* 3200 and *c.* 3130 Cal. yr BP. Values decline back to 5% before rising significantly to a major dust peak of 50% which is measured over a sustained period between *c.* 2880 and *c.* 2730 Cal. yr BP. A smaller dust peak of 25% is found at *c.* 2430 Cal. yr BP.

SH-6 – 2400-1400 Cal. yr BP: Dust levels rise to a peak of 30% at *c.* 2170 Cal. yr BP then decline and remain very low (<3%) for the rest of this period.

SH-7 – 1400 – 600 Cal. yr BP: Dust activity increases and two dust peaks between *c.* 1300 and *c.* 1250 Cal. yr BP and *c.* 1070 and *c.* 970 Cal. yr BP are measured recording an abundance of 25% and 30% respectively. Values then decline and remain low (<3%).

SH-8 – 600-0 Cal. yr BP: Dust values increase at *c.* 410 Cal. yr BP and remain consistently above 15% with a peak of 30% at *c.* 380 Cal. yr BP and another peak of 50% at *c.* 130 Cal. yr BP.

4.4.2 – Heldale

The downcore dust analyses for the Heldale core are shown in Figure 4.4.2 and are presented as a percentage of abundance. The results are divided into 5 zones defined by the Heldale humification record (see Section 4.2.2). The Lairg A, Hoy and Hekla 4 tephra layers are indicated by pale grey dashed lines.

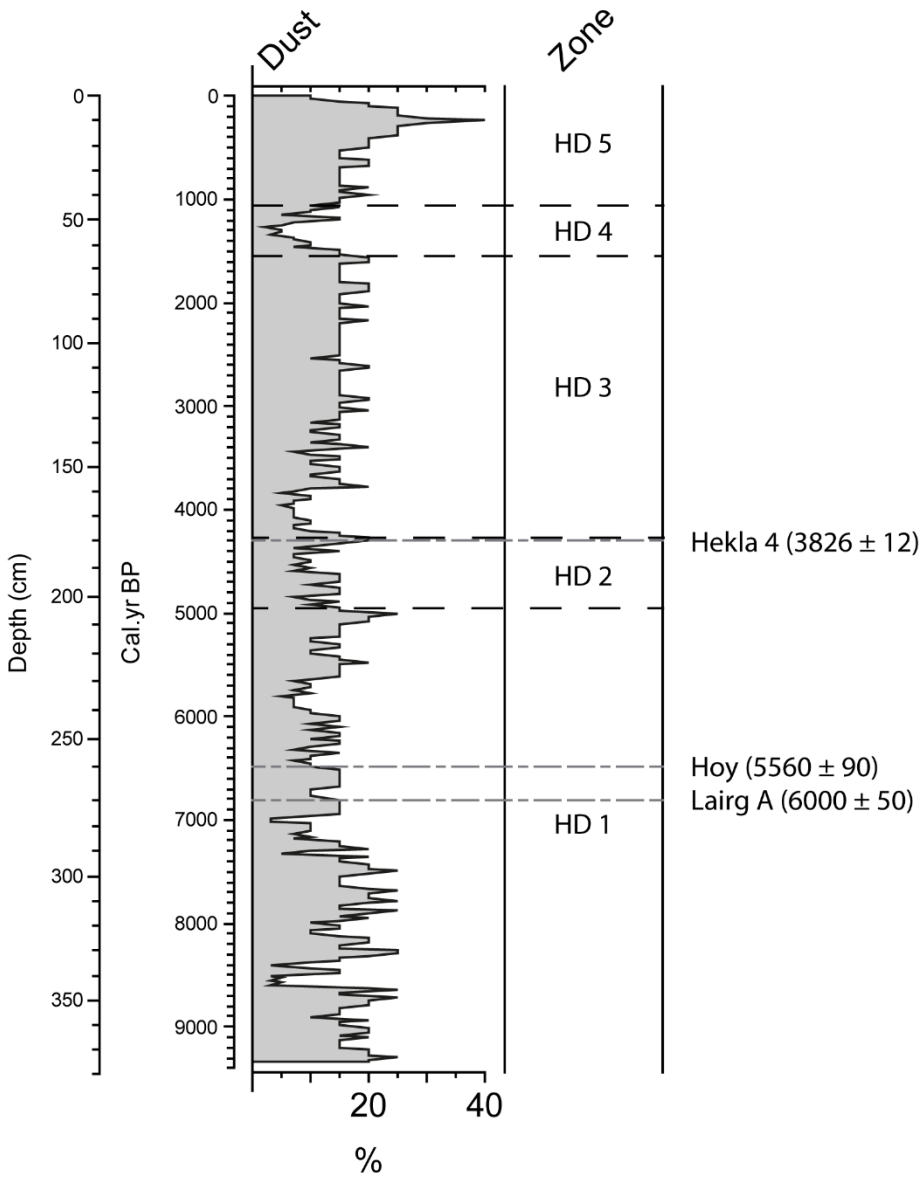

Figure 4.4.2 – Heldale dust profile

HD 1 – 9365 – 4950 Cal. yr BP: Between *c.* 9360 and *c.* 7200 Cal. yr BP, Heldale dust values fluctuate between 15 and 25% with the exception of a significant drop to 3% between *c.* 8600 and *c.* 8400 Cal. yr BP. Values then decline again to 3% at *c.* 7010 Cal. yr BP before rising and fluctuating between 5 and 25%.

HD 2 – 4950 – 4280 Cal. yr BP: Dust values continue to fluctuate between 5 and 25%.

HD 3 – 4280 – 1540 Cal. yr BP: At *c.* 4200 Cal. yr BP, dust values decline and remain low between 5 and 7%. Between *c.* 3800 Cal.yr BP and *c.* 1550 Cal. yr BP, values increase and fluctuate between 10 and 20%

HD 4 – 1540 – 1050 Cal. yr BP: Dust values decline to 2% at *c.* 1270 Cal. yr BP.

HD 5 – 1050 – 0 Cal. yr BP: Dust values increase to 20% at *c.* 960 Cal. yr BP and remain steady between 15 and 20% before rising to a peak of 40% at *c.* 240 Cal. yr BP. Values then decline to 10% at the top of the core.

4.4.3 – Pettawater

The downcore dust analyses for the Pettawater core are shown in Figure 4.4.3 and are presented as a percentage of abundance. The results are split into 8 zones in relation to changes in the Pettawater humification record (see Section 4.2.3). The Hekla 4, Kebister, Hekla 3, Glen Garry and Oraefajokull 1362 tephra layers are indicated by pale grey dashed lines.

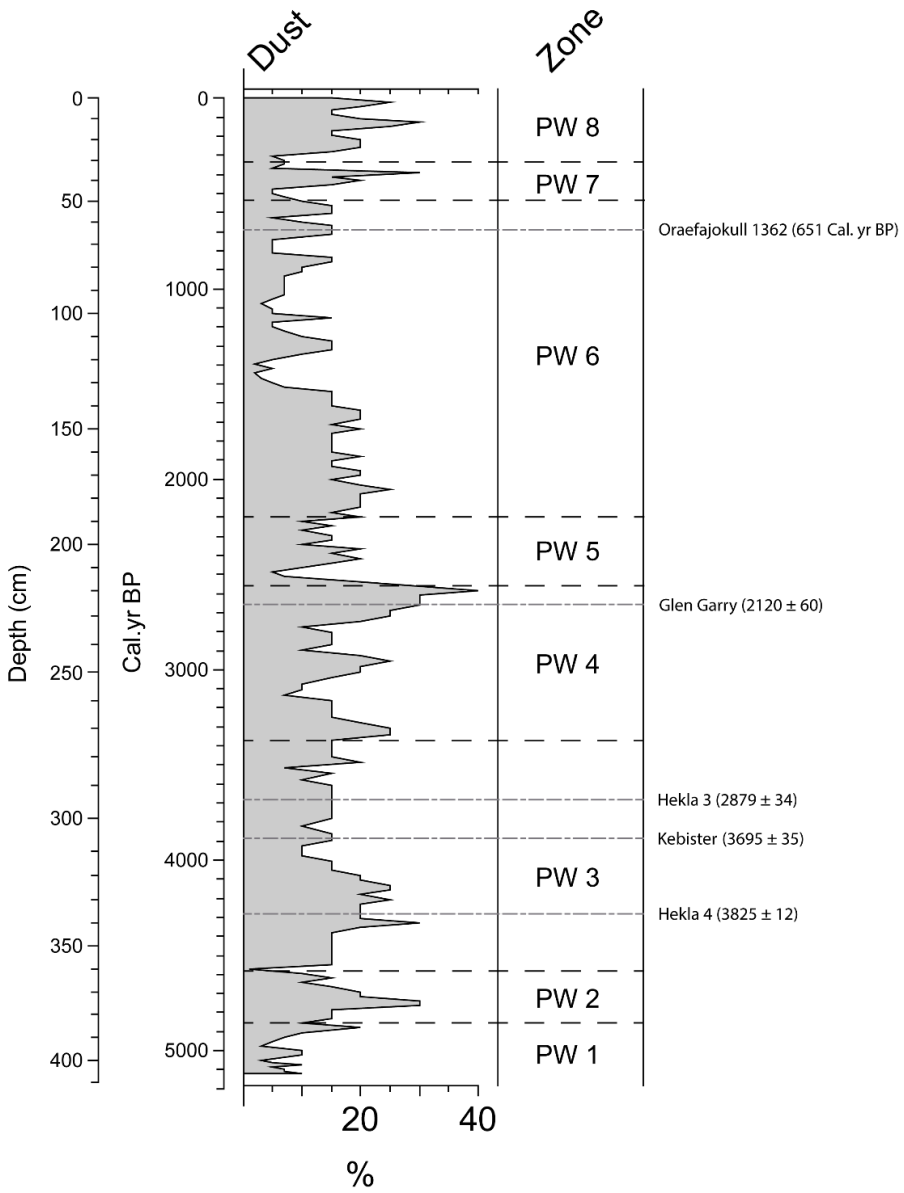

Figure 4.4.3 - Pettawater dust profile

PW 1 – 5134 - 4850 Cal. yr BP: Dust values fluctuate between 3 and 10%.

PW 2 – 4850 – 4580 Cal. yr BP: Dust values follow an increasing trend to a peak of 30% at *c.* 4760 Cal. yr BP

PW 3 – 4580 – 3380 Cal. yr BP: Values fall to 1% at *c.* 4570 Cal. yr BP then increase to 30% at *c.* 4330 Cal. yr BP and remain high, fluctuating between 20 and 25%. Values then decrease to 10% at *c.* 3980 Cal. yr BP and fluctuate between 10 and 15%.

PW 4 – 3380 – 2550 Cal. yr BP: Dust values rise to 25% at *c.* 3340 Cal. yr BP then decline to 7% at *c.* 3130 Cal. yr BP before rising to another peak of 25% at *c.* 2950 Cal. yr BP. Values then briefly decline to 15% at *c.* 2870 Cal. yr BP before rapidly increasing to a large peak of 40% at *c.* 2590 Cal. yr BP.

PW 5 – 2550 – 2200 Cal. yr BP: Dust values decline quickly to 5% at *c.* 2490 Cal. yr BP then fluctuate between 10 and 25%.

PW 6 – 2200 – 530 Cal. yr BP: Dust values decline to 2% at *c.* 1440 Cal. yr BP then fluctuate between 3 and 15%.

PW 7 – 530 – 330 Cal. yr BP: Dust values rise to a peak of 30% at *c.* 390 Cal. yr BP then decrease to 5% at *c.* 370 Cal. yr BP.

PW 8 – 330 – 0 Cal. yr BP: Dust values increase and remain high between 15 and 30%.

4.4.4 – Kedills Mires

The downcore dust analyses for the Kedills Mires core are shown in Figure 4.4.4 and are presented as a percentage of abundance. The results are divided into 5 zones defined by the Kedills Mires humification record (see Section 4.2.4). The Hekla 4, Kebister, Glen Garry and Hekla 1158 tephra layers are indicated by pale grey dashed lines.

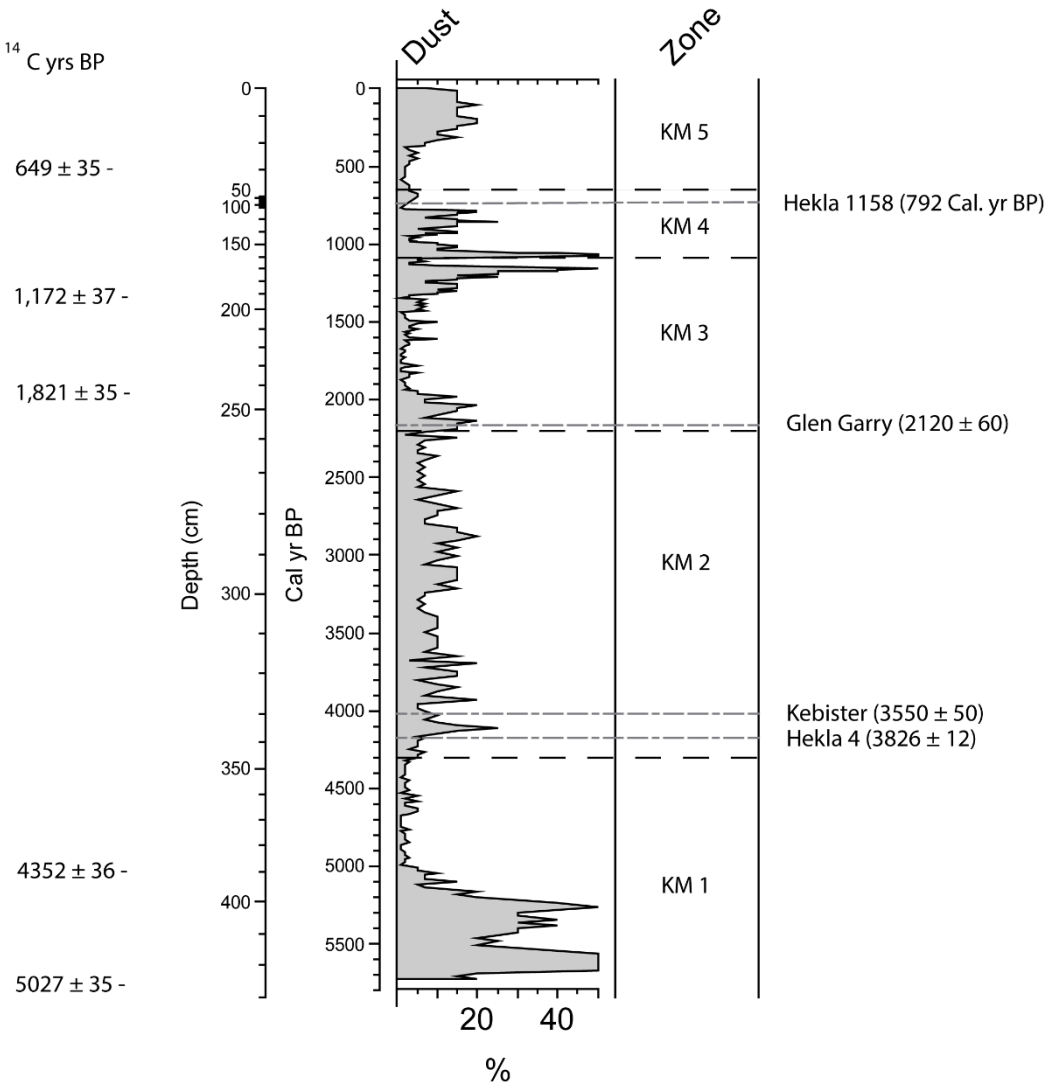

Figure 4.4.4 – Kedills Mires dust profile

KM 1 – 5730 - 4300 Cal. yr BP: Dust values increase from 20% at *c.* 5730 Cal. yr BP to 50% between *c.* 5670 and *c.* 5570 Cal. yr BP. There is then a small decline to 25% at *c.* 5480 Cal. yr BP before values rise to another peak of 50% at *c.* 5260 Cal. yr BP. Values then decline at *c.* 5200 Cal. yr BP and remain very low.

KM 2 – 4300 - 2200 Cal. yr BP: Dust values rise to 25% at *c.* 4110 Cal. yr BP and then remain high between 15 and 20%. Values then decline to around 10% at *c.* 3590 Cal. yr BP and remain low until *c.* 3210 Cal. yr BP where they rise to 15%. Levels then fluctuate between 7 and 20% before declining to 5% at *c.* 2570 Cal. yr BP and remain low.

KM 3 – 2200 - 1090 Cal. yr BP: Dust values increase to 20% at *c.* 2130 Cal. yr BP then decline at *c.* 1970 Cal. yr BP and remain low. Values then rapidly increase to a peak of 50% at *c.* 1140 Cal. yr BP.

KM 4 – 1090 - 640 Cal. yr BP: Dust levels increase rapidly to a peak of 50% at *c.* 1070 Cal. yr BP then decrease sharply to a low of 3% at *c.* 990 Cal. yr BP. Values then increase to a peak of 25% at *c.* 850 Cal. yr BP before declining at *c.* 770 Cal. yr BP.

KM 5 – 640 - 0 Cal. yr BP: Dust values remain low until *c.* 380 Cal. yr BP when values increase and remain high until the top of the core, measuring around 15% with a double peak of 20% at *c.* 230 and *c.* 100 Cal. yr BP.

4.5 Radiogenic Isotope Analysis

This section describes the results of radiogenic isotope analysis on microscopic dust particles, or layers, found within the sampled peat cores. Radiogenic Isotope analysis was undertaken at the British Geological Survey (BGS-NIGL, Keyworth) as a means to potentially identify the source of the dust layers identified in each core (see previous section, Chapter 4.4). Samples from the Shebster, Heldale and Kedills Mires cores were analysed to provide isotopic data along a latitudinal transect from Caithness to Shetland. Dust samples from Pettawater were omitted from the analyses due to funding constraints. 15 dust samples, chosen from sections of the Shebster core which demonstrated increased dust levels (>25 %), were analysed for strontium (Sr) analysis. The analyses yielded $^{87}Sr/^{86}Sr$ values ranging between 0.713035 and 0.732467 (Figure 4.5.1). Unfortunately, Neodymium (Nd) analysis was not completed on dust from the Shebster core due to insufficient quantity of sample material.

8 dust samples were analysed for strontium and neodymium isotopes in the Kedills Mires core. These were chosen from sections of the core where elevated dust levels were present. This provided $^{87}Sr/^{86}Sr$ values ranging between 0.717102 and 0.721828 and Epsilon Nd alues ranging between -6.9 to 4.87.

9 dust samples were analysed from the Heldale core, also chosen from areas of the core where elevated dust levels were present. This provided $^{87}Sr/^{86}Sr$ values ranging between .725689 and 0.778059 and Epsilon Nd values ranging between -16.4 to 3.01. In addition, 3 dust samples collected in Iceland were also analysed for strontium and neodymium. These

silt-sized particles were taken from three different sites in Iceland: a small deflated dune on Skeidararsandur (63° 58' 30" N, 17° 02' 56" W); a small dessicated glacial lake bed adjacent

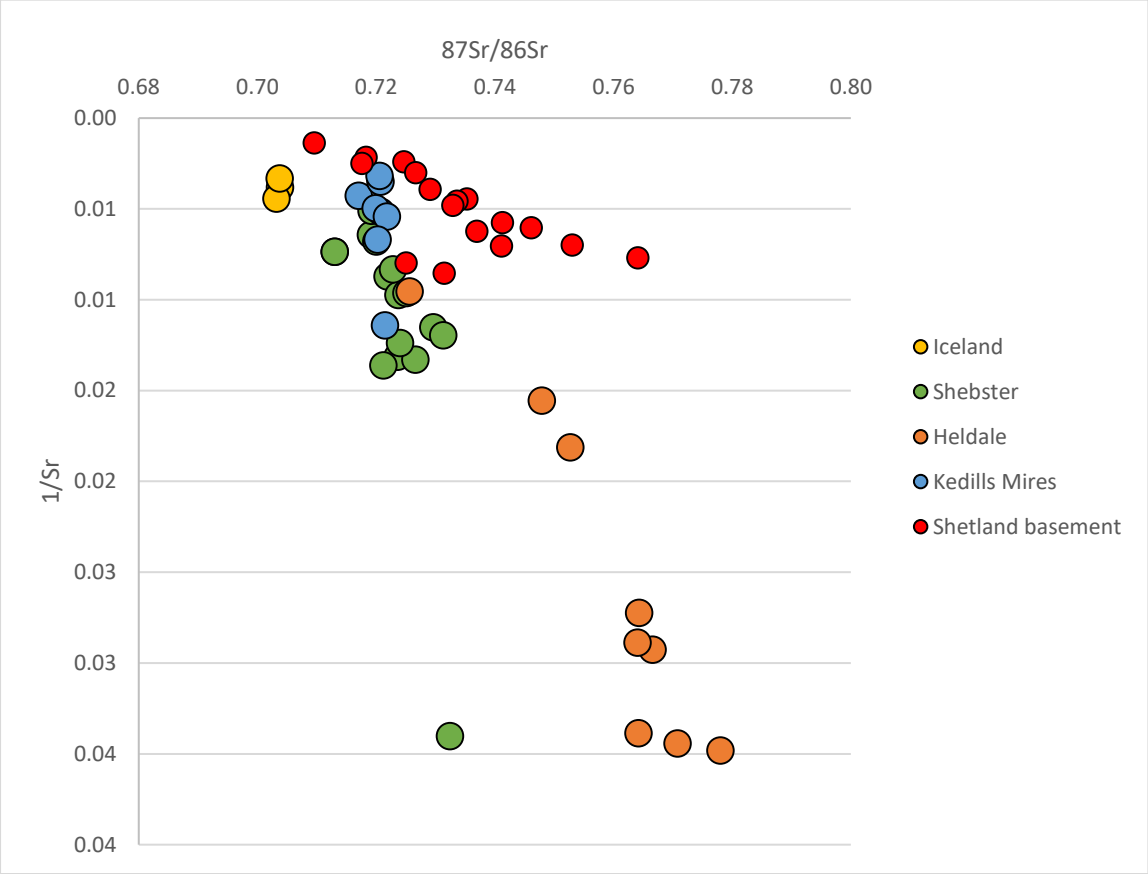

Figure 4.5.1: $^{87}Sr/^{86}Sr$ v 1/Sr values for dust from Iceland, Shebster, Heldale, Kedills Mires (this study) and Shetland base rocks (Walker et al., 2015)

to Virkisjokull (63° 57' 17" N, 16° 50' 46" W); suspended sediment from the Virkisa river, the main outflow from the Virkisjokull glacier (63°57'11" N, 16°50'51" W). This 3 samples yielded $^{87}Sr/^{86}Sr$ values ranging between 0.703253 and 0.703844. These are compared to Shetland basement rocks which yield a $^{87}Sr/^{86}Sr$ range between 0.709545 and 0.735172 (Walker et al., 2015). Radiogenic isotope data for the Basement rocks in the Shebster and Heldale catchments could not be found. The Shebster and Kedills Mires strontium data

(Figure 4.5.1) lie much closer to the Icelandic data points than the Heldale samples. They also exhibit a more constrained range than the values presented by the Shetland basement rocks. Unfortunately, Neodymium analysis was not conducted on the Icelandic dust samples, therefore, Epsilon Nd values have been used from published data (Farmer et al., 2003). Typical Saharan dust values have also been taken from published data and are represented by a yellow box alongside Greenland dust and Gobi sand isotopic data (Figure 4.5.2).

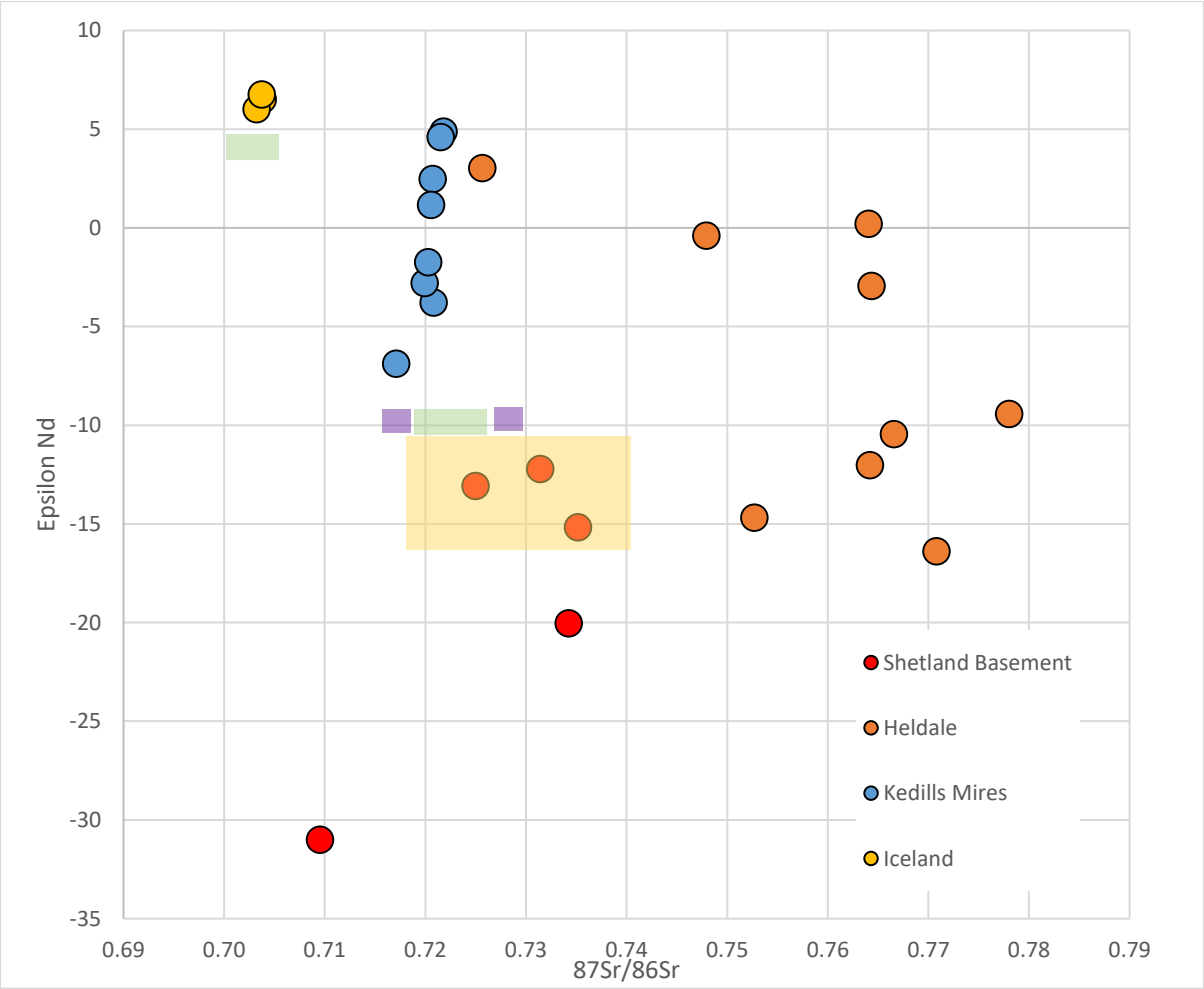

Figure 4.5.2: $^{87}Sr/^{86}Sr$ v Epsilon Nd values for Iceland (Farmer et al., 2003), Heldale, Kedills Mires and Shetland base rocks (Walker et al., 2015). The yellow box represents the spread of Saharan dust values (Thevenon et al., 2012), the green boxes represent dust found in Greenland ice cores and the purple box represents Gobi sand and China loess.

The data collected from the Kedills Mires dust samples are presented in Figure 4.5.2. The position of these samples on the Sr/Nd plot suggest that they lie within a mixing curve between the Icelandic and Shetland basement rock points. Despite having similar $^{87}Sr/^{86}Sr$ values to the Saharan dust data points, the Epsilon Nd values for Kedills Mires have significantly higher values and therefore are unlikely to include Saharan input. Also, there is very little correlation between the Kedills Mires data and the Greenland dust or Gobi sand values. The Heldale data points, with the exception of one, appear not to match with any of the distal source data points and therefore may primarily reflect local (Orkney) sediment sources.

Chapter 5: Discussion

This chapter will discuss and interpret the new datasets presented in the Results chapter. For each individual site, storminess data including humification (as an indicator of mire surface wetness) and bromine will be discussed first, followed by the dust and μ-XRF results.

5.1: Shebster

5.1.1: Shebster storminess data: interpretation

The Shebster humification and bromine records are presented in figure 5.1.1.

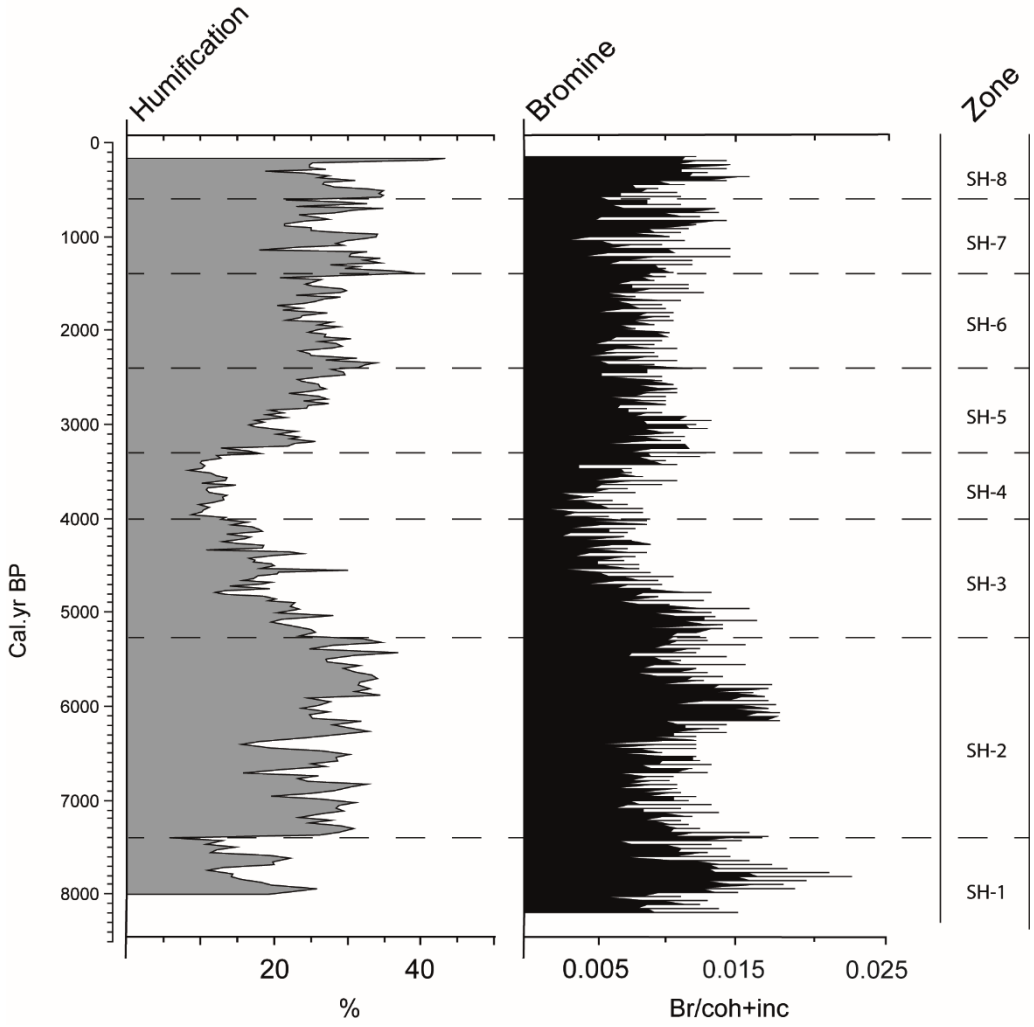

Figure 5.1.1 – The Shebster humification and bromine records

Starting at the base of the record, *c*. 8200 Cal. yr BP, bromine values are low which suggests a calmer climatic period with lower levels of storminess. Between 8000 and 7400 Cal. yr BP, mire surface wetness (MSW) values are relatively low. However, this part of the record is dominated by the largest peak in bromine centred on *c.* 7800 Cal. yr BP, suggesting a period of enhanced storminess lasting ~300 to 400 years. Between *c.* 7400 and 5270 Cal. yr BP there is a marked increase in MSW which suggests a change to more persistent wetter conditions. Bromine values in the Shebster core decrease from the large peak at *c.* 7800 Cal. yr BP but remain higher and relatively stable, suggesting a shift to more frequent precipitation but perhaps less intense storms. From *c.* 6330 to *c.* 5270 Cal. yr BP, MSW in remains higher suggesting continued wetter conditions. At the same time, bromine values are also higher with a pronounced peak occurring at *c.* 6000 Cal. yr BP indicating an increase in storminess. Between *c.* 5270 and *c.* 4000 Cal. yr BP, MSW and bromine values at Shebster undergo a period of gradual decline indicating a steady decrease in precipitation and storminess over Northern Scotland. Between *c.* 4000 and *c.* 3300 Cal. yr BP the Shebster MSW and bromine values are at their lowest for the whole 8000 year record. These values probably reflect a sustained period of reduced precipitation and reduced storminess. A marked broadly synchronous increase in MSW and Br indicates a return to wet and stormy conditions in Shebster at *c.* 3300 Cal. yr BP. Between *c.* 2400 and *c.* 1400 Cal. yr BP MSW at Shebster remains relatively high whilst Br levels are somewhat subdued. This suggests a change to a period of increased wetness but reduced storminess. Between *c.* 1100 and *c.* 600 Cal. yr BP, higher but variable MSW occurs alongside relatively high and variable bromine levels in the peat record suggesting a shift towards a wetter and stormier climate in northern mainland Scotland. From *c.* 600 to *c.* 100 Cal. yr BP, the Shebster record is characterised by high but variable MSW and generally high Br values, indicating increased

but not sustained wetness and storminess. The contrast between the records of storminess and wetness at this time likely suggest a change to less frequent but more intense storm events.

5.1.2: Shebster dust and μ-XRF profiles.

The importance of the Shebster dust, potassium, calcium, manganese and iron records are discussed in the following section 5.1.2.

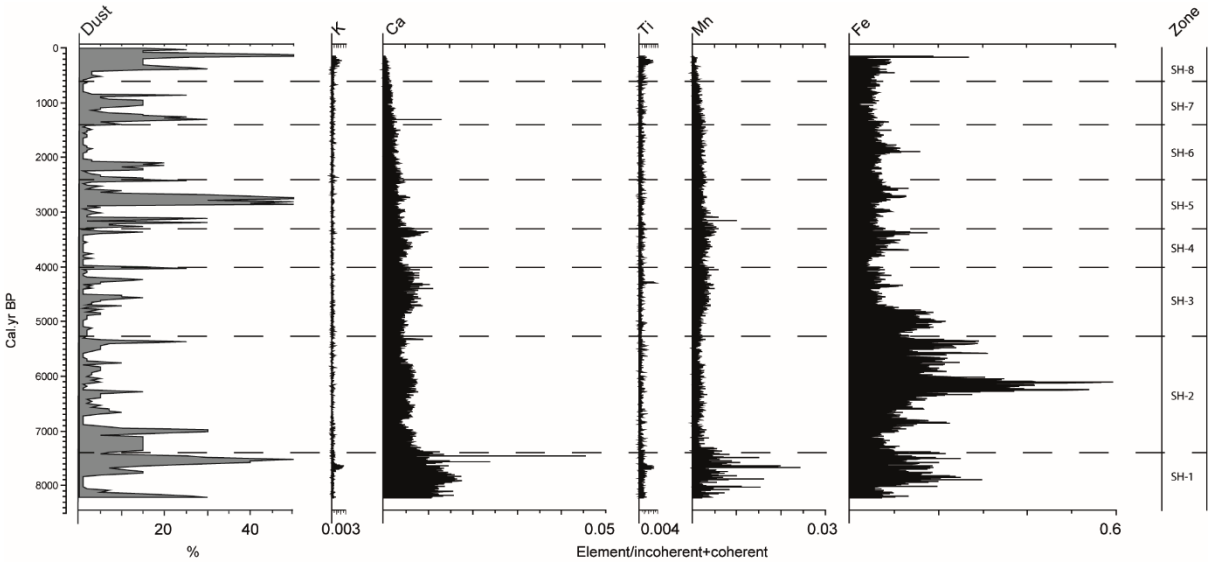

Figure 5.1.2 – The Shebster dust, potassium, calcium, manganese and iron records.

Zirconium does not provide trends in environmental change and therefore is not presented.

The dust record from the Shebster core indicates five periods of increased dust deposition: (1) 8200 Cal. yr BP, (2) 7800 – 6930 Cal. yr BP, (3) 3400 – 2700 Cal. yr BP, (4) 1425 – 810 Cal. yr BP and (5) 410 - 0 Cal. yr BP. These periods provided $^{87}Sr/^{86}Sr$ values ranging between 0.713035 and 0.732467. The highest values around 0.73 are located nearer the base of the peat which may indicate increased levels of local sediment from the underlying lacustrine

sediment. Calcium, manganese and iron values are high at the base of the core which may indicate residual effects of the carbonate-rich lake sediments underneath. There is also a peak in potassium and titanium at *c.* 7650 Cal. yr BP which coincides with one of the major dust peaks. There is a peak in iron values at *c.* 6850 Cal. yr BP and they remain high between *c.* 6300 and 4800 Cal. yr BP, coinciding with high levels of storminess. There is also a small peak in calcium at *c.* 5350 Cal. yr BP which coincides with a small peak in dust abundance. At 4250 Cal. yr BP there is a peak in titanium relating to the Hekla 4 tephra layer and calcium levels are increased between *c.* 4800 and 4000 Cal. yr BP which coincides with increased dust levels between these time periods suggesting increased storminess. Iron values are increased between *c.* 3700 and 3300 Cal. yr BP and there is a small peak in calcium at *c.* 3350 Cal. yr BP. Manganese shows a small peak at *c.* 3150 Cal. yr BP and iron values are increased between *c.* 2800 and 2550 Cal. yr BP which may relate to anthropogenic activity during the neoglacial period. There is an iron peak at *c.* 1900 Cal. yr BP which may also indicate anthropogenic activity during the Roman Warm Period and a peak in calcium is recorded at *c.* 1300 Cal. yr BP which coincides with a peak in dust. There are also potassium, titanium and iron peaks at the top of the core in sync with increased dust deposits from the LIA and recent anthropogenic activity.

5.2: Heldale

5.2.1: Heldale storminess data: interpretation

The Heldale humification and bromine records are presented in figure 5.2.1. Between *c.* 9400 and 7400 Cal. yr BP, the Heldale core shows very low MSW values across this zone but moderate bromine values indicating a period of Early Holocene storminess. Between *c.* 7400 and *c.* 5270 Cal. yr BP, MSW values at Heldale remain low but show an increasing

trend. This is consistent with an increase in bromine levels in the Heldale core suggesting a change to wetter and stormier conditions. Between *c.* 5270 and *c.* 4000 Cal. yr BP, MSW values decline whereas bromine values remain high. This suggests an increase in storm intensity rather than frequency. Between *c.* 4000 and *c.* 3300 Cal. yr BP there is an increase in the Heldale MSW but a significant decrease in bromine values than those seen in the previous zone. We infer that at this time, the climate was dominated by increases in precipitation and storm frequency but a decrease in storm intensity.

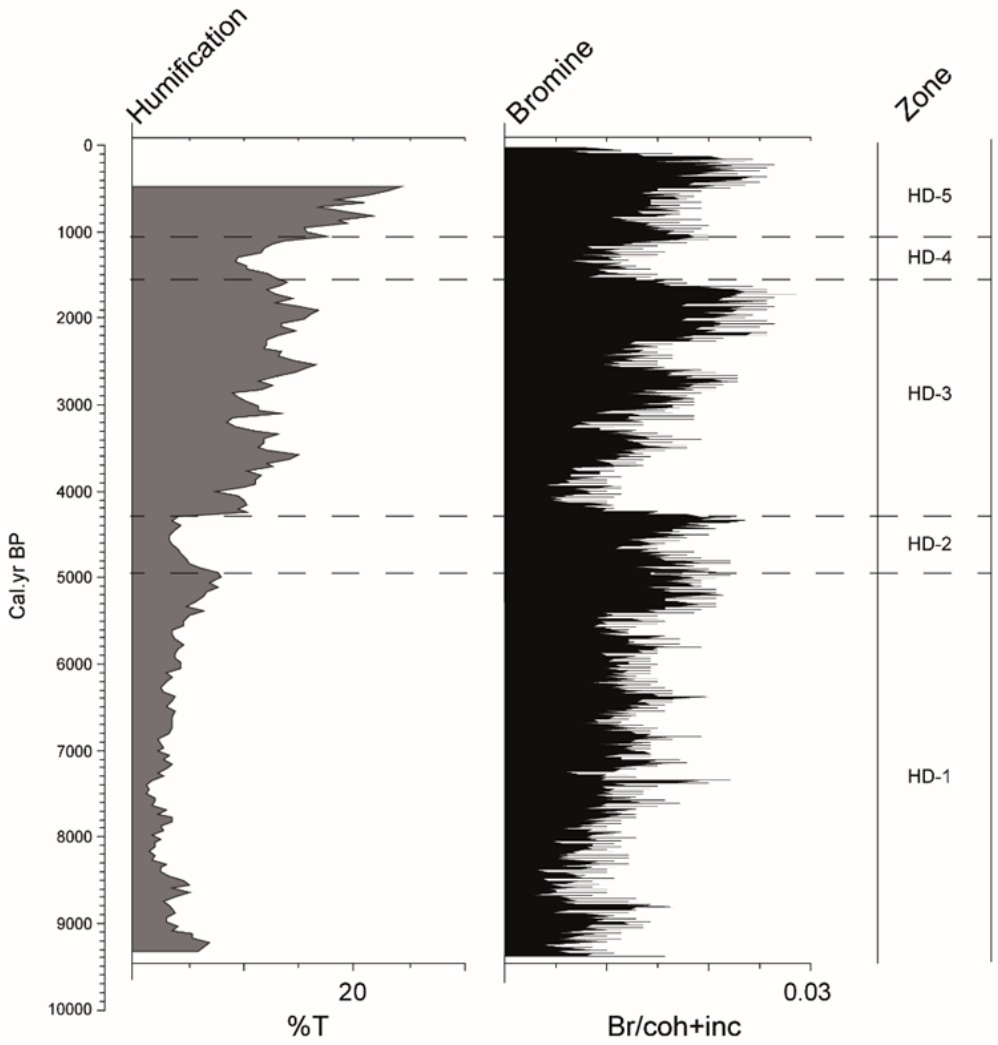

Figure 5.2.1 - The Heldale humification and bromine records

Higher MSW and Br values between *c.* 3300 and *c.* 1400 Cal. yr BP indicate a change to wetter and stormier conditions. Between *c.* 1400 and *c.* 1100 Cal. yr BP, MSW and Br values decline suggesting a change to calmer and less stormy climatic conditions. Between *c.* 1100 and *c.* 600 Cal. yr BP MSW and bromine levels are increasing throughout this period suggesting a gradual return to wetter and stormier conditions. Between *c.* 600 and *c.* 0 Cal. yr BP, high but variable MSW and generally high Br values indicate increased wetness and storminess for much of this 500-year window. Again the contrast between the records of storminess and wetness suggests a change to less frequent but more intense storm events.

5.2.2: Heldale dust and µ-XRF profiles

The Heldale dust, iron and zirconium records are presented in figure 5.2.2. The Heldale core indicates five Holocene periods of increased dust deposition: (1) 9400–7200 Cal. yr BP, (2) 6900-5900 Cal. yr BP, (3) 5600-4200 Cal. yr BP, (4) 3800-1400 Cal. yr BP and (5) 1000-0 Cal. yr BP. These periods provided $^{87}Sr/^{86}Sr$ values ranging between 0.725689 and 0.778059 and Epsilon Nd values ranging between -16.4 to 3.01. The large $^{87}Sr/^{86}Sr$ values suggest that the Heldale core is influenced by local sediment rather than distal aeolian dust. Zirconium values are high at the base of the core, which coincides with increased dust levels. Iron levels are high until *c.* 7900 Cal. yr BP when values start to follow a declining trend. This includes a large peak at *c.* 8200 Cal. yr BP that may relate to the 8.2 ka event. Zirconium values show major peaks at *c.* 6880 Cal. yr BP, *c.* 5260 Cal. yr BP, *c.* 4600 Cal. yr BP and *c.* 3400 Cal. yr BP which all coincide with periods of increased dust deposition. A peak in iron values occurs at *c.* 1080 Cal. yr BP that may be an anthropogenic signal. In zone HD-5, Zirconium values are increased and after *c.* 400 Cal. yr BP iron values are very high which may be due to influence from the LIA and/or an anthropogenic signal at the top of the core.

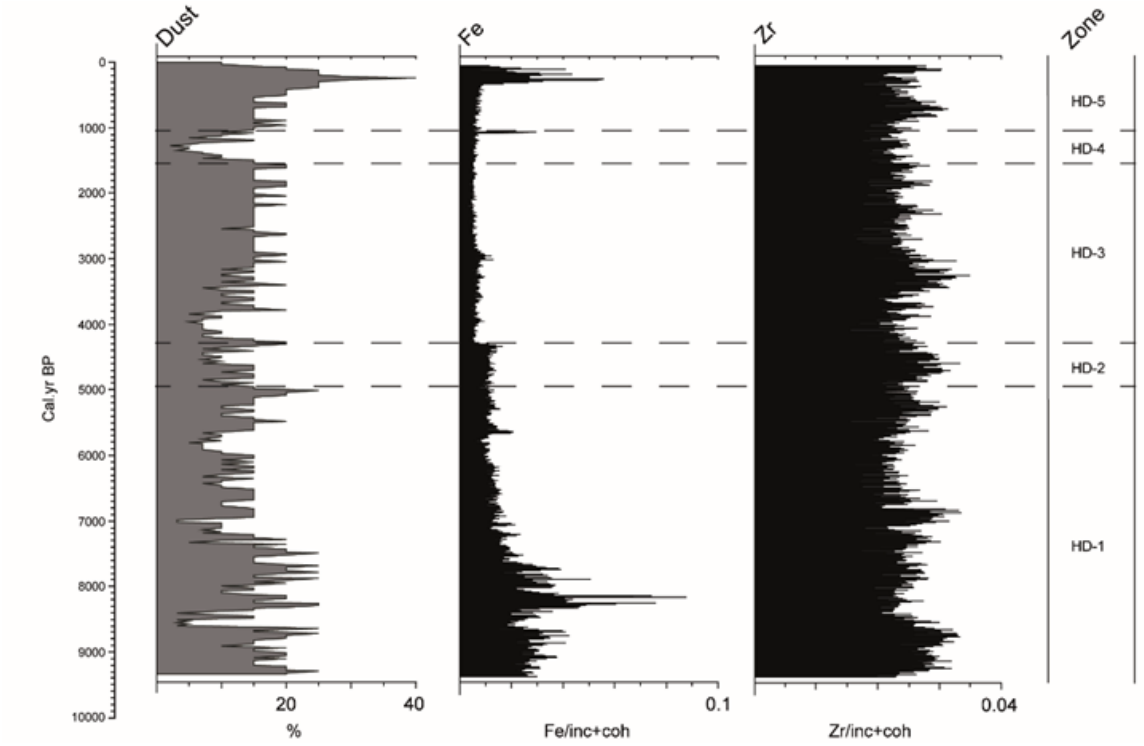

Figure 5.2.2 - The Heldale dust, iron and zirconium records. Iron and zirconium are the only Itrax elements to provide trends in environmental change and therefore are the only ones presented

5.3: Pettawater

5.3.1: Pettawater storminess data: interpretation

The Pettawater humification and bromine records are presented in figure 5.3.1. Between *c.* 5100 and *c.* 4600 Cal. yr BP, bromine values are stable and MSW values are low suggesting a period of reduced precipitation but increased storm intensity. At *c.* 4600 Cal. yr BP, there is an increase in the MSW and bromine values suggesting an increase to wetter and stormier conditions until *c.* 3300 Cal. yr BP. MSW values decline at *c.* 3300 Cal. yr BP and remain low until *c.* 2400 Cal. yr BP. However, high bromine values are maintained suggesting an increase in storm intensity rather than frequency. Between *c.* 2400 and *c.* 1100 Cal. yr BP

the Pettawater core shows increased levels of MSW but subdued bromine values suggesting a change to wetter but less stormy conditions. Between *c.* 1100 and *c.* 600 Cal. yr BP, mire wetness and bromine levels are increased which we infer as a shift to a wetter and stormier period. After *c.* 600 Cal. yr BP there is a decline in MSW, however bromine values remain high suggesting a change to lower frequency but high intensity storm events. MSW levels increase again at *c.* 300 Cal. yr BP and together with the higher bromine values suggest a period of wetter and generally stormier climate.

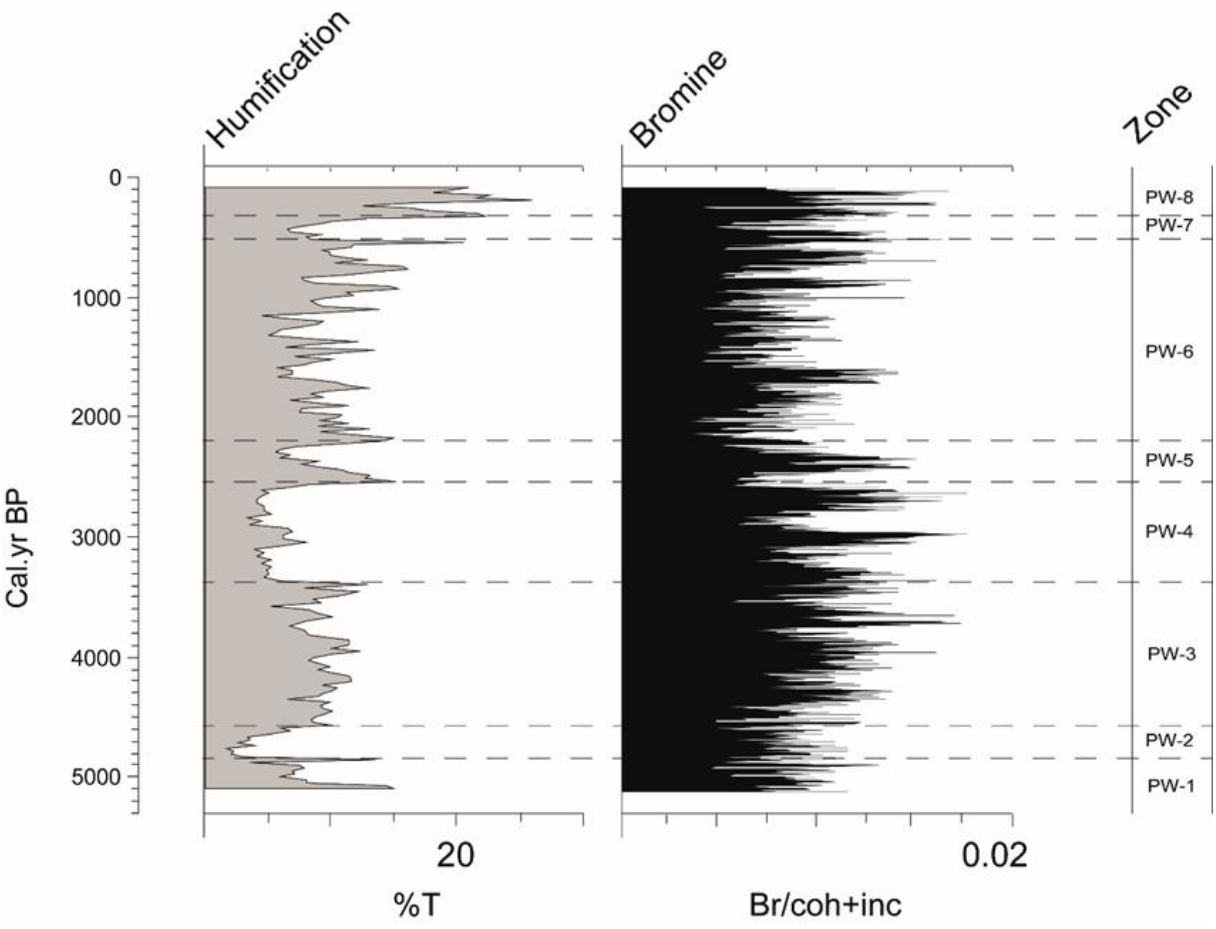

Figure 5.3.1 - The Pettawater humification and bromine records

5.3.2: Pettawater dust and µ-XRF profiles.

The Pettawater dust, iron and zirconium records are presented in figure 5.3.2. The dust record established for the Pettawater record indicates three main periods of Holocene dust deposition: (1) 4750 Cal. yr BP, (2) 4300-1400 Cal. yr BP and (3) 400-0 Cal. yr BP. Iron values are high at the base of the core and there is a small peak at 4300 Cal. yr BP. This may reflect waning influence of substrate in the peat profile or relative loch water level to the accumulating peat. Zirconium values show peaks at *c.* 3920 Cal. yr BP and 2290 Cal. yr BP which coincide with intervals of increased dust deposition. Another peak identified at *c.* 1220 Cal. yr BP may be an anthropogenic signal during the Dark Ages Cold Period.

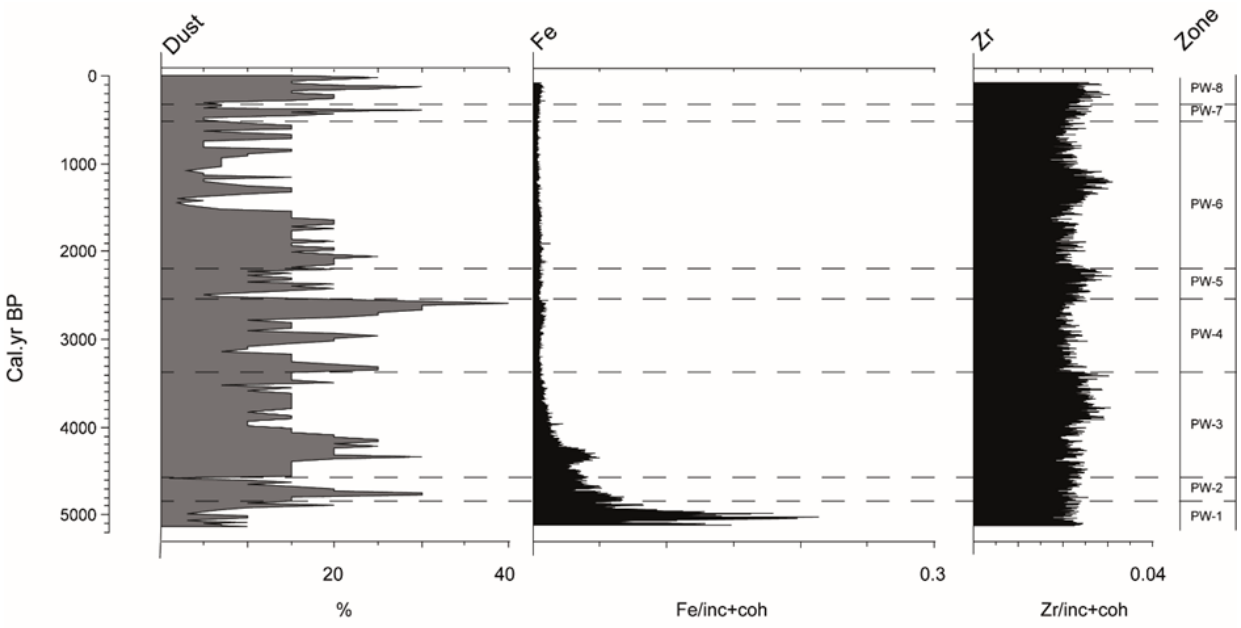

Figure 5.3.2 - The Pettawater dust, iron and zirconium records. Iron and zirconium are the only Itrax elements to provide trends in environmental change and therefore are the only ones presented.

Zirconium values are high in zones PW-7 and PW-8 that may be due to influence from the LIA and an anthropogenic signal at the top of the core.

5.4: Kedills Mires

5.4.1: Kedills Mires storminess data: interpretation

The Kedills Mires humification and bromine records are presented in figure 5.4.1. Between *c.* 5800 and *c.* 5300 Cal. yr BP, MSW values are low, however, bromine values are high suggesting a period of less frequent but more intense storminess and less precipitation. This set of conditions indicates that these intense storms were sourced in moisture-starved areas, such as the Arctic Ocean or northern Scandinavia/Russia.

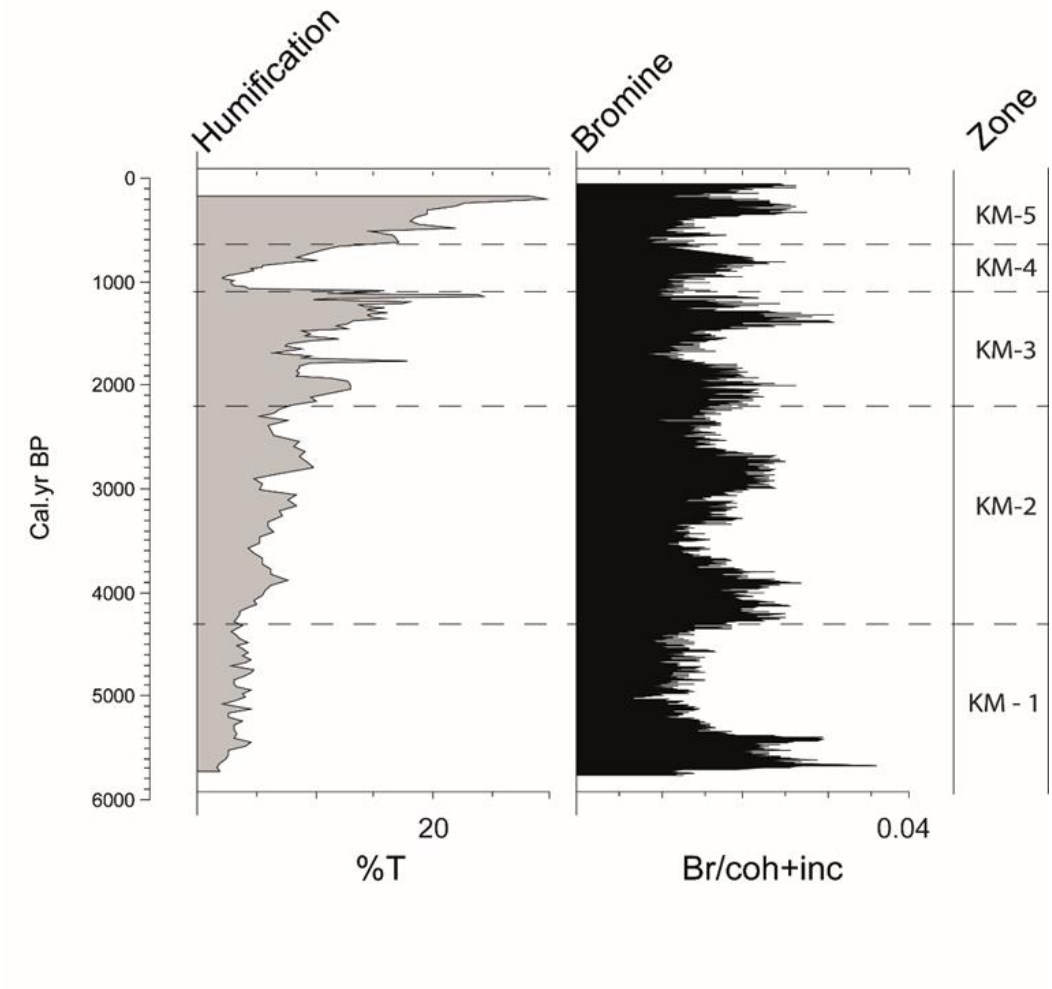

Figure 5.4.1 - The Kedills Mires humification and bromine records

Between *c.* 5270 and *c.* 4200 Cal. yr BP, MSW values remain low. However, there is a decline in the bromine record suggesting a shift towards a much calmer climate. At *c.* 4300 Cal. yr BP there is an increase in bromine at Kedills Mires but only a very small increase in the

MSW. This may be indicative of a return to more intense storms rather than an overall increase in storminess.

Between *c.* 3800 and *c.* 3300 Cal. yr BP there is a reduction in the Kedills Mires MSW and bromine record which may be inferred to represent a period of reduced precipitation and storminess. An increase in MSW and bromine values in the Kedills Mires core between *c.* 3300 and *c.* 2600 Cal. yr BP indicates a return to wet and stormy conditions. Between *c.* 2600 and *c.* 2200 Cal. yr BP, there is a change back to low MSW and low bromine values suggesting a period of reduced storminess. This reverses between *c.* 2200 and *c.* 1800 Cal. yr BP to a period of increased wetness and storminess. After *c.* 1800 Cal. yr BP MSW values remain high however bromine values are subdued suggesting a period of generally wetter but less stormy weather. Between *c.* 1400 and *c.* 1100 Cal. yr BP, the Kedills Mires core shows very high bromine and MSW values suggesting a change back to stormy conditions. Between *c.* 1100 and *c.* 600 Cal. yr BP MSW and bromine values are on a downward trend suggesting a change to calmer and less stormy conditions. After *c.* 600 Cal. yr BP, MSW and bromine values are higher indicating wetter and stormier climatic conditions.

5.4.2: Kedills Mires dust and μ-XRF profiles

The Kedills Mires dust, titanium, iron and zirconium records are presented in figure 5.4.2. The dust record obtained from Kedills Mires indicates four Holocene periods of increased dust deposition: (1) 5728 – 5260 Cal. yr BP, (2) 4111 – 2058 Cal. yr BP, (3) 1298 – 783 Cal. yr BP and (4) 312-0 Cal. yr BP. This provided $^{87}Sr/^{86}Sr$ values ranging between 0.717102 and 0.721828 and Epsilon Nd values ranging between -6.9 to 4.87. These points lie on a mixing curve between Shetland basement rocks and Icelandic sediment that suggests that the

smallest particles may originate from Iceland. Between *c.* 5800 and *c.* 5300 Cal. yr BP there is a large peak in iron and a peak in titanium at *c.* 5690 Cal. yr BP which coincides with a large peak in dust abundance. Both iron and zirconium values increase slightly between *c.* 4600 and *c.* 4300 Cal. yr BP that may be due to anthropogenic activity. A large peak identified at *c.* 4100 Cal. yr BP may relate to the Kebister tephra layer.

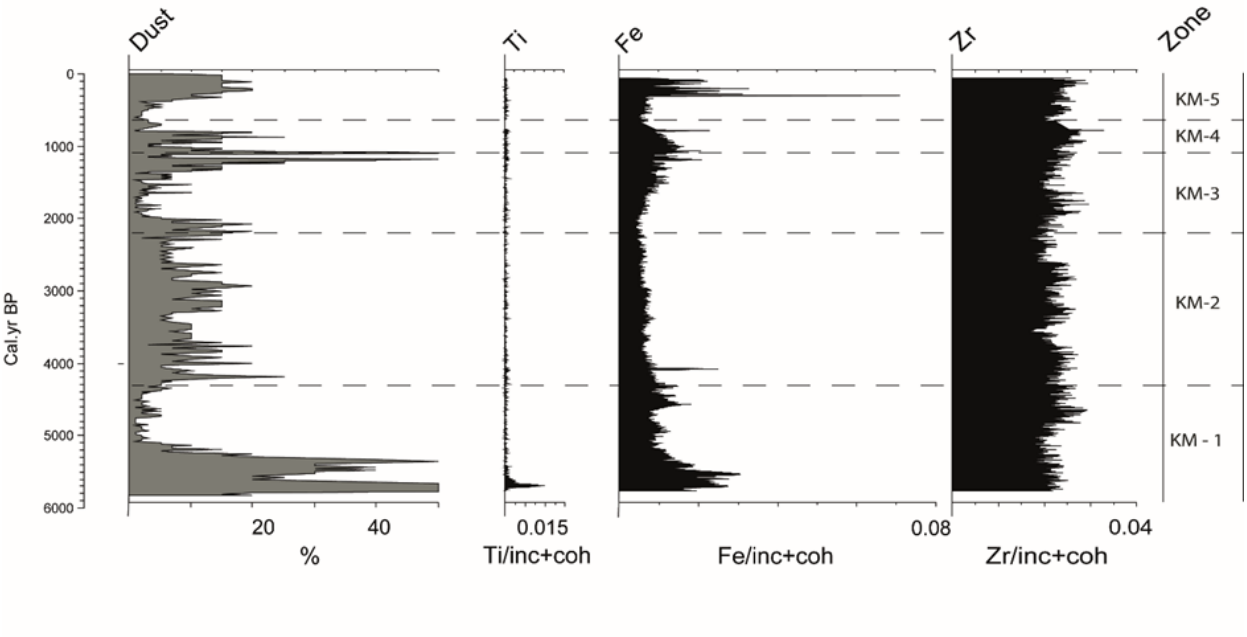

Figure 5.4.2- The Kedills Mires dust, titanium, iron and zirconium records. Titanium, iron and zirconium are the only Itrax elements to provide trends in environmental change and therefore are the only ones presented.

Between *c.* 3500 Cal. yr BP and *c.* 2500 Cal. yr BP, zirconium values are increased which coincides with a period of high dust deposition. Zirconium values increase at *c.* 1810 Cal. yr BP that may relate to anthropogenic activity during the Roman Warm Period. Iron and zirconium values are also increased between *c.* 1650 and *c.* 800 Cal. yr BP that coincides with a very large peak in dust. However, a large iron peak at *c.* 800 Cal. yr BP coincides with the Hekla 1158 tephra layer. Both iron and zirconium values are increased in zone KM-5

that may be due to a climatic influence from the LIA and/or an anthropogenic signal at the top of the core.

5.5: Summary

This chapter has discussed the trends in mire surface wetness (MSW), bromine (Br) and dust abundance for each of the four sampling sites. Figure 5.5 compares these trends between the sampling sites and is zoned in regards to the Shebster humification record.

The main trends identified in Figure 5.5 are simplified in Table 6 below:

Table 6 - Summary of the main trends seen within each sampling site

ZONE (CAL. YR BP)	SHEBSTER	HELDALE	PETTAWATER	KEDILLS MIRES
1 (9400 – 7400)	Low MSW High Br High Dust	Low MSW Moderate Br High dust	N/A	N/A
2 (7400-5270)	High MSW High Br Low dust	Low MSW High Br Low dust	N/A	Low MSW High Br High dust
3 (5270-4000)	Decline MSW Decline Br Low dust	Low MSW High Br High dust	Variable MSW Stable Br Variable dust	Low MSW Low Br Low dust
4 (4000-3300)	Low MSW Low Br Low dust	High MSW Low Br High dust	High MSW High Br Low dust	Low MSW Variable Br Variable dust
5 (3300 – 2400)	Increase MSW High Br High dust	High MSW High Br High dust	Low MSW High Br High dust	Increase MSW Variable Br Variable dust
6 (2400-1400)	High MSW Subdued Br Low dust	High MSW High Br High dust	High MSW Reduced Br High dust	Increase MSW Variable Br Variable dust
7 (1400 – 600)	High MSW High Br High dust	Variable MSW Low Br Low dust	Variable MSW Low Br Low dust	Variable MSW High Br High dust
8 (600-0)	High MSW High Br High dust	High MSW High Br High dust	High MSW High Br High dust	High MSW High Br High dust

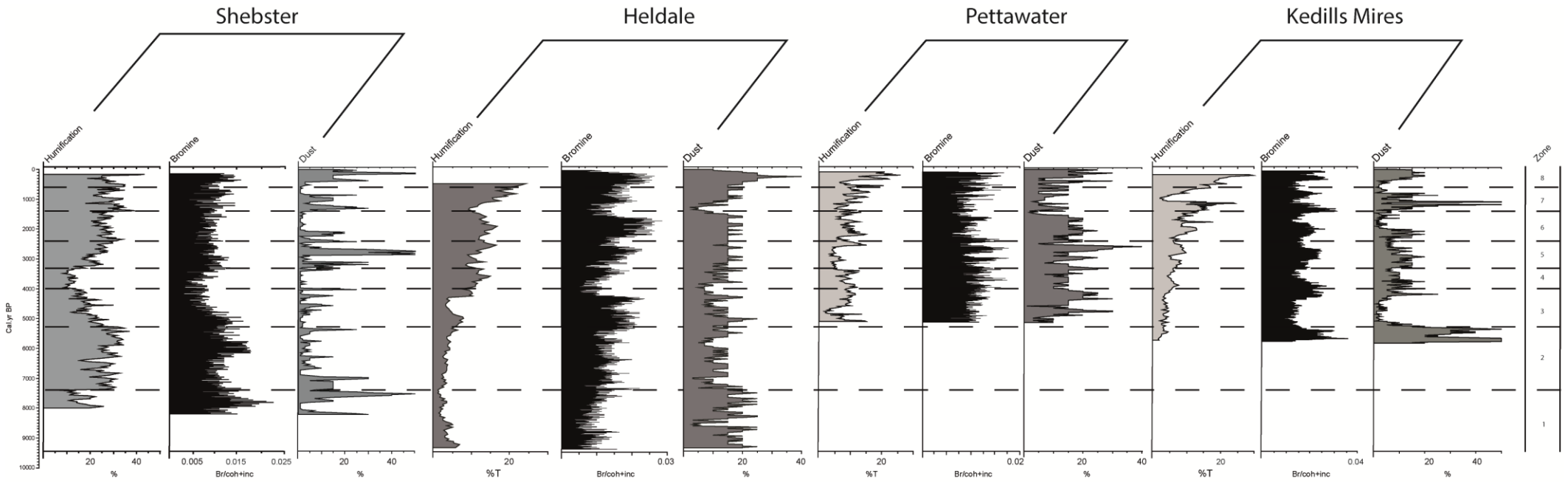

Figure 5.5 - Mire surface wetness, bromine and dust results for Shebster, Heldale, Pettawater and Kedills Mires

The trends highlighted by figure 5.5 and table 6 will be discussed in detail in the following chapter. This will combine the results from the four sites and compare them to other records across the North Atlantic and discuss them in a wider context.

Chapter 6: Synthesis

This chapter discusses the data and interpretations presented in the previous chapters and examines the wider implications of this work. The results obtained for Shebster, Heldale, Pettawater and Kedills Mires can be interpreted alongside other key proxy records from around the North Atlantic to place the inferred palaeoenvironmental trends in the wider context of Holocene climate and atmospheric circulation changes. For examining indicators of past storminess these proxy records include: a ~5000-year glacier and precipitation reconstruction from Folgefanna in Southern Norway which provides a latitudinal comparison (Bakke *et al.*, 2008); a reconstructed 5000-year NAO index based on a lake-sediment core from SW Greenland which allows a comparison to another NAO record (Olsen *et al.*, 2012); a Scottish speleothem record which provides a local comparison (Baker *et al.*, 2015) and an Iberian speleothem record which provides comparisons to an area expected to show the opposite climate from the UK during the different NAO phases (Walkzak *et al.*, 2015) (Figure 6.1). The data sets are zoned in terms of changes in the Shebster MSW record as Shebster is the most southerly site and MSW is the local indicator.

6.1: Indicators of Storminess

Zone-1: 9400 – 7400 Cal. yr BP: Both the Shebster and Heldale cores show very low mire surface wetness values within this lowermost zone. The Heldale core has stable bromine values during this period, however, the Shebster record is dominated by a large bromine peak centred at *c.* 7800 Cal. yr BP, suggesting a period of enhanced storminess. This anti-phase relationship between MSW and bromine may suggest that these storms were cold, moisture-

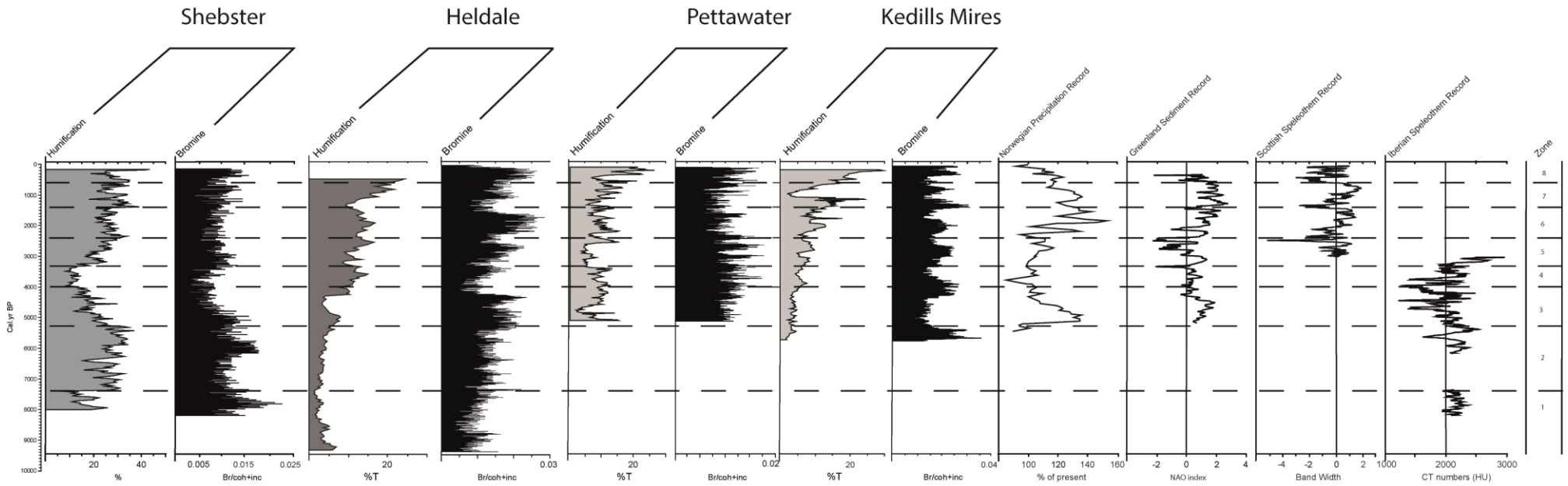

Figure 6.1 - Mire surface wetness, bromine, 5000 year glacier record from Folgefanna in Southern Norway (Bakke et al., 2008), a reconstructed 5000 year NAO index based on a lake-sediment core in SW Greenland (Olsen et al., 2012), a Scottish speleothem record (Baker et al., 2015) and an Iberian speleothem record (Walkzak et al., 2015)

starved Polar vortex systems rather than moisture-bearing westerly winds. This is supported by the Iberian speleothem record, which shows a stable, positive record indicating warmer and wetter conditions. Rainfall in southern Iberia was more evenly distributed throughout the year, typical of a more temperate climate lacking a clear dry season (Walczak *et al.*, 2015) and may indicate a more southerly position of the jet stream at this time (Figure 6.2/6.3).

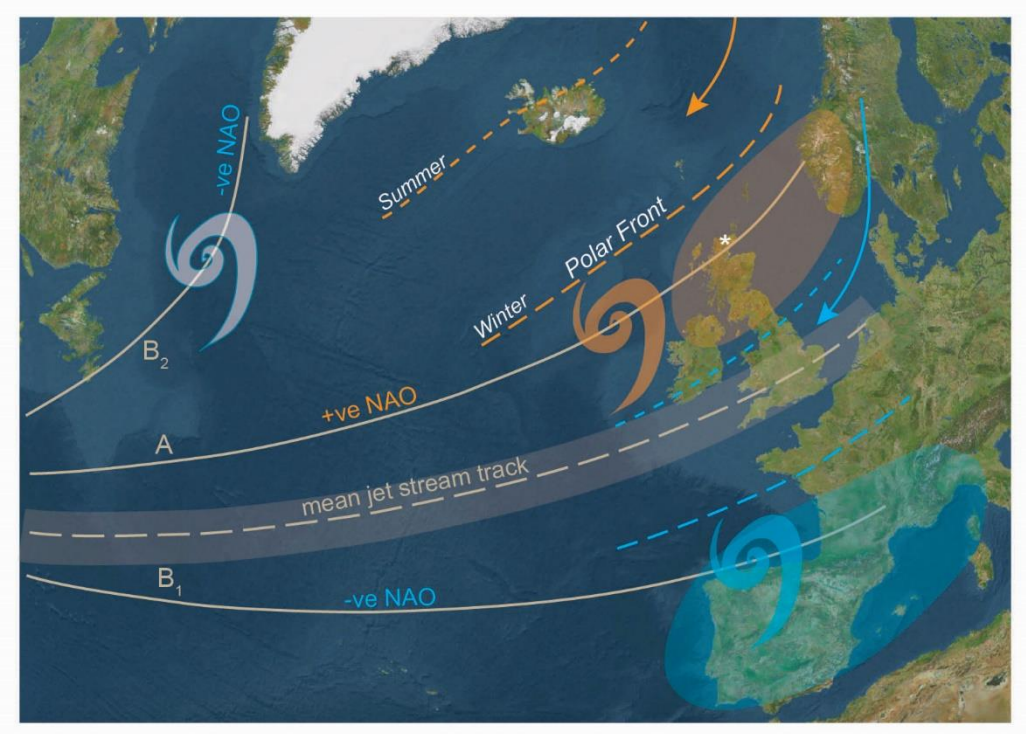

Figure 6.2: The tripole latitudinal distribution of the PFJ stream and its relationship with the dominant modes of the NAO

Zone-2: 7400-5270 Cal. yr BP: This zone shows a marked increase in MSW at Shebster and although the values fluctuate between c. 7400 and 6330 Cal. yr BP, and they remain higher suggesting the persistence of wetter conditions. Although MSW values at Heldale continue to be lower they are on an increasing trend and bromine values in the Shebster core decrease

Zone 1: 9400 – 7400 Cal. yr BP

Zone 2: 7400 - 5270 Cal. yr BP

Zone 3: 5270 - 4000 Cal. yr BP

Zone 4: 4000 - 3300 Cal. yr BP

Zone 5: 3300 – 2400 Cal. yr BP

Zone 6: 2400 - 1400 Cal. yr BP

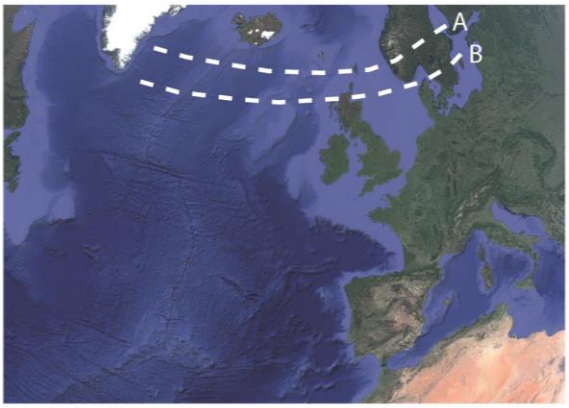

Zone 7: A -1400 - 1100 Cal.yr BP
B -1100 - 600 Cal.yr BP

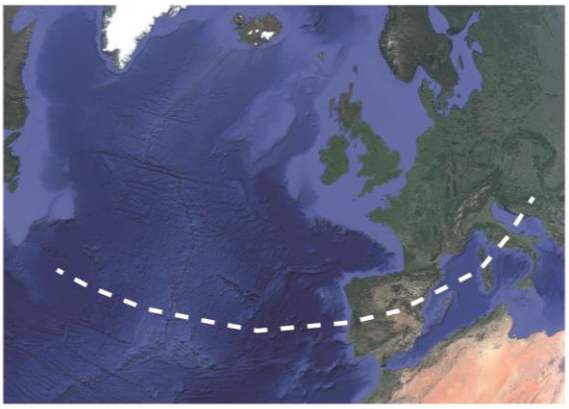

Zone 8: 600 - 0 Cal. yr BP

Figure 6.3: Latitudinal distribution of the PFJ stream within each zone

from the initial peak in zone 1 but remain higher and relatively stable, suggesting a shift to more frequent precipitation and numerous but perhaps less intense storms. This period probably indicates a migration of the North Atlantic storm tracks to a position located over northern mainland Scotland (Figure 6.3). This atmospheric circulation pattern is best described by the positive mode of the NAO (Figure 2.2).

In the second half of Zone-2, from *c.* 6330 to 5270 Cal. yr BP, the higher levels of MSW in both the Shebster and Heldale cores continue to reflect increased wetness but in a less changeable climate than the early half of zone-2 (*c*. 7400 – 6300 Cal. yr BP). At the same time, bromine values remain high in both cores indicating higher levels of storminess with a pronounced peak in storminess in the Shebster record at *c.* 6000 Cal. yr BP. There are also higher levels of bromine at the base of the Kedills Mire record between 5800 and 5300 Cal. yr BP. The Iberian speleothem record is characterised by a decline in growth rates between 6100 and 5300 Cal. yr BP suggesting decreased moisture availability (Walczak *et al.*, 2015). This is consistent with a stronger polar-front jet stream bringing an increase in the number and intensity of storms tracking over Northern Scotland and a more strongly positive NAO than in the first half of zone-2.

Zone-3: 5270-4000 Cal. yr BP: Between *c.* 5270 and 4000 Cal. yr BP, MSW and bromine values at Shebster undergo a period of gradual decline indicating a steady decrease in precipitation and storminess over Northern Scotland. This is supported by the decline in the Kedills Mires bromine record as well as low mire surface wetness values in the Heldale and Kedills Mires cores. This also marks the beginning of the Pettawater core, which shows stable bromine values and low mire surface wetness values also l suggesting low frequency but moderate

intensity levels of storminess. The glacier-ELA-reconstructed winter precipitation record from Bakke *et al.* (2005) indicates a comparable near-continuous decrease in wetness over most of this period (*c.* 5000-4000 Cal. yr BP). The Iberian speleothem record similarly shows a shift to drier conditions with the exception of an increase in wetness at *c.* 4200 BP. This climate period is captured by the earliest part of the SW Greenland lake-sediment-reconstructed NAO index that shows a sustained positive NAO phase between *c.* 5200 and 4400 Cal. yr BP (Olsen *et al.*, 2012). These climatic conditions are all compatible with a period of unstable jet stream position and/or declining jet stream strength bringing generally warmer, drier summer conditions to NW Europe accompanied by a decline in cyclogenesis with fewer storms tracking across northern Scotland. After *c.* 4400 Cal. yr BP, the reconstructed NAO index (Olsen *et al.*, 2012) enters a relatively neutral phase consistent with a decrease in jet stream vigour. However, throughout this period bromine levels in the Heldale core are very high in comparison to the other cores. This suggests that Orkney may have experienced an increase in storminess rather than a decrease at this time (Figure 6.3). Also at *c*. 4600 Cal. yr BP, the MSW and bromine values slightly increase in the Pettawater record, although they remain lower than other parts of the record. At *c*. 4300 Cal. yr BP there is also an increase in the bromine record at Kedills Mires. However, this may be indicative of more intense storms rather than an overall increase in wetter climate across Orkney and Shetland between *c*. 4600 and 4300 Cal. yr BP.

Zone-4: 4000-3300 Cal. yr BP: Between *c.* 4000 and 3300 Cal. yr BP the Shebster MSW and bromine values are at their lowest for the whole of the 8000-year record. This is consistent with a reduction in the Kedills Mires MSW and bromine record as well. We relate these values to a sustained period of drier and calmer climatic conditions. Pettawater shows a slight

decline in MSW although while maintaining higher bromine values. At this time, there is also an increase in the Heldale MSW but much lower bromine values than those seen in the previous zone. The data collected from the Heldale and Pettawater cores is not deemed as accurate or environmentally sensitive as the data collected from the Kedills Mires and Shebster cores therefore we infer that this period is defined by a weaker PFJ and drier, calmer conditions (as indicated by the Shebster and Kedills Mires cores).

We find that this exceptional period of drier, unusually calm and more stable climate between *c*. 4000 and 3300 Cal. yr BP (seen in the Shebster peat record) is not restricted to Caithness, but is also seen widely in other European Holocene palaeoclimate proxies. Peat surface-wetness records from a composite of 12 sites in Northern Britain (Charman *et al.*, 2012) show a period of considerably decreased wetness from *c.* 3900 to 3400 Cal. yr BP, the most pronounced in the mid to Late Holocene (interrupted by a brief wet spike at *c.* 3750 BP). In southern Europe, often in antiphase with the climate of northern Britain, Mediterranean records, including the Iberian speleothem record, record an unusual period of enhanced aridity between *c.* 4000 and 3400 Cal. yr BP (e.g. Di Rita and Magri, 2009; Genty et al 2006; Walczak *et al.*, 2015). The Norwegian glacier record also shows lower than present precipitation levels between *c*. 4000-3300 Cal. yr BP whilst temperatures in south-west Ireland inferred from speleothems show a broad thermal maximum *c.* 3800 to 3400 Cal. yr BP (McDermott *et al.*, 2001).

A marked decrease in North Atlantic storminess in Northern Scotland could be associated with two different atmospheric circulation scenarios: (1) a migration of the storm tracks to a latitude that is more southerly equating to a strongly negative winter NAO phase; or (2)

reduced jet stream strength and a low-value or neutral NAO index. The collected multi-proxy evidence points towards the latter scenario, i.e. jet stream weakening, during zone-4, leading to a marked decrease in cyclonic activity. Negative NAO conditions normally result in increased rainfall and storminess over southern Europe (e.g. Hurrell *et al.*, 2003; Pinto *et al.*, 2009), something which is not seen in most of the proxy records between *c.* 4000-3300 Cal. yr BP. In addition, many studies have linked strongly negative NAO phases with meridional airflow and strong temperature contrasts causing enhanced but intermittent cyclogenesis in north-west Europe (Trouet *et al.*, 2012; Vliet Lanoe *et al.*, 2014). This is not evident in the Shebster record during zone-4 and there is an overall reduction in storminess across the other three cores as well. Combined with the prolonged neutral phase of the reconstructed NAO index (Olsen *et al.*, 2012), these results are consistent with a 500-700 year period of decreased jet stream strength during zone-4 (Figure 6.3).

Zone-5: 3300 – 2400 Cal. yr BP: A marked broadly synchronous increase in MSW and bromine values in the Shebster core *c.* 3200-3300 Cal. yr BP indicates a return to wetter and stormier, more typical, conditions in northern Scotland (Figure 6.3). This is consistent with high MSW and bromine values in the Heldale cores and high bromine values in both of the Shetland cores. Supporting proxy data suggest more vigorous cyclogenesis, increased precipitation and raised water tables in north-west Europe at this time (Hughes *et al.*, 2000; Charman, 2010; Swindles *et al.*, 2007; Oldfield *et al.*, 2010). A marked concomitant rise in air temperatures and winter precipitation, seen in the Irish speleothem, Norwegian glacier and Iberian speleothem proxy-records between *c*. 3300 and 2700 Cal. yr BP would also suggest a return to the previously seen atmospheric circulation patterns over north-west Europe with strongly zonal moisture-bearing winds and moderate levels of cyclogenesis. However, the

reconstructed (Greenland) NAO index displays a strong fluctuation from initially positive (*c.* 3300-3000 Cal. yr BP) to strongly negative values (*c.* 3000-2400 Cal. yr BP) (Olsen *et al.*, 2010). This period of negative NAO values coincides with generally lower MSW values across all cores than seen in previous time periods and may suggest a jet stream position located south of Northern Scotland. The annually resolved north-west Scotland speleothem record also starts during this time (Baker *et al.*, 2015). Although no overall trend in the composite speleothem climate-index is apparent during the first 500 years, relatively high-magnitude peaks in speleothem growth rates at c. 2900 and 2600 Cal. yr BP probably reflect multi-decadal to centennial periods of higher precipitation in northern Scotland (Baker *et al.*, 2015).

Zone-6: 2400-1400 Cal. yr BP: Between *c.* 2400 and 1400 Cal. yr BP MSW at Shebster remain relatively high whilst Br levels are somewhat subdued. The Heldale core shows high levels of bromine and MSW and both the Pettawater and Kedills Mires cores show increased levels of MSW but subdued bromine values. This suggests a period of decreased storminess across Shebster and the Shetland sites that may be explained by a poleward shift of the westerly storm tracks to a position focused over Orkney (Figure 6.3). The north-west Scotland speleothem record exhibits high growth rates suggesting moist but more stable climatic conditions. Elsewhere around Europe this millennium is synonymous with the 'Roman Warm Period' (Wang *et al.*, 2012) and is characterised by a predominantly positive (>1.0) NAO index shown by the Greenland deep-water anoxia record (Olsen *et al.*, 2012).

Zone-7: 1400 – 600 Cal. yr BP: Between 1400 and 1100 Cal. yr BP, the Kedills Mires core shows very high bromine and MSW values whereas the other cores are in decline indicating a northwards shift in the storm tracks. Between *c.* 1100 and 600 Cal. yr BP, a period that

includes the Medieval Climate Anomaly (MCA: 1100-700 Cal. yr BP; Mann and Jones, 2003), higher but variable MSW occurs alongside relatively high and variable bromine levels in the peat record at Shebster. Mire wetness and bromine levels are also increasing throughout this period in both the Heldale and Pettawater records. However, the Kedills Mires MSW and Br values are on a downward trend suggesting a southward shift in the storm tracks focused over Northern Scotland. This suggests a wetter and stormier period in Northern Scotland consistent with the unusually long and unbroken, strongly positive, NAO phase seen in the Greenland lake-sediment record from *c.* 1400 to 600 Cal. yr BP (Olsen *et al.*, 2012). A positive NAO mode is normally associated with a vigorous jet stream and a North Atlantic winter storm track focused between 55-60°N (at the latitude of northern mainland Scotland) (Hurrell *et al.*, 2003; Woollings *et al.*, 2008, 2010). This circulation pattern is supported by several other palaeoenvironmental proxies from the British Isles and adjacent areas. Firstly, the composite British peat-surface wetness record compiled by Charman (2006, 2010) shows a continuous phase of elevated water tables spanning the entire 800-year period with a peak *c.* 1100-1200 Cal. yr BP. Secondly, the Irish speleothem record shows several centuries of increasing above-average (inferred) temperatures, with a peak *c.* 700-900 Cal. yr BP (McDermott *et al.*, 2001). Thirdly, the winter moisture index from Norwegian glaciers shows well above-average precipitation (120-140% present day) in this time interval (Bakke *et al.*, 2008). Fourthly, the occurrence of outsized wave-transported boulders (cliff-top storm deposits) 15-60 m above sea level in Shetland, northern Scotland, dated to between *c.* 1300 and 800 Cal. yr BP (Hansom and Hall, 2009), indicate enhanced storminess at ~60^{o}N. Finally, lower values of bromine at Cors Fochno peat bog, relative to the preceding period (Orme *et al.*, 2015), suggest that the main westerly storm tracks were not focused at this latitude (52^{o}N) but probably further north over Scotland. However, more complexity is introduced when comparing these proxy records

with growth rates from the north-west Scotland speleothem record. Baker *et al.* (2015) reconstruct strongly negative NAO-like conditions from *c.* 1400 to 1100 Cal. yr BP, at which point the trend is reversed and their reconstruction shows a strongly positive phase throughout the MCA, akin to the Olsen *et al.* (2012) NAO record. Therefore, we interpret the MCA period to be one of a strong polar-front jet stream and enhanced cyclogenesis, bringing westerly storms tracking across northern Scotland (57-60^{o}N) (Figure 6.3). Although the variable antiphase relationship between MSW and bromine records at all cores perhaps suggest, at times, decreased storm frequency but higher storm intensity across the northern British Isles, consistent with the generation of high-energy storm deposits around northern Scotland's coasts (Hansom and Hall, 2009).

Zone-8: 600-0 Cal. yr BP: The most recent period captured in the peat records spans from *c.* 600 to 100 Cal. yr BP and corresponds to the Little Ice Age (LIA: *c.* 700-150 Cal. yr BP), as defined by Mann and Jones (2003). This period is characterised in all records by higher but variable MSW and generally higher bromine values, suggesting increased wetness and storminess for much of this 500-year window. The LIA is consistently recognised in numerous Northern Hemisphere palaeoenvironmental proxies. A clear LIA signal is seen in the proxy-reconstructed NAO indices of Olsen *et al.* (2012) and Baker *et al.* (2015), where an abrupt shift from strongly positive to negative index occurs at *c.* 600 Cal. yr BP in both records. The Zone-7 record suggests that this dominantly negative NAO phase was associated with a vigorous jet stream, a high incidence of moisture-bearing winds and a high frequency of storms generally tracking across the latitude of Northern Britain (55-60^{o}N) for much of LIA (*c.*100-600 Cal. yr BP). The normal negative NAO configuration involves a significant southward shift in dominant westerly winds and storm tracks, to the latitude of southern France, northern Iberia

and the western Alps (40-45°N) (Woollings *et al.*, 2008, 2010). Other records from around Scotland show with a high level of certainty that the LIA period (particularly from 400-100 Cal. yr BP) was one of periodically enhanced storminess, increased wave activity, and generally disrupted weather patterns (Sommerville *et al.*, 2003; McIlvenny *et al.*, 2013; Orme *et al.*, 2016). However, the speleothem and MSW records do not agree with this trend and reflect a shift to relatively drier although perhaps less stable conditions. By way of reconciling this evidence, it is suggested that the speleothem and MSW records may be predominantly influenced by changes in precipitation-driven water table changes and are therefore less sensitive to transient storminess and cylogenesis trends. Furthermore, it is also possible that the contrast between the records of storminess and local wetness is due to the LIA being dominated by overall colder and drier conditions, but still heavily affected by low-frequency high-intensity storm events driven by a more vigorous jet stream.

6.2 Indicators of Dust

The dust records obtained by this study are now compared to the Greenland sediment record for an NAO comparison (Olsen *et al.*, 2012), an ~8000-year Icelandic fjord seawater temperature record for a comparison to local temperature records (Ólafsdóttir, 2010) and an ~8000-year Icelandic glacier advance record to compare dust flux changes to the changes in Icelandic glacier advance and retreat (Gudmundsson, 1997)(Figure 6.4).

Zone-1: 9400 – 7400 Cal. yr BP: At the base of the Heldale core, dust levels are high which coincide with lower fjord seawater temperatures and a peak in the glacier advance record corresponding to the Búdi advance period of the Icelandic Ice Sheet (Gudmundsson, 1997). This was a cold period and mostly birch tree free in Iceland (Gudmundsson, 1997). Between

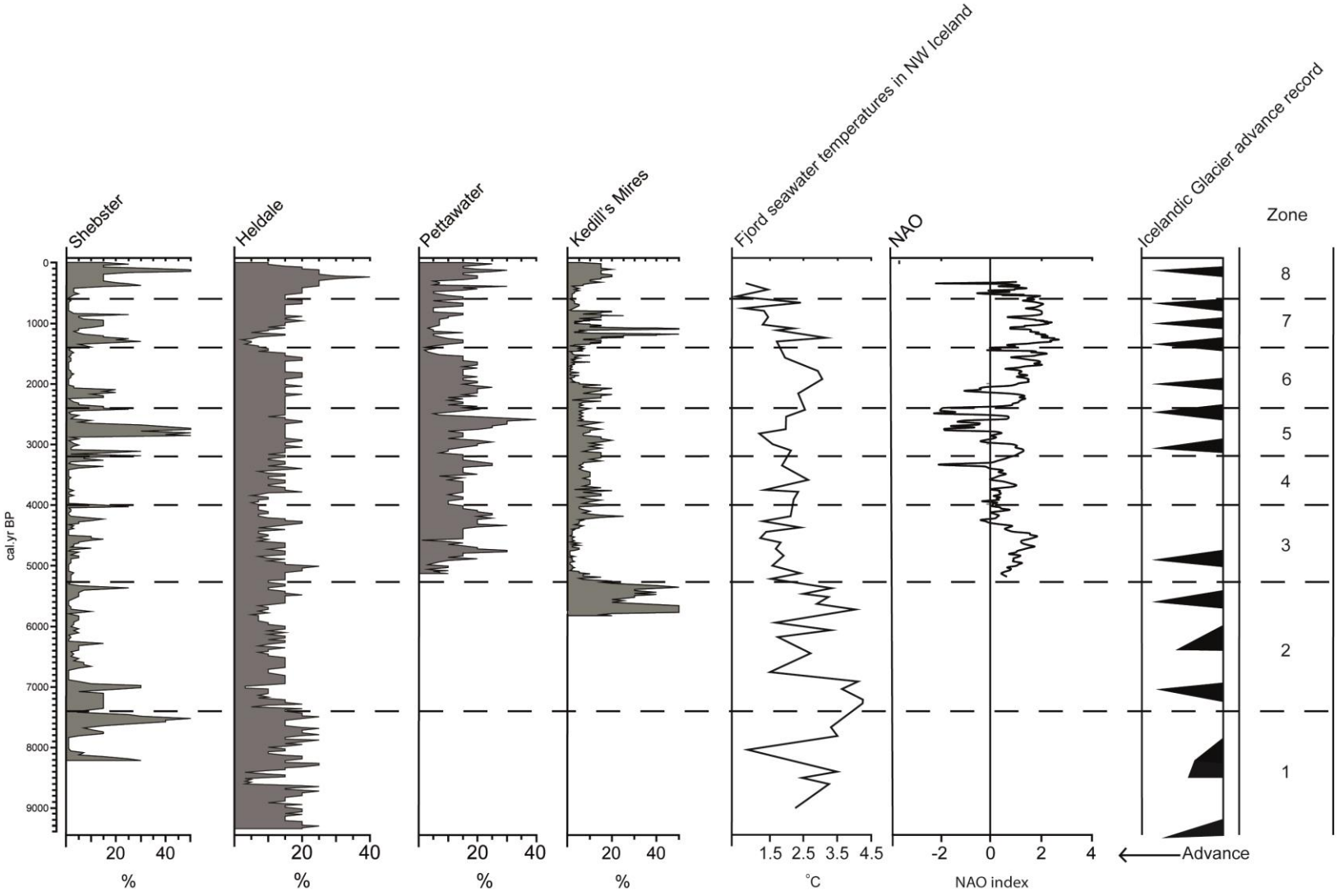

Figure 6.4 - Dust, 8000 year Icelandic fjord seawater temperature record (Ólafsdóttir, 2010), a reconstructed 5000-yr NAO index based on a lake-sediment core in SW Greenland (Olsen et al., 2012) an 8200-year southern Iceland glacier advance record (Gudmundsson, 1997)

8600 and 8300 Cal. yr BP, dust levels decline which correlates with rising seawater temperatures and a change to warmer climatic conditions. Dust values increase again in the Heldale core after 8300 Cal. yr BP in line with a small peak in dust activity in the Shebster core. This occurs at the same time as a period of glacier advance in Iceland and very low seawater temperatures coincident with the 8200 Cal. yr BP event (Flowers et al., 2008; Larsen et al., 2012; Balascio *et al.*, 2015) which is expressed as a marked rapid negative temperature anomaly across much of the Northern Hemisphere (Larsen *et al.*, 2012; Tipping *et al.*, 2012). Dust values in both cores then decline at *c*. 8000 Cal. yr BP which coincides with an increase in Icelandic fjord seawater temperatures (Ólafsdóttir, 2010) and a decrease in Icelandic ice-rafted debris (Larsen *et al.*, 2012). We suggest that this decline in dust abundance is related to a period of stability or glacial retreat due to warming temperatures by *c*. 7900 Cal. yr BP (Larsen *et al.*, 2012) marking the onset of the Holocene Thermal maximum (Geirsdóttir *et al.*, 2009). Dust values in both the Shebster and Heldale records then increase again between 7800 and 7400 Cal. yr BP.

Zone-2: 7400-5270 Cal. yr BP: Between *c*. 7800 and 6900 Cal. yr BP higher levels of dust were deposited in the Shebster core. Dust levels in the Heldale core also increased until *c*. 7200 Cal. yr BP followed by a small decline. These increased dust levels coincide with higher fjord seawater temperatures (Ólafsdóttir, 2010) and the expansion of birch (Hallsdóttir, 1995; Gudmundsson, 1997; Geirsdóttir *et al.*, 2009) which suggests a period of warmer and drier conditions in Iceland (Björck *et al.*, 1992; Hallsdóttir, 1995; Gudmundsson, 1997; Geirsdóttir *et al.*, 2009; Larsen *et al.*, 2012) and possibly a period of glacier retreat. Previous studies have suggested ice-free conditions in Iceland between 7800 and 6900 Cal. yr BP (Geirsdóttir *et al.*,

2009; Larsen *et al.*, 2012; Balascio *et al.*, 2015; Solomina *et al.*, 2015). However, advances at *c*. 7000 BP and 7400 BP suggest that glaciers in Iceland never fully disappeared (Gudmundsson, 1997; Jackson *et al.*, 2005). We infer continuous glacial activity and favourable conditions for dust transport led to higher levels of dust being deposited in the Shebster and Heldale cores at this time.

After *c*. 6930 Cal. yr BP, Shebster dust levels are greatly reduced although small amounts are being deposited consistently. Heldale dust levels are reduced as well. This period also marks the beginning of the Kedills Mires and the Pettawater record. Between 6900 and 6000 Cal. yr BP, there is a small increase in the Heldale dust abundance levels that coincide with a decline in fjord seawater temperatures and a peak in the Icelandic glacier advance record. A large peak in dust abundance is recorded in the Kedills Mires core between *c*. 5800 and 5300 Cal. yr BP which coincides with a peak in the glacier advance record (Gudmundsson, 1997), stable dust levels in the Heldale record and a period of glacier advance in Iceland at this time (Jackson *et al.*, 2005; Kirkbride and Dugmore, 2006; Geirsdóttir *et al.*, 2009). This also coincides with the Drangagil glacier advance stage in Southern Iceland and the Vatnsdular I advance stage in Northern Iceland (Gudmunsson, 1997). We infer a change to a cooler climate and the end of the Holocene Thermal maximum (Larsen *et al.*, 2012; Solomina *et al.*, 2015) which is consistent with a large-scale Holocene cooling event described by Mayewski *et al.*, 2004.

Zone-3: 5270-4000 Cal. yr BP: Between *c*. 5200 and 4250 Cal. yr BP, there is a very little dust in the Kedills Mires core that coincides with the low dust abundance in the Shebster core and stability in the Heldale dust levels. The Pettawater dust record begins at *c*. 5100 Cal. yr

BP and rises to a small peak at *c*. 4750 Cal. yr BP, shortly after a peak in the Icelandic glacier advance record. The Pettawater record then declines again to match the trends seen in the other cores. This is also where the Greenland deepwater anoxia NAO record begins (Olsen et al, 2012) which shows a positive NAO period throughout this time. We infer that this is the Mid-Holocene transition period and there is general stability in glacial behaviour (Larsen *et al.*, 2012).

Zone-4: 4000-3300 Cal. yr BP: Between *c*. 4300 and 3300 Cal. yr BP, there is an increase in Kedills Mires dust abundance that coincides with stability dust levels in the Pettawater core and a less positive NAO. Dust levels in the Heldale core are reduced between 4200 and 3800 Cal. yr BP before increasing again. Shebster dust levels also remain low. This is identified as a period of cooling and glacial advance in Iceland (Gudmundsson, 1997; Stötter *et al.*, 1999; Jackson *et al.*, 2005; Kirkbride and Dugmore, 2006; Geirsdóttir *et al.*, 2009; Larsen *et al.*, 2012; Balascio *et al.*, 2015; Solomina *et al.*, 2015) and overall cooling in the wider Northern hemisphere (Mayewski *et al.*, 2004). Other studies have linked this renewed ice growth in Iceland, or Neoglaciation, with a shift towards a wetter and/or cooler climate in Northern Hemisphere higher latitudes after ~4.2 ka BP (Blaauw *et al.*, 2004; Swindles *et al.*, 2007; Wang *et al.*, 2012). Discrepancies in dust levels between the northerly sites relative to the southerly sites are probably due to the direction rather than the strength of atmospheric circulation patterns.

Zone-5: 3300 – 2400 Cal. yr BP: This is a very dusty period recorded in all cores that coincides with lower Icelandic fjord temperatures and a more negative NAO period. This also coincides with notable advances in the Icelandic glacier record and glacier advances

elsewhere (Jackson *et al.*, 2005; Kirkbride and Dugmore, 2006; Larsen *et al.*, 2011; Larsen *et al.*, 2012; Balascio *et al.*, 2015; Solomina *et al.*, 2015;). The period before *c*. 3000 Cal. yr BP coincides with the Hólsárgil advance stage in southern Iceland and the Vatnsdalur II advance stage in northern Iceland (Gudmundsson, 1997). There is also a coincidence with Holocene cooling between 3500 and 2500 Cal. yr BP (Mayewski *et al.*, 2004). Between *c*. 3000 and 2850 Cal. yr BP previous studies have reported reduced North Atlantic Deep Water formation (Oppo *et al.*, 2003), increased ice rafted debris (Bond *et al.*, 2001), declining birch forests and increased soil erosion in Iceland (Hallsdóttir, 1995).

Zone-6: 2400-1400 Cal. yr BP: Both Shebster and Kedills mires dust levels are unusually low after *c*. 2000 Cal. yr BP. Evidence from the other records show a change to a more positive NAO index and warmer fjord seawater temperatures. Elsewhere around Europe, this is synonymous with the 'Roman Warm Period' (Wang *et al.*, 2012). We infer a change to warmer and more stable conditions with stability or decline in glacial activity. The Heldale and Pettawater dust records still maintain increased dust levels however which coincide with a glacier advance in Iceland around 2000 Cal. yr BP (Gudmundsson, 1997; Geirsdóttir *et al.*, 2009) and another around 1600 Cal. yr BP (Schomacker *et al.*, 2003). Discrepancies between dust abundance in the cores may be due to the orientation of atmospheric circulation patterns focusing the deposition of Icelandic glacial dust over these areas. However, an equally likely explanation is an increase in local sediment to the Pettawater and Heldale cores at this time.

Zone-7: 1400 – 600 Cal. yr BP: This period is defined by high levels of dust in the Shebster and Kedills Mires record. At *c.* 1400 Cal. yr BP there is a sharp decline to a more negative

NAO mode alongside a peak in the glacier advance record and a declining trend in fjord seawater temperatures. This may be related to a period of glacial advance occurring during the Dark Ages Cold period (Stötter *et al.*, 1999; Kirkbride and Dugmore, 2008; Larsen *et al.*, 2011; Larsen *et al.*, 2012; Balascio *et al.*, 2015) and coincides with the Ystagil advance period in southern Iceland (Gudmundsson, 1997; Kirkbride and Dugmore, 2008). Studies also describe an increase in soil erosion (Geirsdóttir *et al.*, 2009; Larsen *et al.*, 2011) and the disappearance of birch forests in Iceland (Andrews *et al.*, 2001; Larsen *et al.*, 2011). This corresponds well with overall Holocene cooling between *c*. 1200 and 1000 Cal. yr BP (Mayewski *et al.*, 2004). However, between *c*. 1300 and 800 Cal. yr BP, the NAO record changes to a positive NAO mode and the Heldale and Pettawater records show reduced dust levels. This is consistent with the Medieval Warm Period (1100-800 BP, Jackson *et al.*, 2005; Larsen *et al.*, 2011) which is expressed as a period of warming in the North Atlantic (Larsen *et al.*, 2011; Balascio *et al.*, 2015). However, the Icelandic glacier record shows an advance at this time consistent with a decrease in fjord seawater temperatures and increased dust levels. This is known as the Medieval Glacier Advance and may describe a period of colder conditions in Iceland compared to other areas of Europe (Gudmundsson, 1997). This may explain the increased dust levels in the Shebster and Kedills Mires cores at this time. Between *c*. 800 and 600 Cal. yr BP there are low dust abundance levels in the Shebster and Kedills Mires cores. There is also a small increase in fjord seawater temperatures and a positive NAO. This may indicate a milder climatic period less favourable for glacier advance (Gudmundsson, 1997). Increasing dust levels in the Pettawater and Heldale cores may suggest an input of local sediment rather than aeolian dust.

Zone-8: 600-0 Cal. yr BP: At *c*. 600 Cal. yr BP, there is a change to a negative NAO index and a decline in fjord seawater temperatures that coincides with a change to colder conditions across the Northern Hemisphere as described by Mayewski *et al.*, 2004. This corresponds with a peak in the Icelandic glacial advance record, with Larsen *et al.*, 2012 reporting a period of glacial advance starting at *c*. 700 Cal. yr BP. We infer this period as a transition between the Medieval Warm Period and the Little Ice Age. The transition from the MCA to the LIA included a general weakening of the Atlantic Meridional Overturning Circulation (AMOC) and a transition to more negative NAO conditions, resulting in a strong cooling of the North Atlantic region (Trouet *et al.*, 2012). Between *c*. 400 Cal. yr BP and the top of the core, dust abundance values in all cores are very high coinciding with an advance in the Icelandic glacier record, low seawater temperatures and a negative NAO index. This corresponds with an increase in mid-latitude blocking anticyclones during the LIA consistent with a negative NAO phase (Trouet *et al.*, 2012). The LIA was the most severe multi-centennial cold interval of the Late Holocene (Larsen *et al.*, 2011). Low solar activity during this time between the periods of AD 1645-1715 and AD 1790-1830 has been linked with changes in Atlantic storm tracks, anomalously cold summer and winter temperatures in Scandinavia and the repositioning of the polar front and changing sea ice cover (Clarke and Rendell, 2009). The Little Ice Age period was also when most of Europe's glaciers (including Iceland) were at their Late Holocene maximum (Mackintosh *et al.*, 2002; Jackson *et al.*, 2005; Kirkbride and Dugmore, 2008; Geirsdóttir *et al.*, 2009; Larsen *et al.*, 2011).

6.3: Radiogenic Isotope Analysis

The 15 dust samples analysed for strontium analysis in the Shebster core provided $^{87}Sr/^{86}Sr$ values ranging between 0.713035 and 0.732467 (Figure 4.5.1). Neodymium analysis could

not be completed due to insufficient quantity of sample material. The samples displaying higher strontium values (>0.73) nearer the base of the core which may suggest influence from the underlying lacustrine sediment. There is no defined trend in $^{87}Sr/^{86}Sr$ values moving upwards through the core as the majority of samples lie between 0.72 and 0.73. However, the lowest values (<0.72) are found (in descending order) between *c*. 2880 - 2700 Cal. yr BP, c. 329 - 324 Cal. yr BP and *c*. 5439 – 5369 Cal. yr BP. These data points do not directly coincide with the peaks in glacier advance described by Gudmundsson (1997) however they all correlate with cooler climates, dusty periods defined in the other cores and a predominantly negative NAO (as discussed in section 6.2).

Eight dust samples were analysed for strontium and neodymium isotopes in the Kedills Mires core and 9 dust samples were analysed from the Heldale core. For the Kedills Mires core, this provided $^{87}Sr/^{86}Sr$ values ranging between 0.717102 and 0.721828 and Epsilon Nd values ranging between -6.9 to 4.87. For the Heldale core, this provided $^{87}Sr/^{86}Sr$ values ranging between 0.725689 and 0.778059 and Epsilon Nd values ranging between -16.4 to 3.01 (Figure 5.3.2). Strontium and neodymium results from the Kedills Mires and Heldale cores were compared to an Icelandic dust record (Farmer *et al.*, 2003), Saharan dust record (Thevenon *et al.*, 2012), Greenland dust record, Gobi/China loess record and Shetland basement rock record (Walker *et al.*, 2015). Unfortunately, a basement rock record for Caithness and Orkney could not be sourced. Figure 4.5.2 shows that the Icelandic dust record has a $^{87}Sr/^{86}Sr$ range between 0.703253 and 0.703844 and a Epsilon Nd range around 6 (Farmer *et al.*, 2003). The Shetland basement rocks have a $^{87}Sr/^{86}Sr$ range between 0.709545 and 0.735172 and an Epsilon Nd range between -12.2 and -31 (Walker *et al.*, 2015).

As the Kedills Mires $^{87}Sr/^{86}Sr$ values fall within the ranges seen for the Shetland basement rocks it is therefore more relevant to assess differences in this core through analysis of the Epsilon Nd values. The most negative Nd value of -6.9 is identified between *c*. 30 – 135 Cal. yr BP. This suggests influence from anthropogenic activity over the past 150 years leading to an input of local sediment. There are no down core trends observed for the remaining data points, however they all lie above those identified in the Shetland basement rocks. The values identified between *c*. 870 – 780 Cal. yr BP, *c*. 2175 – 2140 Cal. yr BP and *c*. 5665 – 5644 Cal. yr BP all coincide with periods of glacier advance in Iceland (Gudmundsson, 1997). The data points with the most positive values are identified between *c*. 3575 – 3489 Cal. yr BP and *c*. 5380 – 5218 Cal. yr BP. These data points do not directly coincide with the peaks in glacier advance described by Gudmundsson (1997), however, they do correspond with cooler climates, dusty periods defined in the other cores, and a negative NAO (as discussed in section 5.2). The data point established between c. 5380 – 5218 Cal. yr BP also overlaps with the data point with the lowest $^{87}Sr/^{86}Sr$ values in the Shebster core.

The majority of the Heldale $^{87}Sr/^{86}Sr$ values are much higher than those identified in the Kedills Mires and Shebster cores suggesting a predominantly local influence rather than distal. The data point established between *c*. 340 - 195 Cal. yr BP shows a $^{87}Sr/^{86}Sr$ value of 0.726 and an Epsilon Nd value of 3.01. This approximates with the end of the LIA and may suggest an Icelandic dust origin at this point.

The Kedills Mires radiogenic isotopic dust signatures fall between the Icelandic dust values and Shetland base rock values (Figure 5.3.2) and, therefore, may show a mixing trend

between local Shetland sediment and far-travelled Icelandic dust. The Saharan data (Thevenon *et al.*, 2012) shows $^{87}Sr/^{86}Sr$ values between 0.714 and 0.738, a range that encompasses the Shebster and Kedills mires values. However, the Epsilon Nd values range between -10 and -16, which does not correlate with the Kedills Mires samples and we infer that Saharan dust is an unlikely contributor to the majority of the dust found in the Kedills Mires core. The Greenland and Gobi/ China loess values are also not included within the Kedills Mires isotopic ranges and therefore can be excluded as potential dust sources. The Heldale samples show much higher $^{87}Sr/^{86}Sr$ values than the other two sites. However, from the dust record it is likely that slope wash may provide a significant contribution to this record. This may lead to the samples being dominated by higher levels of local sediment and support the contention that the Kedills Mires and Shebster sites are more influenced by far-travelled aeolian sediment from areas such as Iceland.

Chapter 7: Conclusion

The results presented in this thesis provide useful insights into the timing and nature of North Atlantic climate changes. Four peat cores have been analysed across a ~300km transect from Caithness in Northern Scotland to Yell in the Shetland isles and provide a significant advance to the existing records in that they span much of the Holocene rather than just the past ~1000-2000 years. The combined bromine and MSW records highlight the millennial to centennial scale changes to the position of the polar jet stream that is a significant driver of environmental change in northern Scotland. The minerogenic dust record and radiogenic isotope analysis data highlight changes in the climate of the wider north Atlantic region.

The record of storminess established across the four peat cores is consistent with the Norwegian glacier record, Greenland sedimentary inferred NAO index, Scottish speleothem record and Iberian speleothem record but most importantly advances our understanding of the development and fluctuations of the polar front jet stream and NAO from the early Holocene. We infer from the data that periods of high bromine and mire wetness levels may relate to a jet stream position over Northern Scotland and, therefore, increased storminess and a positive NAO signal. Periods of reduced bromine and mire wetness levels may relate to a more southerly position of the jet stream and, therefore, a decline in storminess and a negative NAO. Variations between the cores has provided an insight in to the jet stream position within a specific positive NAO phase. This allows us to determine whether the jet stream is positioned across Northern Scotland or further North over Orkney and the Shetland Isles. Between *c*. 4300 and 3300 cal. yr BP there are very low levels of

bromine and mire wetness in the Shebster core which is consistent with a drier period across the northern hemisphere and may relate to a neutral NAO state and a weaker jet stream. However indicators of storminess in the Orkney and Shetland sites suggest intense storms were still present, perhaps just less frequent. Also, subtle differences between MSW and bromine suggest that single indicators of storminess may not necessarily be used to reconstruct changes in jet stream movement and the NAO alone. They also suggest that high intensity but perhaps less frequent periods of storminess are not necessarily associated with a wetter climate which may be correlated to the conditions displayed during the Little Ice Age.

The introduction of a brand new proxy in the form of aeolian minerogenic dust allows us to reconstruct climate changes over the wider North Atlantic region. The dust records identified at all four sites correlate with the Icelandic fjord seawater temperature record, Greenland sedimentary inferred NAO index and Icelandic glacier advance record. We infer from the data that periods with high levels of dust may relate to periods of glacier advance and a negative NAO signal in the North Atlantic. Periods of reduced dust deposition may relate to periods of glacier stability or decline and a positive NAO signal. Variation between the cores may relate to changes in atmospheric circulation patterns which determine the area the dust was deposited in. It also may relate to the specific glaciers that were advancing at certain times. We also infer that the smallest dust particles may be Icelandic in origin due to the mixing trend observed through the radiogenic isotope data. This is consistent with the dust peaks in all four cores correlating with an Icelandic glacier advance event identified within the existing literature.

There is strong correlation between the MSW, bromine and dust records in all four cores (Figure 5.5). Between *c*. 9400 and 7400 Cal.yr BP low levels of storminess but high levels of dust are highlighted in the Heldale and Shebster cores. This is indicative of a southerly position of the polar front jet stream and a negative NAO period. The climate then changes with an increase in storminess and a decline in dust levels in the Shebster and Heldale cores. This suggests a change to a wetter and stormier period consistent with a positive NAO period and a storm track positioned over Northern Scotland. This is contrary to the results shown in Kedill's Mires at *c*. 5800 cal.yr BP that is dominated by a very large dust peak and low MSW values. However this is consistent with a jet stream positioned south of the Kedill's Mires latitude and we interpret this data is showing an increase in storm intensity, rather than storm frequency at this site. Between *c.* 5300 and 4000 cal. yr BP, MSW, bromine and dust values show a marked decline at the Shebster site. This is consistent with a decline in the storminess and dust records for the other cores as well. These climatic conditions are all compatible with a period of unstable jet stream position and/or declining jet stream strength. However, throughout this period bromine levels in the Orkney core are very high in comparison to the other cores. At *c.* 4600 Cal. yr BP, there is an increase in Pettawater storminess and dust levels and at *c*. 4300 cal. yr BP there is also an increase in the Kedills Mires bromine and dust record. This may be indicative of more intense storms rather than an overall increase in storminess and increased dust may be indicative of a less positive NAO and a stability in glacier advance. Between *c*. 4000 and 3300 cal. yr BP the Shebster MSW and bromine values are at their lowest for the whole ~8000 year record. Dust values are also very low. This is consistent with a reduction in the Kedills Mires MSW and bromine record as well. We relate these values to a sustained period of relative climate aridity and greatly reduced storminess. Pettawater shows a slight decline in MSW however

maintains high bromine values and there is an increase in the Heldale MSW but much lower bromine values than those seen in the previous zones. We infer that the Heldale and Pettawater cores are therefore showing an increase in storm intensity rather than frequency. This is consistent with higher dust levels in the Kedills Mires and Heldale cores and a stability in the Pettawater dust record as well suggesting a much cooler climate in the higher latitudes during this time period. Between *c*. 3300 and 2400 Cal. yr BP an increase in Br values in all cores indicates the gradual return stormy conditions. Lower MSW values in all cores however may suggest a jet stream positioned south of Northern Scotland. High dust levels in all cores also suggests increased glacier activity in Iceland at this time. Between *c*. 2400 and 1400 cal. yr BP MSW at all cores are increased. The Heldale cores shows high levels of bromine however bromine in the other three cores are reduced suggesting a poleward shift of the westerly storm tracks to a position focused over Orkney and a positive NAO. Shebster and Kedills mires dust levels are very low throughout this period, however, the Heldale and Pettawater dust records are increased which may relate to the changes in atmospheric circulation and therefore deposition patterns. Between *c*. 1400 and 1100 cal. yr BP, the Kedills Mires core shows very high bromine and MSW values whereas the other cores are in decline. This may indicate a northwards shift in the storm tracks over northern Shetland during the Dark Ages Cold Period. Between *c*. 1100 and 800 cal.yr BP, high levels of dust are recorded in the Shebster and Kedills Mires record, however, the Heldale and Pettawater records show reduced dust levels. This period coincides with the Medieval Warm Period and a positive NAO period however there is evidence of glacial advance in Iceland at this time. This period also shows high but variable MSW and bromine levels in the peat record at Shebster. Mire wetness and bromine levels are increasing throughout this period in both the Heldale and Pettawater cores however the Kedills Mires

values are on a downward trend suggesting a southward shift in the storm tracks over Northern Scotland. Between *c*. 800 and 600 cal.yr BP, there are low dust levels in the Shebster and Kedills Mires cores and increasing dust levels in the Pettawater and Heldale cores. This may indicate a period of glacial stability. Between *c*. 600 and 0 cal. yr BP there are high levels of storminess and dust in all cores. This period relates to the Little Ice Age and a negative NAO period however the high levels of storminess found are opposite of what is expected. We infer that the high levels of storminess can be described by an increase in storm intensity rather than storm frequency and the high levels of dust relate to an increase in Icelandic glacier activity.

This thesis has undertaken pioneering research and has therefore established areas of success, failure and opportunities to progress in the future. Micro-XRF analysis was undertaken using the Itrax™ core scanner at the University of Aberystwyth to determine if dust and tephra layers could be identified through faster methods than the established acid digestion and microscopy method. This proved unsuccessful due to the complex nature of peat and the microscopic size of the dust and tephra layers. However this analysis produced a successful bromine curve which has proved essential in describing the changes in storminess across all four study sites. Dust was therefore identified and quantified using a percentage based score method through light microscopy analysis. For Kedills Mires and Heldale, the mineral residue was also weighed using a precision balance in an attempt to test the accuracy of the microscope estimation of abundance. However this method proved unsuccessful as it could not determine the proportions of the larger, heavier particles and smaller, lighter particles. Furthermore this method also could not distinguish between the dust and tephra. Radiogenic isotope analysis was also undertaken to identify the source of

the dust layers. Due to the microscopic quantities present in my cores however, samples had to be bulked together to provide enough material for analysis and incorporated both small and larger particles. For future analysis, a technique which can separate the smaller particles in sufficient quantities for analysis may provide a more accurate result for this analysis.

This thesis has proved that important high-resolution palaeoenvironmental information can be gleaned by analysis of peat accumulations in cold-temperate climates. We believe that these analyses in combination with other established techniques offer a novel and under-used way to examine the climate record of the recent past on a multi-decadal to multi-millennial scale.

References

Abbott, P.M. & Davies, S.M. (2012) Volcanism and the Greenland ice-cores: the tephra record, *Earth-Science Reviews*, 115, pp.173-191.

Ackert, R.P (2009) Patagonian dust machine, *Nature Geoscience*, 2, pp.244-245.

Alexander, L.V. & Tett, S.F.B. (2005) Recent observed changes in severe storms over the United Kingdom and Iceland. *Geophysical Research Letters*, 32, pp.1-4.

Allan, R., Tett, S. & Alexander, L. (2009) Fluctuations in autumn-winter severe storms over the British Isles: 1920 to present. *International Journal of Climatology*, 29, pp.357-371.

Al-Momani, I.F., Momani, K.A., Jaradat, Q.M., Massadeh, A.M., Yousef, Y.A. & Alomary, A.A. (2008) Atmospheric deposition of major and trace elements in Amman, Jordan. *Environmental Monitoring and Assessment,* 136, pp.209–218.

Andresen, C.S. & Bjork, S. (2005) Holocene climate variability in the Denmark Strait region. *Geografiska Annalar,* 1, pp.159-174.

Andresen C.S, Bond G, Kuijpers A, Knutz P.C, Björck S (2005) Holocene climate variability at multidecadal time scales detected by sedimentological indicators in a shelf core NW off Iceland. *Marine Geology*, 214, pp 323-338.

Andrews, J.T., Caseldine, C., Weiner, C. & Hatton, J. (2001) Late Holocene (ca 4ka) marine and terrestrial environmental change in Reykjarfjordur, north Iceland: climate and/or settlement? *Journal of Quaternary Science*, 16, pp.133-143.

Anstey, J.A. & Shepherd, T.G. (2014) High-latitude influence of the quasi-biennial osciallation. *Quarterly Journal of the Royal Meteorological Society*, 140, pp.1-21.

Appenzeller, C., Stocker, T.F. & Anklin, M. (1998) North Atlantic oscillation dynamics recorded in Greenland ice cores. *Science,* 282, pp.446-449.

Arnalds, O. (2010) Dust sources and deposition of aeolian materials in Iceland, Icelandic Agricultural Sciences, 23, pp.3-21.

Arnalds, O., Gisladottir, F.O. & Sigurjonsson, H. (2001) Sandy deserts of Iceland: an overview, Journal of Arid Environments, 47, pp.359-371.

Arnalds, O., Thorarinsdottir, E., Thorsson, J., Waldhauserova, P. & Agustsdottir, A. (2013) An extreme wind erosion event of the fresh Eyjafjallajokull 2010 volcanic ash, Scientific reports, 3, DOI: 10.1038/srep01257.

Arnalds, O., Olafsson, H. & Dagsson-Waldhauserova, P. (2014) Quantification of iron-rich volcanogenic dust emissions and deposition over the ocean from Icelandic dust sources, *Biogeosciences*, 11, pp.6623-6632.

Athanasiadis, P. J., Wallace, J. M. & Wettstein, J. J. (2009) Patterns of jet stream wintertime variability and their relationship to the storm tracks. *Journal of Atmospheric Sciences*, 67, pp.1361-1381.

Auton, C.A., Gillespie, M.R., Lott, G.K., McKervey, J.A., Milodowski, A.E. & Stephenson, M.H. (2005) Palynological and petrological constraints on correlation of Devonian strata across the Dounreay district*,* BGS Commissioned Report CR/05/009. British Geological Survey, Edinburgh.

Ayling, B. F., & McGowan, H.A. (2006) Niveo-eolian sediment deposits in coastal South Victoria Land, Antarctica: Indicators of regional variability in weather and climate, *Article of Antarctic Alpine Research*. 38, pp.313–324.

Bakke, J., Lie, Ø., Dahl, SO., Nesje, A. & Bjune, A.E. (2008) Strength and spatial patterns of the Holocene wintertime westerlies in the NE Atlantic region. *Global and Planetary Change,* 60, pp.28-41.

Baker, A., Hellstrom, J., Kelly, B., Mariethoz, G. & Trouet, V. (2015) A composite annual-resolution stalagmite record of North Atlantic climate over the last three millennia. *Scientific Reports*, 5, doi:10.1038/srep10307.

Balascio, N.L., D'Andrea, W.J. & R. S. Bradley, R.S (2015) Glacier response to North Atlantic climate variability during the Holocene. *Climate of the Past,* 11, pp.1587-1598.

Baldwin, M.P. & Dunkerton, T.J. (2001) Stratospheric harbingers of anomalous weather regimes. *Science,* 294, pp.581-584.

Banner, J. (2003) Radiogenic isotopes: systematics and applications to earth surface processes and chemical stratigraphy, *Earth-Science Reviews*, 65, pp. 141-194.

Barnston, A.G. & Livezey, R.E. (1987) Classification, seasonality and persistence of low-frequency circulation patterns, *Monthly Weather Reviews*, 115, pp.1083-1126.

Basile, I., Grousset, F.E., Revel, M., Petit, J.R., Biscaye, P.E & Barkov, N.I. (1997) Patagonian origin of glacial dust deposited in East Antarctica (Vostok and Dome C) during glacial stages 2, 4 and 6. *Earth and Planetary Science Letters*, 146, pp.573–589.

Bay, R.C, Bramall, N. & Price, P.B. (2004) Bipolar correlation of volcanism with millennial climate change, *PNAS,* 101, pp.6341-6345.

Benedict, J.J., Lee, S. & Feldstein, S. (2004) Synoptic view of the North Atlantic Oscillation. *Journal of Atmospheric Science*, 61, pp.121-144

Björck, G.S., Ingólfsson, Ó., Haflidason, H., Hallsdóttir, M. & Anderson, N.J. (1992) Lake Torfastadavatn: a high resolution record of the North Atlantic Ash zone 1 and the last glacial-interglacial environmental change in Iceland, *Boreas,* 21, pp.15-21.

Blaauw, M., van Geel, B. & van der Plicht, J. (2004) Solar forcing of climatic changes during the mid-Holocene: indications from raised bogs in the Netherlands. *The Holocene*, 14, pp.1-35.

Blaauw, M. & Christen, J.A. (2011) Flexible paleoclimate age-depth models using an autoregressive gamma process. *Bayesian Analysis*, 6, pp.457-474.

Blackburn, M., Methven, J. & Roberts, N. (2008) Large-scale context for the UK floods in summer 2007. *Weather,* 63, pp.280-288.

Blackford, J. (1993) Peat bogs as sources of proxy climatic data: past approaches and future research. *Climate Change and Human Impact on the Landscape*, pp.47-56.

Blechschmidt, A.M., Kristjánsson, J.E., Ólafsson, H., Burkhart, J.F., Hodnebrog, Ø. & Rosenberg, P.D. (2012) Aircraft-based observations and high-resolution simulations of an Icelandic dust storm, *Atmospheric Chemistry and Physics*, 12, pp.10649-10666.

Bond, G., Kromer, B., Beer, J., Muscheler, R., Evans, M.N., Showers, W., Hoffmann, S., Lotti-Bond, R., Hajdas, R. & Bonani, G. (2001) Persistant solar influence on North Atlantic climate during the Holocene, *Science*, 294, pp.2130-2136.

Booth, R.K., S.T. Jackson, S.L. Forman, J.E. Kutzbach, E.A. Bettis, III, Kreig, J. & Wright, D.K. (2005) A severe centennial-scale drought in continental North America 4200 years ago and apparent global linkages. *The Holocene,* 15, pp.321-328.

Boygle, J. (2004) Towards a Holocene tephrochronology for Sweden: geochemistry and correlation with the North Atlantic tephra stratigraphy, *Journal of Quaternary Science*, 19, pp.103-109.

Bradwell, T., Dugmore, A. & Sugden D.E (2006) The Little Ice Age glacier maximum in Iceland and the North Atlantic Oscillation: Evidence from Lambatungnajökull, southeast Iceland, *Boreas,* 35, pp. 61-80.

Briffa, K.R., Jones, P.D, Schweingruber, F.H, Karlen, W. & Shiyatov G. (1996) Tree ring variables as proxy climate indicators: Problems with low-frequency signals, *Climate variations and forcing mechanisms of the last 2000 years,* 141, pp 9-39.

Brönniman, S. (2007) Impact of El-Niño-Southern Oscillation on European climate, *Review of Geophysics,* 45, RG3003, doi: 10.1029/2006RG000199.

Brown, R., Derksen, C. & Wang, L. (2010) A multi-data set analysis of variability and change in Arctic spring snow cover extent, 1967-2008. *Journal of Geophysical Research,* 115, D16111, doi: 10.1029/2010JD013975.

Budikova, D. (2009) Role of Arctic sea ice in global atmospheric circulation: a review. *Global Planetary Change*, 68, pp.149-163

Bullard, J.E. (2012) Contemporary glacigenic inputs to the dust cycle, *Earth Surface Processes and Landforms,* 38, pp.71-89.

Bullard, J.E. & Austin, M.J. (2011) Dust generation on a proglacial flood plain, West Greenland, *Aeolian Research*, 3, pp.43-54.

Bullard, J.E., Harrison, S.P., Baddock, M.C., Drake, N., Gill, T.E., McTainsh, G. & Sun, Y. (2011), Preferential dust sources: A geomorphological classification designed for use in global dust-cycle models, *Journal of Geophysical Research*, 116, DOI: 10.1029/2011JF002061.

Bullard, J.E., Baddock, M., Bradwell, T., Crusius, J., Darlington, E., Gaiero, D., Gassó, S., Gisladottir, G., Hodgkins, R., McCulloch, R., McKenna-Newman, C., Mockford, T., Stewart, H & Thorsteinsson, T. (2016) High-latitude dust in the Earth system, *Reviews of Geophysics*, 54, pp.447–485.

Burningham, H. & French, J. (2013) Is the NAO winter index a relaiable proxy for wind climate and storminess in northwest Europe?, *International Journal of Climatology*, 33, pp.2036-2049.

Carslaw, K.S., Boucher, O., Spracklen, D.V., Mann, G.W., Rae, J.G.L., Woodward, S. & Kulmala, M. (2010) A review of natural aerosol interactions and feedbacks within the Earth system, *Atmospheric Chemistry and Physics*, 10, pp.1701-1737.

Charman, D.J. (2010) Centennial climate variability in the British Isles during the mid-late Holocene. *Quaternary Science Reviews*, 29, pp.1539-1554.

Charman, D.J., Blundell, A., Chiverrell, R.C., Hendon, D. & Langdon, P.G. (2006) Compilation of non-annually resolved Holocene proxy climate records: stacked Holocene peatland palaeo-water table reconstructions from northern Britain. *Quaternary Science Reviews,* 25, pp.336–350.

Charman, D.J., Barber, K.E., Blaauw, M., Langdon, P.G., Mauquoy, D., Daley, T.J., Hughes, P.D.M. & Karofeld, E. (2009) Climate drivers for peatland paleoclimate reconstructions. *The Holocene,* 17, pp.217-227.

Cheng, X., Xie, S-P., Tokinaga, H. & Du, Y. (2011) Interannual Variability of High-Wind Occurrence over the North Atlantic. *Journal of Climate*, 24, p.p.6515-6527.

Clarke, M., Rendell, H. & Tastet, J-P. (2002) Late-Holocene sand invasion and North Atlantic storminess along the Aquitaine coast, southwest France. *The Holocene,* 12, pp.231–238.

Clarke, M.L. & Rendell, H.M. (2006) Effects of storminess, sand supply and the North Atlantic Oscillation on sand invasion and coastal dune accretion in western Portugal, *The Holocene*, 16, pp.341-355

Clarke, M.L. & Rendell, H.M. (2009) The impact of North Atlantic storminess on western European coasts: A review. *Quaternary International*, 195, pp.31-41.

Cohen, J.L., Furtado, J.C., Barlow, M.A., Alexeev, V.A. & Cherry, J.E. (2012) Arctic warming, increasing snow cover and widespread boreal winter cooling. *Environmental Research Letters,* 7, 014007, doi: 10/1088/1748-9326/7/1/014007.

Cook, E., D'Arrigo, R. & Briffa, K. (1998) A reconstruction of the North Atlantic Oscillation using tree-ring chronologies from North America and Europe, *The Holocene,* 8, pp.9-17.

Cowie, J. (2013) Climate Change Biological and Human Aspects second edition

Crusius, J., Schroth, A.W., Gassó, S., Moy, C.M., Levy, R.C. & Gatica, M. (2011) Glacial dust flour storms in the Gulf of Alaska: Hydrologic and meteorological controls and their importance as a source of bioavailable iron. *Geophysical Research Letters,* 38, L06602, doi: 10,1029/2010GL046573.

Cullen, H., D'Arrigo, R., Cook, E. & Mann, M.E. (2001) Multiproxy-based reconstructions of the North Atlantic Oscillation over the past three centuries. *Paleoceanography,* 15, pp.27–39.

Dagsson-Waldhauserova, P., Arnalds, O. & Olafsson, H. (2014) Long-term variability of dust events in Iceland (1949-2011), *Atmospheric Chemistry and Physics*, 14, pp.13411-13422.

Dagsson-Waldhauserova, P., Arnalds, O., Olafsson, H., Skrabalova, L., Sigurdardottir, G., Branis, M., Hladil, J., Skala, R., Navratil, T., Chadimova, L., Von Lowis of Menar, S., Thorsteinsson, T., Carlsen, H. and Jonsdottir, I. (2014) Physical properties of suspended dust during moist and low wind conditions in Iceland, *Icelandic Agricultural Sciences*, 27, pp.25-39.

Davies, S.M., Larsen, G., Wastegård, S., Turney, C.S.M., Hall, V.A., Coyle, L. & Thordarson, T. (2010) Widespread dispersal of Icelandic tephra: how does the Eyjafjöll eruption of 2010 compare to past Icelandic events?, *Journal of Quaternary Science*, 25, pp.605-611.

Davies, S., Lamb, H. & Roberts, S.J. (2015) Micro-XRF core scanning in palaeolimnology: recent developments. Micro-XRF Studies of Sediment Cores : Applications of a non-destructive tool for the environmental sciences. *Developments in Paleoenvironmental Research*, 17, pp.189-226.

Dawson, A.G., Elliot, L., Mayewski, P., Lockett, P., Noone, S., Hickey, K., Holt, T., Wadhams, P. & Foster, I. (2003) Late Holocene North Atlantic climate 'seesaws', storminess changes and Greenland ice sheet (GISP2) paleoclimates. *The Holocene*, 13, pp.381-392.

Dawson, A.G., Hickey, K., Holt, T., Elliot, L., Dawson, S., Foster, I.D.L., Wadhams, P., Jonsdottir, I., Wilkinson, J., McKenna, J., Davis, N.R. & Smith, D.E. (2002) Complex North Atlantic Oscillation (NAO) Index signal of historic North Atlantic storm-track changes, *The Holocene*, 12, pp.363-369.

Dawson, A.G., Elliot, L., Noone, S., Hickey, K., Holt, T., Wadhams, P. & Foster, I. (2004) Historical storminess and climate 'seesaws' in the North Atlantic region, *Marine Geology*, 210, pp.247-259.

Dean, W.E. Jr. (1974) Determination of carbonate and organic matter in calcareous sediments ad sedimentary rocks by loss on ignition: Comparison with other methods. *Journal of Sedimentary Petrology,* Vol 44, pp 242-248.

Delmonte, B., Andersson, P.S., Hansson, M., Schoberg, H., Petit, J.R., Basile-Doelsch, I. & Maggi, V. (2008) Aeolian dust in East Antarctica (EPICA-Dome C and Vostok): Provenance during glacial ages over the last 800 kyr. Geophysical Research Letters, 35, L07703, doi:10.1029/2008GL033382.

Di Rita, F. & Magri, D. (2009) Holocene drought, deforestation and evergreen vegetation development in the central Mediterranean: A 5500 year record from Lago Alimini, Piccolo, Apulia, southeast Italy. *The Holocene*, 19, pp.295-306.

Doran, P. T., McKay, C.P., Clow, G.D., Dana, D.L., Fountain, A.G., Nylen, T. & Lyons, W.B (2002), Valley flood climate observations from the McMurdo Dry Valleys, Antarctica, 1986–2000, *Journal of Geophysical Research*, 107, 4772, doi:10.1029/2001JD002045.

Dugmore, A. (1989) Icelandic volcanic ash in Scotland, *Scottish Geographical Magazine*, 105, pp.168-172.

Dugmore, A. & Newton, A.J. (1992) Thin Tephra Layers in Peat Revealed by X-Radiography, *Journal of Archaeological Science*, 19, pp.163-170.

Dugmore, A.J., Larsen, G., Newton, A.J. & Sugden, D.E. (1992) Geochemical stability of fine-grained silicic tephra layers in Iceland and Scotland. *Journal of Quaternary Science,* 7, pp.173-83.

Dugmore, A.J., Larsen, G. & Newton, A.J. (1995) Seven tephra isochrones in Scotland. *The Holocene*, 5, pp.257-266.

Dugmore, A.J., Cook, G.T., Shore, J.S., Newton, A.J., Edwards, K.J. & Larsen, G. (1995) Radiocarbon Dating Tephra Layers in Britain and Iceland. *Radiocarbon,* 37, pp.379-388.

Dugmore, A.J., Newton, A.J., Edwards, K.J., Larsen, G., Blackford, J.J., Cook, G.T. (1996) Long-distance marker horizons from small-scale eruptions: British tephra deposits from the AD 1510 eruption of Hekla, Iceland, *Journal of Quaternary Science*, 11, pp.511-516

Durant, A.J., Harrison, S.P., Watson, I.M. & Balkanski, Y. (2009) Sensitivity of direct radiative forcing by mineral dust to particle characteristics, *Progress in Physical Geography*, 33, pp.80-102.

Durant, A.J., Bonadonna, C. & Horwell, C.J. (2010) Atmospheric and Environmental Impacts of Volcanic Particulates, *Elements*, 6, pp.235-240.

Eden, D.N. & and Hammond, A.P. (2003) Dust accumulation in the New Zealand region since the last glacial maximum, *Quaternary Science Reviews*, 22, pp.2037-2052.

Farmer, G.L., Barber, D. & Andrews, J. (2003) Provenance of Late Quaternary ice-proximal sediments in the North Atlantic: Nd, Sr and Pb isotopic evidence. *Earth and Planetary Science Letters*, 209, pp.227-243.

Fereday, D.R., Maidens, A., Arribas, A., Scaife, A.A. & Knight, J.R. (2012) Seasonal forecasts of Northern Hemisphere winter 2009/10*. Environmental Research Letters,* 7, 034031.

Feser, F., Barcikowska, M., Krueger, O., Schenk, F., Weisse, R. & Xia, L. (2014) Storminess over the North Atlantic and Northwestern Europe – A Review, *Quarterly Journal of the Royal Meteorological Society*, 141, pp.350-382.

Flowers, G.E., Björnsson, H., Geirsdóttir, Á., Miller, G.H., Black, J.L. & Clarke, G.K.C. (2008) Holocene climate conditions and glacier variation in central Iceland from physical modelling and empirical evidence, *Quaternary Science Reviews*, 27, pp.797-813.

Folland, C.K., Knight, J., Linderholm, H.W., Fereday, D., Ineson, S. & Hurrrell, J.W. (2009) The Summer North Atlantic Osciallation: past, present and future. *Journal of Climate,* 22, pp.1082-1103

Francis, J.A. & Vavrus, S.J. (2012) Evidence linking Arctic amplification to extreme weather in mid-latitudes. *Geophysical Research Letters,* 39, L06801, doi: 10.1029/2012GL051000.

Franzke, C., Lee, S. & Feldstein, S.B. (2004) Is the North Atlantic Oscillation a breaking wave? *Journal of Atmospheric Science,* 64, pp.145-160.

Gaiero, D. M., Probst, J.L., Depetris, P.J., Bidart, S.M. & Leleyter, L. (2003) Iron and other transition metals in Patagonian riverborne and windborne materials: Geochemical control and transport to the southern South Atlantic Ocean, *Geochim. Cosmochim. Acta*, 67, pp.3603–3623, doi:10.1016/s0016-7037(03)00211-4.

Geirsdóttir, Á., Miller, G.H., Axford, Y. & Ólafsdóttir, S. (2009) Holocene and latest Pleistocene climate and glacier fluctuations in Iceland, *Quaternary Science Reviews*, 28, pp.2107-2118.

Genty D., Blamart D., Ghaleb B., Plagnes V., Causse Ch., Bakalowicz M., Melières M.A., Zouari K. & Chkir N. (2006) Timing and Dynamics of the Last Deglaciation from European and

North African 13C stalagmite profiles – Comparison with South-Hemisphere stalagmite records. *Quaternary Science Review*, 25, pp.2118-2142.

Gerber, E.P., Orbe,C. & Polvani, L.M. (2009) Stratospheric influence on the tropospheric circulation revealed by idealized ensemble forecasts. *Geophysical Research Letters,* 36, L24801, doi: 10.1029/2009GL040913.

Gerber, E.P. & Polvani, L.M. (2009) Stratosphere-troposphere coupling in a relatively simple AGCM. *Journal of Climate,* 22, pp.1920-1933.

Gísladóttir, F.O., Arnalds, Ó. & Gísladóttir, G. (2005) The Effect of Landscape and Retreating Glaciers on Wind Erosion in South Iceland, *Land Degradation and Development*, 16, pp.177-187.

Gómara, I., Rodríguez-Fonseca, B., Zurita-Gotor, P. and Pinto, J. (2014) On the relation between explosive cyclones affecting Europe and the North Atlantic Oscillation, *Geophysical Research Letters,* 41, pp. 2182-2190.

Goossens, D. (2000) Dry aeolian dust accumulation in rocky deserts: a medium-term field experiment based on short-term wind tunnel simulations. *Earth Surface Processes and Landforms,* 25, pp.41–57.

Goudie, A. (2009) Dust storms: Recent developments, *Journal of Environmental Management*, 90, pp.89-94.

Grudd, H., Briffa, K.R., Gunnarson, B.E & Linderholm, H.W. (2000) Swedish tree rings provide new evidence in support of a major, widespread environmental disruption in 1628 BC. *Geophysical Research Letters*, 27, pp. 2957-2960.

Grudd, H., Briffa, K.R., Karlén, W., Bartholin, T.S., Jones, P.D. & Kromer, B. (2002) A 7400-year tree-ring chronology in northern Swedish Lapland: natural climatic variability expressed on annual to millennial timescales. *The Holocene,* 12, pp.657-665.

Gudmundsson, H.J. (1997) A review of the Holocene environmental history of Iceland, *Quaternary Science Reviews*, 11, pp.81-92.

Gudmundsson, M., Larsen, G., Höskuldsson, Á. & Gylfason, Á.G. (2008) Volcanic hazards in Iceland, *Jökull*, 58, pp.251-268.

Gudmundsson, M.T., Thordarson, T., Höskuldsson, Á., Larsen, G., Björnsson., Prata, H.F.J., Oddsson, B., Magnússon, E., Högnadóttir, T., Petersen, G.N., Hayward, C.L., Stevenson, J.A. & Jónsdóttir, I. (2012) Ash generation and distribution from the April-May 2010 eruption of Eyjafjallajökull, Iceland. *Scientific Reports,* 2, doi:10.1038/srep00572.

Haflidason H., Eiriksson J. & Van Kreveld, S. (2000) The tephrochronology of Iceland and the North Atlantic region during the Middle and Late Quaternary: a review. *Journal of Quaternary Science*, 15, pp.3-22.

Hall, R., Erdélyi, R., Hanna, E., Jones, J.M. & Scaife, A.A. (2015) Review Drivers of North Atlantic Polar Front jet stream variability, *International Journal of Climatology,* 35, pp.1697-1720.

Hall, V.A., Pilcher, J.R. & McVicker, S.J. (1994) Tephra-linked studies and environmental archaeology, with special reference to Ireland, *Circaea*, 11, pp.17-22.

Hall, V.A. & Pilcher, J.R. (2002) Late-Quaternary Icelandic tephras in Ireland and Great Britain: detection, characterization and usefulness, *The Holocene*, 12, pp.223-230.

Hallsdóttir, M. (1995) On the pre-settlement history of Icelandic vegetation, *Buvísindi,* 9, pp.17-29.

Hanna, E., Cappelen, J., Allan, R., Jónsson, T., Le Blanq, F., Lillington, T. & Hickey, K. (2008) New insights into North European and North Atlantic surface pressure variability, storminess, and related climate change since 1830. *Journal of Climate*, 21, pp.6739-6766.

Hansom, J.D. & Hall. A.M. (2009) Magnitude and frequency of extra-tropical North Atlantic cyclones: A chronology from cliff-top storm deposits. *Quaternary International*, 195, pp 42-52.

Haslett, S.K. & Bryant, E.A. (2007) Reconnaissance of historic (post AD-1000) high-energy deposits along the Atlantic coasts of southwest Britain, Ireland and Brittany, France, *Marine Geology,* 242, pp.207-220.

Hass, H.C. (1996) Northern Europe climate variations during late Holocene: evidence from marine Skagerrak. *Palaeogeography Palaeoclimatology Palaeoecology,* 123, pp.121-145.

Haug, G.H., Hughen, K.A., Sigman, D.M., Petersen, L.C. & Röhl, U. (2001), Southward migration of the Intertropical Convergence Zone through the Holocene. *Science,* 293, pp.1304-1308.

Hayward, C. (2013) High spatial resolution electron probe microanalysis of tephras and melt inclusions without beam-induced chemical modification. *The Holocene*, 22, pp.119–125.

Hickey, K.R. (2001) The Storm of 31 January to 1 February 1953 and its Impact on Scotland, *Scottish Geographical Journal*, 117, pp.283-295.

Hobbs, W. H. (1931) Loess, pebble bands and boulders from the glacial outwash of the Greenland continental glacier. *Journal of Geology*, 39, pp.381–385.

Hobbs, W. H. (1942) Wind: The dominant transporting agent within extramarginal zones to continental glaciers. Journal of Geology, 50, pp.556–559.

Hoskins, B.J., James, I.N. & White, G.H. (1983) The shape, propagation and mean-flow interaction of large scale weather systems, *Journal of Atmospheric Science*, 40, pp.1595-1612.

Hugenholtz, C.H. & and Wolfe, S.A. (2010) Rates and environmental controls of aeolian dust accumulation, Athabasca River Valley, Canadian Rocky Mountains, *Geomorphology,* 121, pp.274-282.

Hughes, P.D.M., Mauquoy, D., Barber, K.E. & Langdon, P.G. (2000) Mire-development pathways and paleoclimatic records from a full Holocene peat archive at Walton Moss, Cumbria, England. *The Holocene,* 10, pp.465-479.

Hunt, J.B., Hill, P.G. (1993) Tephra geochemistry: a discussion of some persistent analytical problems. *The Holocene*, 3, pp.271-278.

Hurrell J.W (1995), Decadal Trends in the North Atlantic Oscillation: Regional Temperatures and Precipitation. *Science*, 269, No.5224, pp 676-679.

Hurrell, J.W. & Deser, C. (2009), North Atlantic climate variability: The role of the North Atlantic Oscillation. *Journal of Marine Systems*, 78, pp.28-41.

Hurrell, J.W., Kushnir, Y., Visbeck, M. & Ottersen G. (2003) The North Atlantic Oscillation, Climatic Significance and Environmental Impact. *AGU Geophysical Monograph,* 134, pp.1-35.

Jackson, M.G., Oskarsson, N., Trønnes, R.G., McMannes, J.F., Oppo, D.W., Grönvold, K., Hart, S.R. & Sachs, J.P. (2005) Holocene loess deposition in Iceland: Evidence for millennial-scale atmosphere-ocean coupling in the North Atlantic, *Geology,* 33, pp.509-512.

Jarvis, S., Croudace, I.W. & Rothwell, R.G. (2015) Parameter Optimization for the ITRAX core scanner, Micro-XRF studies of sediment cores. *Developments in Paleoenvironmetal research*. 17, pp.535-562.

Jickells, T.D., An, Z.N., Andersen, K.K., Baker, A.R., Bergametti, G., Brooks, N., Cao, J.J., Boyd, P.W., Duce, R.A., Hunter, K.A., Kawahata, H., Kubilay, N., laRoche, J., Liss, P.S., Mahowald, N., Prospero, J.M., Ridgwell, A.J., Tegen, I. & Torres, R. (2005) Global Iron Connections Between Desert Dust, Ocean Biogeochemistry and Climate. *Science*, 308, pp.67-71.

Johannesson, T. & Sigurðsson, O. (1998) Interpretation of glacier variations in Iceland, 1930-1995, *Jokull,* 45, pp.27-35.

Johnson, M.S., Meskhidze, N., Kiliyanpilakkil, V.P., Gassó, S. (2011) Understanding the transport of Patagonian dust and its influence on marine biological activity in the South Atlantic Ocean, *Atmospheric Chemistry and Physics*, 11, pp.2487-2502.

Jong, R., Björck, S., Björckman, L. & Clemmensen, L.B. (2006) Storminess variation during the last 6500 years as reconstructed from an ombotrophic peat bog in Halland, Southwest Sweden, Journal of Quaternary Science, 21, pp.905-919.

Jowsey, P.C. (1966) An improved peat sampler. *New Phytologist*, 65, 245-248

Kendon, M. & McCarthy, M. (2015) The UK's wet and stormy winter of 2013/2014. *Weather*, 70, pp.40-47.

Kidston, J., Scaife, A.A., Hardiman, S.C., Mitchell, D.M., Butchart, N., Baldwin, M.P. & Gray, L.J. (2015) Stratospheric influence on tropospheric jet streams, storm tracks and surface weather. *Nature Geoscience*, 8, doi: 10.1038/NGEO2424.

Kirkbride, M.P. (2002) Icelandic climate and glacier fluctuations through the terminus of the "Little Ice Age", *Polar Geography,* 26, pp.116-123.

Kirkbride, M.P. & Dugmore, A.J. (2008) Two millennia of glacier advances from southern Iceland dated by tephrochronology, *Quaternary Research*, 70, pp.398-411.

Knight, J.R., Folland, C.K. & Scaife, A.A. (2006) Climate impacts of the Atlantic Multidecadal Oscillation. *Geophysical Research Letters,* 33, L17706, doi: 10.1029/2006GL026242.

Kocak, M., Kubilay, N., Herut, B. & Nimmo, M. (2005) Dry atmospheric fluxes of trace metals (Al, Fe, Mn, Pb, Cd, Zn, Cu) over the Levantine basin: a refined assessment. *Atmospheric Environment,* 39, pp.7330–7341.

Kockum, P.C.F., Herbert, R.B. & Gislason, S.R. (2006) A diverse ecosystem response to volcanic aerosols, *Chemical Geology*, 231, pp.57-66.

Kodera, K., Yamazaki, K., Chiba, M. & Shibata, K. (1990) Downward propagation of upper stratospheric mean zonal wind perturbation to the troposphere. *Geophysical Research Letters,* 17, pp.1263-1266.

Lacasse, C. (2001) Influence of climate variability on the atmospheric transport of Icelandic tephra in the subpolar North Atlantic, *Global and Planetary Change*, 29, pp.31-55.

Lacasse, C., Karlsdótir, S., Larsen, G., Soosalu, H., Rose, W.I. & Ernst, G.G.J. (2004) Weather radar observations of the Hekla 2000 eruption cloud, Iceland, *Bull Volcanol*, 66, pp.457-473.

Lamb, H.H. (1995) *Climate, History and the Modern World*. Routledge, London

Langdon, P.G. & Barber, K.E. (2004) Snapshots in time: precise correlations of peat-based proxy climate records in Scotland using mid-Holocene tephras, *The Holocene*, 14, pp.21-33.

Langmann, B., Folch, A., Hensch, M. & Matthias, V. (2012) Volcanic ash over Europe during the eruption of Eyjafjallajökull on Iceland, April-May 2010, *Atmospheric Environment*, 48, pp.1-8.

Larsen, G. & Eiríksson, J. (2008) Late Quaternary terrestrial tephrochronology of Iceland – frequency of explosive eruptions, type and volume of tephra deposits, *Journal of Quaternary Science*, 23, pp.109-120.

Larsen, D.J., Miller, G.H., Geirsdóttir, Á. & Thordarson T. (2011) A 3000-year varved record of glacier activity and climate change from the proglacial lake Hvítárvatn, Iceland, *Quaternary Science Reviews*, 30, pp.2715-2731.

Larsen, D.J., Miller, G.H., Geirsdóttir, Á. & Ólafsdóttir, S. (2012) Non-linear Holocene climate evolution in the North Atlantic: a high-resolution, multi-proxy record of glacier activity and environmental change from Hvítárvatn, central Iceland. *Quaternary Science Reviews,* 39, pp.14-25.

Lawrence, C.R. & Neff, J.C. (2009) The contemporary physical and chemical flux of aeolian dust: A synthesis of direct measurements of dust deposition, *Chemical Geology*, 267, pp.46-63.

Li, J., Okin, G.S., Alvarez, L. & Epstein, H. (2008) Effects of wind erosion on the spatial heterogeneity of soil nutrients in two desert grassland communities. *Biogeochemistry,* 88, pp.73–88.

Lozano, I., Devoy, R.J.N., May, W. & Andersen, U. (2004), Storminess and vulnerability along the Atlantic coastlines of Europe: analysis of storm records and of greenhouse gases induced climate scenario. *Marine geology*, 210, pp.205-225.

MacKintosh, A.N., Dugmore, A. & Hubbard A.L. (2002) Holocene climatic changes in Iceland: evidence from modelling glacier length fluctuations at Sólheimajökull, *Quaternary International,* 91, pp.39-52.

Mann, M.E. & Jones, P.D. (2003). Global surface temperatures over the past two millennia. *Geophysical Research Letters,* 30, 10.1029/2003GL017814.

Martinez-Garcia, A. & Winkler, G. (2014) Iron fertilization in the glacial ocean, *PAGES Magazine*, 22, pp.82-83.

Martini, I.P, Martinez-Cortizas, A. & Chesworth, W. (2006) Peatlands: a concise guide to the volume, *Peatlands: Evolution and Records of Environmental and Climate Changes,* pp.1-14.

Mauri, A., Davis, B.A.S., Collins, P.M. & Kaplan, J.O (2014) The influence of atmospheric circulation on the mid-Holocene climate of Europe: a data-model comparison. *Climates of the Past*, 10, pp.1925–1938.

Mayewski, P.A., Rohling, E.E., Stager, J.C., Karlen, W., Maasch, K.A., Meeker, L.D., Meyerson, E.A., Gasse, F., van Kreveld, S., Holmgren, K., Lee-Thorp, J., Rosqvist, G., Rack, F., Staubwasser, M., Schneider, R.R. & Steig, E.J. (2004) Holocene climate variability. *Quaternary Research,* 62, 243–255.

McDermott, F., Mattey, D.P. & Hawkesworth, C. (2001) Centennial-scale Holocene climate variability revealed by a high-resolution speleothem delta O-18 record from SW Ireland. *Science*, 294, pp. 1328–1331.

McGee, D., Broecker, W. & Winckler, G. (2010) Gustiness: The driver of glacial dustiness?, *Quaternary Science Reviews*, 29, pp.2340-2350.

McGowan, H. A. (1997) Meteorological controls on wind erosion during foehn wind events in the eastern Southern Alps, New Zealand. Canadian Journal of Earth Science, 34, pp.1477–1485.

McGowan, H. A., Sturman, A.P. & Owens, I.F. (1996) Aeolian dust transport and deposition by foehn winds in alpine environment, Lake Tekapo, New Zealand, *Geomorphology*, 15, pp.135–146

McIlvenny, J.D., Muller, F.L.L. & Dawson, A. (2013) A 7600-year sedimentary record of climatic instability in Dunnet Nay, North Scotland. *Marine Geology,* 335, pp.100-113.

McTainsh, G. & Strong, C. (2007) The role of aeolian dust in ecosystems, *Geomorphology*, 89, pp 39-54.

Meeker, L.D. & Mayewski, P.A. (2002) A 1400-year high-resolution record of atmospheric circulation over the North Atlantic and Asia. *Holocene*, 12, 257 – 266.

Metcalfe, S.E., Barron, J.A. & Davies, S.J. (2015) The Holocene history of the North American Monsoon: known knowns and known unknowns in understanding its spatial and temporal complexity. *Quaternary Science Reviews,* 120, pp. 1-27.

Moore, G.W.K., Renfrew, I.A. & Pickart, R.S. (2013) Multidecadal mobility of the North Atlantic Osciallation. *Journal of Climate,* 26, pp.2453-2466.

Msadek, R., Frankignoul, C. & Li, L.Z.X. (2011) Mechanisms of the atmospheric response to North Atlantic multidecadal variability: a model study. *Climate Dynamics*, 36, pp.1255-1276.

Mysak, L. & Venegas, S. (1998) Decadal climate oscillations in the Arctic: a new feedback loop for atmospheric-ice-ocean interactions, *Geophysical Research Letters,* 25, pp.3607-3610.

Newton, A.J. (1996) Tephrabase: A Tephrochronological Database. Quaternary Newsletter. 78, pp.8-13.

Neuman, C.M. (2003) Effects of Temperature and Humidity upon the Entrainment of Sedimentary Particles by Wind. *Boundary-Layer Meteorology*. 108, pp.61-89.

North Greenland Ice Core Project members. (2004) High-resolution record of Northern Hemisphere climate extending into the last interglacial period. *Nature*, 431, pp.147-151.

O`Brien, S.R., Mayewski, P.A., Meeker, L.D., Meese, D.A., Twickler, M.S. & Whitlow, S.I. (1995) Complexity of Holocene climate as reconstructed from a Greenland ice core. *Science,* 270, pp.1962–1964.

Ólafsdóttir, S. (2010) Holocene marine and lacustrine paleoclimate and paleomagnetic records from Iceland: land-sea correlations. PhD. Thesis, University of Iceland

Óladóttir, B., Larsen, G. & Sigmarsson, S. (2012) Deciphering eruption history and magmatic processes from tephra in Iceland, *Jökull*, 62, pp.21-38.

Ólafsdóttir, S., Jennings, A.E, Geirsdóttir, Á., Andrews, J.T. & Miller, G.H. (2010) Holocene variability of the North Atlantic Irminger current on the south and northwest shelf of Iceland. *Marine Micropaleontology,* 77, pp.101-118.

Oldfield, F., Batterbee, R.W., Boyle, J.F., Cameron, N.G., Davis, B., Evershed, R.P., McGovern, A.D., Jones, V. & Thompson, R. (2010) Terrestrial and aquatic ecosystem responses to the late Hllocene climate change recorded in the sediments of Lochan Uaine, Cairngorms, Scotland. *Quaternary Science Reviews,* 29, pp.1040-1054.

Olsen, J., Anderson, N.J., & Knudsen, M.F. (2012) Variability of the North Atlantic Oscillation over the past 5200 years. *Nature Geoscience.* 5, pp.808–812.

Oppo, D.W., McManus, J.F. & Cullen, J.L. (2003) Palaeo-oceanography: deepwater variability in the Holocene epoch, *Nature,* 422, pp.277-278.

Orme, L.C., Davies, S.J. & Duller, G.A.T. (2015) Reconstructed centennial variability of Late Holocene storminess from Cors Fochno, Wales, UK. *Journal of Quaternary Science*. 30, pp.478-488.

Orme, L.C., Reinhardt, L., Jones, R.T., Charman, D.J., Barkwith, A. & Ellis, M.A. (2016) Aeolian sediment reconstructions from the Scottish Outer Hebrides: Late Holocene storminess and the role of the North Atlantic Oscillation. *Quaternary Science Reviews,* 132, pp.15-25.

Panetta, R.L. & Held, I.M. (1988) Barolinic eddy fluxes in a one-dimensional model of quasi-geostrophic turbulence, *Journal of Atmospheric Science,* 45, pp.3354-3365.

Payne, R.J. (2012) Volcanic impacts on peatland microbial communities: A tephropalaeoecological hypothesis-test, *Quaternary International*, 268, pp.98-110.

Payne, R. & Blackford, J. (2008) Distal volcanic impacts on peatlands: palaeoecological evidence from Alaska, *Quaternary Science Reviews*, 27, pp.2012-2030.

Penland, C. & Hartten, L. (2014) Stochastic forcing of north tropical Atlantic sea surface temperatures by the North Atlantic Oscillation. *Geophysical Research Letters,* 41, pp. 2126-2132.

Pilcher, J.R., Hall, V.A. McCormac, F.G. (1996) An outline tephrochronology for the Holocene of the north of Ireland, *Journal of Quaternary Science*, 11, pp.485-494.

Pinto, J.G., Zacharias, S., Fink, A.H., Leckebusch, G.C. & Ulbrich, U. (2009) Factors contributing to the development of extreme North Atlantic cyclones and their relationship with the NAO. *Climate Dynamics*. 32, pp.711-737.

Prospero, J.M. (1996) Saharan dust transport over the North Atlantic Ocean and Mediterranean: an overview. *The Impact of Desert Dust Across the Mediterranean*, pp.133-151.

Prospero, J.M., Ginoux, P., Torres, O., Nicholson, S.E. & Gill, T.E. (2002) Environmental characterization of global sources of atmospheric soil dust identified with the nimbus 7 total ozone mapping spectrometer, *Reviews of Geophysics*, 40, DOI: 10.1029/2000RG00009.

Prospero, J.M., Bullard, J.E. & Hodgkins, R. (2012) High-Latitude Dust over the North Atlantic: Inputs from Icelandic Proglacial Dust Storms, *Science*, 335, pp.1078-1082.

Reimer, P.J., Bard, E., Bayliss, A.J., Beck, W., Blackwell, P.G., Bronk Ramsey, C., Buck C.E., Cheng, H., Edwards, R.L., Friedrich, M., Grootes, P.M., Guilderson, T.P., Haflidason, H., Hajdas, I., Hatté, C., Heaton, T.J., Hoffmann, D.L., Hogg, A.G., Hughen, K.A., Kaiser, K.F., Kromer, B., Manning, S.W., Niu, M., Reimer, R.W., Richards, D.A., Marian Scott, E.M., Southon, J.R., Staff, R.A., Turney, C.S.M. and Van der Plicht, J. (2013) INTCAL13 and MARINE13 Radiocarbon Age Calibration Curves 0–50,000 years cal. BP. *Radiocarbon*. 55, pp. 1869–1887.

Rex, D.F. (1950) Blocking action of the middle troposphere and its affect upon regional climate. 1. An aerological study of blocking action. *Tellus,* 2, pp.196-211.

Robock, A. & Mao, J. (1992) Winter warming from large volcanic eruptions. *Geophysical Research Letters,* 12, pp.2405-2408.

Sabatier, P., Dezileau, L. & Colin, C. (2012) 7000 years of paleostorm activity in the NW Mediterranean Sea in response to Holocene climate events. *Quaternary Research,* 77, pp.1–11.

Schepanski, K., Merkel, U. & Tegen, I. (2014) Mineral dust: Meteorological controls and climate impacts, *PAGES magazine*, 22, pp.62-63.

Schroth, A.W., Crusius, J., Sholkovitz, E.R. & Bostick, B.C. (2009) Iron solubility driven by speciation in dust sources to the ocean, *Nature Geoscience*, 2, pp.337-340.

Screen, J.A. & Simmonds, I. (2010) Increasing fall-winter energy loss from the Arctic Ocean and its role in Arctic temperature amplification. *Geophysical Research Letters,* 37, L16707, doi: 10.1029/2010GL044136.

Sigurjónsson, H., Gísladóttir, F. & Arnalds, Ó. (1999) Rala Report – Fjölrit Rala 201, Agricultural Research Institute.

Smith, D., Scaife, A., Eade, R. & Knight, J. (2014) Seasonal to decadal prediction of the winter North Atlantic Oscillation: emerging capability and future prospects. *Quarterly Journal of the Royal Meteorological Society,* DOI: 10.1002/qj.2479.

Solanki, S.K., Usoskin, I.G., Kromer, B., Schüssler, M. & Beer, J. (2004) Unusual activity of the Sun during recent decades compared to the previous 11,000 years, *Nature,* 431, pp.1084-1087.

Solomina, O.N., Bradley, R.S., Hodgson, D.A., Ivy-Ochs, S., Jomelli, V., MacKintosh, A.N., Nesje, A., Owen, L.A., Wanner, H., Wiles, G.C. & Young, N.E. (2015) Holocene glacier fluctuations, *Quaternary Science Reviews*, 111, pp.9-34.

Sommerville A.A, Hansom J.D, Sanderson D.C.W, Housley R.A (2003), Optically stimulated luminescence dating of large storm events in Northern Scotland. *Quaternary Science Reviews*, 22, pp.1085-1092.

Stenchikov, G., Hamilton, K., Stouffer, R.J., Robock, A., Ramaswamy, V., Santer, B. Grf, H-F. (2006) Arctic Oscillation response to volcanic eruptions in the IPCC AR4 climate models, Journal of Geophysical Research, 111, D07107, doi: 10.1029/2005JD006286.

Stevenson, J.A., Millington, S.C., Beckett, F.M., Swindles, G.T, & Thordarson, T. (2015) Big grains go far: understanding the discrepancy between tephrochronology and satellite infrared measurements of volcanic ash. *Atmospheric Measurement Techniques*, 8, pp.2069–2091

Stötter, J., Wastl, M., Caseldine, C. & Haberle, T. (1999) Holocene paleoclimatec reconstruction in northern Iceland: approaches and results, *Quaternary Science Reviews,* 18, pp.457-474.

Stroeve, J.C., Markus, T., Boisvert, L., Miller, J. & Barrett, A. (2014) Changes in Arctic melt season and implications for sea ice loss, *Geophysical Research Letters,* 41, pp.1216-1225.

Strong, C. & Magnusdottir, G. (2008) Tropospheric Rossby Wave Breaking and the NAO/NAM. *American Meteorological Society,* pp.2861-2876.

Stuiver, M. & Reimer, P. J. (1993) Extended 14C database and revised CALIB radiocarbon calibration program. *Radiocarbon,* 35, pp.215-230.

Stuut, J-B. & Prins, M. (2014) The significance of particle size of long-range transported mineral dust, *PAGES Magazine*, 22, pp.70-71.

Sugden, D.E., McCulloch, R.D., Bory, A.J.-M. & Hein, A.S. (2009) Influence of Patagonian glaciers on Antarctic dust deposition during the last glacial period, *Nature Geoscience*, 2, pp.281-285.

Swindles, G., Plunkett, G. & Roe, H.M. (2007) A delayed response to solar forcing at 2800 cal.BP: multiproxy evidence from three Irish peatlands. *The Holocene,* 17, pp.177-182.

Swindles, G.T., Lawson, I.T., Savov, I.P., Connor, C.B. & Plunkett, G. (2011) A 7000 yr perspective on volcanic ash clouds affecting northern Europe, *Geology*, 39, pp.887-890.

Tegen, I. & Fung, I. (1994) Modeling of mineral dust in the atmosphere—sources, transport, and optical-thickness. *Journal of Geophysical Research-Atmospheres,* 99, pp.22897–22914.

Tegen, I., Harrison, S.P., Kohfeld, K.E., Engelstaedter, S. & Werner, M. (2002) Emission of soil dust aerosol: anthropogenic contribution and future changes. *Geochimica Et Cosmochimica Acta,* 66, A766-A766.

Terry, R.D. & Chilinger, G.V. (1995) Comparison chart for estimating percentage composition, *Journal of Sedimentary Petrography*, 25, pp.229-234.

Thevenon, F., Chiaradia, M., Adatte, T., Hueglin, C & Poté, J. (2012) Characterization of Modern and Fossil Mineral Dust Transported to High Altitude in the Western Alps: Saharan Sources and Transport Patterns, *Advances in Meteorology*, pp. 1-14.

Thompson, D.W.J. & Wallace, J.M. (1998) The Arctic Oscillation signature in the wintertime geopotential height and temperature fields, *Geophysical Research Letters*, 25, pp.1297-1300.

Thompson, D.W.J. & Wallace, J.M. (2001) Regional Climate Impacts of the Northern Hemisphere Annular Mode, *Science*, 293, pp.85-89.

Thorncroft, C.D., Hoskins, B.J. & McIntyre, M.E. (1993) Two paradigms of baroclinic life-cycle behaviour. *Quarterly Journal of the Royal Meteorological Society,* 119, pp.17-55.

Thorsteinsson, T., Gísladóttir, G., Bullard, J. & McTainsh, G. (2011) Dust Storm Contributions to Airborne Particulate Matter in Reykjavík, Iceland, *Atmospheric Environment*, 45, pp.5924–5933.

Tipping, R., Bradley, R., Sanders, J., McCulloch, R. & Wilson, R. (2012), Moments of crisis: climate change in Scottish prehistory. *Society of Antiquaries of Scotland*, 142, pp.9-25.

Tisdall, E., McCulloch, R., Sanderson, D., Simpson, I. & Woodward, N. (2013) Living with sand: A record of landscape change and storminess during the Bronze and Iron Ages Orkney, Scotland, *Quaternary International*, 308-309, pp.205-215

Trouet, V., Scourse, J.D. & Raible, C.C. (2012) North Atlantic storminess and Atlantic Meriodional Overturning Circulation during the last millennium: Reconciling contradictory proxy records of NAO variability. *Global and Planetary Change*, 84-85, pp.48-55.

Turner, T.E., Swindles, G.T. & Roucoux, K.H. (2014) Late Holocene ecohydrological and carbon dynamics of a UK raised bog: impact of human activity and climate change. *Quaternary Science Reviews*, 84, pp.65-85.

Valis, G.K. & Gerber, E.P. (2008) Local and hemispheric dynamics of the North Atlantic Oscillation, annular patterns and zonal index, *Dynamics of Atmosphere and Oceans,* 44, pp.184-212

Vliet-Lanoë, B., Penaud, A.I., Hénaff, A., Delacourt, C., Fernane, A., Goslin, J.R.M., Hallégouët, B. & Le Cornec, E. (2014) Middle-to-late Holocene storminess in Brittany (NW France): Part II – the chronology of events and climate forcing, *Holocene*, 24, pp.296-310.

Walczak, I.W., Baldini, J.U.L., Baldini, L.M., McDermott, F., Marsden, S., Standish, C.D., Richards, D.A., Andreo, B. & Slater, J. (2015) Reconstructing high-resolution climate using CT scanning of unsectioned stalagmites: A case study identifying the mid-Holocene onset of the Mediterranean climate in southern Iberia. *Quaternary Science Reviews,* 127, pp.117-128.

Walker, S., Thirlwall, M.F., Strachan, R.A. & Bird, A.F. (2015) Evidence from Rb–Sr mineral ages for multiple orogenic events in the Caledonides of Shetland, Scotland, *Journal of the Geological Society,* 173, pp. 1-15.

Wang, X.L., Zwiers, F.W., Swail, V.R. & Feng, Y. (2009) Trends and variability of storminess in the Northeast Atlantic region. 1874-2007. *Climate Dynamics*, 33, pp.1179-1195.

Wang, T., Surge, D. & Mithen, S. (2012) Seasonal temperature variability of the Neoglacial (3300–2500 BP) and Roman Warm Period (2500–1600 BP) reconstructed from oxygen isotope ratios of limpet shells (Patella vulgata), Northwest Scotland. *Palaeogeography, Palaeoclimatology, Palaeoecology,* 317–318, pp.104–113.

Wanner, H., Brönnimann, S., Casty, C., Gyalistras, D., Luterbacher, J., Schmutz, C., Stephenson, D.B. and Xoplaki E. (2001) North Atlantic Oscillation – Concepts and Studies. *Surveys in Geophysics*, 22, pp.321-382.

Wastegård, S. & Davies, S.M. (2009) An overview of distal tephrochronology in northern Europe during the last 1000 years, *Journal of Quaternary Science*, 24, pp.500-512.

Weinzierl, B., Sauer, D., Minikin, A., Reitebuch, O., Dahlkötter, F., Mayer, B., Emde, C., Tegen, I., Gasteiger, J., Petzold, A., Veira, A., Kueppers, U. & Schumann, U. (2012) On the visibility of airborne volcanic ash and mineral dust from the pilot's perspective in flight, *Physics and Chemistry of the Earth*, 45-46, pp.87-102.

William, G.P. (1979) Planetary circulations: 2. The Jovian quasi-geostrophic regime. *Journal of Atmospheric Science*, 36, pp.932-968.

Winckler, G. & Mahowald, N. (2014) DICE: Dust impact on climate and environment, *PAGES magazine*, 22, pp.61.

Woollings, T. (2011) Ocean effects of blocking. *Science*, 334, pp.612-613.

Woollings, T. & Blackburn, M. (2012) The North Atlantic jet stream under climate change and its relation to the NAO and EA patterns. *Journal of Climate*, 25, pp.886-902.

Woollings, T., Hoskins, B., Blackburn, M. & Berrisford, P. (2008) A new Rossby wave-breaking interpretation of the North Atlantic Oscillation. *Journal of the Atmospheric Sciences,* 65, pp.609-626.

Woollings, T., Czuchnicki, C. & Franzke, C. (2014) Twentieth century North Atlantic jet variability, *Quarterly Journal of the Royal Meteorological Society.* 140, pp.783-791.

Woollings, T., Hannachi, A. & Hoskins, B. (2010) Variability of the North Atlantic eddy-driven jet stream. *Quarterly journal of the Royal Meteorological Society*, 136, pp.856-868.

Appendix 1 -Tephrochronology

Shebster

Sample	Na2O	MgO	Al2O3	K2O	CaO	FeO	SiO2	P2O5	TiO2	MnO	Total
SHEB 340-346 no1	4.562	0.0274	12.5854	2.6954	1.3209	1.9234	75.9807	0.0086	0.0741	0.0749	99.2528
SHEB 340-346 no2	4.8277	0.022	12.5014	2.8955	1.3058	2.0016	72.7301	0.0047	0.0942	0.0773	96.4603
SHEB 340-346 no3	5.0554	0.0886	13.8156	2.1437	3.1539	5.3416	68.4287	0.0214	0.2549	0.2073	98.511
SHEB 340-346 no4	4.5812	0.0164	12.8537	2.9226	1.205	1.9028	73.7714	0.0086	0.0944	0.0754	97.4315
SHEB 340-346 no5	4.2926	0.0402	11.8268	2.9867	1.0043	1.9696	73.7569	0.0064	0.0872	0.0749	96.0457
SHEB 340-346 no6	4.541	0.0037	12.6884	2.8214	1.2574	1.7645	73.0026	0.0086	0.0925	0.072	96.2523
SHEB 340-346 no7	5.1161	0.3842	16.524	1.7122	4.8654	5.6158	64.5211	0.2712	0.7126	0.1661	99.8888
SHEB 340-346 no8	5.0852	0.124	27.8492	0.177	11.5556	0.6408	54.6456	0.012	0.1254	-0.0035	100.2113
SHEB 340-346 no10	5.0341	0.2817	12.6969	1.2837	2.6002	3.2145	69.6512	0.0812	0.2881	0.1101	95.2418
SHEB 340-346 no11	4.4462	0.0385	12.7086	3.2877	1.3043	1.1623	77.098	0.0072	0.0774	0.0409	100.1712
SHEB 340-346 no13	4.4789	0.008	11.8754	3.2438	1.2105	1.9142	72.9149	0.0152	0.094	0.0909	95.846
SHEB 340-346 no14	5.626	0.4654	14.2674	1.1418	4.143	6.4853	67.1795	0.1207	0.4094	0.1808	100.0192
SHEB 340-346 no15	4.2644	0.0434	12.5985	2.7749	0.9971	1.5358	73.8746	0.0111	0.0882	0.0814	96.2693
SHEB 340-346 no16	4.9186	0.0027	12.7017	2.6435	1.2636	1.7108	74.2053	0.0085	0.0853	0.0765	97.6166
SHEB 340-346 no17	4.6913	0.0165	12.2878	3.0834	1.1002	1.8905	74.4324	0.0096	0.0982	0.096	97.7059
SHEB 340-346 no18	4.7622	0.0086	12.9235	2.8344	1.3037	2.073	74.4908	0.0067	0.0779	0.0832	98.5639
SHEB 340-346 no19	4.6462	0.0104	12.3856	2.7451	1.3106	1.679	72.5465	0.0059	0.0894	0.0751	95.4938
SHEB 340-346 no20	4.7729	-0.0275	12.7873	2.761	1.2725	2.0086	73.4059	0.0053	0.0817	0.0755	97.1431
SHEB 340-346 no21	4.9216	-0.0055	13.0496	2.9704	1.3955	2.0689	75.4176	0.0108	0.0962	0.0834	100.0084

340-346 (Hekla 4)

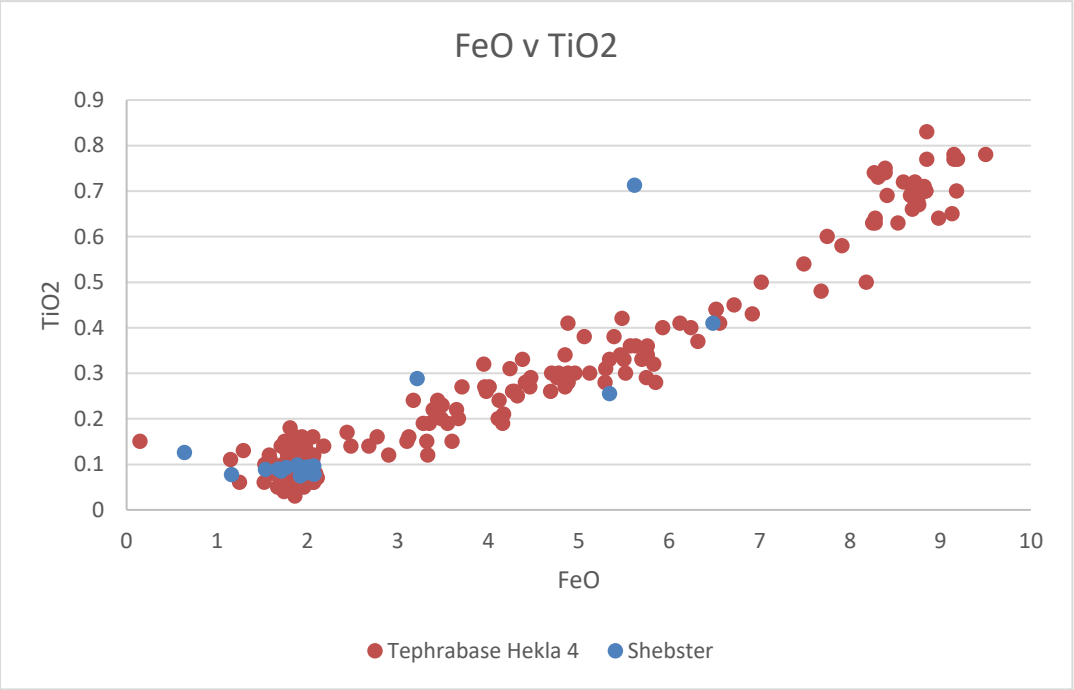

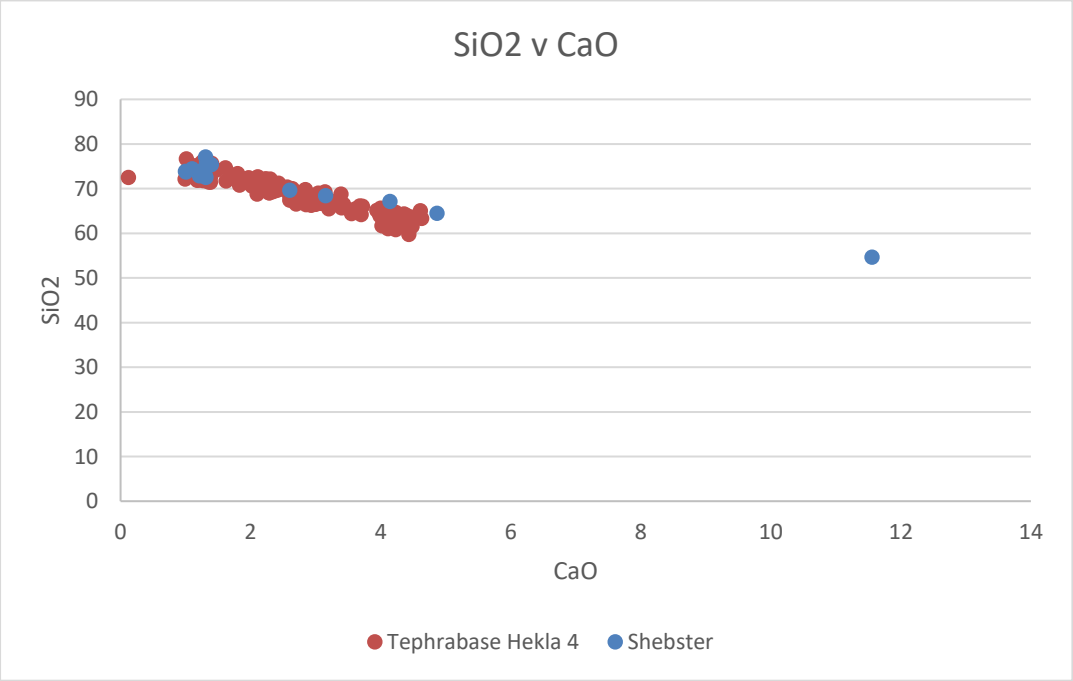

Heldale

Sample	Na2O	MgO	Al2O3	FeO	K2O	CaO	SiO2	P2O5	TiO2	MnO	Total
HD 179-183 002	5.1146	0.0403	14.0613	4.3427	2.4836	2.4681	69.6994	0.0355	0.2605	0.1677	98.6738
HD 179-183 003	4.5196	0.0232	12.5373	2.1466	2.8223	1.2961	72.1431	0.0074	0.0986	0.0925	95.6868
HD 179-183 004	4.9934	0.0474	13.6273	4.3308	2.3015	2.4783	69.4899	0.028	0.2521	0.1721	97.7208
HD 179-183 005	4.7038	-0.0047	12.7167	1.6899	2.9968	1.1947	73.1058	0.0049	0.0961	0.079	96.5831
HD 179-183 006	4.7317	0.0372	12.8324	2.211	2.7113	1.2662	73.1444	0.0034	0.0926	0.0797	97.1098
HD 179-183 007	5.1251	0.0214	13.992	4.3891	2.4642	2.6227	69.7249	0.0293	0.2456	0.1672	98.7813
HD 179-183 008	4.7701	0.0372	12.7289	1.7988	2.9204	1.1453	73.4145	0.0102	0.1179	0.0656	97.0089
HD 179-183 009	4.7747	-0.0256	12.8483	1.9384	2.6873	1.3063	73.1533	0.0033	0.0983	0.0811	96.8653
HD 179-183 010	4.8687	0.0188	14.1123	3.7107	2.4572	2.2132	70.9988	0.03	0.2133	0.1492	98.7721
HD 179-183 011	4.542	-0.007	13.3539	2.9976	2.573	1.8903	70.8631	0.0137	0.1582	0.1019	96.4866
HD 179-183 012	4.5317	0.644	14.6002	9.3909	1.6511	4.4242	63.0384	0.2307	0.7149	0.3001	99.526
HD 179-183 021	4.7871	0.1927	14.2792	7.1264	1.9543	3.5858	65.6344	0.0914	0.455	0.2549	98.3611
HD 179-183 023	4.7173	0.0209	12.4396	2.019	2.8767	1.3483	72.8885	0.0113	0.0944	0.0783	96.4944
HD 179-183 024	5.0766	0.0188	13.6241	3.4282	2.4977	2.1071	71.027	0.0203	0.1896	0.1227	98.1123
HD 179-183 026	4.6416	-0.0023	12.7239	1.9382	2.9447	1.2913	73.2587	0.0115	0.0961	0.0817	96.9854
HD 179-183 027	4.8142	0.1309	14.2293	5.3443	2.2048	3.0042	67.6882	0.0486	0.3264	0.2083	97.9991
HD 179-183 028	4.8227	0.0349	13.3461	2.1014	2.963	1.3159	74.1497	0.011	0.1083	0.0933	98.9463
HD 179-183 029	5.074	0.0867	13.5668	3.2713	2.4978	2.0199	72.9124	0.0275	0.1512	0.1018	99.7094
HD 179-183 030	4.7702	0.1309	14.1771	5.3559	2.2334	3.0445	67.1183	0.063	0.3382	0.2112	97.4429
HD 179-183 031	4.7684	-0.0069	13.051	1.7521	2.9299	1.3958	74.6078	0.0118	0.0972	0.0647	98.6716
HD 258-261 001	5.3477	0.1685	13.7216	2.1551	4.6296	0.6422	70.5207	0.0241	0.1962	0.0595	97.4651
HD 258-261 002	5.2078	0.1449	13.8407	2.1563	4.8632	0.7191	69.9655	0.0324	0.1894	0.0607	97.1801
HD 258-261 003	5.5768	0.178	13.6106	2.1535	4.6045	0.8026	69.8542	0.0264	0.2188	0.0711	97.0965
HD 258-261 004	4.4878	0.1977	14.1683	2.3337	4.4683	0.8582	69.8419	0.0408	0.252	0.0778	96.7265
HD 258-261 005	5.0034	0.1602	13.8105	2.0123	4.4792	0.6791	70.478	0.014	0.1915	0.0681	96.8962
HD 258-261 006	4.9628	0.1374	13.5687	1.903	4.5251	0.7404	69.9146	0.0229	0.1878	0.0679	96.0305
HD 258-261 008	5.1968	0.1329	13.8414	2.1451	4.5078	0.6803	70.0225	0.0133	0.1925	0.0624	96.795
HD 258-261 009	5.0284	0.1816	13.741	2.0588	4.4475	0.6489	69.3616	0.0219	0.1967	0.0695	95.756
HD 258-261 010	5.3642	0.1443	13.7971	1.9624	4.4524	0.6919	70.8145	0.0231	0.1931	0.0521	97.4951
HD 258-261 011	5.2433	0.1795	14.077	2.2248	4.4183	0.6757	70.8782	0.0137	0.2096	0.0594	97.9795
HD 270-272 001	4.4258	0.0254	13.148	1.6979	2.8263	1.3802	75.4757	0.0046	0.0808	0.0652	99.1297
HD 270-272 002	4.3843	0.0324	12.3268	1.7713	2.7137	1.3682	73.7376	0.0144	0.0819	0.0775	96.5083
HD 270-272 003	4.4565	0.0278	12.2558	1.7375	2.7288	1.2196	73.4029	-0.0046	0.0736	0.0698	95.9677
HD 270-272 005	4.5113	0.0347	12.2922	1.5901	2.6286	1.4402	73.5714	0.0021	0.0876	0.068	96.2262
HD 270-272 006	4.6253	0.0371	12.2517	1.6874	2.7049	1.3073	73.9067	0.0085	0.0769	0.0661	96.6718
HD 270-272 007	4.2955	0.0185	12.2208	1.768	2.8564	1.3394	73.4886	0.0146	0.0797	0.0758	96.1573
HD 270-272 008	4.3888	0.0484	12.6195	1.73	2.749	1.2338	73.7641	0.0079	0.0794	0.0621	96.683
HD 270-272 009	4.3774	0.0139	12.165	1.6987	2.756	1.2541	73.3038	0.0038	0.0838	0.0636	95.72
HD 270-272 011	4.2687	0.0578	12.6195	1.4411	2.6985	1.3197	74.0214	0.0162	0.0719	0.0714	96.5861
HD 270-272 012	4.1816	0.0023	12.3472	1.6304	2.6864	1.2827	73.4574	0.0041	0.0777	0.071	95.7409

179-183 cm (Hekla 4)

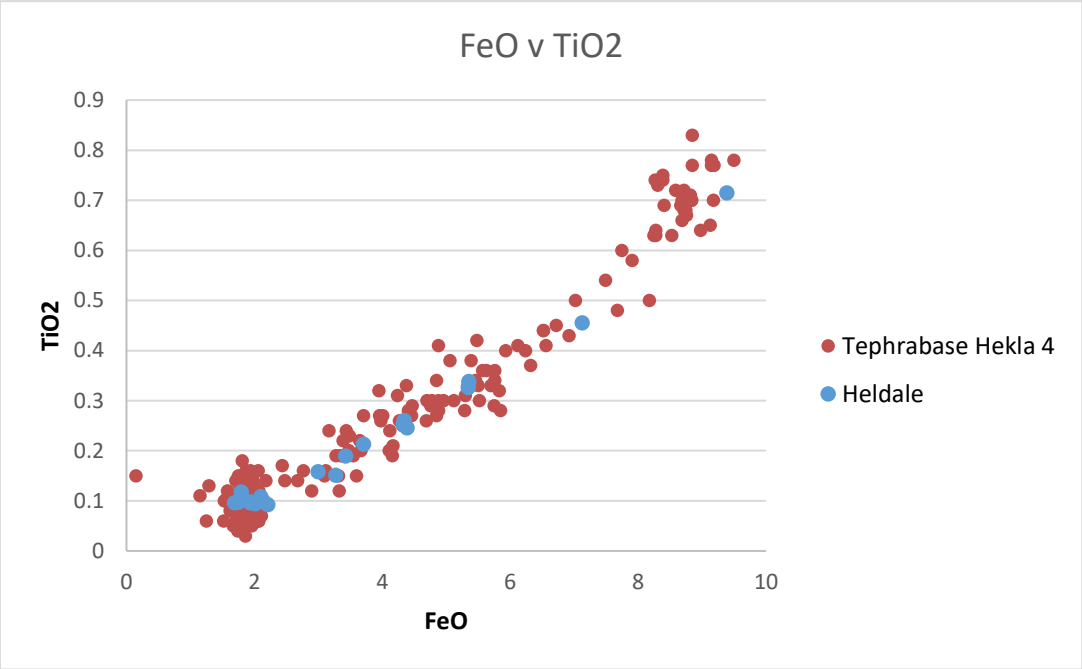

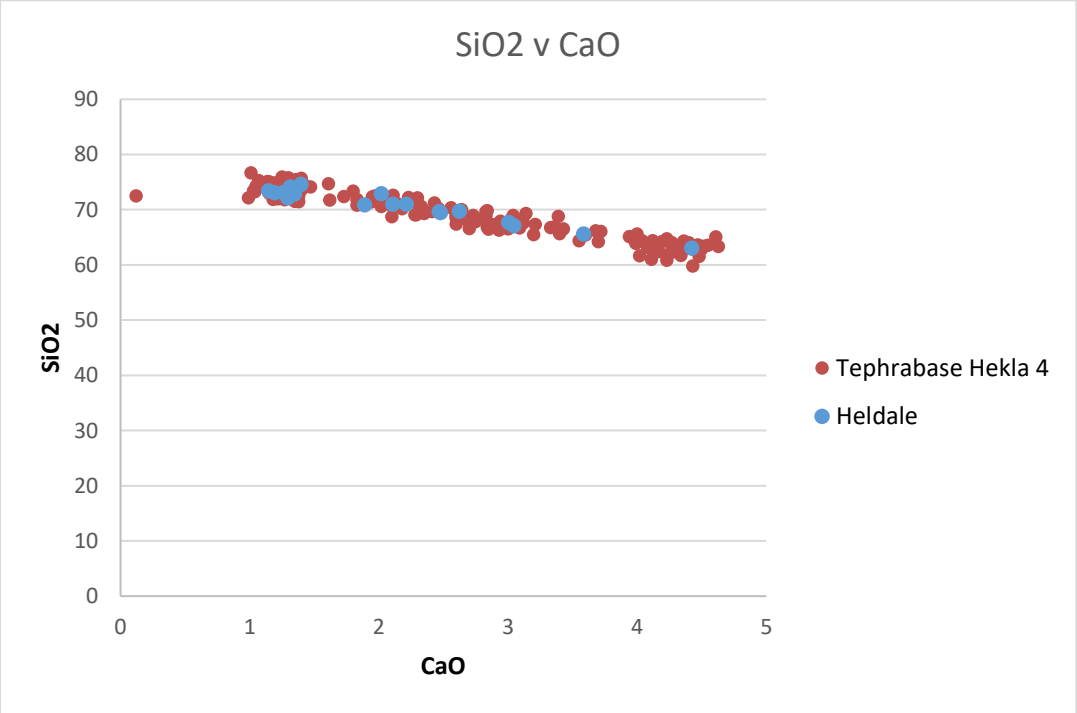

258-261 cm (Hoy)

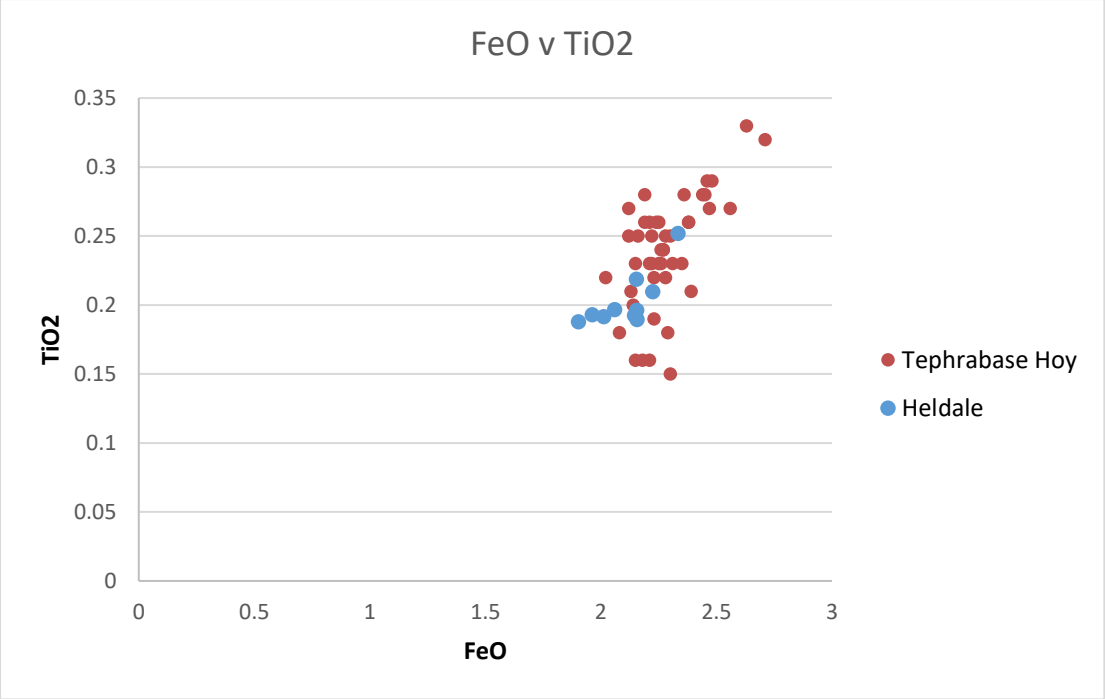

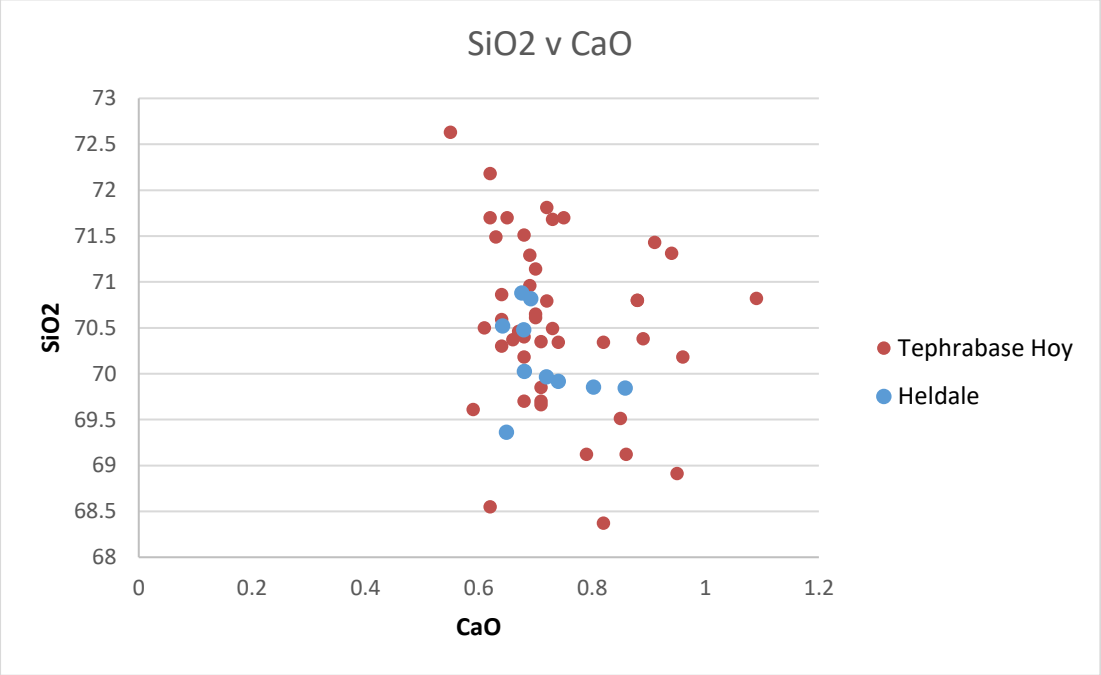

270-272 cm (Lairg A)

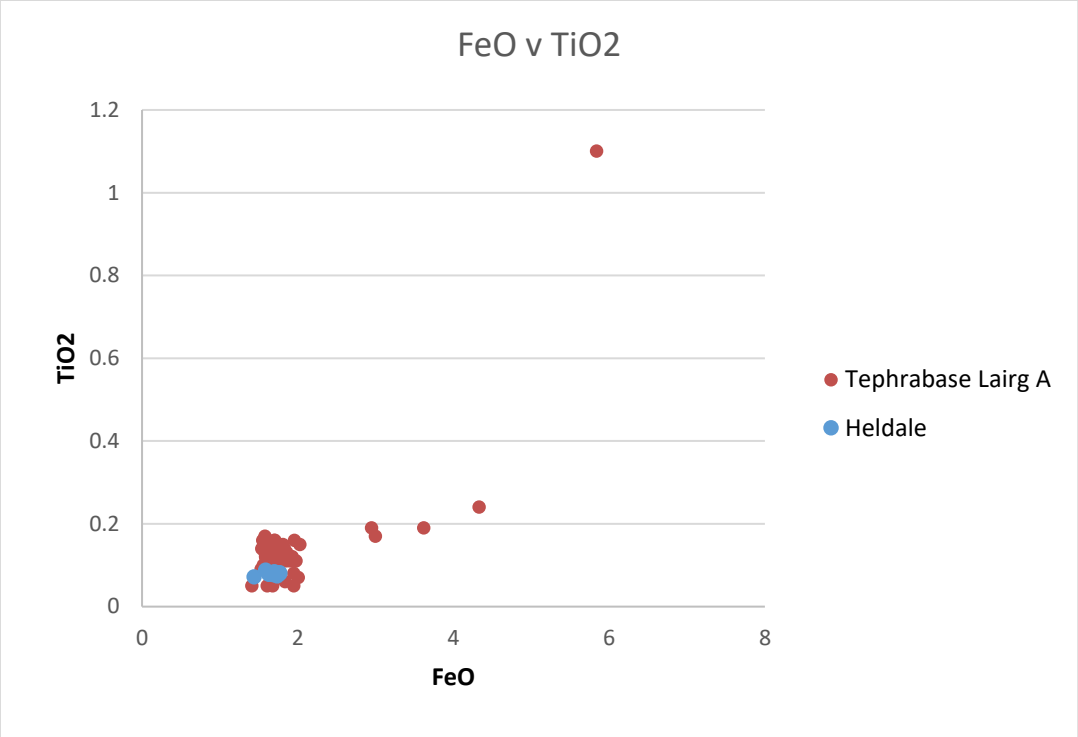

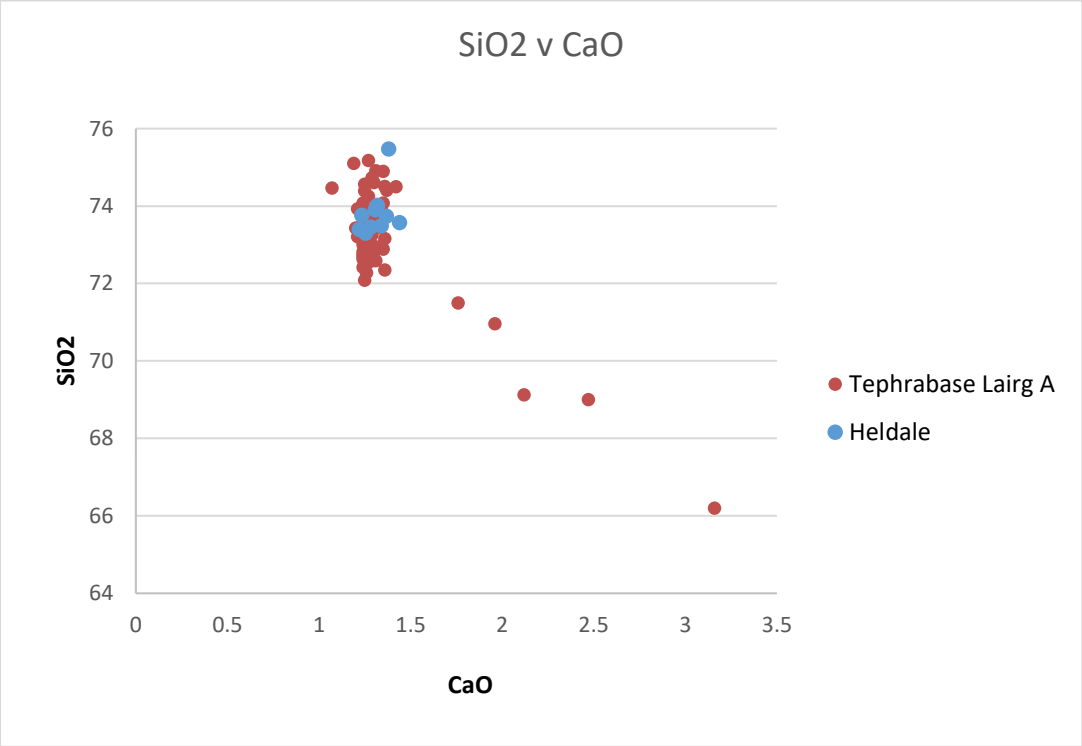

Pettawater

Sample	Na2O	MgO	Al2O3	FeO	K2O	CaO	SiO2	P2O5	TiO2	MnO	Total
PW62-66 001	5.353	0.0165	13.5525	3.2156	3.5082	0.9696	73.2501	0.0173	0.24	0.0979	100.2206
PW62-66 002	5.3678	0.033	12.6948	3.148	3.457	0.9358	72.0374	0.0168	0.2432	0.1094	98.0431
PW62-66 003	5.4849	0	12.9891	3.2081	3.4854	1.0498	73.1662	0.0149	0.2398	0.1078	99.7459
PW62-66 004	5.7752	0.0449	13.129	3.3075	3.4402	0.993	73.0752	0.0084	0.2344	0.0972	100.1051
PW62-66 005	5.5353	0.0424	13.3775	3.2599	3.4088	0.9581	72.0736	0.0146	0.2245	0.0979	98.9925
PW62-66 006	5.5468	0.0094	14.0873	3.0965	3.4332	1.0901	71.2919	0.0112	0.2318	0.1092	98.9074
PW62-66 007	5.6252	0.0283	13.1636	3.3208	3.4519	0.9738	73.5468	0.0215	0.2349	0.1062	100.4731
PW62-66 008	5.1252	0.0258	14.0563	3.1835	3.4193	1.0485	70.9222	0.0178	0.2301	0.107	98.1358
PW62-66 009	5.3864	0.0471	13.2118	3.1677	3.3713	1.0396	70.9909	0.0134	0.2234	0.0969	97.5484
PW62-66 010	5.69	0.0189	13.0977	3.3172	3.294	1.0711	71.9899	0.0173	0.2291	0.0931	98.8183
PW224-6 001	4.2074	0.1079	12.678	1.5665	3.8722	0.751	74.2119	0.0107	0.1516	0.04	97.5971
PW224-6 002	3.8283	1.1865	13.2282	6.2591	1.557	4.1575	66.9783	0.3066	1.0336	0.1529	98.6881
PW224-6 003	3.8917	0.4219	12.6411	3.6785	2.0606	2.2574	73.0689	0.09	0.5125	0.0935	98.716
PW224-6 004	4.433	0.6235	16.8522	4.6189	1.6693	4.7761	64.3861	0.2419	0.6499	0.1181	98.3689
PW224-6 006	3.9231	0.3331	12.774	3.6854	2.7758	1.8534	73.8996	0.0856	0.5718	0.0859	99.9876
PW224-6 007	4.0478	0.3897	12.6036	3.7685	2.132	2.3912	74.5121	0.0987	0.5175	0.1065	100.5678
PW224-6 009	4.3766	0.0299	12.4659	1.6301	3.7138	0.7423	74.8339	0.0062	0.1366	0.0493	97.9847
PW224-6 010	4.4557	0.0808	12.6317	1.9606	3.6889	0.9253	74.7754	0.0153	0.1696	0.048	98.7514
PW224-6 011	4.2228	0.3982	12.7424	3.6708	2.0185	2.3806	74.0654	0.0825	0.5225	0.085	100.1886
PW 288-298 002	4.8952	0.4766	15.0808	5.5377	2.0442	3.2588	68.5617	0.1105	0.445	0.1721	100.5826
PW 288-298 004	4.837	0.5868	15.3875	5.6455	2.1213	3.316	68.3012	0.1006	0.4231	0.157	100.8761
PW 288-298 005	4.7936	0.1569	14.2035	2.9268	2.4724	2.0422	72.2348	0.0201	0.1827	0.0965	99.1294
PW 288-298 006	4.7267	0.4945	15.2672	5.5391	2.1315	3.2045	67.6663	0.1076	0.4413	0.1763	99.755
PW 288-298 007	4.91	0.0985	13.8925	3.0779	2.6834	1.9614	72.0884	0.0266	0.185	0.1092	99.0327
PW 288-298 008	4.9328	0.1495	13.5944	2.6924	2.4511	1.9532	73.1804	0.0301	0.1823	0.0987	99.2649
PW 288-298 009	4.7182	0.5413	15.1895	5.6509	1.9397	3.1999	67.1748	0.1209	0.4478	0.1732	99.1563
PW288-98 002	4.7357	0.5312	14.5764	5.2741	2.0492	3.2877	66.284	0.0937	0.445	0.1705	97.4475
PW288-98 003	4.873	0.506	15.3499	5.6676	1.9512	3.3827	65.983	0.1062	0.4645	0.1801	98.4642
PW288-98 004	5.238	0.2066	13.8438	2.8518	2.5649	1.9761	70.7	0.0268	0.1876	0.1013	97.6969
PW288-98 008	4.772	0.4912	14.4398	5.308	1.9634	3.2523	65.966	0.1153	0.4685	0.167	96.9437
PW288-98 010	4.5156	0.0325	13.3141	1.9253	2.8317	1.2893	71.6945	0.0092	0.0887	0.0743	95.7752
PW288-98 012	4.666	0.539	14.6663	5.4043	2.0994	3.4562	66.6195	0.1161	0.4381	0.1605	98.1654
PW 300-312 001	4.8665	0.1639	13.822	2.8192	2.5373	1.8153	72.29	0.029	0.1747	0.0949	98.6127
PW 300-312 002	0.2374	0.0906	13.2373	2.3869	9.806	1.8285	68.146	0.0214	0.1794	0.0886	96.022
PW 300-312 003	4.7935	0.1468	13.8809	2.8521	2.4924	1.8981	72.5393	0.0225	0.1764	0.0856	98.8874
PW300-12 004	4.5344	0.5629	14.9466	5.145	1.956	3.2862	66.6726	0.1014	0.4494	0.1696	97.8241
PW300-12 005	4.8681	0.2185	14.255	4.1317	2.4284	2.3847	70.7637	0.0498	0.2742	0.1368	99.5109
PW300-12 006	4.9096	0.152	13.49	2.9225	2.4743	1.8882	70.8787	0.0185	0.189	0.101	97.0238
PW300-12 007	4.6661	0.5212	14.5487	5.7944	1.9332	3.0995	67.3479	0.1	0.4148	0.1669	98.5925
PW300-12 008	5.09	0.126	14.8474	2.4451	2.2734	2.1151	72.3273	0.022	0.1592	0.0753	99.4807
PW300-12 009	5.0252	0.5861	14.9398	5.9381	2.0481	3.2919	67.4851	0.0967	0.4631	0.1762	100.0502
PW300-12 011	4.4684	0.5103	14.3751	5.3195	1.942	3.0858	64.7752	0.0953	0.4302	0.1756	95.1774
PW300-12 012	4.6098	0.3549	13.8805	4.6928	2.0011	2.9898	68.0423	0.0775	0.3874	0.1592	97.1953
PW300-12 013	4.8418	0.105	13.6229	2.832	2.4342	1.7616	72.0144	0.0183	0.1844	0.085	97.8998
PW 326-338 002	4.6211	0.0208	12.9461	1.9268	2.8791	1.274	73.6664	0.0118	0.0969	0.0861	97.5291
PW326-338 002	5.0332	0.0282	13.8777	3.3362	2.4562	2.1415	71.284	0.0247	0.196	0.1354	98.5132
PW326-338 003	4.7299	0.3745	14.8823	7.1145	1.9501	3.6972	65.3464	0.1111	0.5027	0.2548	98.9635
PW326-338 005	4.9181	0.0232	13.2828	2.1462	2.7502	1.5265	71.9371	0.013	0.1367	0.1	96.8339
PW326-338 006	4.7382	0.0232	13.0104	1.7988	3.0706	1.2464	74.292	0.0112	0.0884	0.0893	98.3685
PW326-338 007	4.7761	0.0255	12.5157	1.9709	2.8353	1.3279	73.353	0.0079	0.0923	0.0924	96.997
PW326-338 008	4.3878	0.0139	12.8947	1.9628	2.662	1.2001	72.5328	0.0131	0.0967	0.0792	95.8431
PW326-338 009	4.627	0.0116	12.6556	1.6777	2.8345	1.2206	73.5643	0.0179	0.0898	0.0811	96.7803
PW326-338 010	4.7797	0.0488	13.0768	1.9921	2.7608	1.2986	73.8485	0.0007	0.0869	0.0816	97.9747
PW326-338 012	4.594	0.0394	12.4955	1.9259	2.8987	1.2917	73.5265	0.0008	0.0953	0.0801	96.9478

62- 66 cm (Oraefajokull 1362)

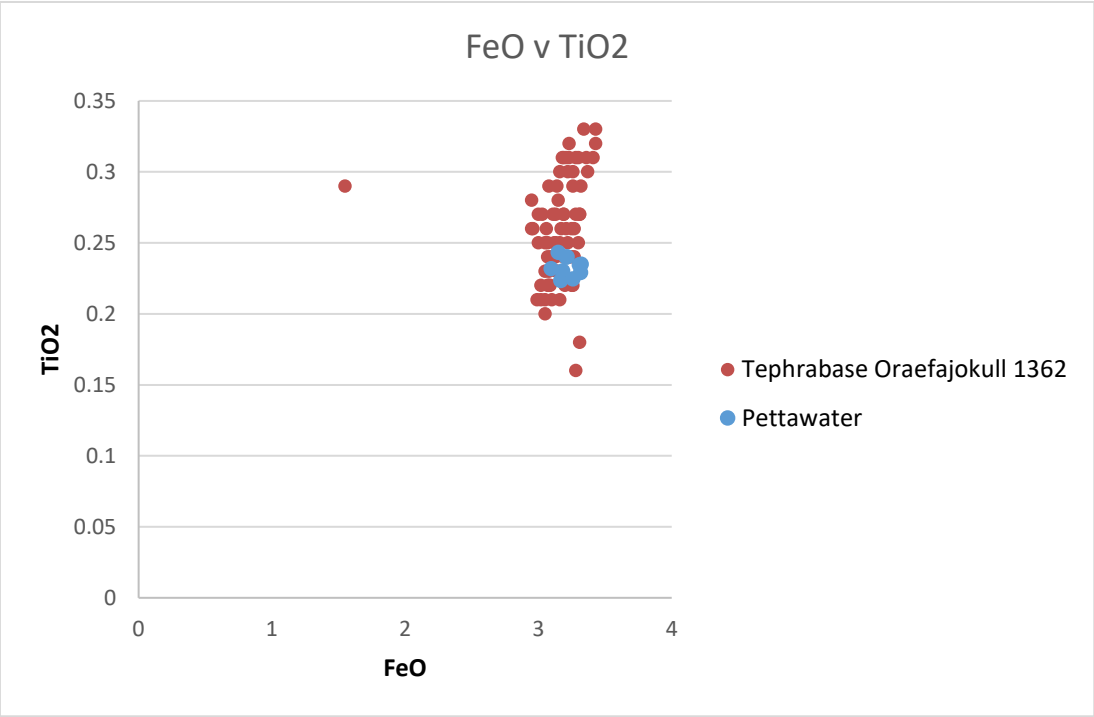

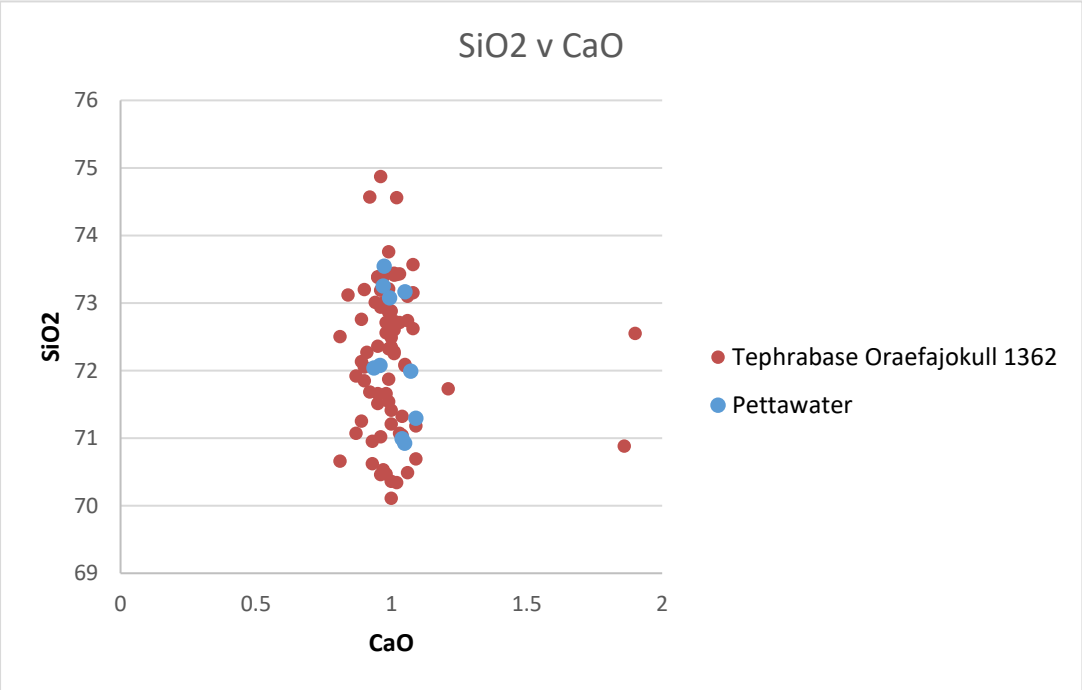

224-226 cm (Glen Garry)

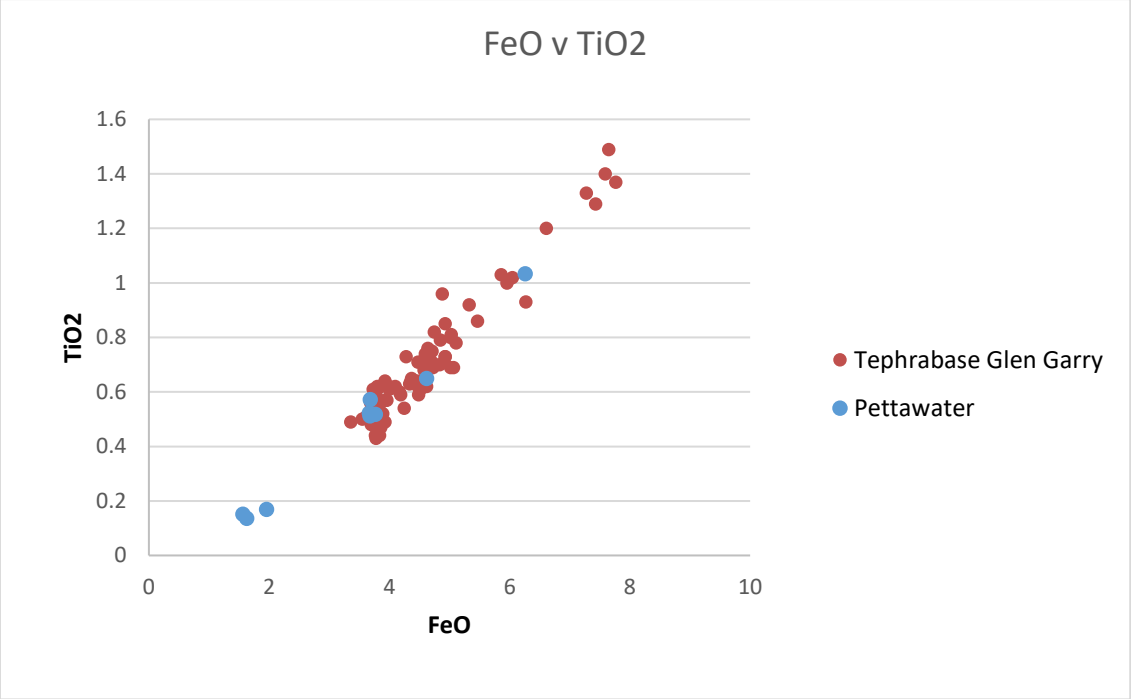

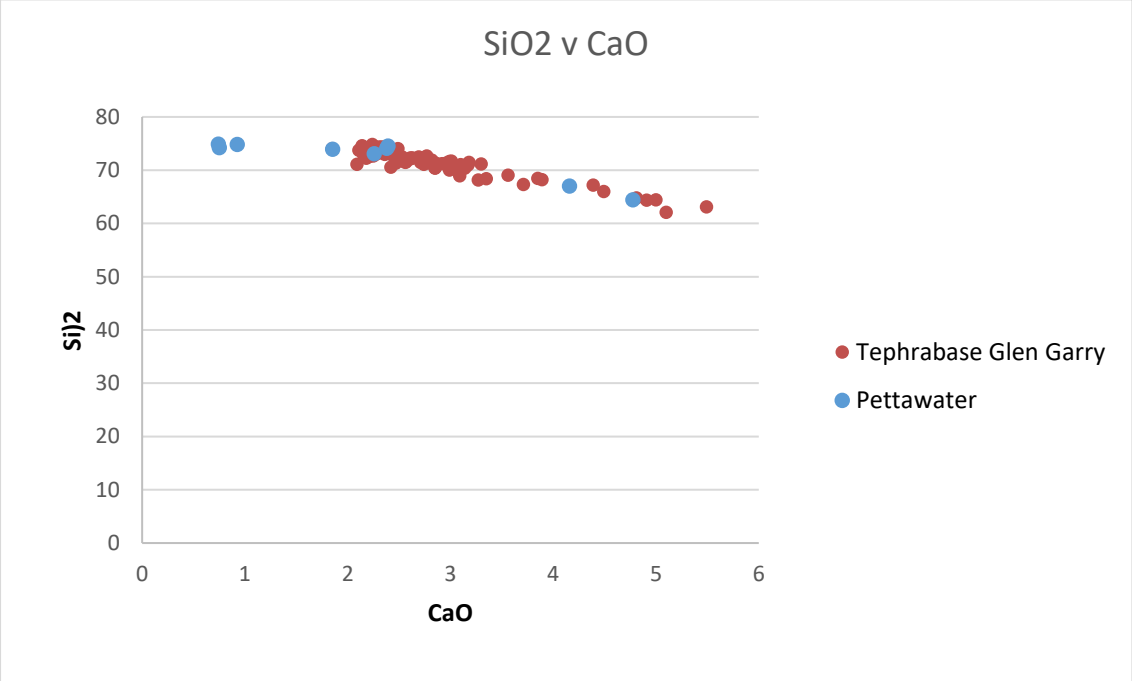

288-298 cm (Hekla 3)

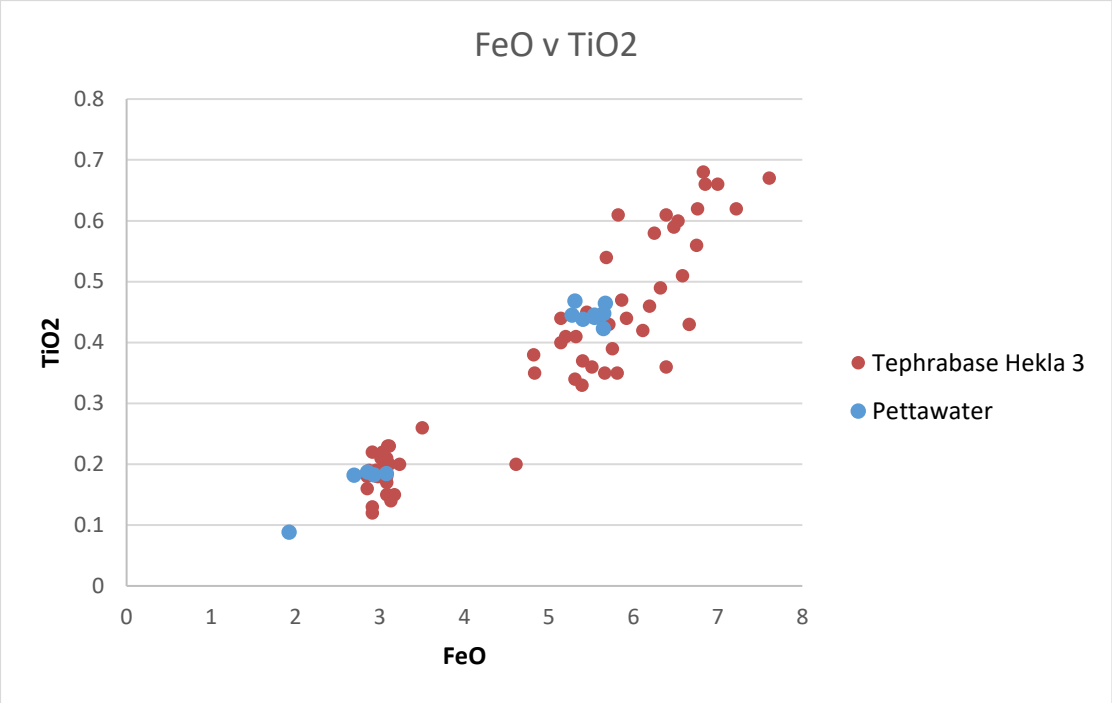

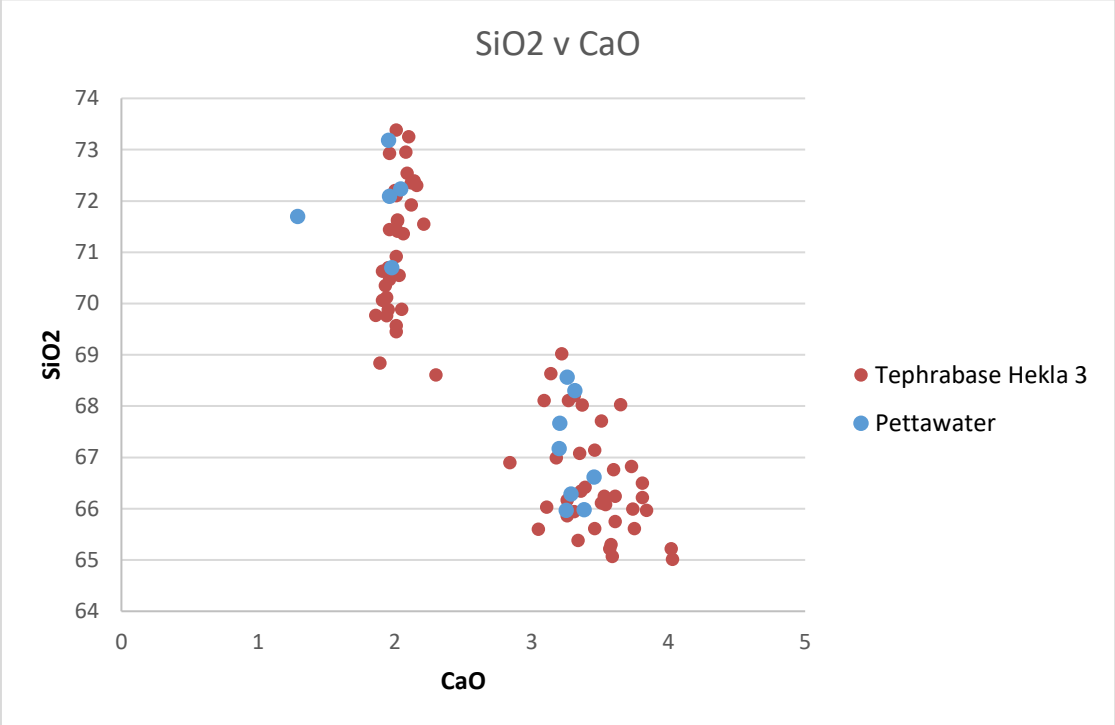

300-312 cm (Kebister)

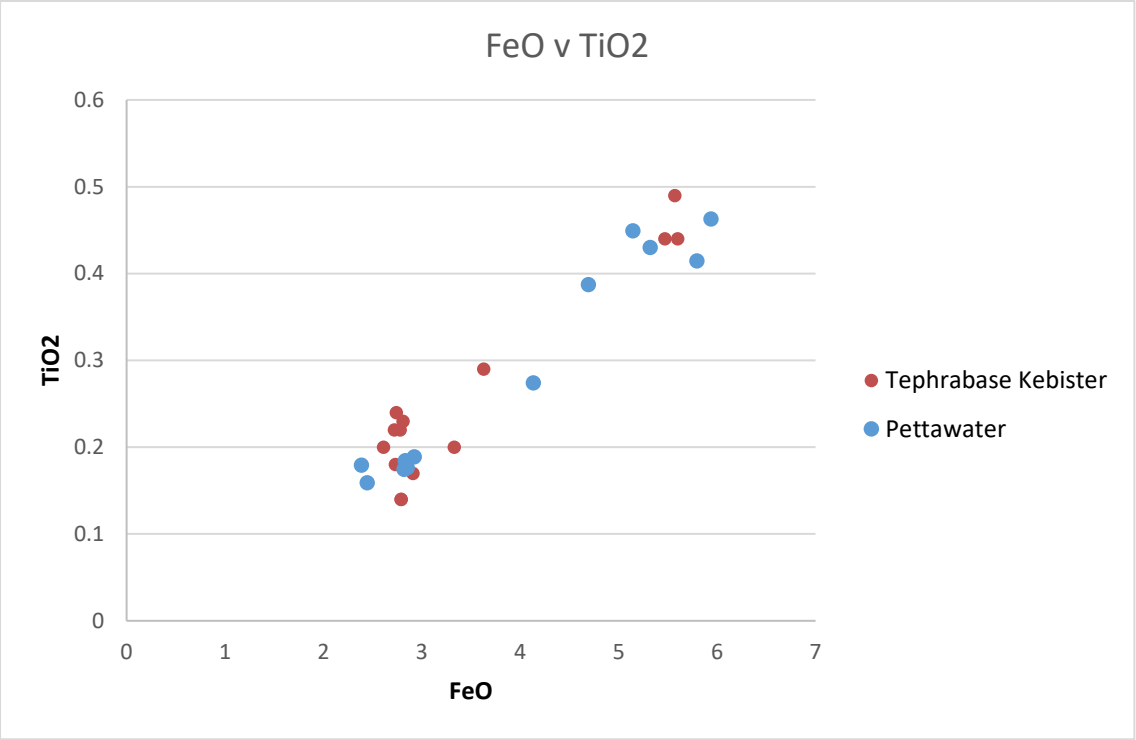

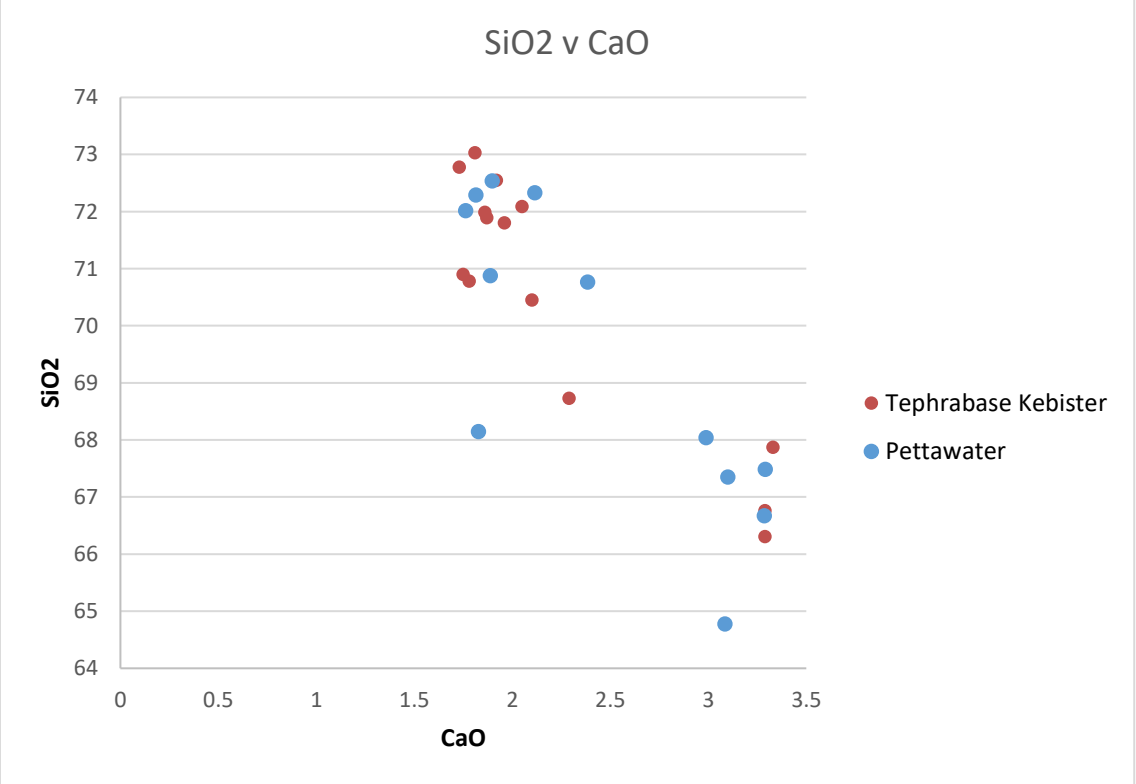

326-338 cm (Hekla 4)

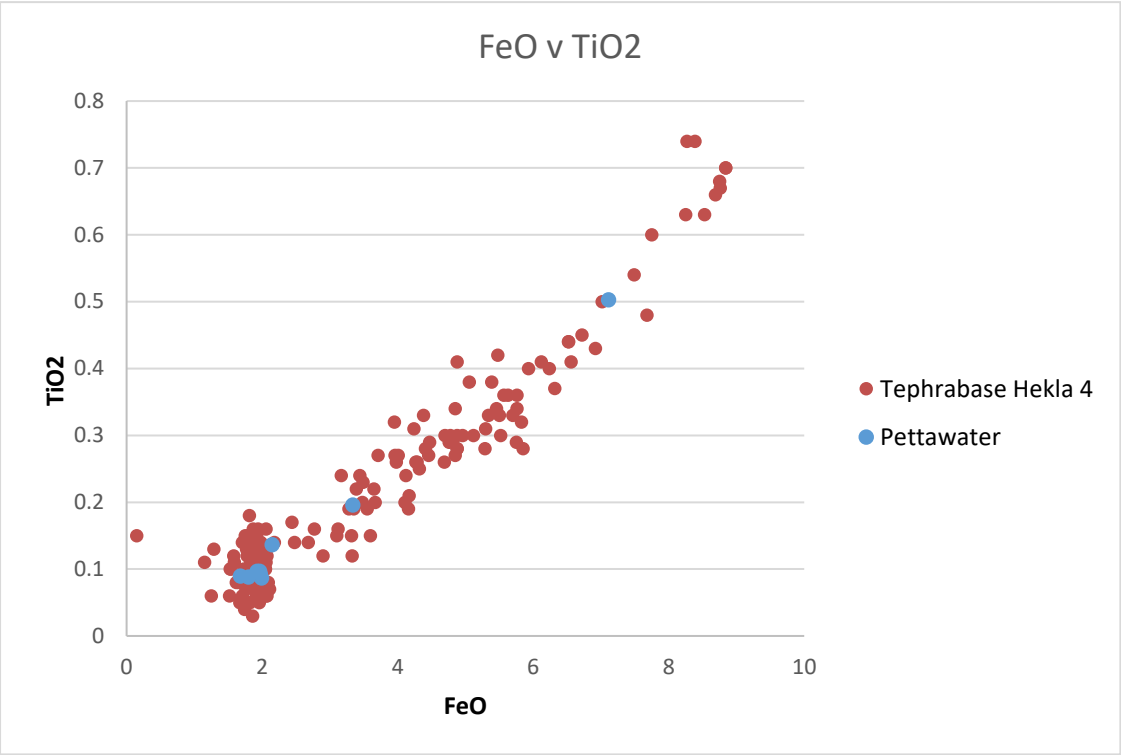

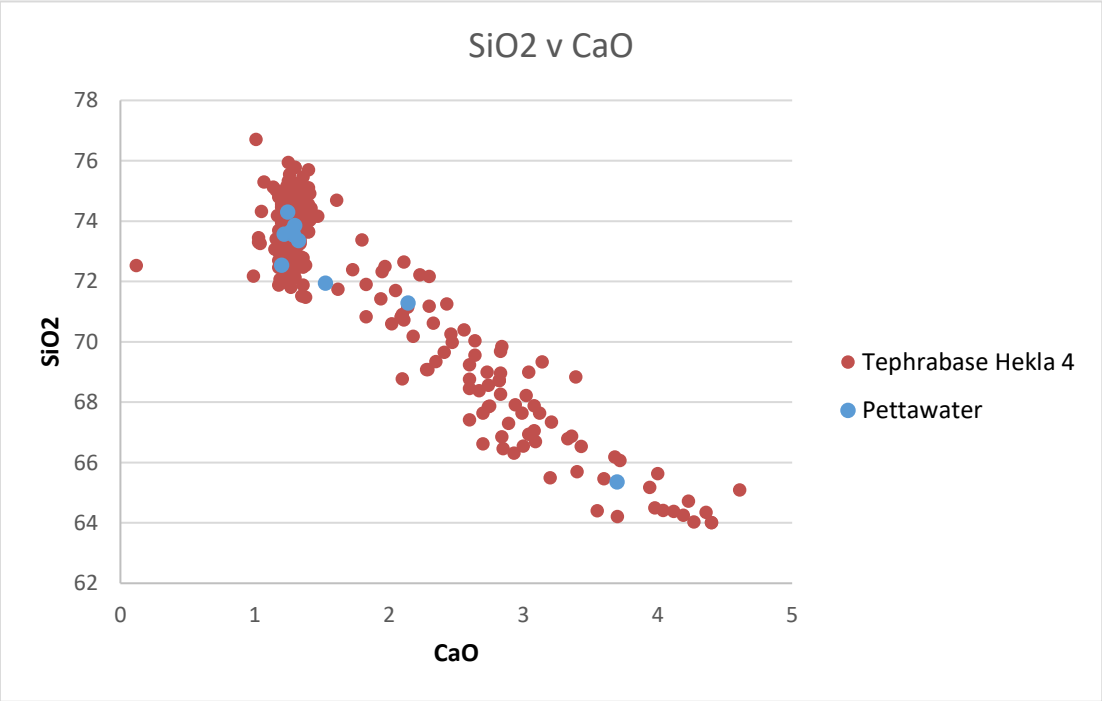

Kedills Mires

Sample	Na2O	MgO	Al2O3	K2O	CaO	FeO	SiO2	P2O5	TiO2	MnO	Total
KM1 120-121 No1	4.798	0.5386	14.6542	2.0771	3.4113	5.478	66.3941	0.1123	0.4755	0.1712	98.1103
KM1 120-121 No2	5.0169	0.1233	13.8651	2.5492	1.9673	2.6087	71.6205	0.0176	0.176	0.0887	98.0335
KM1 120-121 No3	4.5273	0.4681	14.6159	2.109	3.3147	5.3863	67.3492	0.09	0.4242	0.1695	98.4542
KM1 120-121 No4	4.7338	0.5599	14.2235	2.1115	3.1316	5.6263	66.2656	0.0924	0.4299	0.1821	97.3567
KM1 120-121 No5	4.8346	0.5537	14.4716	2.0847	3.3141	5.9017	67.0455	0.1122	0.457	0.1774	98.9526
KM1 120-121 No6	4.9413	0.4394	14.6504	2.0483	2.9659	5.3185	68.1675	0.0927	0.3792	0.1557	99.1589
KM1 120-121 No7	4.5783	0.5244	14.3897	1.9871	3.2706	5.4835	66.2779	0.109	0.4511	0.1749	97.2466
KM1 120-121 No9	5.0075	0.5278	14.2382	2.0871	3.4892	5.623	67.17	0.1126	0.433	0.1856	98.8741
KM1 120-121 No10	4.6562	0.4649	14.0179	2.1472	3.0834	5.4009	65.1036	0.0885	0.4086	0.1676	95.5389
KM1 120-121 No11	4.7306	0.4508	14.752	2.1451	3.1718	5.5157	66.7151	0.1079	0.4345	0.1583	98.1817
KM1 120-121 No12	5.0286	0.5052	14.9393	2.1127	3.3313	5.4921	66.3711	0.1084	0.4373	0.1884	98.5144
KM1 120-121 No13	5.5806	0.098	14.0254	2.4435	2.1478	2.8578	71.0766	0.0228	0.1663	0.0854	98.5043
KM1 120-121 No14	4.9771	0.5836	14.5851	2.0656	3.4387	6.1915	66.0502	0.1217	0.468	0.1862	98.6676
KM2 264-266 No1	4.12	0.3812	12.257	2.0158	2.2613	3.8863	75.2155	0.0795	0.5134	0.0927	100.8226
KM2 264-266 No2	3.8756	0.3931	12.5343	1.9771	2.3066	3.4138	75.3014	0.0794	0.5047	0.0919	100.4779
KM2 264-266 No3	4.6573	0.6232	13.0607	1.8341	3.0864	4.3155	70.3598	0.1275	0.5956	0.1004	98.7605
KM2 264-266 No5	4.1869	0.3745	12.5639	2.1024	2.349	3.3481	74.9359	0.0757	0.5171	0.0936	100.5472
KM2 264-266 No6	4.0655	1.3176	12.4541	1.7672	3.7981	5.8849	70.3884	0.1335	0.74	0.1226	100.6718
KM2 264-266 No7	4.2763	0.4472	12.3064	2.0491	2.3157	3.5832	72.7734	0.0757	0.4892	0.1096	98.4257
KM2 264-266 No8	3.8869	0.3646	12.9982	2.0797	2.4204	3.6868	74.6612	0.0669	0.5097	0.0909	100.7653
KM2 264-266 No9	3.9309	0.3896	12.1481	2.0925	2.3813	3.6079	73.9648	0.0895	0.5057	0.1022	99.2125
KM2 264-266 No10	4.4921	0.4112	11.927	2.0817	2.4317	4.0576	72.8489	0.0781	0.5239	0.0986	98.9508
KM2 264-266 No11	4.0749	0.483	12.4921	1.9524	2.4687	4.2888	72.8	0.1019	0.5969	0.0968	99.3554
KM3 330-331 No1	4.9051	0.2467	14.2067	2.2872	2.5275	4.0759	71.1795	0.0523	0.2795	0.1196	99.88
KM3 330-331 No2	5.0143	0.5276	14.9642	2.1195	3.2881	5.3599	67.6861	0.1057	0.451	0.172	99.6884
KM3 330-331 No3	5.2294	0.1477	14.2779	2.4803	1.9106	3.1125	73.4237	0.0143	0.1868	0.1067	100.89
KM3 330-331 No4	4.8189	0.5307	14.8387	2.1177	3.391	5.7342	67.8094	0.1191	0.4592	0.1543	99.9731
KM3 330-331 No5	4.8629	0.482	15.0264	2.1147	3.3411	5.6219	67.763	0.1108	0.4526	0.1724	99.9478
KM3 330-331 No6	4.8617	0.5193	14.9511	2.0705	3.3881	5.878	67.8953	0.1216	0.4554	0.1679	100.3089
KM3 330-331 No7	4.9701	0.531	14.4165	2.0267	3.6071	6.1347	67.9248	0.1065	0.4482	0.1812	100.3467
KM3 330-331 No9	5.0338	0.1391	13.6157	2.4632	1.8116	6.2745	70.0242	0.0203	0.2149	0.104	99.7013
KM3 330-331 No10	4.7236	0.5052	14.9615	2.0598	3.4446	6.0311	66.8386	0.1146	0.4362	0.176	99.2912
KM3 330-331 No11	5.0082	0.1221	14.3585	2.6089	1.9759	3.0847	73.7666	0.021	0.1775	0.093	101.2164
KM3 330-331 No13	4.7348	0.5091	14.6585	1.9953	3.5374	5.8828	66.077	0.1075	0.4443	0.1803	98.127
KM3 330-331 No14	4.8514	0.5456	15.1997	2.1782	3.392	5.6771	67.749	0.1124	0.4616	0.1665	100.3335
KM3 344-345 No2	4.882	-0.0148	12.3808	2.8165	1.2247	1.9911	73.3532	0.0026	0.0898	0.0871	96.8131
KM3 344-345 No3	4.538	0.0115	12.1919	2.8876	1.0529	1.7333	75.4832	0.0028	0.097	0.0684	98.0668
KM3 344-345 No4	4.8186	0.0263	12.54	2.879	1.3252	2.1426	74.2615	0.0042	0.0952	0.084	98.1766
KM3 344-345 No5	4.9171	0.5538	14.2674	1.7781	4.4186	8.5989	64.3383	0.186	0.6722	0.2812	100.0115
KM3 344-345 No6	4.7275	0.3902	14.3362	1.9045	4.0453	7.8519	66.1405	0.139	0.5573	0.2887	100.3811
KM3 344-345 No7	4.6406	0.001	12.6655	2.913	1.2369	1.8976	74.1073	0.0052	0.0894	0.0852	97.6419
KM3 344-345 No8	4.8948	0.516	14.2237	1.7177	4.2887	8.5485	64.5762	0.1737	0.6309	0.2804	99.8504
KM3 344-345 No9	4.84	0.0345	12.632	2.8427	1.2682	1.7796	72.8154	0.0044	0.0981	0.0764	96.3914
KM3 344-345 No10	5.0053	-0.0108	12.621	2.8883	1.3606	1.8767	75.2814	0.0086	0.0954	0.0793	99.2058
KM3 344-345 No11	4.7537	-0.0078	12.6642	2.7975	1.3149	2.2273	73.598	0.0093	0.0839	0.0859	97.5268
KM3 344-345 No12	4.8777	0.0337	12.5889	2.9149	1.3692	1.9334	73.0585	0.0098	0.0978	0.0908	96.9749

120-121 cm (Hekla 1158)

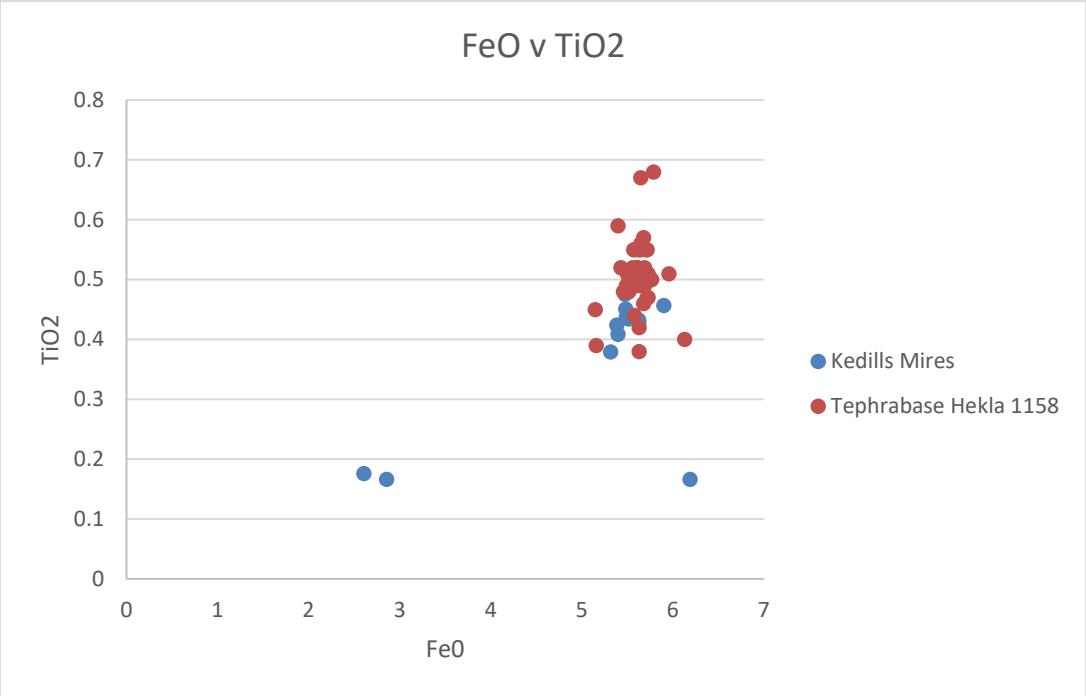

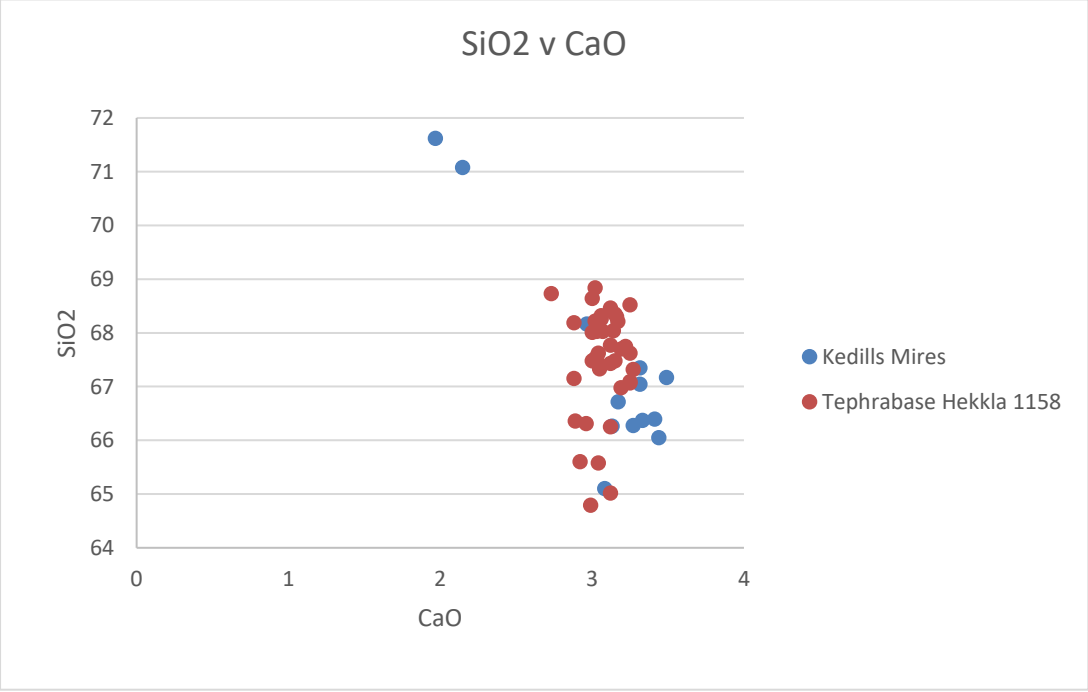

264-266 cm (Glen Garry)

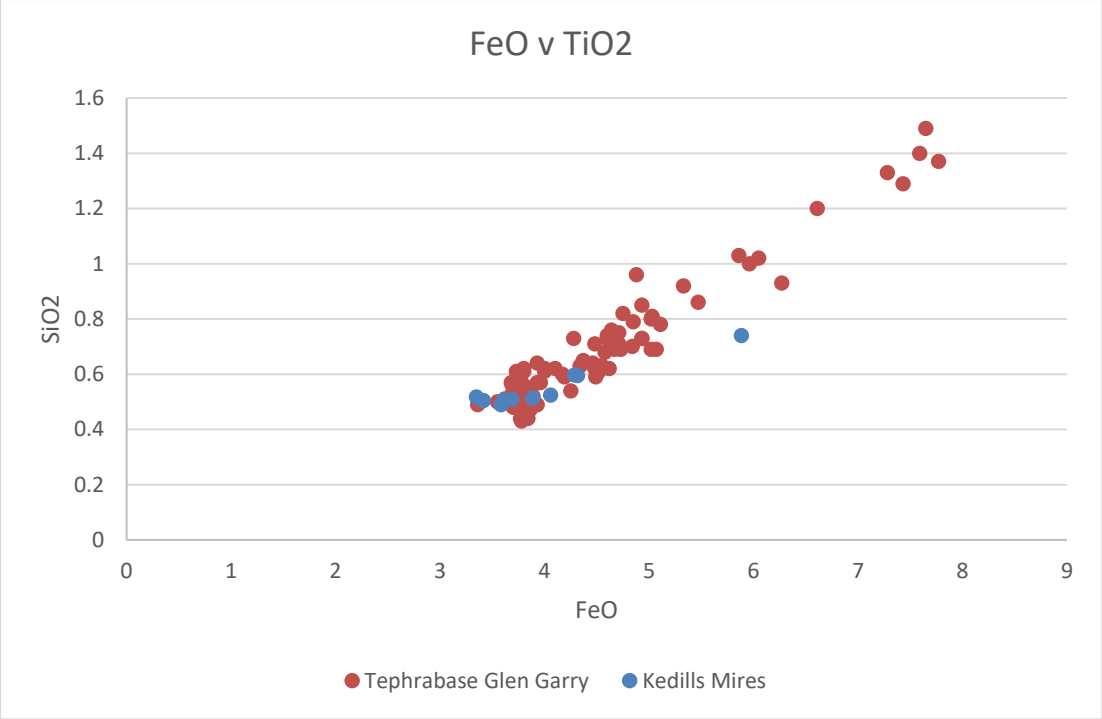

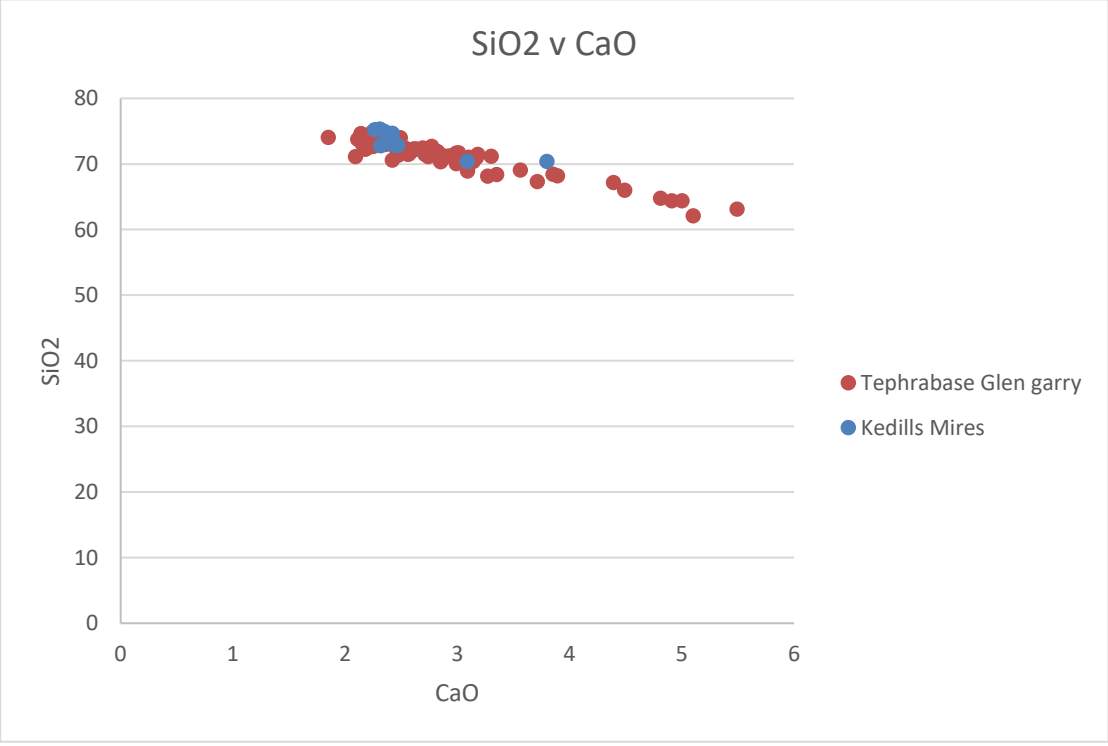

330-331 cm (Kebister)

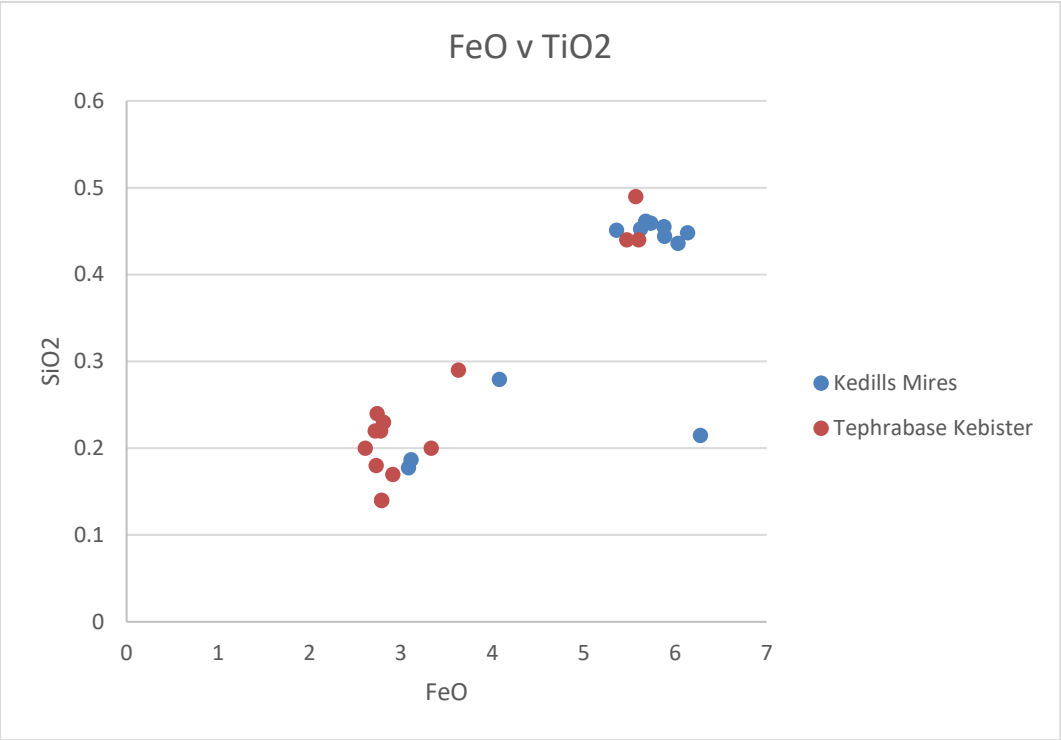

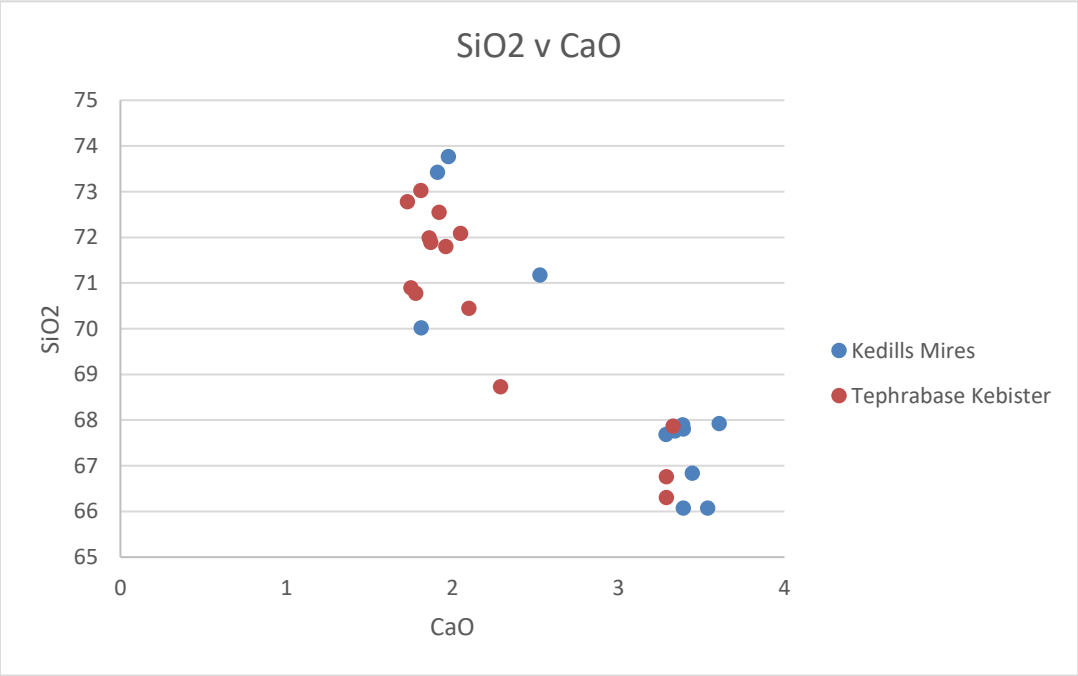

344-345 cm (Hekla 4)